

# Growing up in the city: a study of galaxy cluster progenitors at $z > 2$

Proefschrift

ter verkrijging van  
de graad van Doctor aan de Universiteit Leiden,  
op gezag van de Rector Magnificus prof. mr. P. F. van der Heijden,  
volgens besluit van het College voor Promoties  
te verdedigen op dinsdag 24 januari 2012  
klokke 15.00 uur

door

Ernst Kuiper

geboren te Amersfoort  
in 1984

## Promotiecommissie

Promotor: Prof. dr. H. J. A. Röttgering

Co-promotor: Prof. dr. G. K. Miley

Overige leden: Prof. dr. M. Franx

dr. H. Hoekstra

Prof. dr. F. P. Israel

Prof. dr. K. Kuijken

dr. N. H. Hatch (School of Physics and Astronomy, Nottingham)

dr. P. Rosati (European Southern Observatory, Garching)

dr. B. P. Venemans (Max Planck Institut für Astronomie, Heidelberg)

The work presented in this thesis is funded by the Netherlands Organization for Scientific Research (NWO).



Cover design by Bakabaka Design, [www.bakabaka.nl](http://www.bakabaka.nl)

Photo credit: cocoip, [www.flickr.com/photos/cocoip](http://www.flickr.com/photos/cocoip)



---

# TABLE OF CONTENTS

1. INTRODUCTION	1
1.1 The beginning	1
1.2 Galaxy clusters	1
1.2.1 The influence of environment	2
1.2.2 Galaxy clusters and cosmology	2
1.3 Galaxy clusters across cosmic time	3
1.4 Galaxy clusters at $z > 1.5$	4
1.5 HzRGs: powerhouses in the early Universe	5
1.6 This thesis	6
1.7 Outlook	8
2. KINEMATICS OF A $z \sim 2$ PROTOCLUSTER CORE	13
2.1 Introduction	14
2.2 Data	15
2.3 Results	18
2.3.1 Cluster membership	18
2.3.2 Overdensity	20
2.3.3 Velocity distribution	23
2.4 Discussion	26
2.4.1 A galaxy cluster progenitor	26
2.4.2 Formation scenarios	28
2.5 Conclusions	34
3. A GALAXY POPULATIONS STUDY OF A RADIO-SELECTED PROTOCLUSTER AT $z \sim 3.1$	39
3.1 Introduction	40
3.2 Data	41
3.2.1 Ground-based UV-optical imaging	41
3.2.2 HST/ACS optical imaging	43
3.2.3 Near-infrared data	43
3.2.4 Mid-infrared data	43
3.2.5 Further reduction	44
3.3 Photometry	44
3.4 Sample selection	46
3.4.1 Ly $\alpha$ and [OIII] excess objects	46

---

3.4.2	Lyman Break candidates . . . . .	46
3.4.3	Balmer Break Galaxy candidates . . . . .	49
3.4.4	Spectroscopic redshifts . . . . .	51
3.4.5	Completeness: photometric redshift selection . . . . .	52
3.5	SED fitting . . . . .	53
3.6	Results . . . . .	55
3.6.1	Number densities of galaxy populations . . . . .	55
3.6.2	Properties of protocluster galaxy candidates . . . . .	59
3.6.3	Dependance of galaxy properties on location within the proto- cluster . . . . .	65
3.7	Discussion . . . . .	68
3.7.1	Surface and volume overdensities . . . . .	68
3.7.2	Field and cluster ensemble properties . . . . .	70
3.7.3	The future of MRC 0316–257 . . . . .	72
3.8	Summary and conclusions . . . . .	73
4.	SPECTROSCOPY OF $z\sim 3$ PROTOCLUSTER CANDIDATES . . . . .	79
4.1	Introduction . . . . .	80
4.2	Sample selection & data . . . . .	82
4.3	Results . . . . .	83
4.3.1	Redshift determination . . . . .	83
4.3.2	Redshift distribution . . . . .	84
4.4	Discussion . . . . .	89
4.4.1	A possible superstructure and implications for the overdensity . . . . .	89
4.4.2	Spatial distribution . . . . .	90
4.4.3	Influence of protocluster environment on galaxy properties . . . . .	91
4.4.4	Interacting or unrelated structures? . . . . .	97
4.5	Conclusions . . . . .	100
5.	PROTOCLUSTERS WITH TUNABLE FILTERS . . . . .	105
5.1	Introduction . . . . .	106
5.2	Data . . . . .	107
5.2.1	Data reduction . . . . .	108
5.2.2	Source detection and photometry . . . . .	110
5.3	Results . . . . .	110
5.3.1	Selection of LAEs . . . . .	110
5.3.2	Redshift distribution . . . . .	114
5.3.3	Contamination . . . . .	117
5.4	Does 6C0140+326 reside in a protocluster? . . . . .	118
5.5	Conclusions & outlook . . . . .	122
6.	DISSECTING HIGH REDSHIFT RADIO GALAXIES . . . . .	127

---

6.1	Introduction . . . . .	128
6.2	Observations . . . . .	128
6.3	Results . . . . .	129
6.3.1	Colour images . . . . .	129
6.3.2	Decomposing the light from HzRGs . . . . .	130
6.3.3	Sizes of HzRGs . . . . .	134
6.3.4	Large-scale environment . . . . .	135
6.4	Discussion . . . . .	136
7.	APPENDIX . . . . .	139
7.1	Data . . . . .	140
7.1.1	Integral field spectroscopy . . . . .	140
7.1.2	Additional data . . . . .	140
7.2	Results . . . . .	140
7.2.1	Kinematics of individual objects . . . . .	140
	NEDERLANDSE SAMENVATTING . . . . .	155
	CURRICULUM VITAE . . . . .	163
	LIST OF PUBLICATIONS . . . . .	165
	DANKWOORD . . . . .	167



## INTRODUCTION

In this introduction we will present the background and framework that is necessary to better understand the work presented in this thesis. The focus of this thesis is on the progenitors of present day galaxy clusters in the early Universe. Because of this, we will give some background on the most important properties of galaxy clusters, especially in terms of the influence of environment on galaxy evolution. We will discuss several methods that are commonly used to identify galaxy clusters and we will introduce the topic of high- $z$  radio galaxies and the link these special galaxies have with forming galaxy clusters. We will also present an outlook of what the next steps will be to further this line of research.

### 1.1 The beginning

Although there are many mysteries about how our Universe was born and what, if anything, came before it, we do know from many observations that it must have started with the Big Bang. The fact that everything on large scales is moving away from each other implies that the Universe must have started out in a single point.

In the first  $10^{-32}$  seconds after the Big Bang, during the inflationary period, the Universe is thought to have expanded exponentially in volume by a factor of at least  $10^{78}$ . After the first inflation, the Universe kept on expanding, but at a slower pace and during this expansion the temperature of the Universe dropped. After  $10^{-6}$  seconds the temperature decreased enough for the first protons and neutrons to form, which after a few minutes produced the first deuterium and helium in the Big Bang nucleosynthesis. What is left after this is like a primordial soup, consisting mostly of protons, electrons and photons. This soup was almost homogeneously spread across the Universe, apart from some small variations in the matter density. And these small variations would shape the Universe into what we observe today.

### 1.2 Galaxy clusters

The variations in the matter density distribution directly after the Big Bang have shaped how our Universe currently looks. As gravity draws more matter towards

the densest regions, a characteristic web-like structure emerges. Matter falls together in sheets, which in turn collapse to filaments. These filaments themselves connect and feed the nodes of highest large-scale density in the Universe: galaxy clusters.

Galaxy clusters are large structures that can contain hundreds to thousands of galaxies, they can have masses exceeding  $10^{15} M_{\odot}$  and have radii of the order of 1 Mpc. They were first identified as large concentrations in the projected galaxy distribution on the sky (e.g. Abell 1958). The Virgo and Coma clusters are well-known local galaxy clusters. Galaxy clusters also presented the first evidence for the existence of dark matter as the dynamical mass of the Virgo cluster seemed to significantly exceed that of the luminous matter (Smith 1936).

### 1.2.1 The influence of environment

One of the most striking properties of galaxy clusters is that the innermost and densest regions contain predominantly red early-type galaxies and lack blue late-type galaxies (Dressler 1980; Butcher & Oemler 1984), whereas the fraction of blue late-type galaxies increases as the density decreases. These are also known as the morphology-density and colour-density relation. These relations are a strong indication that the cluster environment must influence the galaxy evolution in some way, transforming star-forming spiral galaxies into red-and-dead ellipticals.

There are also differences between early-type galaxies in clusters and in the field. Early-type galaxies in cluster environments are typically older by 1.5 Gyr in the local Universe (Clemens et al. 2006; Sánchez-Blázquez et al. 2006). This means that elliptical galaxies in the field formed their stars 1.5 Gyr later than ellipticals in clusters. Similar studies have also been done at higher redshifts finding age differences of  $\sim 0.5$  Gyr (van Dokkum & van der Marel 2007; Gobat et al. 2008).

Galaxy clusters are also the home of cD galaxies, the most massive galaxies known with masses exceeding  $10^{12} M_{\odot}$ . The fact that these galaxies are exclusively located in galaxy clusters is strong evidence that the cluster environment has played a pivotal role in shaping these galaxies.

It is thus clear that the environment somehow influences galaxy evolution, but what processes cause this effect is mostly unknown. A few are proposed in the literature, such as ram-pressure stripping (Gunn & Gott 1972; Brüggén & De Lucia 2008), galaxy mergers (Barnes & Hernquist 1996; Murante et al. 2007), harassment (i.e. rapid tidal encounters, Farouki & Shapiro 1981; Moore et al. 1998), strangulation (i.e. loss of the hot halo, Larson et al. 1980; McCarthy et al. 2008) and AGN feedback (Nesvadba et al. 2006; Bower et al. 2006), but how these processes interplay, which one is dominant and when these processes act is still unclear.

### 1.2.2 Galaxy clusters and cosmology

Although this will not be treated in this thesis, galaxy clusters are also important cosmological tools. The space density of galaxy clusters depends strongly on the

exact cosmological parameters and the observed number of clusters at a given mass and given redshift can be used to get direct estimates of  $\sigma_8$  and  $\Omega_m$  (e.g. Frenk et al. 1990; Viana & Liddle 1996; Bahcall et al. 1997; Borgani et al. 2001; Gladders et al. 2007; Sahlén et al. 2009; Mantz et al. 2010). Studying galaxy clusters thus serves as an excellent independent test for the  $\Lambda$  Cold Dark Matter model.

### 1.3 Galaxy clusters across cosmic time

Understanding galaxy formation and evolution is one of the most important tasks of present day astronomy. To achieve this it is essential to understand what the influence of environment is, what physical processes cause this environmental effect and when these processes occur. Therefore, we must study galaxy clusters across cosmic time. To be able to do this in a meaningful way it is necessary to identify a sufficiently large sample of galaxy clusters at all possible redshifts. In this section we discuss some of the methods currently used to locate galaxy clusters.

#### X-ray emission

Clusters contain different kinds of material. The vast majority of the matter is dark matter and the remainder is baryonic matter. The baryonic matter can be roughly divided into the galaxies and their stellar and gaseous content and the intracluster medium (ICM). The latter is gas that is not locked in galaxies and makes up approximately 15 per cent of the cluster mass. Because of the deep potential well of the cluster, it has been shock-heated to very high temperatures ( $10^6$ - $10^7$  K) as it entered the dark matter halo. This hot ICM is fully ionised and because of this emits X-rays through non-thermal brehmsstrahlung.

The total luminosity of the X-ray emission can be up to  $10^{43}$ - $10^{45}$  erg  $s^{-1}$  making it detectable even at cosmological distances. Since it also acts as a powerful diagnostic tool, the extended X-ray emission is one of the prime ways of identifying and studying galaxy clusters. The ROSAT X-ray satellite was one of the first X-ray satellites that could robustly detect large numbers of galaxy clusters up to  $z < 1$  (e.g. Truemper 1993; Ebeling et al. 1998; Burenin et al. 2007). Recent works with, in particular, the XMM satellite are pushing this to higher redshifts (e.g. Mehrrens et al. 2011).

#### Red sequence searches

One of the most straightforward methods of identifying galaxy clusters uses the fact that clusters host a large number of more evolved, red galaxies. Observing a field with a galaxy cluster should therefore show an overdensity of red galaxies which are possibly spatially concentrated.

Several surveys have used this method to identify large numbers of galaxy clusters across the sky. A well-known survey aimed at finding galaxy clusters is the Red-sequence Cluster Survey (RCS, Gladders & Yee 2005) which found  $> 400$  galaxy clusters in  $100 \text{ deg}^2$ , with  $\sim 15$  per cent at  $z > 0.9$ .

The success of the RCS has led to multiple follow-up surveys aimed at finding both  $z < 1$  and  $z > 1$  galaxy clusters. One of the most ambitious surveys for  $z < 1$  is RCS-2, the direct follow-up of RCS. RCS-2 is still ongoing and will use the MegaCam on the Canada-France-Hawaii Telescope to cover  $\sim 1000 \text{ deg}^2$ .

To effectively select clusters at  $z > 1$  the *Spitzer* Space Telescope can be used. Two surveys are currently doing this. The first is the *Spitzer* Adaptation of the Red-sequence Cluster Survey (SpARCS, Wilson et al. 2008; Muzzin et al. 2009) which is ongoing and will cover  $41.9 \text{ deg}^2$ . Another high- $z$  cluster survey is the *Spitzer* IRAC Shallow Survey (Eisenhardt et al. 2008) which identified  $> 300$  galaxy clusters in a field of  $7.25 \text{ deg}^2$ . Approximately 30% of these clusters are located at  $z > 1$ .

### The Sunyaev-Zeldovich effect

With the advent of the Planck satellite in 2009 and the ground-based South Pole Telescope (SPT) and Atacama Cosmology Telescope (ACT) in 2007, recent years have seen a strong increase in the detection of galaxy clusters discovered by using the Sunyaev-Zeldovich (SZ) effect. The SZ effect is caused by inverse Compton scattering of CMB photons on high energy electrons. The hot, ionised intracluster gas contains many of such electrons, which will cause the low energy CMB photons to be upscattered. A galaxy cluster will therefore leave a distortion (a hot or cold spot) in the CMB, which can be observed.

One of the most important properties of the SZ effect is that clusters are identified by observing a difference with respect to the CMB. This makes it independent of redshift and allows for the detection of galaxy clusters in a large redshift interval. At the moment of writing, galaxy clusters have been detected with the SZ effect up to  $z \sim 1.1$  (e.g. Staniszewski et al. 2009; Menanteau et al. 2010; Williamson et al. 2011; Planck Collaboration et al. 2011).

## 1.4 Galaxy clusters at $z > 1.5$

The problem with the methods described above is that they work very well for  $z < 1.5$ , but they break down for larger redshifts. This is partially due to limitations on the observations. For instance, the X-ray emission becomes too faint to be detected. However, it is likely also caused by the fact that galaxy clusters as we observe them locally are simply incredibly rare at  $z > 1.5$ . Instead, there are structures that are still in the process of formation, that will become galaxy clusters but are not there yet. These galaxy cluster progenitors may not be virialised or may not be massive enough to show strong X-ray emission. Similarly, the red sequence in these early galaxy clusters is not well established yet.

This has led to something of a barrier at  $z = 1.5$ , beyond which finding galaxy clusters, or galaxy cluster progenitors, becomes increasingly difficult. In fact, at the moment of writing only a handful of galaxy clusters at  $z > 1.5$  with X-ray emission and spectroscopic confirmation are known. The first galaxy cluster above  $z = 1.5$  was found at  $z \sim 1.62$  independently by both Papovich et al. (2010) and



Tanaka et al. (2010). Since then a few others have been found with  $1.5 < z < 1.75$  (Henry et al. 2010; Fassbender et al. 2011; Santos et al. 2011), with the current record holder being the cluster at  $z = 2.07$  discovered by Gobat et al. (2011).

It is, however, important to go beyond  $z = 1.5$ . The cosmic star formation rate density peaks at  $z \sim 2$  which heralds an important stage in galaxy evolution. Also, there is a clear relation between star formation rate and galaxy density in the local Universe as the star formation rate decreases with increasing density. Various recent studies have shown that at earlier times this relation turns around and that in the densest regions the star formation is higher (Elbaz et al. 2007; Cooper et al. 2008; Tran et al. 2010; Hilton et al. 2010; Popesso et al. 2011). This indicates that there is an important period in galaxy cluster evolution at  $z > 1.5$  that we have not yet been able to observe.

## 1.5 HzRGs: powerhouses in the early Universe

In this thesis we use high- $z$  radio galaxies (HzRGs, Miley & De Breuck 2008) to find galaxy cluster progenitors. As the name implies, HzRGs are galaxies located at  $z > 2$  that show large radio luminosities. These large radio luminosities are caused by an active supermassive black hole at the centre of the galaxy.

The extreme nature of HzRGs makes these objects well worth investigating, but what links these objects to galaxy clusters? HzRGs have been shown to have large restframe optical luminosities. Since restframe optical light traces the bulk of the stellar mass of a galaxy, this means that HzRGs have large stellar masses. Seymour et al. (2007) have studied a large number of HzRGs with the *Spitzer* IRAC and MIPS cameras to determine their stellar masses and found in general values of  $10^{11} - 10^{12} M_{\odot}$ .

Apart from this there are many other indications that HzRGs are forming massive galaxies. Many radio galaxies are, for instance, at the centre of Ly $\alpha$  halos indicating a large reservoir of ionised gas; gas that can be used for star formation. Also, the morphology of many radio galaxies is clumpy and irregular, implying active merging. Finally, the restframe UV and millimetre light indicate large SFRs of the order of  $500-1000 M_{\odot} \text{ yr}^{-1}$ . All of these observations indicate that HzRGs will end up as very massive galaxies.

This is important because in the case of hierarchical galaxy formation, the smaller galaxies form first. These small galaxies then merge and coalesce to form the larger, more massive galaxies. According to this picture, a massive galaxy must have been built up from a large number of smaller galaxies. So the area around a massive galaxy should have a larger density. Since the HzRGs are very massive, it is therefore logical that they should reside in overdense regions. If the overdensity is strong enough, such a region may then evolve into a local massive galaxy cluster.

That HzRGs are possibly at the centre of forming clusters is also confirmed by the large rotation measures of the order of  $1000 \text{ rad m}^{-2}$  that are measured for some HzRGs (Carilli et al. 1994, 1997; Athreya et al. 1998). This is commonly interpreted

as the HzRGs being embedded in dense hot gas. Locally, these large rotation measures are only observed in galaxy clusters and therefore this can be considered as circumstantial evidence that HzRGs are indeed at the centre of forming galaxy clusters.

Targeting the environment of HzRGs could thus lead to the discovery of galaxy cluster progenitors at  $z > 2$ , which could in turn significantly expand our knowledge of galaxy cluster formation and the role of the environment on galaxy evolution. Furthermore, since HzRGs are massive, they are excellent candidates for becoming cD galaxies.

Many recent studies have tried to prove that this concept of HzRGs as tracers of galaxy cluster progenitors is true (e.g. Pascarelle et al. 1996; Knopp & Chambers 1997; Pentericci et al. 2000; Kurk et al. 2004b,a; Overzier et al. 2006, 2008; Venemans et al. 2007; Matsuda et al. 2011). This is often done using narrowband filters, which allows for the selection of emission line galaxies at the redshift of interest and has proved to be the most efficient method of finding overdensities.

The past few years have seen some interesting results in the field of protoclusters and HzRGs. For instance, Venemans et al. (2007) conducted the largest study of protoclusters to date and found that the velocity dispersion of these structures increases with decreasing redshift. This is consistent with the results of simulations of cluster formation. Furthermore, Zirm et al. (2008) and Kodama et al. (2007) have found evidence that some  $z \sim 2$  protoclusters show evidence for an emerging red sequence. Finally, Hatch et al. (2011) have shown that the  $H\alpha$  emitters in a  $z \sim 2$  protocluster are more massive than the same galaxies in the field, thereby supplying powerful evidence that the influence of environment is already apparent at  $z \sim 2$ .

## 1.6 This thesis

In this thesis we attempt to further the work done on both protoclusters and HzRGs in order to better establish a picture of galaxy cluster progenitors at  $z > 2$ . We have done this both in terms of the galaxies that inhabit these clusters and the structures as a whole.

### Chapter 2

We begin the thesis with a study of the Spiderweb galaxy at  $z \sim 2.15$ . It is one of the most studied HzRGs and is known to be at the centre of a protocluster. We obtained deep SINFONI data of the radio galaxy and its immediate surroundings which harbours a large number of small galaxies.

We show that 10 of the satellite galaxies are located at the redshift of the radio galaxy and are therefore in the protocluster. This implies that the central region of the protocluster is as dense as the outskirts of local galaxy clusters. We also find a broad, bimodal velocity distribution that cannot be explained by the presence of one massive virialised halo. A merger scenario, however, is able to reproduce the

observations.

### Chapter 3

For this chapter we attempt to obtain a complete galaxy census for the protocluster around HzRG MRC 0316-257 at  $z = 3.13$ . We do this using photometry in 18 bands ranging from  $U$  band to *Spitzer* 8.5  $\mu\text{m}$ . Applying different colour cuts we select blue, star forming Lyman Break Galaxies (LBGs) and red Balmer Break Galaxies (BBGs) that are approximately at the redshift of the protocluster.

We find a mild surface overdensity for the LBGs, but not for the BBGs. We also attempt to compare to literature studies in order to determine whether there are systematic differences between field and protocluster galaxies. We find no significant differences in terms of stellar mass and star formation rate. However, within the protocluster there is tentative evidence that galaxies near to the radio galaxy are more massive and form more stars.

### Chapter 4

A follow-up to the work presented in Chapter 3 is presented here. In order to draw meaningful conclusions on environmental influence it is necessary to be able to distinguish between field galaxies and protocluster galaxies. This could not be done accurately with the data available in Chapter 3. Therefore, in this chapter we present spectroscopic observations of a number of the LBGs identified in Chapter 3. By obtaining spectroscopic redshifts for these galaxies we can unequivocally say which galaxies truly belong to the protocluster. This thus allows for a fully self-consistent comparison between galaxy properties in the field and in the protocluster.

Out of a sample of 20 objects we find three to be in the protocluster and five to reside in a structure directly in front of the 0316 protocluster. However, in contrast to the results presented in Chapter 2, we find that these two structures are likely unrelated. Comparing the properties of the galaxies within both structures and the field, the only difference we find is in the strength of the  $\text{Ly}\alpha$  flux. The 0316 protocluster galaxies show larger  $\text{Ly}\alpha$  flux than field galaxies, whereas the galaxies in the foreground structure show very little  $\text{Ly}\alpha$  flux. The strong  $\text{Ly}\alpha$  flux in the 0316 galaxies could possibly be attributed to a lack of dust. Why the two protocluster structures differ so strongly remains unknown for now.

### Chapter 5

In this chapter we present the first results of a large observing program with the OSIRIS instrument at the Gran Telescopio Canarias, aimed to identify a large sample of protoclusters around HzRGs. By using a relatively new technique that employs tunable narrowband filters we can efficiently search for emission line galaxies at any arbitrary redshift. The pilot study focuses on the HzRG 6C0140+326 at  $z \sim 4.4$ .

We find a total of 27 Ly $\alpha$  emitters in the field. Due to the nature of the tunable filters and multiple passes at different central wavelengths we are able to obtain a rough redshift distribution and we distinguish between a foreground and protocluster field. This shows that the foreground field contains significantly fewer emitters than the protocluster field. If we compare to the literature we find that the protocluster field is a factor  $9 \pm 5$  denser than a blank field. Also, the redshift distribution is significantly different from the expected distribution, with the Ly $\alpha$  emitters concentrated at  $z > 4.38$ . There is thus evidence for a protocluster in this field.

## Chapter 6

For this chapter we focus less on the protocluster environment and more on the radio galaxies. We study two HzRGs at  $z \sim 2.5$  using optical and near-infrared imaging obtained with the new WFC3 instrument aboard the Hubble Space Telescope. Both HzRGs show a complex morphology with clumps and filaments, which we attempt to explain by dissecting the light into different contributing sources.

In both cases the light from the extended structures is consistent with being scattered AGN light and nebular emission, with a possible contribution from young stars. The red population, commonly associated with older stars, is located in a single clump that shows no signs of recent disturbances. The size of the red population is consistent with that of other distant, massive galaxies. We also investigate the surrounding field and find no overdensities. Therefore, it seems that these HzRGs are very similar to other massive galaxies at  $z > 2$  and the difference in appearance is mostly due to the strong AGN feedback.

## Chapter 7

This chapter will act as an appendix showing some additional results obtained from the SINFONI data of the Spiderweb galaxy, but which were not included in Chapter 2. These results may lead to future research.

### 1.7 Outlook

Scientific research will exist as long as there are questions to be asked. This is most definitely the case for the field of protoclusters and HzRGs. One of the most important issues for protocluster research is the limited sample size. As already mentioned, the largest study of protoclusters at the moment is the work of Venemans et al. (2007) which included a total of 6 protocluster fields. This is hardly enough to conduct a meaningful statistical study. Therefore, one of the main objectives is to expand this sample. The groundwork for this is done in Chapter 5, where we conduct a pilot study employing tunable narrowband filters. A large number of at least 15 HzRG fields are still waiting to be observed and this may yield a large sample of new protoclusters to study. This may shed light on the

formation history of these structures. Similarly, the South African Large Telescope with its large number of narrowband filters, could prove very worthwhile in this.

Of course, there is also a large number of new and exciting astronomical facilities that will significantly increase our knowledge of both HzRGs and protoclusters over the coming years and decades. The LOw Frequency ARray (LOFAR) will, for instance, be able to detect HzRGs out to  $z \sim 8$ , opening up a unique new window for studying the very early Universe. Also, the new generation of 30-m-class ground-based telescopes and the James Webb Space Telescope will further this field of research by leaps and bounds.

## References

- Abell G. O., 1958, *ApJS*, 3, 211
- Athreya R. M., Kapahi V. K., McCarthy P. J., van Breugel W., 1998, *A&A*, 329, 809
- Bahcall N. A., Fan X., Cen R., 1997, *ApJ*, 485, L53+
- Barnes J. E., Hernquist L., 1996, *ApJ*, 471, 115
- Borgani S. et al., 2001, *ApJ*, 561, 13
- Bower R. G., Benson A. J., Malbon R., Helly J. C., Frenk C. S., Baugh C. M., Cole S., Lacey C. G., 2006, *MNRAS*, 370, 645
- Brüggen M., De Lucia G., 2008, *MNRAS*, 383, 1336
- Burenin R. A., Vikhlinin A., Hornstrup A., Ebeling H., Quintana H., Mescheryakov A., 2007, *ApJS*, 172, 561
- Butcher H., Oemler Jr. A., 1984, *ApJ*, 285, 426
- Carilli C. L., Owen F. N., Harris D. E., 1994, *AJ*, 107, 480
- Carilli C. L., Roettgering H. J. A., van Ojik R., Miley G. K., van Breugel W. J. M., 1997, *ApJS*, 109, 1
- Clemens M. S., Bressan A., Nikolic B., Alexander P., Annibali F., Rampazzo R., 2006, *MNRAS*, 370, 702
- Cooper M. C. et al., 2008, *MNRAS*, 383, 1058
- Dressler A., 1980, *ApJ*, 236, 351
- Ebeling H., Edge A. C., Bohringer H., Allen S. W., Crawford C. S., Fabian A. C., Voges W., Huchra J. P., 1998, *MNRAS*, 301, 881
- Eisenhardt P. R. M. et al., 2008, *ApJ*, 684, 905
- Elbaz D. et al., 2007, *A&A*, 468, 33
- Farouki R., Shapiro S. L., 1981, *ApJ*, 243, 32
- Fassbender R. et al., 2011, *A&A*, 527, L10+
- Frenk C. S., White S. D. M., Efstathiou G., Davis M., 1990, *ApJ*, 351, 10
- Gladders M. D., Yee H. K. C., 2005, *ApJS*, 157, 1
- Gladders M. D., Yee H. K. C., Majumdar S., Barrientos L. F., Hoekstra H., Hall P. B., Infante L., 2007, *ApJ*, 655, 128
- Gobat R. et al., 2011, *A&A*, 526, A133+
- Gobat R., Rosati P., Strazzullo V., Rettura A., Demarco R., Nonino M., 2008, *A&A*, 488, 853
- Gunn J. E., Gott III J. R., 1972, *ApJ*, 176, 1
- Hatch N. A., Kurk J. D., Pentericci L., Venemans B. P., Kuiper E., Miley G. K., Röttgering H. J. A., 2011, *MNRAS*, 415, 2993
- Henry J. P. et al., 2010, *ApJ*, 725, 615
- Hilton M. et al., 2010, *ApJ*, 718, 133
- Knopp G. P., Chambers K. C., 1997, *ApJS*, 109, 367
- Kodama T., Tanaka I., Kajisawa M., Kurk J., Venemans B., De Breuck C., Vernet J., Lidman C., 2007, *MNRAS*, 377, 1717
- Kurk J. D., Pentericci L., Overzier R. A., Röttgering H. J. A., Miley G. K., 2004a, *A&A*, 428, 817
- Kurk J. D., Pentericci L., Röttgering H. J. A., Miley G. K., 2004b, *A&A*, 428, 793
- Larson R. B., Tinsley B. M., Caldwell C. N., 1980, *ApJ*, 237, 692
- Mantz A., Allen S. W., Rapetti D., Ebeling H., 2010, *MNRAS*, 406, 1759
- Matsuda Y. et al., 2011, *MNRAS*, 1087
- McCarthy I. G., Frenk C. S., Font A. S., Lacey C. G., Bower R. G., Mitchell N. L., Balogh M. L., Theuns T., 2008, *MNRAS*, 383, 593

- Mehrtens N. et al., 2011, ArXiv e-prints
- Menanteau F. et al., 2010, ApJ, 723, 1523
- Miley G., De Breuck C., 2008, A&A Rev, 15, 67
- Moore B., Lake G., Katz N., 1998, ApJ, 495, 139
- Murante G., Giovalli M., Gerhard O., Arnaboldi M., Borgani S., Dolag K., 2007, MNRAS, 377, 2
- Muzzin A. et al., 2009, ApJ, 698, 1934
- Nesvadba N. P. H., Lehnert M. D., Eisenhauer F., Gilbert A., Tecza M., Abuter R., 2006, ApJ, 650, 693
- Overzier R. A. et al., 2008, ApJ, 673, 143
- Overzier R. A. et al., 2006, ApJ, 637, 58
- Papovich C. et al., 2010, ApJ, 716, 1503
- Pascarelle S. M., Windhorst R. A., Driver S. P., Ostrander E. J., Keel W. C., 1996, ApJ, 456, L21+
- Pentericci L. et al., 2000, A&A, 361, L25
- Planck Collaboration, Ade P. A. R., Aghanim N., Arnaud M., Ashdown M., Aumont J., Baccigalupi C., Balbi A., Banday A. J., Barreiro R. B., et al., 2011, ArXiv e-prints
- Popesso P. et al., 2011, A&A, 532, A145+
- Sahlén M. et al., 2009, MNRAS, 397, 577
- Sánchez-Blázquez P., Gorgas J., Cardiel N., González J. J., 2006, A&A, 457, 809
- Santos J. S. et al., 2011, A&A, 531, L15+
- Seymour N. et al., 2007, ApJS, 171, 353
- Smith S., 1936, ApJ, 83, 23
- Staniszewski Z. et al., 2009, ApJ, 701, 32
- Tanaka M., Finoguenov A., Ueda Y., 2010, ApJ, 716, L152
- Tran K.-V. H. et al., 2010, ApJ, 719, L126
- Trümper J., 1993, Science, 260, 1769
- van Dokkum P. G., van der Marel R. P., 2007, ApJ, 655, 30
- Venemans B. P. et al., 2007, A&A, 461, 823
- Viana P. T. P., Liddle A. R., 1996, MNRAS, 281, 323
- Williamson R. et al., 2011, ApJ, 738, 139
- Wilson G. et al., 2008, in Astronomical Society of the Pacific Conference Series, Vol. 381, Infrared Diagnostics of Galaxy Evolution, R.-R. Chary, H. I. Teplitz, & K. Sheth, ed., pp. 210–+
- Zirm A. W. et al., 2008, ApJ, 680, 224





---

# A SINFONI VIEW OF FLIES IN THE SPIDERWEB: A GALAXY CLUSTER IN THE MAKING

The environment of the high- $z$  radio galaxy PKS 1138-262 at  $z \sim 2.2$  is a prime example of a forming galaxy cluster. We use deep SINFONI integral field spectroscopy to perform a detailed study of the kinematics of the galaxies within 60 kpc of the radio core and we link this to the kinematics of the protocluster on the megaparsec scale. Identification of optical emission lines shows that 11 galaxies are at the redshift of the protocluster. The density of line emitters is more than an order of magnitude higher in the core of the protocluster with respect to the larger scale environment. This implies a galaxy overdensity in the core of  $\delta_g \sim 200$  and a matter overdensity of  $\delta_m \sim 70$ , the latter of which is similar to the outskirts of local galaxy clusters. The velocity distribution of the confirmed satellite galaxies shows a broad, double-peaked velocity structure with  $\sigma = 1360 \pm 206 \text{ km s}^{-1}$ . A similar broad, double-peaked distribution was found in a previous study targeting the large scale protocluster structure, indicating that a common process is acting on both small and large scales. Including all spectroscopically confirmed protocluster galaxies, a velocity dispersion of  $1013 \pm 87 \text{ km s}^{-1}$  is found. We show that the protocluster has likely decoupled from the Hubble flow and is a dynamically evolved structure. Comparison to the Millenium simulation indicates that the protocluster velocity distribution is consistent with that of the most massive haloes at  $z \sim 2$ , but we rule out that the protocluster is a fully virialized structure based on dynamical arguments and its X-ray luminosity. Comparison to merging haloes in the Millennium simulation shows that the structure as observed in and around the Spiderweb galaxy is best interpreted as being the result of a merger between two massive haloes. We propose that the merger of two subclusters can result in an increase in star formation and AGN activity in the protocluster core, therefore possibly being an important stage in the evolution of massive cD galaxies.

E. Kuiper, N. A. Hatch, G. K. Miley, N. P. H. Nesvadba, H. J. A. Röttgering,  
J. D. Kurk, M. D. Lehnert, R. A. Overzier, L. Pentericci, J. Schaye,  
B. P. Venemans

*Monthly Notices of the Royal Astronomical Society*, **415**, 2245 (2011)

## 2.1 Introduction

Galaxy clusters are the densest large scale environments in the known Universe and are therefore excellent laboratories for studying several of the key questions in present day astronomy. The morphology-density relation (e.g. Dressler 1980) observed in local galaxy clusters indicates that the environment of galaxies influences galaxy evolution, but when and how this happens is still unknown. Also, local galaxy clusters harbour cD galaxies, the most massive known galaxies in the Universe. Since these galaxies are exclusively located in the centres of galaxy clusters, it is likely that the cluster environment is pivotal in their formation. Finally, the emergence of large scale structure puts a strong constraint on cosmological models and parameters.

To fully understand the role of galaxy clusters in these issues, it is essential to study galaxy clusters across cosmic time. Recent years have seen the discovery of a few galaxy clusters at  $z > 1.5$  (Wilson et al. 2008; Papovich et al. 2010; Tanaka et al. 2010; Henry et al. 2010; Gobat et al. 2011), but these structures remain elusive and difficult to find at such high redshifts. One of the few methods of locating galaxy clusters at  $z > 2$  is targeting the environment of high- $z$  radio galaxies (hereafter HzRGs, Miley & De Breuck 2008). These HzRGs show powerful extended radio emission and have large stellar masses of  $10^{11}$  to  $10^{12} M_{\odot}$  (Rocca-Volmerange et al. 2004; Seymour et al. 2007). As hierarchical galaxy formation dictates that the most massive galaxies originate in the densest environments, it is likely that these HzRGs are at the centres of overdensities. These overdensities may in turn be the progenitors of massive galaxy clusters. In recent years many studies have focused on finding galaxy overdensities around HzRGs (e.g. Pascarelle et al. 1996; Knopp & Chambers 1997; Pentericci et al. 2000; Venemans et al. 2005; Overzier et al. 2006, 2008; Kuiper et al. 2010; Galametz et al. 2010; Hatch et al. 2011).

One of the most studied HzRGs is PKS 1138-262 at  $z \sim 2.15$  (see Fig. 2.1). The stellar mass of this radio galaxy is estimated to be  $\sim 10^{12} M_{\odot}$  (Seymour et al. 2007; Hatch et al. 2009, hereafter H09), among the largest known at  $z > 2$  and similar to the stellar masses found for local cD galaxies. It is surrounded by a giant Ly $\alpha$  halo powered by the AGN and young, hot stars and it is embedded in dense hot ionized gas ( $RM \sim 6200 \text{ rad m}^{-2}$ , Pentericci et al. 1997; Carilli et al. 1997). Furthermore, high resolution VLA radio observations show the presence of a radio jet with a bend. This all implies that this radio galaxy sits at the centre of a dense cluster like medium with possibly a cooling flow (Pentericci et al. 1997).

Deep HST imaging shows tens of satellite galaxies, many of which are thought to be merging with the central galaxy (Miley et al. 2006). The restframe FUV continuum morphology of the radio galaxy is clumpy and disturbed, further strengthening the notion of strong active merging and has earned it the name of ‘Spiderweb Galaxy’. Such a complex morphology agrees qualitatively with predictions of hierarchical galaxy formation models (e.g. Saro et al. 2009).

Surrounding the central HzRG are overdensities of Ly $\alpha$  and H $\alpha$  emitting galax-

ies, extremely red objects (EROs), X-ray emitters and sub-mm bright galaxies (Pentericci et al. 2000; Kurk et al. 2004b,a; Stevens et al. 2003; Croft et al. 2005; Zirm et al. 2008; Kodama et al. 2007). Furthermore, Kurk et al. (2004a) have shown that the galaxies are spatially segregated, with the  $H\alpha$  emitting galaxies and EROs being more centrally concentrated than the  $Ly\alpha$  emitting galaxies. H09 showed that if the many nearby satellites are truly located in the protocluster, then a fraction may merge with the radio galaxy before  $z = 0$ . Tidal stripping of these satellites could in turn lead to a substantial extended stellar halo as seen in local cD galaxies. Also, Hatch et al. (2008) provide evidence for in-situ star formation between the individual clumps, indicating another possible method for forming such an extended stellar halo. All these aspects make the Spiderweb system a unique laboratory for studying not only important ingredients of massive galaxy formation, such as merging, downsizing and the effect of AGN feedback, but also the formation of galaxy clusters and the influence of the protocluster environment on galaxy evolution.

In this work we present results obtained using deep integral field spectroscopy data of the core of the Spiderweb protocluster<sup>1</sup>. Previous work on this particular region using integral field data has been done by Nesvadba et al. (2006) (hereafter N06). The N06 study focused on the central radio core and its host galaxy and found evidence for the presence of strong outflows with velocities of the order of  $\sim 2000 \text{ km s}^{-1}$ . These outflows are consistent with being powered by the AGN, indicating that AGN feedback plays an important role in expelling gas from galaxies thus truncating star formation.

In this follow-up study we focus on the immediate environment of the radio core and the satellite galaxies located within 60 kpc of it. We combine the integral field data with all available spectroscopic redshifts in the literature to obtain the best census of the cluster population to date. We also investigate the nature of such a protocluster structure by comparing our results to simulations. An indepth study of the internal dynamics of the brightest individual satellites will be presented in an upcoming work (see Chapter 7 for preliminary results). Throughout this Chapter we use a standard  $\Lambda$ CDM cosmology with  $H_0 = 71 \text{ km s}^{-1} \text{ Mpc}^{-1}$ ,  $\Omega_M = 0.27$  and  $\Omega_\Lambda = 0.73$ .

## 2.2 Data

We observed the Spiderweb Galaxy ( $\alpha = 11 : 40 : 48.3$ ,  $\delta = -26 : 29 : 08.7$ ) with the Spectrograph for INtegral Field Observations in the Near Infrared (SINFONI, Eisenhauer et al. 2003) in seeing limited mode on UT4 at the Very Large Telescope (VLT) on several nights in December 2007 and February 2008. SINFONI is a medium-resolution, image-slicing integral-field spectrograph that has a  $8'' \times 8''$  field

---

<sup>1</sup>There is no evidence that the radio galaxy is truly at the centre of the structure. However, the radio galaxy is a viable cD galaxy progenitor and the density of protocluster candidates around it is large. Therefore, for the sake of brevity we refer to the SINFONI field as the ‘core’ of the protocluster.

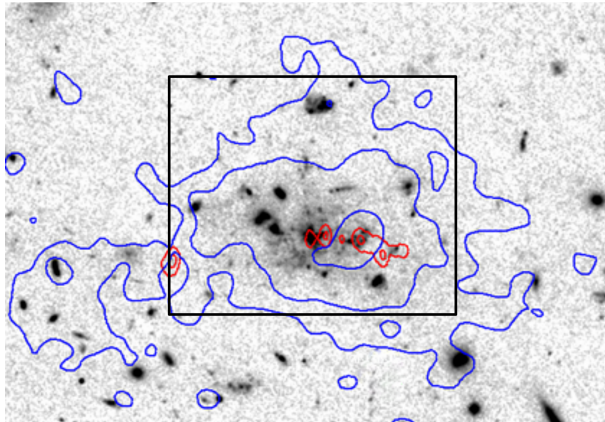


**Figure 2.1** – A composite ACS ( $g_{475}+I_{814}$ ) image of a  $275 \times 200$  kpc<sup>2</sup> field centered on the radio galaxy PKS 1138-262. The blue and red contours, respectively, indicate the extent of the Ly $\alpha$  emission line halo and the location of non-thermal radio emission in the 8 GHz band caused by a jet (Pentericci et al. 1997). The black rectangle shows the approximate outline of the field as covered by SINFONI.

of view and a spectral resolution of approximately  $R = 2000 - 4000$  depending on the band.

The field was observed in the  $J$ ,  $H$  and  $K$  bands. Based on previous work (Pentericci et al. 2000; Kurk et al. 2004a) the redshift of the protocluster is established to be  $z \sim 2.15$ . Therefore, the  $J$  band covers the [OII] $\lambda$ 3726, 3729 doublet, the  $H$  band contains the [OIII] $\lambda$ 4959, 5007 and H $\beta$  emission lines and H $\alpha$ , [NII] $\lambda$ 6548, 6584 and [SII] $\lambda$ 6719, 6730 are redshifted into the  $K$  band. The  $H$  band was given more integration time as the blue star forming satellite galaxies are likely to show [OIII] emission. Furthermore, this line is least likely to be contaminated by neighbouring lines making it the most reliable kinematic tracer.

A special dithering pattern was adopted to obtain a wide field of view around the central radio galaxy, leading to an effective coverage of approximately  $15'' \times 15''$  centred on the radio core. Details on the observations for the various bands can be found in Table 2.1.

Details of the data reduction can be found in N06 and Nesvadba et al. (2008), but a brief summary is given here. The data are dark subtracted and flatfielded. Curvature is measured and removed using an arc lamp after which the spectra are shifted to an absolute vacuum wavelength scale based on the OH lines in the data. This is done before sky subtraction to account for spectral flexure between the frames. The subsequent sky subtraction is done for each wavelength separately, with the sky frame being normalized to the average of the object frame in order to account for variations in the night sky emission. The three dimensional data are then reconstructed and spatially aligned using the telescope offsets as recorded in the header data. Before cube combination the individual cubes are corrected for telluric absorption. Flux calibration is done based on standard star observations and from the standard star light profile a FWHM spatial resolution of 0.7–0.9'' is measured.

**Table 2.1** – Details of the observations. Values for the seeing are measured from the standard star observations, with the uncertainties given by the rms of individual measurements. The difference between the seeing values for  $\alpha$  and  $\delta$  is a natural consequence of the SINFONI image slicer being in the light path.

Band	Exp. time (sec.)	Seeing in $\alpha$ and $\delta$ (")	Coverage	Dispersion ( $\text{\AA}/\text{pixel}$ )	Spectral Resolution ( $\Delta\lambda/\lambda$ )
<i>J</i>	16200	$0.9 \pm 0.3, 0.7 \pm 0.4$	$13'' \times 12.5''$	1.5	2000
<i>H</i>	45600	$0.9 \pm 0.3, 0.7 \pm 0.3$	$16.5'' \times 16.5''$	2.0	3000
<i>K</i>	28800	$0.9 \pm 0.2, 0.8 \pm 0.3$	$15'' \times 12.5''$	2.5	4000

We also use deep Hubble Space Telescope (HST) data to supplement the SINFONI data. These data were obtained with the Advanced Camera for Surveys (ACS, Ford et al. 1998) in the  $g_{475}$  and  $I_{814}$  bands (Miley et al. 2006) and with the Near Infrared Camera and Multi-Object Spectrometer (NICMOS) in the  $J_{110}$  and  $H_{160}$  bands (Zirm et al. 2008).

## 2.3 Results

### 2.3.1 Cluster membership

In each of the panels of Fig. 2.2 the field covered by SINFONI is shown. The greyscale image is the sum of the  $g_{475}$ ,  $I_{814}$ ,  $J_{110}$  and  $H_{160}$  images obtained with ACS and NICMOS. The top-left panel shows the numbering convention for the individual satellites introduced by H09 which is adopted in this work as well. In addition to the 19 galaxies of H09 we add another object to the sample, #20, as we find evidence for line emission at its location. We also mark the region between galaxies #17 and #18 as #21. In H09 a bridge of red light was found at this location and this was interpreted as being a stream of gas or stars between two interacting galaxies. The SINFONI coverage does not include galaxies #2, #3, #15 and #16 and therefore these will not be discussed in this work. Galaxy #14 does have SINFONI coverage in the  $K$  band, but it is located at the edge of the field where data quality is poor. Therefore #14 is also excluded from this work.

The contours in panels **b**, **c** and **d** of Fig. 2.2 indicate the locations of line emission in each of the three bands. The contours have been produced for each satellite galaxy individually. This was done by creating a cut-out at the location of the satellite and summing for each pixel in the cutout over the spectral range where evidence for line emission can be found. The resulting line image was used for calculating the contours.

As can be seen in Fig. 2.2, there are multiple sources of line emission, most of which are associated with the satellite galaxies. Some of the objects that show no clear evidence of line emission in single pixels do show evidence for line emission after summing the pixels associated with continuum emission in the ACS and NICMOS data. One or more emission lines consistent with  $z \sim 2.15$  are detected for 11 galaxies. These galaxies are #1, #5, #6, #7, #8, #10, #11, #12, #13, #20 and #21. Figure 2.3 shows the strongest emission lines for each of these confirmed satellites. The spectra for each of the galaxies have been obtained by summing the spectra of individual pixels with line emission. For the faint or initially undetected objects all pixels within the seeing disk at the location of the galaxy have been summed. Sky spectra for the satellite galaxies are also shown in Fig. 2.3. These have been extracted using the same apertures as used for the individual galaxies and they give an indication of the location and severity of sky line contamination. No significant line emission is found for #4, #17, #18 and #19.

Figure 2.3 also shows the spectrum of one galaxy (#9) that is identified as being a low redshift interloper through the identification of [OIII] and  $H\alpha$  at  $z = 1.677$ .

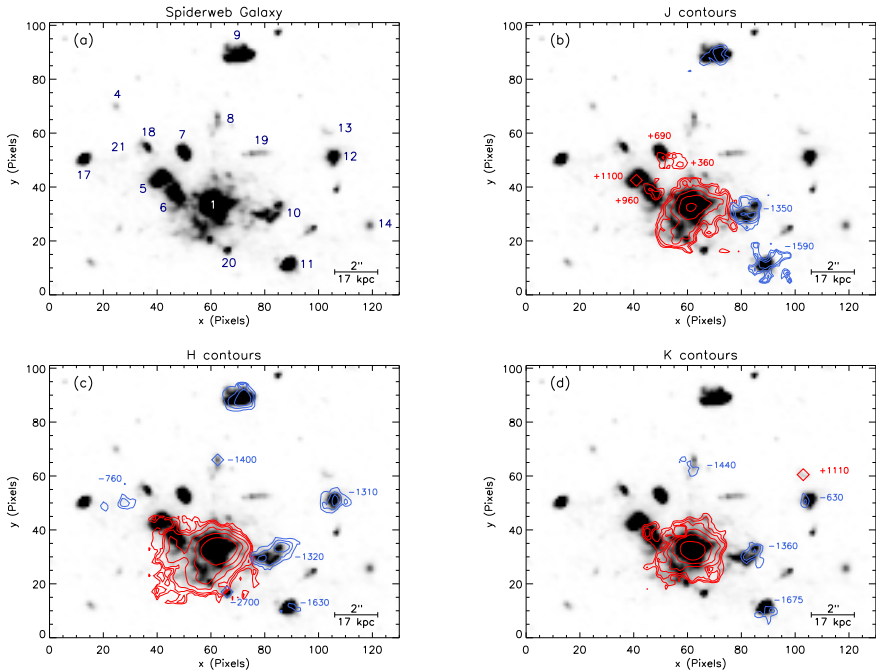


**Figure 2.2** – All panels show a combined  $gIJH$  image of the field as covered by SINFONI. The pixel scale of the HST images has been matched to the pixel scale of the SINFONI data ( $0.125'' \text{ pixel}^{-1}$ ). In panel **a** the numbers follow the labeling of the galaxies used by H09 which is also used in this work. The contours in panels **b**, **c** and **d** show the locations of line emission in the  $J$ ,  $H$  and  $K$  band, respectively. The colours of the contours indicate whether the emission is blue- or redshifted with respect to the radio galaxy. Each set of contours is obtained by summing over a narrow spectral window where line emission can be found. The line emission in question for the protocluster galaxies is  $[\text{OII}]$  emission in  $J$  band,  $[\text{OIII}]$  emission in  $H$  band and  $\text{H}\alpha$  in  $K$  band. The outermost and innermost contours indicate flux levels of  $2.5 \times 10^{-19}$  and  $45 \times 10^{-19} \text{ erg s}^{-1} \text{ cm}^{-2} \text{ \AA}^{-1}$ , respectively. Diamond symbols indicate objects that are too faint to yield proper contours, but do show line emission in summed spectra. The velocity offset in  $\text{km s}^{-1}$  with respect to the central radio galaxy ( $z_{\text{sys}} = 2.1585$ ) is given for all objects that have line emission consistent with  $z \sim 2.1 - 2.2$ .

This is surprising, as previous studies have provided ample evidence for it being at the redshift of the protocluster. The Ly $\alpha$  narrowband imaging of Pentericci et al. (1997) shows a significant and distinct source of emission at the location of galaxy #9 and subsequent spectroscopy detected an emission line that is consistent with being Ly $\alpha$  at  $z \sim 2.15$  (Kurk 2003). There are no strong emission lines at  $z = 1.677$  that could mimic Ly $\alpha$  at the protocluster redshift. It is therefore most likely that the emission at  $\sim 3840 \text{ \AA}$  is Ly $\alpha$  emission from the extended Ly $\alpha$  halo surrounding the central radio galaxy rather than Ly $\alpha$  emission from the galaxy itself.

In addition to #9, several of the other objects in the SINFONI field have been previously targeted for spectroscopy (Kurk 2003). Objects #1, #5/#6, #7, #10 and #11 have all been shown to have Ly $\alpha$  emission at  $z \sim 2.15$ . However, a comparison between the results presented in this Chapter and those obtained from Ly $\alpha$  spectroscopy shows in general large differences. Five out of six objects have velocities based on Ly $\alpha$  that differ by  $500 \text{ km s}^{-1} - 1500 \text{ km s}^{-1}$  with respect to the velocities presented in this Chapter. Only object #11 shows consistent redshifts. The offsets found for the other objects do not indicate any systematic trend. This is in accordance with Pentericci et al. (1997), who found no evidence for ordered motion such as rotation. The resonant nature of the Ly $\alpha$  line can thus cause the measured redshift to deviate significantly from the true redshift. Therefore caution must be used when interpreting the redshifts obtained through spectroscopic confirmation of Ly $\alpha$  alone.

A full list of all detected emission lines and their corresponding redshifts, velocities and fluxes can be found in Table 2.2. The brightest galaxies for which emission lines are detected in individual pixels have been corrected for internal kinematic structure. This has been done by shifting the individual spectra such that the line centres in the individual pixels match the redshift of the galaxy as a whole. Uncertainties are calculated by varying the summed spectra using a normal distribution characterized by the rms noise of the spectrum in question. This is repeated 1000 times and the standard deviation of the resulting parameter distributions are taken as the  $1\sigma$  uncertainties.

### 2.3.2 Overdensity

The confirmation of 11 protocluster galaxies within a  $\sim 60 \text{ kpc}$  radius makes this field extraordinarily dense. The surface number density of the core region is  $1.8 \times 10^2 \text{ arcmin}^{-2}$  or  $7 \times 10^{-4} \text{ kpc}^{-2}$  in physical units. This is likely a lower limit to the actual value as quiescent galaxies without line emission cannot be spectroscopically confirmed with the SINFONI data.

To illustrate the extreme denseness of the region around the Spiderweb galaxy we compare the density in the SINFONI field to that of the larger protocluster field. Kurk et al. (2000) found a total of 50 Ly $\alpha$  emitter candidates in a  $35.4 \text{ arcmin}^2$  field centered on the radio galaxy. In Kurk et al. (2004a) (hereafter K04) a sample of 40 candidate H $\alpha$  emitters was identified within a field of  $\sim 12 \text{ arcmin}^2$ . Re-



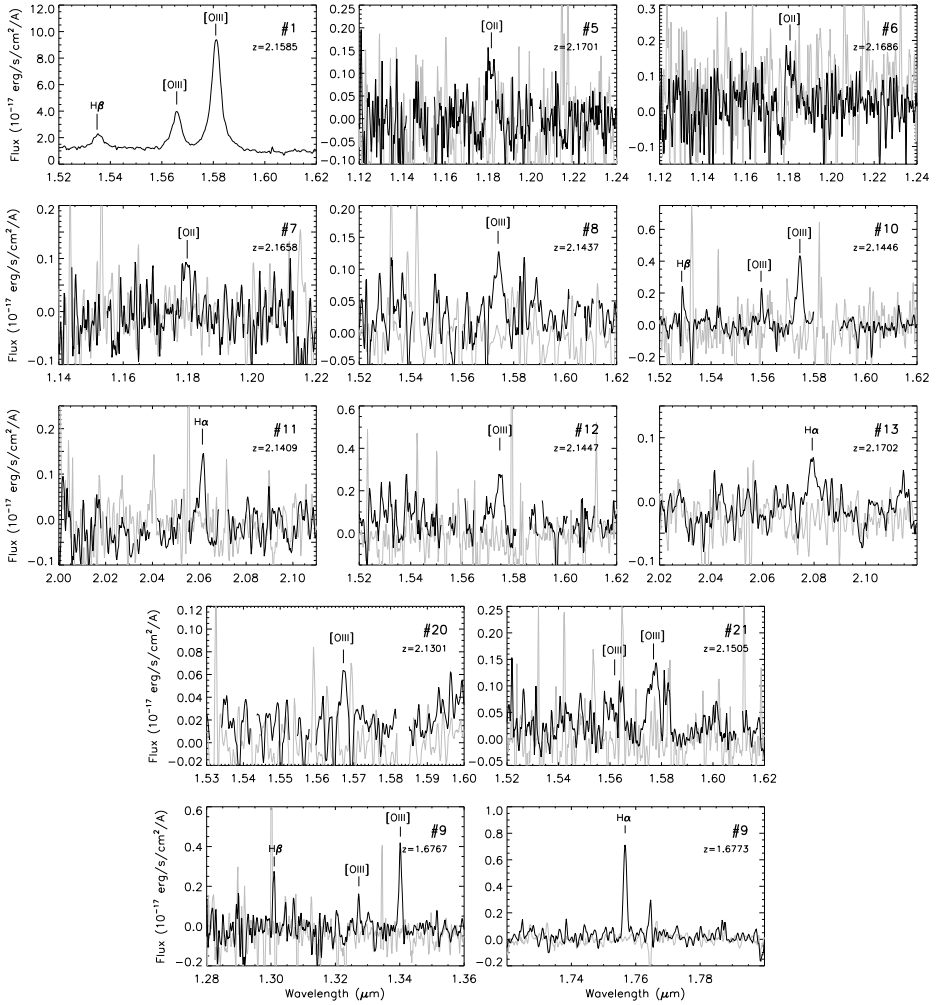


**Figure 2.3** – Summed spectra of the galaxies in the SINFONI field that show emission lines. Only the strongest emission lines are shown. For the satellite galaxies sky spectra are also shown in gray. The sky spectra have been extracted from locations close to the galaxies using the same apertures. For clarity, the emission lines have been labeled and patches of poor night-skyline residuals have not been plotted. Eleven galaxies are identified as protocluster members and one galaxy (#9) is identified as a foreground galaxy.

**Table 2.2** – Line properties for each of the protocluster candidates. The systemic redshift is taken to be the redshift of #1 as measured from the [OIII] $\lambda$ 5007 emission line. <sup>a</sup>Where possible the galaxies have been corrected for internal kinematic structure. <sup>b</sup>Values given are for H $\alpha$ + [NII]. <sup>c</sup>The [SII] doublet is unresolved. <sup>d</sup> $3\sigma$  upper limits in  $J/H/K$  band for a FWHM of 500 km s<sup>-1</sup>. <sup>e</sup>Lines likely contaminated by emission from the central radio source.

Object	Line	$z$	$v$ (km s <sup>-1</sup> )	Flux (10 <sup>-17</sup> erg s <sup>-1</sup> cm <sup>-2</sup> Å <sup>-1</sup> ) <sup>a</sup>
#1/RG	[OII]	2.1590 ± 0.0002	+40	128 ± 3
	[NIII] $\lambda$ 3869	2.1595 ± 0.0010	+10	35.9 ± 4.7
	[NIII] $\lambda$ 3968	2.1555 ± 0.0015	+10	16.7 ± 2.7
	H $\beta$	2.1590 ± 0.0002	+47	50.2 ± 0.9
	[OIII] $\lambda$ 4959	2.1584 ± 0.0001	-15	137 ± 1
	[OIII] $\lambda$ 5007	2.1585 ± 0.0001	0	477 ± 1
	H $\alpha$	2.1585 ± 0.0001	-5	582 ± 4 <sup>b</sup>
	[SII] <sup>c</sup>	2.1590 ± 0.0018	+40	149 ± 4
#4	-	-	-	< 2.5/0.6/0.7 <sup>d</sup>
#5	[OII]	2.1701 ± 0.0016	+1100	5.6 ± 0.8
	[OIII]	2.1695 ± 0.0004	+1040	5.9 ± 0.7
	H $\alpha$	2.1699 ± 0.0015	+980	4.3 ± 0.7
#6	[OII]	2.1686 ± 0.0018	+950	5.8 ± 1.0
	[OIII]	2.1683 ± 0.0002	+925	18.1 ± 1.1 <sup>e</sup>
	H $\alpha$	2.1706 ± 0.0005	+1220	35.8 ± 2.2 <sup>e</sup>
#7	[OII]	2.1658 ± 0.0011	+690	3.2 ± 0.9
#8	[OIII]	2.1437 ± 0.0007	-1410	4.0 ± 0.7
	H $\alpha$	2.1434 ± 0.0002	-1440	5.5 ± 0.9
#9	[OIII]	1.6767 ± 0.0005	-	4.6 ± 0.6
	H $\alpha$	1.6773 ± 0.0001	-	9.1 ± 0.6
#10	[OII]	2.1443 ± 0.0006	-1350	11.6 ± 1.4
	[OIII]	2.1446 ± 0.0001	-1325	11.1 ± 1.0
	H $\alpha$	2.1442 ± 0.0002	-1360	10.4 ± 1.0
#11	[OII]	2.1418 ± 0.0004	-1590	6.4 ± 1.2
	[OIII]	2.1415 ± 0.0008	-1620	2.6 ± 0.7
	H $\alpha$	2.1409 ± 0.0004	-1675	3.9 ± 0.6
#12	[OIII]	2.1447 ± 0.0023	-1315	8.2 ± 1.5
#13	H $\alpha$	2.1702 ± 0.0011	+1110	2.6 ± 0.4
#17	-	-	-	< 1.7/0.6/1.0 <sup>d</sup>
#18	-	-	-	< 1.1/0.6/0.7 <sup>d</sup>
#19	-	-	-	< 0.7/0.4/0.6 <sup>d</sup>
#20	[OIII]	2.1301 ± 0.0010	-2700	0.9 ± 0.3
#21	[OIII]	2.1505 ± 0.0010	-765	6.1 ± 0.7

spectively, six and three<sup>2</sup> of these line emitters are located in the SINFONI field of 0.0756 arcmin<sup>2</sup>. Thus, it is found that the SINFONI field is  $\sim 56 \pm 10$  times denser than the protocluster as a whole for the Ly $\alpha$  emitters and  $\sim 12 \pm 4$  times as dense for the H $\alpha$  emitters. Here the uncertainties are determined using Poisson statistics. Since the large scale protocluster field is respectively  $4 \pm 2$  and  $14 \pm 2$  times denser than the field at  $z \sim 2.2$  (Kurk et al. 2004b; Hatch et al. 2011) this indicates that the protocluster core has a galaxy overdensity of  $\sim 200$ .

The bias factor of star forming galaxies at high redshift is typically 1–5 (e.g. Adelberger et al. 1998; Giavalisco et al. 1998; Ouchi et al. 2004). Thus for our  $z \sim 2$  star forming galaxies we assume a bias factor of 3, which is roughly consistent with the trend observed in Marinoni et al. (2005). This implies a matter overdensity in the core of  $\sim 70$ . Local galaxy clusters have matter overdensities at their virial radii of  $\sim 100$ . The matter overdensity in the core of the Spiderweb protocluster is thus similar to what is observed in the outskirts of local galaxy clusters.

Such core overdensities are rare, but not unique, among high- $z$  protoclusters. Out of the sample of eight protoclusters studied in Venemans et al. (2007) none have Ly $\alpha$  emitters within 60 kpc of the radio galaxy<sup>3</sup>. For the H $\alpha$  emitters only two other radio-galaxy protoclusters have been imaged. Tanaka et al. (2010a) found an overdensity of  $\delta_g = 4 \pm 2$  of H $\alpha$  emitters around 4C23.56 ( $z \sim 2.48$ ), but none were found in direct vicinity of the radio galaxy. In another study by Hatch et al. (2011) an overdensity of  $\delta_g = 12 \pm 2$  was found in the field of radio galaxy 4C10.48 at  $z \sim 2.35$ . A significant number of these was found close to the radio galaxy. The spatial distribution, however, shows a striking alignment of the galaxies with the radio jet indicating that these objects may be experiencing jet-induced star formation. It is thus not clear whether the origin of the overdensity in 4C10.48 is of the same nature as that seen around the Spiderweb galaxy.

### 2.3.3 Velocity distribution

We have obtained redshifts for a large number of objects in the field. Before, protocluster candidacy was determined using Ly $\alpha$  narrowband imaging and follow-up spectroscopy, but as we have shown for satellite #9 in Sect. 2.3.1, the presence of the extended Ly $\alpha$  halo can lead to incorrect redshifts. No extended optical line emission is seen at distances larger than  $\sim 15$  kpc from the radio core and thus these emission lines are likely to originate from the satellite galaxies.

The velocity distribution of the spectroscopically confirmed protocluster core galaxies is shown in the top panel of Fig. 2.4. Velocities are taken with respect to the systemic redshift of the radio galaxy. The detection of stellar absorption features would unequivocally set the redshift of the stellar content of the radio galaxy. However, none are found and therefore we rely on emission lines. As shown in N06, the internal dynamics of the central radio source covers a large range of

---

<sup>2</sup>#5, #6 and #10 were taken as part of #1 in K04 and therefore not identified as individual H $\alpha$  emitters. #8 and #13 were too faint to be included in the H $\alpha$  emitter sample.

<sup>3</sup>Here the assumption is made that the radio galaxy traces the core of the protocluster

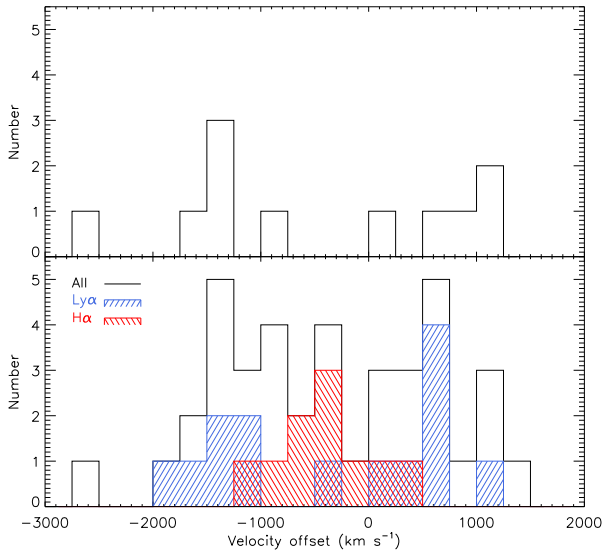


**Figure 2.4** – Top panel: velocity distribution of the confirmed protocluster members found in this work. Velocities are with respect to  $z_{[\text{OIII}]}$  of the radio core (#1). Two groups can be identified that are blue- and redshifted with respect to the radio galaxy. Bottom panel: velocity distribution of the full Spiderweb sample. The velocity distributions of P00 and K04 are indicated by the blue and red hatched regions, respectively.

velocities of  $\sim 1500 \text{ km s}^{-1}$  ( $2.158 < z < 2.173$ ). This indicates the presence of strong outflows. It is therefore not trivial to assign a systemic redshift to this object. In this work the systemic redshift ( $z = 2.1585$ ) is chosen to be the redshift of the location of the HST continuum emission (zone 3 in N06). It may be that this region hosts an outflow that is blueshifted with respect to the stellar content of the galaxy. This means the actual redshift of the central radio source may be significantly higher; up to  $z \sim 2.170$ . This would result in a shift of the zeropoint in Fig. 2.4 of several  $100 \text{ km s}^{-1}$  towards larger positive velocities. The shape of the velocity distribution, however, will remain the same.

In Fig. 2.4 a striking subclustering in the velocity distribution can be seen with two subgroups at  $\Delta v \sim -1500 \text{ km s}^{-1}$  and  $\Delta v \sim +900 \text{ km s}^{-1}$ . The large separation between the subgroups implies a large velocity dispersion of the satellite galaxies as a whole. Assuming that the underlying distribution is a single Gaussian, a value of  $1360 \pm 206 \text{ km s}^{-1}$  is found using the Gapper scale estimator (Beers et al. 1990).

A comparison of the velocity distribution to the results of previous studies shows both resemblances and differences. Pentericci et al. (2000, P00) used the Ly $\alpha$  emission line to spectroscopically confirm 14 objects as being at the protocluster redshift. All 14 objects are located outside the SINFONI field of view. They thus trace the large scale protocluster structure and contamination from the extended Ly $\alpha$  halo is unlikely. Another study by K04 obtained spectroscopy on candidate H $\alpha$  emitters in the Spiderweb protocluster. Nine objects were confirmed to be in the protocluster. Finally, the studies of Croft et al. (2005) and Doherty et al. (2010) have respectively confirmed two X-ray emitting objects and two red galaxies to be part of the protocluster structure. The resulting full velocity distribution, including all confirmed galaxies, is shown in the bottom panel of Fig. 2.4. For

clarity the distributions of P00 and K04 have been indicated by blue and red hatched histograms, respectively.

First considering the P00 distribution, we see that even though these studies are fully independent and target different scales within the protocluster, the velocity distribution of the Ly $\alpha$  emitters is qualitatively the same as in the protocluster core. The subgroups in the P00 distribution are located at  $z = 2.145 \pm 0.002$  and  $z = 2.164 \pm 0.002$  which is similar to the locations of the subgroups found in this work (see Table 2). The fact that both the large and small scale velocity distribution are broad and double-peaked indicates that there is a common process acting on both large and small scales. Therefore, the evolution of the central Spiderweb galaxy and the larger protocluster structure may be linked. We will come back to this in Sect. 2.4.2.3.

In contrast to this, the K04 velocity distribution shows neither a resemblance to the velocity distribution found in this study nor to that of P00. The nine confirmed H $\alpha$  emitters have a relatively narrow velocity distribution with redshifts in the range  $2.1463 < z < 2.1636$ . It is not clear why the H $\alpha$  emitters show such a different velocity distribution, because the narrowband transmission curve covers the entire velocity range spanned by the protocluster galaxies. Considering the poor number statistics it may therefore be attributed to sampling. Nevertheless, the full distribution, including the velocities of all confirmed objects, is broad and yields a velocity dispersion of  $1013 \pm 87 \text{ km s}^{-1}$ .

Are such high velocity dispersions common in high- $z$  protoclusters? In Venemans et al. (2007) a sample of six protoclusters with redshifts in the range of  $2 < z < 5$  was studied. Most of the protoclusters have velocity dispersions significantly smaller than  $1000 \text{ km s}^{-1}$ , but the protocluster around MRC 0052-241 (0052) at  $z = 2.8600$  was found to have a velocity dispersion of  $980 \pm 120 \text{ km s}^{-1}$ . Also, the velocity distribution of 0052 shows signs of bimodality. It thus seems that although the Spiderweb protocluster is exceptional, it is not unique in showing these characteristics.

Venemans et al. (2007) also found an increase in velocity dispersion with decreasing redshift. Although the Spiderweb protocluster is in line with this trend, its velocity dispersion is significantly higher than the  $z \sim 1.2$  galaxy cluster which was used as a ‘low’ redshift control case in the Venemans et al. (2007) study. This indicates that even when considering this trend, the Spiderweb protocluster remains an exceptional case.

Another possible cause for the large velocity dispersion has been proposed by P00. P00 speculated that the double-peaked profile hints at a possible merger of two groups of galaxies. Several cases of merging clusters are known at low  $z$  and some do show a clear segregation in velocity space (e.g. Abell 1750, Abell 2744, Ramírez & Quintana 1990; Owers et al. 2011). Considering this possibility, we fit a double Gaussian to the full Spiderweb velocity distribution. We find that the two groups are separated by a velocity difference of  $1600 \text{ km s}^{-1}$  and have velocity dispersions of  $492 \text{ km s}^{-1}$  and  $417 \text{ km s}^{-1}$ .

A Kolmogorov-Smirnov (KS) test was used to investigate whether the single or double component model fits the observations better. Although formally both models are consistent with the observed distribution, the probability that the two distributions match is 0.98 for the double component model whereas it is 0.66 for the single component model. Also, a normalized tail index (Bird & Beers 1993) yields 0.82 indicating that a uniform distribution better describes the complete distribution rather than a single Gaussian. Note that if the Spiderweb protocluster is indeed a double or merging system, then the comparisons to the results of Venemans et al. (2007) discussed above will yield significantly different results.

Could the subclustering found in the core of the protocluster be an artefact of the data? The wavelength range  $15800 \leq \lambda \leq 15850$  ( $2.156 \leq z \leq 2.166$ ) in the *H* band is one of the regions particularly affected by poor night-skyline residuals. This may lead to the galaxies with weak optical emission lines in this particular wavelength range being missed. If all of the four unconfirmed protocluster candidates are indeed in this specific range then the core distribution would more closely resemble a flat distribution. However, we argue that the velocity distribution of the complete sample will remain broad and its shape will not change significantly.

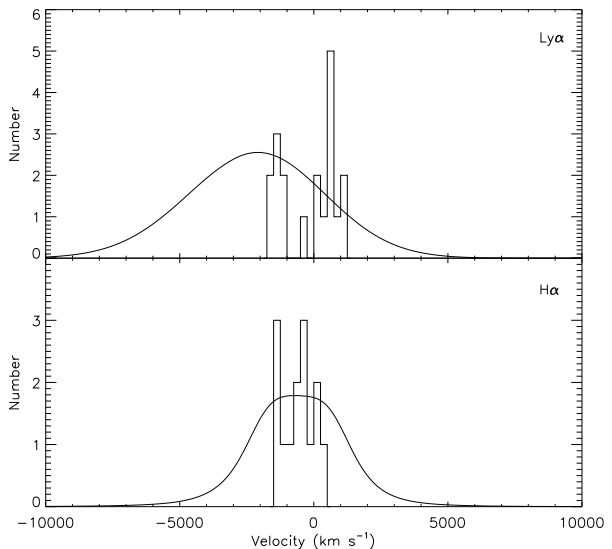
## 2.4 Discussion

### 2.4.1 A galaxy cluster progenitor

The Spiderweb protocluster is known to harbour galaxy overdensities (see Sect. 2.1) and is therefore thought to evolve into a galaxy cluster. It is however not guaranteed that an overdensity at high- $z$  will evolve into a present day massive galaxy cluster. To determine whether the Spiderweb protocluster is truly a forming galaxy cluster, we attempt to determine whether the dynamical state of the galaxies in the overdensity is significantly different from what is expected in field environments.

Shown in Fig. 2.5 are the velocity distributions of all spectroscopically confirmed galaxies that have been marked as line emitters in P00 and K04. Also plotted are the selection functions based on the transmission curves of the narrowband filters used in those studies. These selection functions should be good approximations of the expected field velocity distributions. The  $H\alpha$  emitters shown in the bottom panel follow the expected distribution quite well. A KS test yields a probability of 20 per cent that the observed distribution is drawn from the expected velocity distribution. This indicates that we cannot conclude whether there is a significant difference between the two distributions. All of the 19  $Ly\alpha$  emitters, however, are located at higher velocities than the mean velocity implied by the selection function. Applying a KS test we determine that there is a  $5 \times 10^{-6}$  probability that the  $Ly\alpha$  emitters in the overdensity are drawn from the expected field velocity distribution. Thus the two distributions are different at the  $\sim 4.5\sigma$  level. From this we conclude that the  $Ly\alpha$  emitters are associated with the radio galaxy. In fact, this is likely the case for all the galaxies considered, since the  $Ly\alpha$  emitters cover the same velocity range.

**Figure 2.5** – The velocity distributions of all spectroscopically confirmed Ly $\alpha$  and H $\alpha$  emitter candidates. Also shown are the respective transmission curves (or selection functions) as function of velocity with respect to the radio galaxy. The Ly $\alpha$  velocity distribution differs from the selection function indicating it is not a field environment.



These results also imply that the protocluster structure has dropped out of the Hubble flow. Assuming this is indeed the case, how does the dynamical state of the protocluster compare to that of the field if the Hubble flow is removed? To investigate this we compare to galaxies that reside in field environments at  $z \sim 2$  in the Millennium simulation (Springel et al. 2005; De Lucia & Blaizot 2007). The Millennium simulation traces cosmological evolution at a number of discrete redshift ‘snapshots’. The resulting field velocity distribution will therefore indicate the deviation from the Hubble flow. The redshift chosen for this purpose is  $z = 2.24$ , which is the snapshot closest to the redshift of the actual protocluster.

The total area probed by P00 is approximately 100 comoving  $\text{Mpc}^2$ . To obtain proper statistics, we therefore select three separate boxes with sides of 50 comoving Mpc from the Millennium simulation. Each of the  $xy$ ,  $xz$  and  $yz$  planes is subsequently divided into a grid of  $10 \times 10 \text{ Mpc}^2$  fields, thus yielding a total of 75 fields per box. To ensure that no large scale structures are present, we exclude all fields with number densities that satisfy  $n - \bar{n} > 2\sigma$ , with  $\bar{n}$  the median number density. Approximately 10 per cent of the fields are excluded this way. Changing this limit does not strongly influence the final result. We also apply a magnitude cut to the restframe  $R$  band magnitude of the simulated galaxies. This cut is placed arbitrarily at  $R < 27$  since varying the exact value of the cut between  $26 < R < 30$  does not alter any of the conclusions presented here.

A composite galaxy velocity distribution of the remaining fields is shown in Fig. 2.6. When compared to the protocluster distribution, it is seen that the composite field velocity distribution is relatively narrow. A KS test is used to determine whether the full Spiderweb velocity distribution is consistent with the field velocity distribution. A probability of  $9 \times 10^{-7}$  is found, indicating that the two

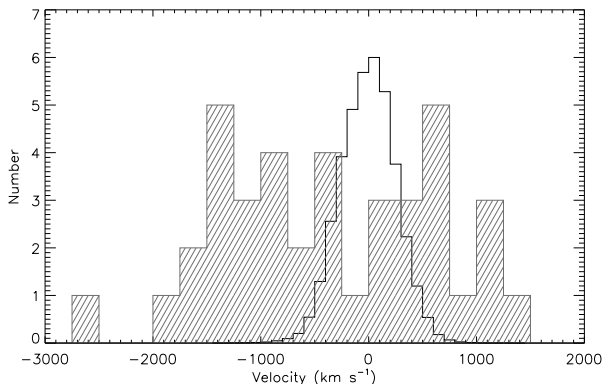


**Figure 2.6** – Composite field velocity distribution of peculiar velocities obtained from the Millennium simulation. Also shown as the hatched histogram is the Spiderweb velocity distribution. The Millennium field distribution has been scaled down to facilitate comparison. The field velocity distribution is significantly narrower than the Spiderweb velocity distribution.

distributions differ at the  $\sim 5\sigma$  level. Applying a KS test to each of the individual field distributions shows that all differ at least at the  $3\sigma$  level with 95 per cent of the fields differing at  $> 4\sigma$ . Therefore, if the protocluster has indeed fully dropped out of the Hubble flow, then it differs significantly from what is expected from a field environment.

We conclude that the Spiderweb field is not only overdense, but also kinematically distinct from regions where the Hubble flow dominates. The Spiderweb protocluster is thus a dynamically evolved, collapsing (or collapsed) structure.

## 2.4.2 Formation scenarios

With the confirmation of a total of 38 galaxies at the redshift of the radio galaxy and from the fact that this is a dynamically evolved structure, it is apparent that the Spiderweb is the progenitor of a galaxy cluster. As it is still unclear how galaxy clusters are formed, we review here two possible formation scenarios.

### 2.4.2.1 Single virialized structure

The first option we consider is the scenario in which the Spiderweb protocluster is a single virialized structure. This can be considered by comparing the velocity distribution presented in this work to results obtained with the Millennium simulation. Although we know little of the dark matter halo that hosts the protocluster, the dense nature of the Spiderweb field indicates that this is likely one of the most massive dark matter haloes at  $z \sim 2.15$ . We therefore investigate the properties of the 25 most massive dark matter haloes at  $z = 2.24$  in the Millennium simulation. These haloes have masses ranging from  $0.75\text{--}1.4 \times 10^{14} M_{\odot}$  and galaxy velocity dispersions in the range of  $450\text{--}900 \text{ km s}^{-1}$ . Visual inspection shows that one of the haloes is in the process of merging with another massive halo. This particular halo is not included in the comparison for the single halo scenario.

Using a KS test we investigate whether the double-peaked structure found for the Spiderweb can be drawn from the velocity distributions obtained for the Mil-



lennium haloes. This is done for all three velocity components separately. Using the full Spiderweb velocity distribution we find that 19 haloes yield probabilities indicating that they are different from the protocluster distribution at at least the  $2\sigma$  level. The remaining 6 haloes yield probabilities of  $\sim 10$  per cent. The possibility that the Spiderweb protocluster is a single massive structure can therefore not be wholly excluded on these grounds.

Another test for the virialized structure scenario is supplied by the protocluster mass. If virialized, it is possible to determine the mass contained within the area covered by the SINFONI field using (Small et al. 1998):

$$M_{\text{vir}} = \frac{6}{G}\sigma^2 r_{\text{vir}} \quad (2.1)$$

with  $\sigma$  the velocity dispersion obtained in Sect. 2.3.3 and  $r_{\text{vir}}$  the mean projected harmonic separation given by

$$r_{\text{vir}} = \frac{\pi N(N-1)}{2} \left( \sum_{i<j} \frac{1}{|r_i - r_j|} \right)^{-1}. \quad (2.2)$$

Here  $N$  is the number of objects considered. Using  $\sigma = 1360 \text{ km s}^{-1}$  and finding  $r_{\text{vir,core}} = 55 \text{ kpc}$ , a dynamical mass of  $\sim 10^{14} M_{\odot}$  is found for the core region of the protocluster.

For the complete Spiderweb galaxy sample the velocity dispersion is  $1013 \text{ km s}^{-1}$  and we approximate  $r_{\text{vir}}$  by using only the objects of P00 as the K04 and SINFONI objects are taken from data with smaller field of view: including these would therefore bias the radius to smaller values. We find that the virial radius of the Spiderweb is  $1.2 \text{ Mpc}$ , implying a total mass of  $\sim 2 \times 10^{15} M_{\odot}$ .

Using the scaling relations presented in Rykoff et al. (2008) and the total protocluster mass of  $2 \times 10^{15} M_{\odot}$ , the X-ray luminosity of the cluster gas in restframe  $0.1\text{--}2.4 \text{ keV}$  can be calculated to be  $\sim 1.5 \times 10^{45} \text{ erg s}^{-1}$ . Assuming  $k_{\text{B}}T_{\text{X}} \sim 5\text{--}7 \text{ keV}$  we convert this to the range  $2\text{--}10 \text{ keV}$  and find  $3\text{--}6 \times 10^{44} \text{ erg s}^{-1}$ . This can be compared to the upper limit on the X-ray luminosity of an extended cluster atmosphere of  $1.5 \times 10^{44} \text{ erg s}^{-1}$  presented in Carilli et al. (2002). If the protocluster is indeed virialized, it would have been detected. This has been indicated in K04 as well. Furthermore, a total mass of  $\sim 10^{15} M_{\odot}$  would rank this halo among the most massive known haloes and the probability that such a massive halo exists at this redshift is negligible according to  $\Lambda\text{CDM}$  cosmology (e.g. Jee et al. 2009). We thus conclude that the protocluster is not a virialized structure. If only the core region were virialized the expected X-ray luminosity would drop to  $8 \times 10^{42} \text{ erg s}^{-1}$ . This possibility can therefore not be excluded.

Saro et al. (2009), who presented high resolution hydrodynamical simulations of high- $z$  protoclusters modelled after the Spiderweb system, also argued that the inner region of a Spiderweb-like protocluster ( $r < 400 \text{ kpc}$ ) can be virialized at  $z \sim 2$ . However, the velocity dispersion in the simulated cluster is significantly

lower than what is presented in this study, making it unclear whether it is applicable to the Spiderweb system.

#### 2.4.2.2 Merger of haloes

Given the broad double-peaked velocity distribution on both small and large scales, we now investigate whether it is possible that there are two separate structures in the Spiderweb field. These two structures are possibly in the act of merging with each other, thus creating a larger protocluster structure. We therefore consider the scenario where two haloes, each containing their own group or cluster of galaxies, merge to form a more massive structure.

One quantitative way to tell whether this scenario is feasible is to determine whether the velocity dispersion of  $> 1000 \text{ km s}^{-1}$  and velocity separation between the two groups of  $\sim 1600 \text{ km s}^{-1}$  can be reproduced by a merger of two massive dark matter haloes. For this comparison the halo is used that was excluded before due to it being in the process of merging. Based on the number of dark matter particles, these haloes have masses of  $2 \times 10^{13}$  and  $6 \times 10^{13} M_{\odot}$ .

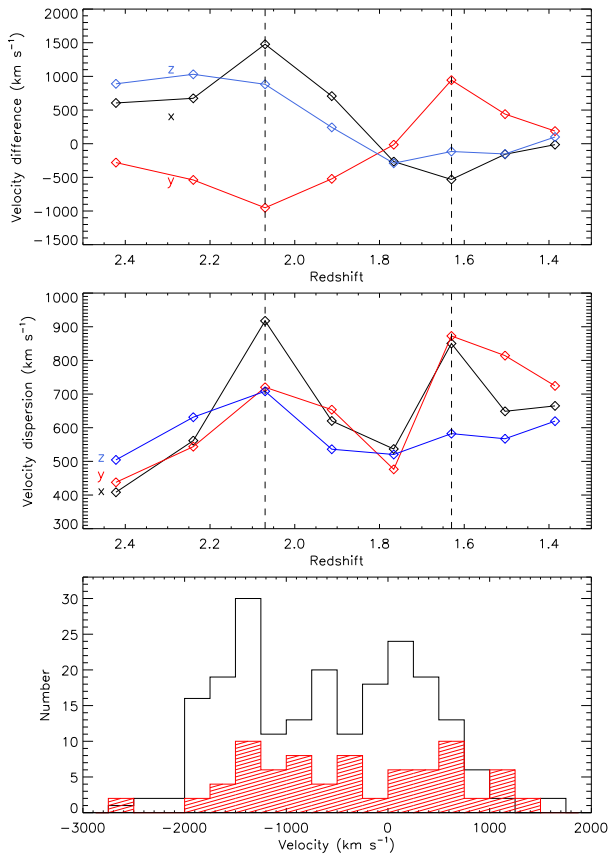
To trace the velocity evolution, the galaxies belonging to both subhaloes are identified. The locations of the subhaloes are determined by visual inspection and all galaxies within 0.5 Mpc of the centres are assumed to belong to the respective subhaloes. These two groups of galaxies are subsequently traced from  $z = 2.4$  to  $z = 1.5$  and their median velocities relative to the velocity of the main dark matter halo are assessed.

In the top panel of Fig. 2.7 we plot the velocity differences between the two haloes as a function of redshift for each of the three velocity components. The major merger occurs at  $z \sim 2$  and around this time we see a maximum in the velocity difference for the x-component of approximately  $1500 \text{ km s}^{-1}$ . This is comparable to the velocity difference found for the Spiderweb. The other velocity components show smaller velocity differences, but this is due to the merger being aligned along the x-axis. The x-component of the velocity therefore represents the velocity obtained in a line-of-sight merger event.

The middle panel of Fig. 2.7 shows the evolution of the velocity dispersion of the main halo as a function of redshift. This means that prior to the merger only the velocity dispersion of the most massive halo is considered and during and after the merger both involved haloes are included. We see that at the time of merger the large velocity difference for the x-component results in a sharp increase in the velocity dispersion, reaching a maximum of  $\sim 900 \text{ km s}^{-1}$ . As with the velocity difference, this is similar to what is found for the Spiderweb protocluster. Another merger occurs at  $z \sim 1.6$ , leading to a similar sharp increase in the velocity dispersion.

The distribution of the x-component of the velocities for both haloes as well as the velocity distribution of the Spiderweb system are shown in the bottom panel of Fig. 2.7. To facilitate comparison with the distributions shown in Fig. 2.4, the velocities have been given with respect to the most massive galaxy in the two

**Figure 2.7** – Top panel: Velocity difference between two groups of galaxies as a function of redshift. The different colours indicate the different components of the velocity vector, with black, red and blue being the x, y and z component respectively. The dashed lines indicate the approximate redshifts at which mergers take place. At the redshift of the first merger a maximum velocity difference of  $1500 \text{ km s}^{-1}$  is seen in the x-component. Middle panel: Evolution of the velocity dispersion of the main halo for all three components as a function of redshift. A maximum is reached at the time of the first merging. Bottom panel: Velocity distributions of the galaxies in both of the merging haloes at the approximate time of merging. The full Spiderweb velocity distribution is shown as the red hatched histogram and has been scaled up to facilitate comparison.



haloes. A clear double-peaked structure is seen and in general the resemblance between both distributions is striking. Applying a KS test, we investigate whether the Spiderweb velocity distribution can be drawn from such a velocity distribution and a probability of  $\sim 40$  per cent is found. This is a larger probability than found for any of the single haloes investigated above. The hypothesis that the velocity distribution of the Spiderweb is consistent with the distribution caused by the merger of two haloes can therefore not be ruled out. Furthermore, as indicated above, a direct comparison to the distribution of the Spiderweb system has shown that both the velocity difference and the velocity dispersion are only marginally smaller. We therefore consider the merger origin a viable scenario for this protocluster.

Since there is a significant possibility that the Spiderweb system is the result of a merger of two massive haloes, it is now possible to infer something about the properties of the interacting haloes. Venemans et al. (2007) calculated the masses of the two groups by assuming that the individual groups are virialized and have virial radii of 0.8 and 1.1 Mpc (Kurk et al. 2004b). The velocity dispersions used were 520 and 280 km s<sup>-1</sup> as taken from the P00 study. This yielded halo masses of  $4 \times 10^{14}$  and  $1 \times 10^{14} M_{\odot}$ , respectively. With the addition of the confirmed galaxies presented in this work the velocity dispersions become 492 and 417 km s<sup>-1</sup> as given in Sect. 2.3.3. This yields that both haloes have a mass of  $\sim 2.7 \times 10^{14} M_{\odot}$ . A virialized halo of this mass would have an X-ray luminosity of  $\sim 2 \times 10^{43}$  erg s<sup>-1</sup> in the restframe 2-10 keV range. Two such haloes in the line of sight are thus consistent with remaining undetected considering the upper limit given by Carilli et al. (2002).

The masses calculated above are significantly larger than the halo masses involved in the simulated merger. However, the masses of the simulated haloes are based on the number of dark matter particles in each halo and may give a more accurate estimate of the actual halo mass. Calculating the masses of the simulated haloes at the time of merger using the velocity dispersion yields masses of  $3 \times 10^{14}$  and  $5 \times 10^{14} M_{\odot}$ , where estimated virial radii of 1 Mpc are used. Using the velocity dispersion in a merger situation can therefore overestimate the total mass by over an order of magnitude. We therefore propose that the subhalo masses stated for the Spiderweb protocluster are to be considered upper mass limits.

In the merger scenario as presented here, it seems odd that the central massive galaxy (#1) has a velocity placing it between the two velocity peaks seen in Fig. 2.4. One would expect the central galaxy to be at the centre of either of the two velocity peaks. However, remember that in Sect. 2.3.3 we noted that the redshift of the radio galaxy is highly uncertain due to the large velocity gradients. This could mean that the redshift of the radio galaxy is underestimated. If this is indeed the case, then the radio galaxy would fall exactly within the ‘red’ group.

Finally, it may be argued that this structure is possibly nothing more than a chance superposition of two unrelated structures. It is hard to disprove such a notion, but we must consider that the central radio galaxy is an exceptional object in itself. It has a mass of  $\sim 10^{12} M_{\odot}$ , hosts a powerful AGN and has an extremely

clumpy morphology indicating strong interaction and merging. Furthermore, it has an exceptionally large rotation measure (Carilli et al. 1997). If these are indeed separate, unrelated structures it will be difficult to explain why such an exceptional object is found in a relatively low-mass halo. The merger process, however, may be one of the driving forces behind the unique appearance of the central Spiderweb galaxy. This link between the central galaxy and the merger process is further investigated in Sect. 2.4.2.3.

### 2.4.2.3 The Spiderweb Galaxy

One of the striking results found in this study, is that the core of the protocluster, which is believed to evolve into a massive cD type galaxy by  $z = 0$ , has a similar velocity distribution as the megaparsec scale protocluster structure. This may purely be the effect of the merger of two protoclusters of galaxies as proposed in Sect. 2.4.2.2, but the large number density of confirmed galaxies near the radio core implies that an additional physical mechanism is at work. In this section we briefly explore a scenario that may explain the dense nature of the core region within the merger scenario.

Although not common to all merging clusters, there have been several reports in the literature of triggered star formation in the constituents of merging clusters (Caldwell & Rose 1997; Ferrari et al. 2005; Hwang & Lee 2009; Ma et al. 2010). Numerical simulations have also shown that it is possible to trigger star formation during cluster merger, either through the tidal gravitational field of the merger (Bekki 1999) or caused by an increased ram-pressure of the intracluster medium (Kronberger et al. 2008). As shown in Fig. 2.1, one of the striking properties of the Spiderweb galaxy is the extended Ly $\alpha$  halo enveloping the system. Much in analogy to what has been found for low-redshift clusters, gravitational interactions and ram pressure may enhance star formation in the galaxies falling through this diffuse halo. This will result in a relatively large number of UV bright galaxies near to the radio core. Naturally, these galaxies reflect the velocity structure of the halo merger as is the case in the protocluster core.

In addition to inducing star formation, the merger may also be responsible for an increase in the AGN activity. The halo merger could lead to a period of more frequent and stronger interactions with the central galaxy. The gas within the radio galaxy would lose its angular momentum through torques induced by these interactions and it would subsequently be funneled towards the central black hole. It is thus possible that a halo merger will trigger a radio luminous phase of the central AGN. If these processes indeed happen, then it is evident that such halo mergers should be considered an important phase of massive galaxy evolution.

We must now ask the question whether selecting galaxy cluster progenitors using HzRGs targets predominantly merging clusters. It is beyond the scope of this Chapter to answer this question, but other HzRGs have been shown to have relatively large velocity dispersions or are speculated to be part of superstructures (e.g. the 0052 protocluster at  $z \sim 2.86$  and the protocluster around MRC0316-

257 at  $z \sim 3.13$ , respectively, Venemans et al. 2007; Maschietto et al. 2008). An extensive study of HzRGs and their protocluster environments is needed to answer this question.

## 2.5 Conclusions

We have presented results obtained from deep SINFONI data of the core of the protocluster around the radio galaxy PKS 1138-262 at  $z \sim 2.1$ .

1. We search for emission lines at the locations of the satellite galaxies and find 11 galaxies with one or more emission lines that are consistent with being part of the protocluster. This makes the core region more than an order of magnitude denser than its already overdense large scale environment. Based on the galaxy overdensity of  $\sim 200$  we estimate that the matter overdensity in the core is  $\delta_m \sim 70$ . This is comparable to what is seen in the outskirts of local clusters.
2. The velocity distribution of the satellite galaxies in the central  $120 \times 120$  kpc<sup>2</sup> of the protocluster is broad and double-peaked with a velocity dispersion of  $1360 \pm 206$  km s<sup>-1</sup>. An almost identical velocity distribution was found in a previous study focused on the velocity distribution of the megaparsec scale protocluster structure (Pentericci et al. 2000; Kurk et al. 2004a). This indicates that there is a physical link between the evolution of the central massive galaxy and the larger protocluster structure. Including the results of previous studies, we find that the velocity dispersion of the protocluster is  $1013 \pm 87$  km s<sup>-1</sup>. This is higher than previous estimates of velocity dispersions in other high- $z$  protoclusters.
3. Comparison to the expected field velocity distribution and the peculiar velocity distribution of field environments in the Millennium simulation shows that the protocluster velocity distribution is different at the  $4.5\sigma$  and  $5\sigma$  significance level, respectively. We therefore conclude that the protocluster is decoupled from the Hubble flow and a dynamically evolved structure.
4. A comparison to the 25 most massive haloes at  $z \sim 2$  in the Millennium simulation shows that the majority of the haloes differ from the protocluster at  $> 2\sigma$  level. However, approximately 20 per cent of these haloes have velocity distributions that differ less than  $< 2\sigma$  from the Spiderweb system. Based on the velocity distribution we can therefore not exclude the possibility that this is a single virialized massive halo. If virialized, the cluster core will have a mass of  $\sim 1 \times 10^{14} M_\odot$  and the total protocluster mass will be  $\sim 2 \times 10^{15} M_\odot$ . We conclude that the protocluster cannot be virialized since such a total mass would imply an X-ray luminosity of  $\sim 5 \times 10^{44}$  erg s<sup>-1</sup> and this exceeds the upper limit given in the X-ray study of Carilli et al. (2002). It is possible that only the inner regions have been virialized.
5. We investigate an alternative scenario in which the Spiderweb protocluster consists of two galaxy groups that are in the process of merging. A comparison to a massive halo merger at  $z \sim 2$  in the Millennium simulation shows that

velocity differences and dispersions similar to those found in the Spiderweb system can be obtained this way. Furthermore, a KS test shows that the velocity distribution caused by a massive merger of haloes is consistent with the velocity distribution of the Spiderweb protocluster. We conclude that the merger scenario best describes the properties of the protocluster.

## Acknowledgments

The authors would like to thank the anonymous referee for all the useful comments that have improved the paper. EK acknowledges funding from Netherlands Organization for Scientific Research (NWO). NAH acknowledges support from STFC and the University of Nottingham Anne McLaren Fellowship. JK thanks the DFG for support via German-Israeli Project Cooperation grant STE1869/1-1.GE625/15-1. This work is based on observations with ESO telescopes at the Paranal Observatories under the programme ID 080.A-0109(A). The Millennium Simulation databases used in this paper and the web application providing online access to them were constructed as part of the activities of the German Astrophysical Virtual Observatory.

## References

- Adelberger K. L., Steidel C. C., Giavalisco M., Dickinson M., Pettini M., Kellogg M., 1998, *ApJ*, 505, 18
- Beers T. C., Flynn K., Gebhardt K., 1990, *AJ*, 100, 32
- Bekki K., 1999, *ApJ*, 510, L15
- Bird C. M., Beers T. C., 1993, *AJ*, 105, 1596
- Caldwell N., Rose J. A., 1997, *AJ*, 113, 492
- Carilli C. L., Harris D. E., Pentericci L., Röttgering H. J. A., Miley G. K., Kurk J. D., van Breugel W., 2002, *ApJ*, 567, 781
- Carilli C. L., Roettgering H. J. A., van Ojik R., Miley G. K., van Breugel W. J. M., 1997, *ApJS*, 109, 1
- Croft S., Kurk J., van Breugel W., Stanford S. A., de Vries W., Pentericci L., Röttgering H., 2005, *AJ*, 130, 867
- De Lucia G., Blaizot J., 2007, *MNRAS*, 375, 2
- Doherty M. et al., 2010, *A&A*, 509, A83+
- Dressler A., 1980, *ApJ*, 236, 351
- Eisenhauer F. et al., 2003, in Presented at the Society of Photo-Optical Instrumentation Engineers (SPIE) Conference, Vol. 4841, Society of Photo-Optical Instrumentation Engineers (SPIE) Conference Series, M. Iye & A. F. M. Moorwood, ed., pp. 1548–1561
- Ferrari C., Benoist C., Maurogordato S., Cappi A., Slezak E., 2005, *A&A*, 430, 19
- Ford H. C. et al., 1998, in Society of Photo-Optical Instrumentation Engineers (SPIE) Conference Series, Vol. 3356, Society of Photo-Optical Instrumentation Engineers (SPIE) Conference Series, Bely P. Y., Breckinridge J. B., eds., pp. 234–248
- Galametz A. et al., 2010, *A&A*, 522, A58+
- Giavalisco M., Steidel C. C., Adelberger K. L., Dickinson M. E., Pettini M., Kellogg M., 1998, *ApJ*, 503, 543
- Gobat R. et al., 2011, *A&A*, 526, A133+
- Hatch N. A. et al., 2011, *MNRAS*, 410, 1537
- Hatch N. A., Kurk J. D., Pentericci L., Venemans B. P., Kuiper E., Miley G. K., Röttgering H. J. A., 2011, *MNRAS*, 415, 2993
- Hatch N. A., Overzier R. A., Kurk J. D., Miley G. K., Röttgering H. J. A., Zirm A. W., 2009, *MNRAS*, 395, 114
- Hatch N. A., Overzier R. A., Röttgering H. J. A., Kurk J. D., Miley G. K., 2008, *MNRAS*, 383, 931
- Henry J. P. et al., 2010, *ApJ*, 725, 615
- Hwang H. S., Lee M. G., 2009, *MNRAS*, 397, 2111
- Jee M. J. et al., 2009, *ApJ*, 704, 672
- Knopp G. P., Chambers K. C., 1997, *ApJS*, 109, 367
- Kodama T., Tanaka I., Kajisawa M., Kurk J., Venemans B., De Breuck C., Vernet J., Lidman C., 2007, *MNRAS*, 377, 1717
- Kronberger T., Kapferer W., Ferrari C., Unterguggenberger S., Schindler S., 2008, *A&A*, 481, 337
- Kuiper E. et al., 2010, *MNRAS*, 405, 969
- Kurk J. D. et al., 2000, *A&A*, 358, L1
- Kurk J. D., 2003, PhD thesis, Leiden University, P.O. Box 9504, 2300 RA Leiden, The Netherlands



- Kurk J. D., Pentericci L., Overzier R. A., Röttgering H. J. A., Miley G. K., 2004a, *A&A*, 428, 817
- Kurk J. D., Pentericci L., Röttgering H. J. A., Miley G. K., 2004b, *A&A*, 428, 793
- Ma C., Ebeling H., Marshall P., Schrabback T., 2010, *MNRAS*, 406, 121
- Marinoni C. et al., 2005, *A&A*, 442, 801
- Maschietto F. et al., 2008, *MNRAS*, 389, 1223
- Miley G., De Breuck C., 2008, *A&A Rev*, 15, 67
- Miley G. K. et al., 2006, *ApJ*, 650, L29
- Nesvadba N. P. H., Lehnert M. D., Eisenhauer F., Gilbert A., Tecza M., Abuter R., 2006, *ApJ*, 650, 693
- Nesvadba N. P. H., Lehnert M. D., De Breuck C., Gilbert A. M., van Breugel W., 2008, *A&A*, 491, 407
- Ouchi M. et al., 2004, *ApJ*, 611, 685
- Overzier R. A. et al., 2008, *ApJ*, 673, 143
- Overzier R. A. et al., 2006, *ApJ*, 637, 58
- Owers M. S., Randall S. W., Nulsen P. E. J., Couch W. J., David L. P., Kempner J. C., 2011, *ApJ*, 728, 27
- Papovich C. et al., 2010, *ApJ*, 716, 1503
- Pascarelli S. M., Windhorst R. A., Driver S. P., Ostrander E. J., Keel W. C., 1996, *ApJ*, 456, L21+
- Pentericci L. et al., 2000, *A&A*, 361, L25
- Pentericci L., Roettgering H. J. A., Miley G. K., Carilli C. L., McCarthy P., 1997, *A&A*, 326, 580
- Ramírez A., Quintana H., 1990, *Rev. Mex. Astron. Astrofis.*, 21, 69
- Rocca-Volmerange B., Le Borgne D., De Breuck C., Fioc M., Moy E., 2004, *A&A*, 415, 931
- Rykoff E. S. et al., 2008, *MNRAS*, 387, L28
- Saro A., Borgani S., Tornatore L., De Lucia G., Dolag K., Murante G., 2009, *MNRAS*, 392, 795
- Seymour N. et al., 2007, *ApJS*, 171, 353
- Small T. A., Ma C., Sargent W. L. W., Hamilton D., 1998, *ApJ*, 492, 45
- Springel V. et al., 2005, *Nature*, 435, 629
- Stevens J. A. et al., 2003, *Nature*, 425, 264
- Tanaka I. et al., 2010a, *ArXiv e-prints*
- Tanaka M., Finoguenov A., Ueda Y., 2010, *ApJ*, 716, L152
- Venemans B. P. et al., 2005, *A&A*, 431, 793
- Venemans B. P. et al., 2007, *A&A*, 461, 823
- Wilson G. et al., 2008, in *Astronomical Society of the Pacific Conference Series*, Vol. 381, *Infrared Diagnostics of Galaxy Evolution*, R.-R. Chary, H. I. Teplitz, & K. Sheth, ed., pp. 210–+
- Zirm A. W. et al., 2008, *ApJ*, 680, 224



---

# A GALAXY POPULATIONS STUDY OF A RADIO–SELECTED PROTOCLUSTER AT $z \sim 3.1$

We present a population study of several types of galaxies within the proto-cluster surrounding the radio galaxy MRC 0316–257 at  $z \sim 3.1$ . In addition to the known population of Ly $\alpha$  emitters (LAEs) and [OIII] emitters, we use colour selection techniques to identify protocluster candidates that are Lyman break galaxies (LBG) and Balmer break galaxies (BBGs). The radio galaxy field contains an excess of LBG candidates, with a surface density  $1.6 \pm 0.3$  times larger than found for comparable blank fields. This surface overdensity corresponds to an LBG volume overdensity of  $\sim 8 \pm 4$ . The BBG photometric redshift distribution peaks at the protocluster’s redshift, but we detect no significant surface overdensity of BBG. This is not surprising because a volume overdensity similar to the LBGs would have resulted in a surface density of  $\sim 1.2$  that found in the blank field. This could not have been detected in our sample. Masses and star formation rates of the candidate protocluster galaxies are determined using SED fitting. These properties are not significantly different from those of field galaxies. The galaxies with the highest masses and star formation rates are located near the radio galaxy, indicating that the protocluster environment influences galaxy evolution at  $z \sim 3$ . We conclude that the protocluster around MRC 0316–257 is still in the early stages of formation.

E. Kuiper, N. A. Hatch, H. J. A. Röttgering, G. K. Miley, R. A. Overzier,  
B. P. Venemans, C. De Breuck, S. Croft, M. Kajisawa, T. Kodama, J. D. Kurk,  
L. Pentericci, S. A. Stanford, I. Tanaka, and A. W. Zirm  
*Monthly Notices of the Royal Astronomical Society*, 405, 969 (2010)

### 3.1 Introduction

One of the main aims of astrophysics is to understand the formation and evolution of galaxies. Hierarchical evolution in  $\Lambda$ CDM cosmology means the evolution of a galaxy will depend on whether it is located in a low-density or high-density environment (Toomre 1977). This has been quantified in studies by Clemens et al. (2006) and Sánchez-Blázquez et al. (2006) for the local Universe and for the more distant Universe by van Dokkum & van der Marel (2007) and Gobat et al. (2008). These studies find that early-type galaxies in cluster environments are older than early-type galaxies residing in low-density, field environments, indicating that galaxies in cluster-like environments form at an earlier epoch.

Further evidence that environment influences galaxy evolution is the observation of ‘environment-dependent downsizing’ in galaxy clusters at  $z \sim 1$ . Downsizing (Cowie et al. 1996) implies that the bright, massive galaxies move onto the red sequence first, whilst fainter galaxies are added at a later time. Tanaka et al. (2005, 2007, 2008) show that the red sequence in high density environments extends to fainter magnitudes than in less dense galaxy groups. The red sequence therefore forms at an earlier epoch in dense environments.

To understand galaxy evolution in different environments it is necessary to study galaxy clusters across cosmic time. Galaxy clusters have been detected out to  $z = 1.5$  using conventional techniques such as through observation of the hot X-ray emitting intra-cluster gas or IR red sequence searches (e.g., Mullis et al. 2005; Stanford et al. 2005, 2006).

The most successful technique for finding cluster progenitors at  $z > 1.5$  is to search for emission line galaxies around high-redshift radio galaxies (HzRGs, for a comprehensive review see Miley & De Breuck 2008). HzRGs are among the most luminous and massive objects in the early Universe and are expected to be the progenitors to local cD galaxies (Rocca-Volmerange et al. 2004; Seymour et al. 2007). Several studies have found that they are situated in overdense regions with properties expected of forming galaxy clusters (Pentericci et al. 2000; Venemans et al. 2005, 2007; Intema et al. 2006; Overzier et al. 2006, 2008). The dense cluster-like environments around HzRGs are likely not yet virialized and are commonly termed ‘protoclusters’. They are excellent laboratories for studying the formation and evolution of galaxies in overdense environments.

In this study we investigate galaxy populations around the HzRG MRC 0316–257 (hereafter 0316) located at  $z = 3.13$ . Galaxy selection techniques based on the Lyman break at  $912 \text{ \AA}$  (e.g., Steidel et al. 2003) are most efficient at this redshift. Also at this redshift, strong emission lines fall within existing narrowband filters. This allows the selection of many different types of emission line galaxies in the protocluster. Therefore the redshift of this protocluster makes it ideal for studying its galaxy populations. Venemans et al. (2005) (hereafter V05) showed this region contains an overdensity of Ly $\alpha$  emitters (LAEs) and Maschietto et al. (2008) (hereafter M08) found a number of [OIII] emitters near the redshift of the radio galaxy (RG). Additional galaxy populations are identified using a large set of broadband

images. The properties of the galaxy populations are determined using broadband photometry and spectral energy distribution (SED) fitting. These properties are then compared to the properties of field galaxies to search for environmental influences on galaxy evolution at this redshift.

This chapter is ordered as follows: in Sect. 3.2 the data and its reduction is discussed. This is followed by the photometry in Sect. 3.3 and sample selection in Sect. 3.4. The particulars of the SED fitting process are discussed in Sect. 3.5, after which we show our results in Sect. 3.6. We discuss and compare the results to work by other authors in Sect. 3.7. Finally, the summary and conclusions are presented in Sect. 3.8. Throughout this chapter we use a standard  $\Lambda$ CDM cosmology with  $H_0=71$  km s<sup>-1</sup> Mpc<sup>-1</sup>,  $\Omega_M=0.27$  and  $\Omega_\Lambda=0.73$ . All magnitudes given in this chapter are in the AB magnitude system (Oke & Gunn 1983) unless noted otherwise.

## 3.2 Data

Images of the 0316 field were obtained in 20 passbands spanning the  $U$  band to the 8  $\mu$ m band. A summary of all the data used is given in Table 1 and the filter response curves of each of the filters is shown in Fig. 3.1 together with two example SEDs taken from the Bruzual & Charlot (2003) (BC03) models. The fields covered by the various instruments are illustrated in Fig. 3.9. The reduction of the various data sets is described below.

### 3.2.1 Ground-based UV-optical imaging

$UBVR$  imaging data were obtained using the Visible MultiObject Spectrograph (VIMOS, Le Fèvre et al. 2003) instrument at the Very Large Telescope (VLT). The data were taken during the period of 14–15 November 2003 for the V band and 20–25 November 2003 for the remaining bands. Additional  $U$  band data were obtained on 14 February 2004.

The VIMOS field-of-view consists of 4 separate quadrants, each having a field-of-view of approximately  $7' \times 8'$ . Two pointings were used in which the RG was centered in one of the quadrants. For most of this work only the central quadrant that contains the RG is used, as only this central region has additional data.

The reduction of the UV and optical data was performed using standard tasks in the IRAF<sup>13</sup> software package. The process includes bias subtraction and flat fielding using twilight sky flats. Remaining large scale gradients were removed using a smoothed master flat. This was obtained by median-combining the unregistered, flatfielded science images. Reduced images were registered and combined to form the final science images. Photometric zeropoints were determined using standard star images taken on the same nights as the science frames.

---

<sup>13</sup>IRAF is distributed by the National Optical Astronomy Observatory, which is operated by the Association of Universities for Research in Astronomy, Inc., under cooperative agreement with the National Science Foundation.

**Table 3.1** – Details of the observations. The  $5\sigma$  limiting magnitudes have been calculated for angular diameters of  $2''$  for the ground based data,  $0.5''$  for the ACS data and  $4''$  for the IRAC data.

Band	Instrument	Date of observation	$\lambda_{\text{eff}}$ (Å)	$\Delta\lambda$ (Å)	Exp. time (sec.)	Seeing	$5\sigma$ limiting mag.
$U_k$	LRIS/Keck	2003 Jan. 31, 2003 Feb. 1 & 4	3516	561	17100	$1.3''$	26.33
$U_v$	VIMOS/VLT	2003 Nov. 23–24, 2004 Feb. 14	3744	359	15500	$1.0''$	25.98
$B$	VIMOS/VLT	2003 Nov. 22	4310	832	3720	$0.8''$	26.02
$V_v$	VIMOS/VLT	2003 Nov. 14–15	5448	842	4960	$0.75''$	25.97
$V_f$	FORS2/VLT	2001 Sept. 20–21	5542	1106	4860	$0.7''$	26.10
$R$	VIMOS/VLT	2003 Nov. 20 & 25	6448	1292	6845	$0.9''$	25.90
$I$	FORS2/VLT	2001 Sept. 6–8	7966	1433	4680	$0.65''$	25.83
$r_{625}$	ACS/HST	2004 Dec. 14–31, 2005 Jan. 2–21	6321	1327	23010	-	27.66
$I_{814}$	ACS/HST	2002 Jul. 18, 2004 Dec. 14–31, 2005 Jan. 2–21	8089	1765	52320	-	28.37
$J_i$	ISAAC/VLT	2003 Nov. – 2004 Oct.	12535	2640	19000	$0.5''$	24.60
$K_i$	ISAAC/VLT	2003 Nov.– 2004 Oct.	21612	2735	19000	$0.5''$	24.19
$J_m$	MOIRCS/Subaru	2006 Jan. 6–7	12532	1538	4680	$0.75''$	23.77
$H$	MOIRCS/Subaru	2006 Jan. 6–7	16364	2788	3600	$0.8''$	22.71
$K_m$	MOIRCS/Subaru	2006 Jan. 6–7	21453	3042	3300	$0.75''$	23.07
[3.6]	IRAC/Spitzer	2005 Jan. 17–19	35636	6852	46000	-	23.76
[4.5]	IRAC/Spitzer	2005 Jan. 17–19	45111	8710	46000	-	23.60
[5.8]	IRAC/Spitzer	2005 Jan. 17–19	57598	12457	46000	-	22.24
[8.0]	IRAC/Spitzer	2005 Jan. 17–19	79594	25647	46000	-	21.97
$\text{Ly}\alpha$ NB	FORS2/VLT	2001 Sept. 20–21	5040	61	23400	$0.7''$	25.3
[OIII] NB	ISAAC/VLT	2003 Nov. – 2004 Oct.	20675	437	24840	$0.45''$	22.6

Deep Keck  $u'$  band data ( $U_k$ ) were obtained on 31 January, 1 February and 4 February 2003 using the blue arm of the Low Resolution Imaging Spectrometer (LRIS, Oke et al. 1995). As there are large differences in the filter responses, both  $U$  bands have been included in the analysis. Information regarding the reduction of these data can be found in Venemans et al. (2007).

$V$  and  $I$  band data of the 0316 field were obtained during the respective periods of 20–21 and 6–8 September 2001 using the FORS2 instrument at VLT. Information on these data and their reduction can be found in V05.

### 3.2.2 HST/ACS optical imaging

Deep Hubble Space Telescope (HST)  $r_{625}$  and  $I_{814}$  images of the 0316 field cover approximately half of the VIMOS field-of-view. These images were obtained using the Advanced Camera for Surveys (ACS, Ford et al. 1998) during the periods of 14–31 December 2004 and 2–21 January 2005. The data covered two fields of  $3.4' \times 3.4'$  with approximately  $1'$  overlap between the two fields. The two  $I_{814}$  fields were combined with an additional  $3.4' \times 3.4'$  ACS field which was obtained on 18 July 2002. Details of the data and their reduction can be found in M08 and V05.

### 3.2.3 Near-infrared data

Two sets of near-infrared (NIR) data spanning the  $J$  to  $K_s$  bands were used. Deep  $J$  and  $K_s$  images were obtained with the Infrared Spectrometer And Array Camera (ISAAC, Moorwood et al. 1998) on the VLT on various dates between November 2003 and October 2004 (see M08). These images are deep, but only cover the innermost  $2.5' \times 2.5'$  of the protocluster.

Additional  $JHK_s$  data were obtained using the Multi-Object InfraRed Camera and Spectrograph (MOIRCS, Ichikawa et al. 2006; Suzuki et al. 2008) at the Subaru telescope on 6–7 January 2006. For details concerning the reduction of these data we refer the reader to Kodama et al. (2007), hereafter K07. This set of  $JHK_s$  imaging data is shallower than the ISAAC data described above, but it covers a larger fraction of the 0316 field. To avoid confusion between the ISAAC and MOIRCS data we denote the bands with a subscript ‘i’ or ‘m’, respectively.

### 3.2.4 Mid-infrared data

In the mid-infrared wavelength range we have Spitzer InfraRed Array Camera (IRAC, Fazio et al. 2004) data at  $3.6 \mu\text{m}$ ,  $4.5 \mu\text{m}$ ,  $5.8 \mu\text{m}$  and  $8.0 \mu\text{m}$  (hereafter [3.6], [4.5], [5.8] and [8.0] respectively). IRAC data were obtained in all bands on 17–19 January 2005 covering a  $\sim 5' \times 5'$  field centred on the RG. Deep imaging was obtained using a medium scale cycling dither pattern of 230 frames with a 200 s frame time for a total exposure time of  $\sim 12.7$  hours. The [3.6] and [4.5] basic calibrated level data (BCD) were reduced and mosaiced using the MOPEX software (Makovoz & Khan 2005) following standard procedures. Before the BCD frames were combined, the muxbleed and column pulldown effects were corrected using

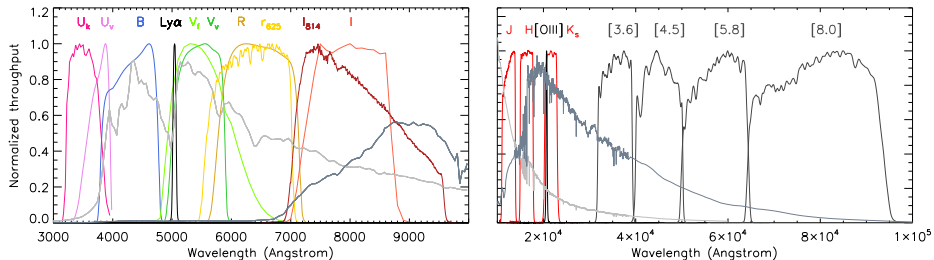


**Figure 3.1** – The filter response curves for the filters used in this study. For illustrative purposes the curves have been scaled to the same maximum throughput. The  $J_m$  and  $K_m$  filter curves are not shown due to their similarity to the corresponding ISAAC filters. Also plotted are two  $z = 3.13$  model SEDs obtained from the BC03 population synthesis models. The light gray SED is for a continuous star forming galaxy of 100 Myr old, whereas the dark gray SED is for a 1 Gyr old galaxy which has an exponentially declining star formation with  $\tau = 10$  Myr.

custom software provided by D. Stern and L. Moustakas. During mosaicing, the images were resampled by a factor of  $\sqrt{2}$  and rotated by  $45^\circ$ . The [5.8] and [8.0] BCD data were further mosaiced using a custom IDL code kindly provided to us by I. Labbé.

### 3.2.5 Further reduction

With the exception of the ACS data, all images were resampled to a common pixel scale of  $0.205''/\text{pixel}$  and transformed to the same image coordinate system using the IRAF tasks GEOMAP and GREGISTER. The images were then convolved with 2D Gaussian profiles to match the PSF FWHM of the VIMOS  $U$  band ( $U_v$ ), which has the largest seeing of approximately  $1''$ . The IRAC bands and the  $U_k$  band are excluded from this process as they have significantly larger PSF sizes. Smoothing the other images to the PSF size of these images would negatively impact the quality of the analysis.

Because of the extreme smoothing required to match the resolution of the ACS images to that of the ground-based data, the ACS data were not used for the SED fitting and photometric redshift determination, but only for the determination of UV slopes of the protocluster galaxy candidates.

## 3.3 Photometry

Photometry was obtained using the SExtractor software (Bertin & Arnouts 1996) in double image mode. Lyman Break Galaxy candidates (LBGs) were detected using the unsmoothed  $R$  band as the detection image. For the Balmer Break Galaxy candidates (BBGs) the unsmoothed  $K_s$  bands were used as detection images.



A detection is defined as an object with 5 adjacent pixels that each exceed the  $3\sigma$  rms noise. Colours were measured in the  $3\sigma$  level isophot apertures as determined from the detection image. If a known object was undetected in an image it was assigned the  $3\sigma$  detection limit of the band in question. Lowering this limit to  $1\sigma$  does not affect any of the conclusions presented in this chapter. Total magnitudes and fluxes in the detection bands were obtained by using the `MAG_AUTO` function of `SEXTRACTOR`. Total fluxes in the remaining bands were obtained by scaling the respective isophotal magnitudes accordingly.

Because of the large size (FWHM) of the PSF in the IRAC images it was not possible to determine consistent colours using the isophotal apertures mentioned above. Instead, the object flux was measured in a circular aperture of 20 pixel ( $4''$ ), and a correction factor applied to match the photometry to the other bands. This correction factor was determined by smoothing the detection images to the spatial resolution of the IRAC data. Object fluxes were measured in the smoothed detection images in  $4''$  circular apertures, and compared to the flux measured from the unsmoothed detection images in the standard  $3\sigma$  isophotal apertures. The ratio between the two fluxes yielded the correction factor. A similar process was applied to determine the colours in the  $U_k$  image.

The large FWHM of the PSF in the IRAC bands also causes source confusion and contamination by neighbouring sources. For faint objects this effect can be a large source of error. All detected objects were visually inspected for contamination, and heavily contaminated objects have been removed from the analysis when relevant.

Finally, all magnitudes were corrected for Galactic foreground extinction determined from the Schlegel et al. (1998) extinction maps.

Photometric uncertainties and limiting magnitudes (listed in Table 3.1) were computed using the method described in Labbé et al. (2003), which is summarized below. After masking all objects, the rms of pixels in the entire image and the rms of fluxes in apertures of various sizes were measured. We determined the noise in an aperture of size  $N$  using the relation

$$\sigma_i(N) = N\bar{\sigma}_i(a_i + b_iN) \quad (3.1)$$

with  $\bar{\sigma}_i$  the rms of pixels over the entire image and  $\sigma_i$  the rms within a certain aperture size  $N$ .  $N$  is defined as  $N = \sqrt{A}$  where  $A$  is the area of the aperture. The subscript 'i' indicates the photometric band in question. The free parameters  $a_i$  and  $b_i$  were then fitted such that it can be calculated what the noise is in an aperture of a given size. The uncertainty calculated using the rms of all the background pixels can be an underestimate, because it does not take into account pixel-to-pixel dependencies introduced in the reduction of the data. Due to the IRAC photometry being more uncertain an additional 10 per cent uncertainty was added in quadrature for those four bands as has been done in previous studies (e.g. Labbé et al. 2005).

The completeness of the detection fields for point sources is shown in Fig. 3.2.

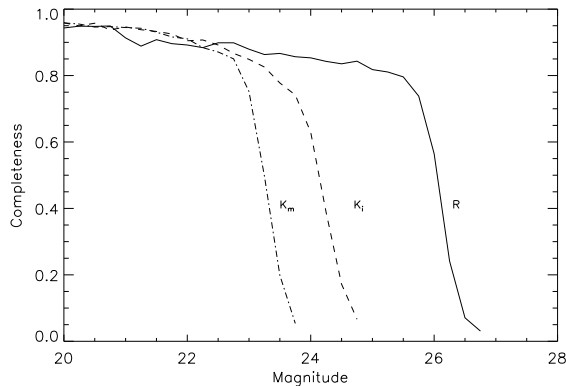


**Figure 3.2** – Completeness of the three detection bands as a function of magnitude for point sources.

The completeness was determined by extracting several bright, unsaturated stars from the images, averaging them to obtain a high signal-to-noise PSF image and then inserting a number of these PSFs at random locations in the images. The source extraction was repeated and the number of recovered artificial stars yielded the completeness as a function of magnitude. To avoid overcrowding only 150 objects were added at a time. This process was repeated ten times for each magnitude to obtain better statistics. Due to the small field size of the ISAAC data the number of added objects was lowered to 50 and the process was repeated fifty times. The data are 50 per cent complete down to  $R = 26$ ,  $K_i = 24.1$  and  $K_m = 23.2$ .

## 3.4 Sample selection

### 3.4.1 Ly $\alpha$ and [OIII] excess objects

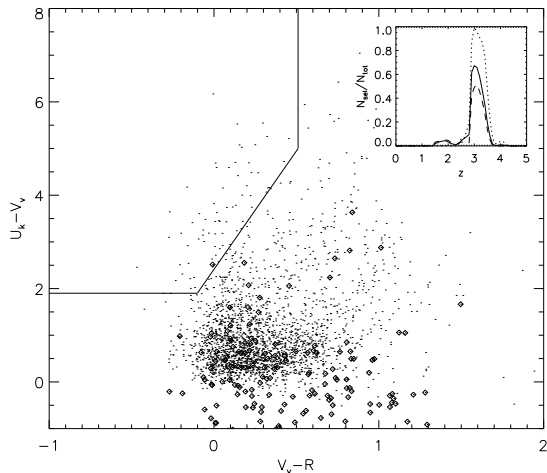
Venemans et al. (2005) spectroscopically confirmed 32 LAEs at the redshift of the RG, and found that the volume density of LAEs in the 0316 field is 2–4 times larger than for the blank field.

Maschietto et al. (2008) found a sample of 13 [OIII] emitting galaxies near the RG, corresponding to a surface density  $3.5^{+5.6}_{-2.2}$  times the field density (uncertainties obtained from Poisson statistics). The [OIII] overdensity is consistent with the LAE overdensity found by V05, but the sample is small and the uncertainties are large. Five of the [OIII] emitters are spectroscopically confirmed LAEs, and three additional [OIII] emitters are spectroscopically confirmed to be at  $z = 3.1$ . These three [OIII] emitters are blueshifted with respect to the RG indicating that the protocluster around 0316 may be part of a larger superstructure.

### 3.4.2 Lyman Break candidates

LBGs were selected using a colour criterion similar to that used by Steidel et al. (2003) to select star forming galaxies at  $z \sim 3$ . The criterion uses the  $U_kVR$  bands. Even though the VIMOS field is larger, the  $U_v$  passband is redder than

**Figure 3.3** –  $U_k - V_v$  vs.  $V_v - R$  diagram of all objects detected in the  $R$  band. Diamonds indicate the points with lower limits to their  $U_k - V_v$  colours. The lines indicate the area in colour-colour space that was used for the LBG selection. The inset shows the selection efficiency for all objects (full line), objects that are younger than 100 Myr and have  $E(B - V) < 0.3$  (dotted line) and objects that are older than 500 Myr (dashed line). The criterion should predominantly select objects in the range  $2.9 < z < 3.4$ .



$U$  passbands used in most other studies. Thus the  $U_k$  band was used to facilitate comparison with other LBG studies.

The colour criterion was devised by creating artificial galaxy spectra using the BC03 evolutionary population synthesis models. Galaxy spectra were synthesized for various star formation histories (SFHs) and a variety of values for extinction and age. The spectra were redshifted from  $z = 0$  to  $z = 5$ . The model spectra were then convolved with the filter curves to obtain synthetic galaxy photometry. Galaxies situated at  $3.0 < z < 3.3$  lie in the upper left corner of the  $U_k - V_v$  vs.  $V_v - R$  colour-colour diagram. This region is parametrized by the relations

$$\begin{aligned}
 U_k - V_v &\geq 1.9, \\
 V_v - R &\leq 0.51, \\
 U_k - V_v &\geq 5.07 \times (V_v - R) + 2.43, \\
 R &\leq 26.
 \end{aligned}
 \tag{3.2}$$

The  $U_k - V_v$  vs.  $V_v - R$  colours for the  $R$  band detected sample are shown in Fig. 3.3. The LBG selection criterion is marked as solid lines. The inset shows the ratio of the number of synthesized objects that are selected to the total number of synthesized objects as a function of redshift. This criterion should predominantly select objects having redshifts between  $2.9 < z < 3.4$  which have low ages and little dust obscuration ( $t < 100$  Myr,  $E(B - V) < 0.3$ ). The 50 per cent completeness limit of  $R = 26$  was adopted as a magnitude cut. A total of 52 objects in the 0316 field satisfy the selection criterion.

Photometric redshifts ( $z_{\text{phot}}$ ) were determined for all  $R$  band detected objects using the EAZY code (Brammer et al. 2008). Since a significant number of objects lack deep NIR coverage we include the more uncertain IRAC bands. To test the influence of the IRAC data on the photometric redshift determination we

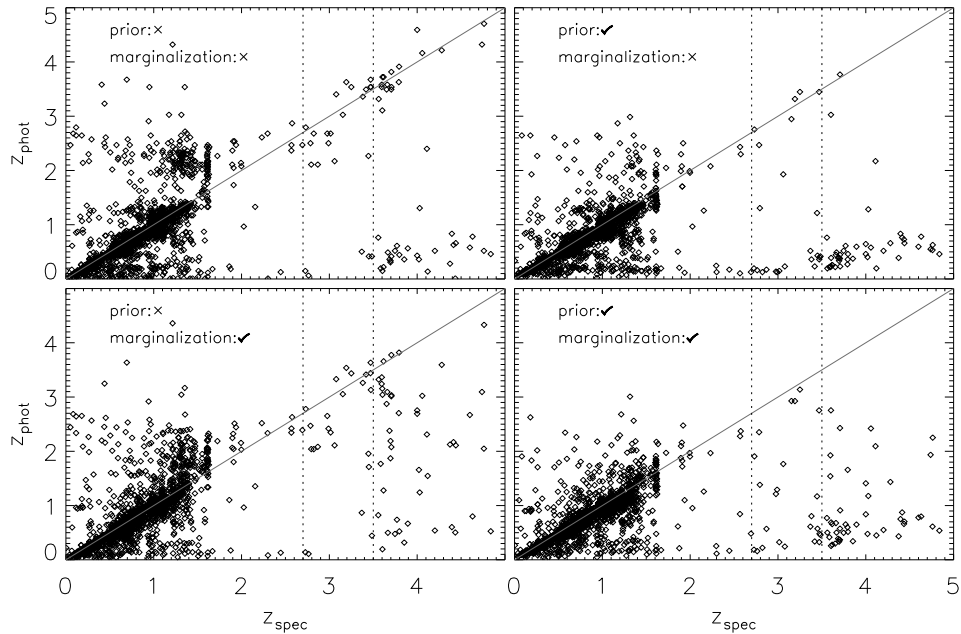


**Figure 3.4** –  $z_{\text{phot}}$  versus  $z_{\text{spec}}$  for a sample of 2469 objects detected in the ECDF-S. No magnitude cut was applied. Photometric redshifts were obtained using the EAZY redshift code and include data in the  $UBVRIJHK_s[3.6][4.5]$  bands. The four panels represent the results for the four different redshift determinations. Each panel indicates whether a prior or marginalization was used. The vertical lines mark the redshift interval of interest. It is apparent that it is best to use neither prior nor marginalization for  $z > 2$  objects.

have determined the photometric redshifts both including and excluding the IRAC photometry.

The EAZY code yields 4 different estimates of the redshift. It offers the options of applying both marginalization<sup>14</sup> and a Bayesian prior. In order to determine which option is best suited for this study we used the Multiwavelength Survey by Yale–Chile (MUSYC) ECDF-S data (Gawiser et al. 2006b; Damen et al. 2009; Taylor et al. 2009) to produce an  $R$  band detected catalogue. The photometric redshifts of this sample were determined using EAZY and subsequently compared to a large sample of spectroscopic redshifts ( $z_{\text{spec}}$ ) from the catalogues of Cimatti et al. (2002), Le Fèvre et al. (2004) and Ravikumar et al. (2007). A total of 2469 objects have spectroscopic redshifts. Note that this will not be a completely consistent test case for the 0316 data, because the objects for which spectroscopic redshifts are available are in general brighter than  $R = 25$ , and the details concerning the depths in certain MUSYC bands are different from the 0316 dataset.

The comparison between  $z_{\text{spec}}$  and  $z_{\text{phot}}$  for the MUSYC galaxies is shown in

<sup>14</sup>The process of marginalization calculates the best photometric redshift value by weighting it according to the redshift probability distribution.

Fig. 3.4. The four panels show the results for four different methods of obtaining the photometric redshift. The scatter is quantified by the median absolute deviation of  $dz = (z_{\text{spec}} - z_{\text{phot}})/(1 + z_{\text{spec}})$ . For  $z_{\text{spec}} < 1.5$  applying both the prior and the marginalization yields the least amount of scatter ( $|dz| = 0.043$ ) and gives in general good agreement. However, application of the prior also shifts the objects with  $z_{\text{spec}} > 2$  to  $z_{\text{phot}} \sim 0.1$ .

Since we target galaxies at  $z \sim 3$ , the photometric redshift determination without prior or marginalization yields the best results. Comparing the scatter for  $z_{\text{spec}} > 2$  yields  $|dz| = 0.22$  for the upper left panel and  $|dz| = 0.69$  and  $|dz| = 0.65$  for the upper and lower right panels, respectively. The option that uses neither prior nor marginalization systematically overestimates the redshifts of objects at  $z \sim 1$ , placing them at  $2 < z_{\text{phot}} < 2.5$  instead. However, only 0.2 per cent of objects with  $z_{\text{spec}} < 1.5$  are placed in the range  $2.7 < z_{\text{phot}} < 3.5$ , so this should have no significant effect on the results. In the remainder of this chapter, photometric redshifts of the 0316 galaxies have been obtained using neither prior nor marginalization.

The photometric redshift distribution of the 0316 LBG candidates is shown in the main panel of Fig. 3.5. The majority of objects is situated at  $z \sim 3.1$  and strong peaks are seen at the redshift of the protocluster and  $z \sim 2.9$ . These peaks are artefacts caused by the discrete number of possible redshifts. Excluding the IRAC data (dotted line) has little influence on the photometric redshift distribution. This is due to the inclusion of both  $U_k$  and  $U_v$ . Both bands sample the strong Lyman break feature of these galaxies and hence the photometric redshifts are well constrained.

All objects within  $2.7 < z < 3.5$  were selected for the final sample of 48 objects. This is based on the photometric redshift uncertainties shown in the inset of Fig. 3.5. Here the redshift uncertainty  $\Delta z$  is taken to be half of the  $1\sigma$  uncertainty interval yielded by EAZY. The inset indicates that an uncertainty of 0.4 is a reasonable value to encompass all possible  $z \sim 3.1$  objects. The accuracy of photometric redshifts is not sufficient to verify if any of these objects are indeed members of the protocluster surrounding 0316; to achieve this spectroscopic redshifts are needed.

### 3.4.3 Balmer Break Galaxy candidates

The Balmer break can be used to select  $z \sim 3$  galaxies in a similar fashion to the Lyman break method discussed in Sect. 3.4.2.

Extracting a sample of distant red galaxies (DRGs) was done by using the simple colour cut  $(J - K_s)_{\text{Vega}} \geq 2.3$  proposed by Franx et al. (2003). The DRG colour criterion samples red, predominantly massive galaxies between a redshift of 2 and 4. Although the NIR filter sets used in this study differ from other studies the  $(J - K)$  colour difference is typically  $\sim 0.02$  mag, which is small compared to the photometric errors. Therefore these colour terms are deemed negligible.

Thirty-four DRGs are found in the ISAAC field-of-view after removing 6 ghost images. After applying a 50 per cent completeness cut at  $K_s = 24$  the final sample

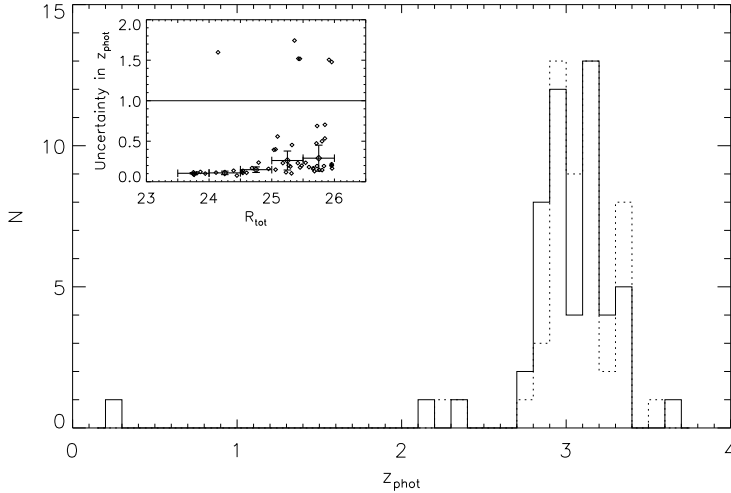


**Figure 3.5** – Redshift distributions of the sources selected using the colour cuts in Eq. 3.2. The full line and dotted line denote results obtained with and without the IRAC bands, respectively. In the inset the redshift uncertainty  $\Delta z$  is plotted as a function of  $R$  band magnitude for all objects that satisfy the LBG colour selection criterion. Also shown are average values for 0.5 mag bins. Objects that have uncertainties larger than 1 (as indicated by the horizontal line) are not included in these average values. These objects are degenerate between  $z \sim 0$  and  $z \sim 3$  and would skew the average to higher values.

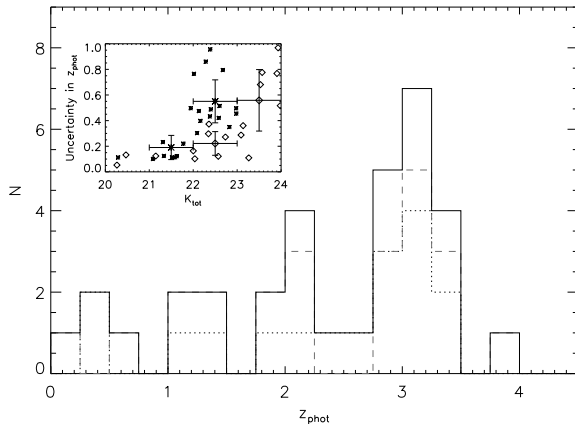
of 17 DRGs remains. Amongst the DRGs are the RG, an LAE and an [OIII] emitter with  $z_{\text{spec}} = 3.104$  (M08).

The MOIRCS data is about 1 magnitude shallower in the  $K_s$  band than the ISAAC data. K07 apply a magnitude cut of  $K_m = 23.7$  and find a total of 54 DRGs in the MOIRCS field, 14 of which are located in the ISAAC field. Using the detection criterion described above (5 adjoining pixels  $3\sigma$  above the background) leads to several spurious detections in the MOIRCS data compared to the ISAAC data. Increasing the detection criterion to  $3.25\sigma$  removes most of the spurious detections including two DRGs detected by K07. These are spurious detections since neither of these two objects have counterparts in the deeper ISAAC data. There may also be spurious DRGs outside the ISAAC field-of-view. DRGs with  $K_m > 23$  (the 50 per cent completeness level) were removed from the sample resulting in a final sample of 23 DRGs in the MOIRCS field. The difference in the number of DRGs in the K07 study and the present study is due to the stricter magnitude cut and the different parameter values used for source detection.

Combining the two separate DRG samples leads to a sample of 33 unique DRGs. In the rest of the chapter we will refer to DRGs as Balmer Break Galaxies (BBGs).

The main panel of Fig. 3.6 shows the photometric redshift distribution that is found for both BBG samples and the combined sample. We find that there is a

**Figure 3.6** – Redshift distribution of the ISAAC detected BBGs and the MOIRCS detected BBGs are shown as a dotted and dashed line, respectively. The redshift distribution for the combined sample is also shown as the full line. Note the peak in number at the redshift of the radio RG.



peak at  $z \sim 3$ , the redshift of the protocluster. The inset shows the uncertainties on the photometric redshifts as a function of  $K_s$  magnitude. As can be seen from the inset the uncertainty on the photometric redshift increases rapidly as the magnitude becomes fainter, with  $1\sigma$  uncertainties  $> 0.5$  for  $K_i \geq 23$ . This is due to the faint  $U_k$  and  $U_v$  magnitudes of these objects resulting in a poorly constrained Lyman break. Such large uncertainties would smooth any peak in the redshift distribution caused by the protocluster.

A Kolmogorov–Smirnov test was used to compute the significance of the peak using the photometric redshift distribution of BBGs from Grazian et al. (2007) as a comparison sample. There is a probability of 0.3 per cent that both distributions have been drawn from the same parent distribution. Thus the photometric redshift distribution of BBGs in the 0316 region differs at the  $3\sigma$  level from that in the field.

Possible protocluster members are identified as the BBGs that lie within  $2.7 < z_{\text{phot}} < 3.5$ . A total of 9 ISAAC BBGs satisfy this criterion. For the MOIRCS BBGs a similar fraction of 11 out of 23 lie within  $2.7 < z_{\text{phot}} < 3.5$ .

### 3.4.4 Spectroscopic redshifts

Within the 0316 field spectroscopic redshifts are known for all 32 LAEs, 7 [OIII] emitters and 16 additional objects (Bram Venemans, private communication). Fig. 3.7 compares these spectroscopic redshifts to the photometric redshifts obtained with the EAZY photometric redshift code.

In general the photometric redshifts agree well with the spectroscopic redshifts. Even the intrinsically faint LAEs (denoted by blue crosses) show good agreement. The scatter around the protocluster’s redshift of approximately  $\sigma_z = 0.3$  is similar to the width chosen for the redshift cut in the LBG and BBG selection. Because of this good agreement we expect that the photometric redshift estimates are adequate representations of the true redshifts.

There are six additional objects with  $z_{\text{spec}} > 3$ , but only three of these are

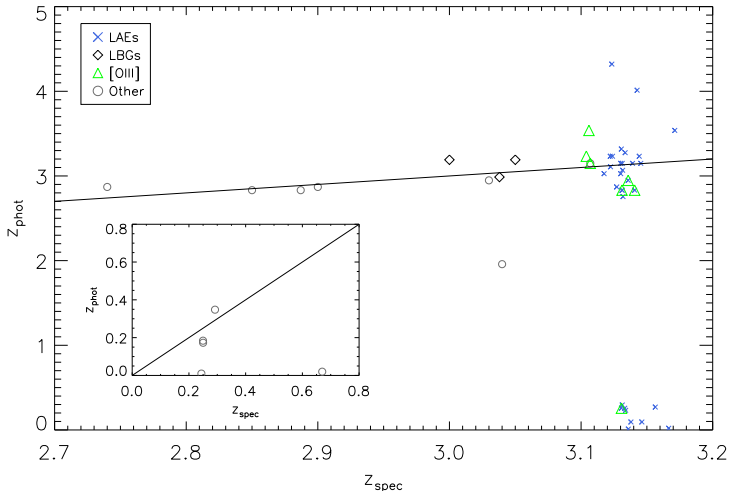


**Figure 3.7** –  $z_{\text{phot}}$  versus  $z_{\text{spec}}$  for all the objects in the 0316 field that have spectroscopic redshifts. The line indicates equality. The main panel shows the redshift range of interest, whereas the inset shows low redshift objects. Circles denote the 13 objects that are unclassified, the diamonds are LBGs, the blue crosses denote the LAEs and the green triangles indicate the [OIII] emitters. The RG is the [OIII] emitter in the lower right corner of the figure.

classified as LBGs. It thus seems that approximately half of the  $z \sim 3$  galaxies have been missed by the colour selection technique. We discuss this further in Sect. 3.4.5. Furthermore, the photometric redshift of the RG differs strongly from its spectroscopic redshift. This is due to its proximity to a foreground galaxy which affects the photometry.

### 3.4.5 Completeness: photometric redshift selection

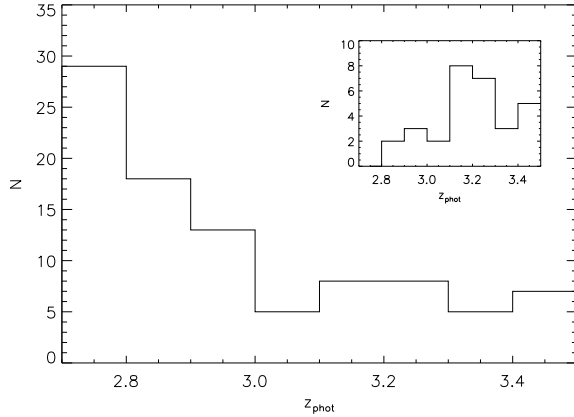
In addition to the selected protocluster galaxy candidates, we selected unclassified objects that have photometric redshifts in the range  $2.7 < z_{\text{phot}} < 3.5$ . The size of this sample gives an estimate of the number of  $z \sim 3$  galaxies that are missed by the above-mentioned colour-selection techniques.

Galaxies with  $2.7 < z_{\text{phot}} < 3.5$  were selected from the  $R$  band and  $K_s$  band detected catalogues. These objects must be located in the field-of-view covered by the  $U_k$  band, since the LBGs are selected from this band. They must also have NIR data in order to have the best constraints on the photometric redshift. All known LBGs, BBGs, ISAAC ghost images, spurious detections and double entries were removed and the appropriate magnitude cuts were applied. A sample of 96 objects was obtained of which 93 were detected in  $R$  band and 3 in either of the  $K_s$  bands.

Figure 3.8 shows the photometric redshift distribution of the  $R$  band detected



**Figure 3.8** – Redshift distributions of ‘non-classified’ objects detected in  $R$  band that have  $2.7 < z_{\text{phot}} < 3.5$  and  $R \leq 26$ . The inset shows the subset of objects that satisfy the redshift,  $V_v - R$  and magnitude criteria for LBG selection but are undetected in  $U_k$ .



galaxies. The distribution differs significantly from the  $z_{\text{phot}}$  distribution of LBGs as there is a large number of objects located at the lower edge of the redshift range.

The majority of galaxies with  $3.0 < z_{\text{phot}} < 3.3$  is undetected in the  $U_k$  band and was assigned lower limits for their  $U_k - V_v$  colours. These  $U_k - V_v$  lower limits are generally too blue for these objects to be classified as LBGs, but deeper  $U$  band data might lead to redder  $U_k - V_v$  colours, shifting them into the LBG region. The inset in Fig. 3.8 shows the  $z_{\text{phot}}$  distribution of these possible LBGs. A peak at the redshift of the protocluster is seen. This peak accounts for a large fraction of the unclassified objects with  $3.0 < z_{\text{phot}} < 3.3$ . There are 55 potential LBGs (pLBGs) that have lower limits on  $U_k - V_v$  that are too blue to be classified as LBGs. The LBG selection therefore misses up to 50 per cent of  $z \sim 3$  galaxies.

In the  $K_s$  band only three additional objects are found to be missing from the BBG sample. The same redshift range yields 15 unique BBGs. Based on this we estimate that the BBG selection yields  $\sim 80$  per cent of all  $z \sim 3$   $K_s$  detected galaxies.

The positions of the objects in the final samples as well as the fields covered by the various instruments used are shown in Fig. 3.9.

### 3.5 SED fitting

Do the properties of the protocluster galaxies differ from those of field galaxies at the same redshift? To compare the protocluster galaxies to field galaxies we determine the galaxy properties by fitting the individual galaxy SEDs with population synthesis models, and then compare the properties to equivalent samples detected in the field.

The fitting of the galaxy SEDs was done using the FAST code described in Kriek et al. (2009). Due to its versatility and speed the use of the FAST code allows us to fit a large range of models and model parameters. Both the BC03 and the updated CB07 models (Charlot & Bruzual, private communication) were used

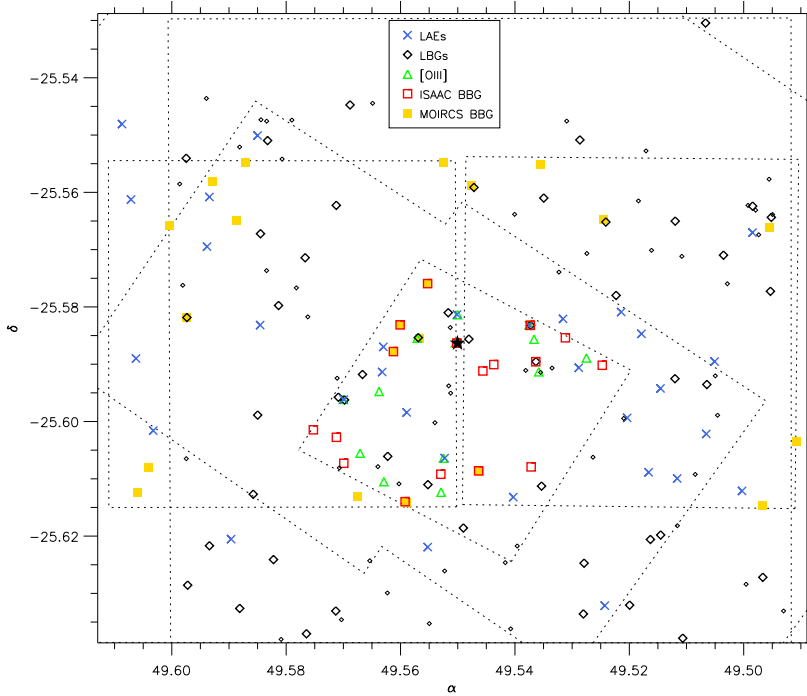


**Figure 3.9** – Sky coordinates of the various populations. Large and small diamonds indicate the LBGs and pLBGs, respectively. Blue crosses denote LAEs, green triangles [OIII] emitters and the squares denote the BBGs. A distinction is made between ISAAC and MOIRCS detected BBGs, with the former indicated by open red squares and the latter by filled yellow squares. The dotted lines indicate the outlines of the fields covered by the various instruments. The FORS data ( $V_fI$ ) covers the entire figure and also includes all VIMOS bands ( $U_vBV_vR$ ). Subsequently, the IRAC data covers the majority of the field with the exception of some of the corners. Going from larger to smaller fields we then have the  $U_k$  field, the field covered by ACS, the two MOIRCS fields and finally, slightly below centre the area covered by ISAAC.

with a Salpeter IMF and  $Z = Z_{\odot}$ . The inclusion of an improved treatment of the TP-AGB phase in the CB07 models results in a more reliable stellar mass estimate for populations older than 100 Myr.

The free parameters in the fitting routine are the age, mass, SFH and the extinction by dust. We considered exponentially declining SFHs with decay times,  $\tau$ , ranging from 10 Myr to 10 Gyr with steps of 0.1 dex. The inclusion of SFHs with values of  $\tau$  much larger than the age of the Universe for our adopted cosmology allowed us to mimic a constant SFH. The age grid that we considered ranges from  $\log(\text{age}/\text{yr})=7$  to 9.3 with age steps of 0.1 dex, where  $\log(\text{age}/\text{yr})=9.3$  equals the age of the Universe at  $z \sim 3.13$ . The redshifts were fixed to the spectroscopic or photometric redshifts, depending on which was available. As the EAZY code is specialized in determining redshifts and is more efficient in use, we have chosen to use the EAZY redshifts rather than including it as a free parameter during the SED fitting. This choice has little effect on the main results for the majority of the objects.

The effect of internal dust extinction on the model SEDs was taken into account using the Calzetti et al. (2000) extinction law for values of  $A_V$  ranging from 0 to 3 with steps of 0.1. The attenuation blueward of the Ly $\alpha$  line due to the IGM was included using the prescription of Madau (1995).

## 3.6 Results

### 3.6.1 Number densities of galaxy populations

#### 3.6.1.1 Lyman Break Galaxy candidates

To determine whether there is an overdensity of LBGs in the 0316 field due to the presence of the protocluster, the number density of LBGs in the 0316 field is compared to the  $\sim 0.3$  degrees<sup>2</sup> MUSYC ECDF-S blank field (see also Sect. 3.4.2). Photometry for the control field was obtained as described in Sect. 3.3.

The Great Observatories Origins Deep Survey-South (GOODS-S) field, which is part of the ECDF-S field, has been shown to be underdense in DRGs (van Dokkum et al. 2006). Comparison of the number density of DRGs and LBGs in 8 ECDF-S subfields reveals that the variation in LBG number density is lower than for DRGs. Furthermore, the central subfield, which has the lowest DRG number density, has a relatively high number density of LBGs. We conclude that the ECDF-S is unlikely to be as underdense in LBGs as the GOODS-S field is in DRGs.

For the MUSYC ECDF-S data an LBG colour criterion was devised that is equivalent to the criterion used for the 0316 field:

$$\begin{aligned}
 U - V &\geq 1.85, \\
 V - R &\leq 0.62, \\
 U - V &\geq 4.0 \times (V - R) + 2.51, \\
 R &\leq 26.
 \end{aligned}
 \tag{3.3}$$

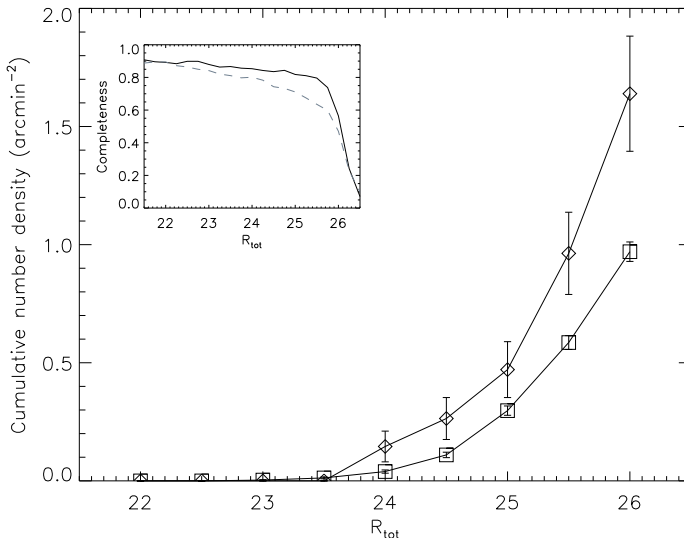


**Figure 3.10** – Completeness-corrected cumulative number density of objects that satisfy the colour selection criterion as function of total  $R$  band magnitude. Diamonds denote values for the 0316 field, whereas the squares indicate the results found for the MUSYC ECDF-S control field. Uncertainties are based on Poisson statistics. An excess of LBGs in the 0316 field is apparent. The inset shows the completeness of the fields as a function of magnitude with the full and dashed line denoting the 0316 and ECDF-S data, respectively.

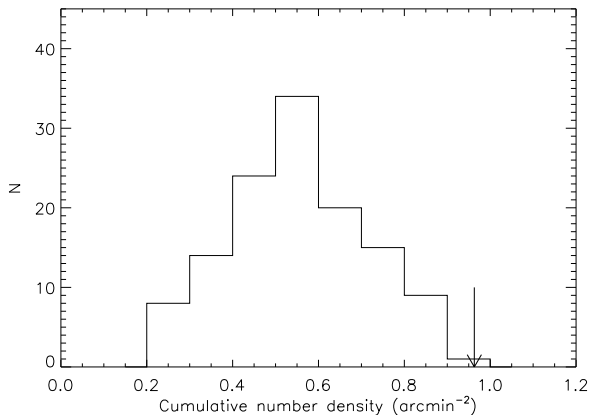
Applying this to the MUSYC data yields a total number of 694 LBG candidates.

Figure 3.10 shows the completeness-corrected cumulative number density of LBGs for both the 0316 and the ECDF-S control field. Note that no information on the redshifts of the objects is used to select these LBG samples. There is an excess in the 0316 field across the entire magnitude range. The 0316 field is a factor of  $1.6 \pm 0.3$  denser than the ECDF-S field for galaxies with  $R \leq 25.5$ , with the  $1\sigma$  uncertainty based on Poisson statistics. Defining the galaxy surface overdensity as  $\delta_g = n_{0316}/n_{\text{ECDF-S}} - 1$ , we find  $\delta_g = 0.6 \pm 0.3$  in the 0316 field. This overdensity is not the result of a difference in general number counts, as the area-normalized completeness-corrected number counts of the two fields differ by less than 1.5 per cent.

The significance of the LBG overdensity in 0316 is quantified by considering field-to-field variations of LBGs on the scale of the 0316 field. The number density of LBGs in 125 subfields of the ECDF-S (each the same size as the 0316 field) is measured, and the resulting distribution displayed in Fig. 3.11; the arrow indicates the number density of LBGs in the 0316 field. Only 1 in 125 fields has a number density that exceeds the 0316 density, thus the significance of the LBG overdensity in the 0316 field is at the  $3\sigma$  level with respect to field-to-field variations.

The surface overdensity of LBGs in the 0316 field is a lower limit to the volume

**Figure 3.11** – Distribution of LBG number densities with  $R \leq 25.5$  in the ECDF-S for 125 randomly chosen Keck-sized ( $40.1 \text{ arcmin}^2$ ) fields. The arrow indicates the value found for the 0316 field. One in 125 ECDF-S subfields is found to host a larger number density than found in the 0316 field.



overdensity of the protocluster in this field. The LBG selection criterion selects galaxies in a relatively large redshift range, so the LBG overdensity within the protocluster is larger than 0.6 (see Sect. 3.7).

The outer VIMOS quadrants are used to assess the LBG number density at greater distances from the RG. There is no  $U_k$  coverage for these outer fields, so the criterion given in Eq. 3.2 cannot be used. Instead, a similar criterion that uses the  $U_v$  filter is applied. The number density in the outlying fields is approximately 10 per cent smaller than the central field. Therefore these outlying fields are overdense with respect to the ECDF-S, but to a lesser degree than the central 0316 field. This indicates that the protocluster extends beyond the central field, out to at least  $15'$  ( $\sim 7 \text{ Mpc}$ ). This is larger than most estimates of protocluster sizes which typically find sizes of 2–5 Mpc (Intema et al. 2006; Venemans et al. 2007), but often size estimates are limited by the field size. Nevertheless, the larger size may be a consequence of the possible superstructure in the field, as hinted at by the redshift distribution of the [OIII] emitters.

### 3.6.1.2 Balmer Break Galaxy candidates

The study of K07 found that the 0316 field is overdense with respect to the GOODS-S field, with approximately 1.5–2 times more BBGs in the 0316 field. However, van Dokkum et al. (2006) has pointed out that the GOODS-S field is underdense, containing only 60 per cent of the number of objects found in the larger MUSYC survey (Gawiser et al. 2006b; Quadri et al. 2007). To ascertain whether there is an overdensity of BBGs in the 0316 field, we compare to the publically available MUSYC data described in Quadri et al. (2007).

The four MUSYC fields cover a total area of  $\sim 400 \text{ arcmin}^2$ . Using these fields as control fields will yield better statistics compared to the GOODS-S, as well as decrease the influence of cosmic variance. The control fields are denoted as HDFS1, HDFS2, 1030 and 1255, respectively. Catalogues were constructed from the four images following the procedure used for the 0316 field. Applying the BBG criterion

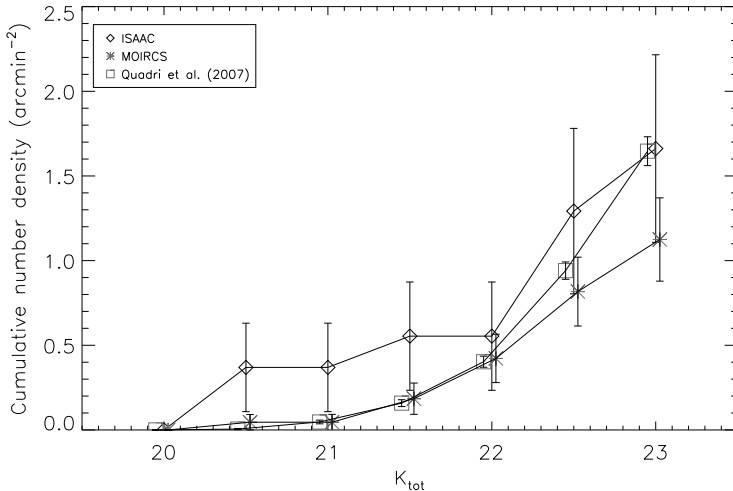


**Figure 3.12** – Completeness-corrected cumulative number density as function of  $K_s$  band magnitude for both populations of BBGs. ISAAC and MOIRCS detected BBGs are denoted by diamonds and asterisks, respectively. Uncertainties are obtained using Poisson statistics. The squares denote the mean cumulative number density of the four individual MUSYC fields. Neither of the 0316 BBG populations shows evidence for an overdensity in the 0316 field.

and a  $K_s \leq 23$  cut yields 123, 116, 197 and 118 BBGs for the HDFS1, HDFS2, 1030 and 1255 fields, respectively, or 554 BBGs in total.

Fig. 3.12 compares the completeness-corrected cumulative number density of BBGs in the 0316 field to the MUSYC control field. The small field-of-view ISAAC data suggests that the 0316 field has an excess of bright BBGs ( $K_s \leq 21.5$ ) close to the radio galaxy, but the sample is small so the number statistics are poor. At fainter magnitudes there is no overdensity. Since the MOIRCS field shows no indication of an excess at bright magnitudes, we conclude that there is no evidence for an overdensity of BBGs in the 0316 field. This is in contradiction with the conclusion of K07.

The lack of an overdensity seems to contradict the presence of a peak in the photometric redshift distribution at the protocluster’s redshift (Fig. 3.6). Nine ISAAC selected BBGs lie in the range  $2.7 < z_{\text{phot}} < 3.5$ . Only four of these have  $K_i \leq 23$ , so more than half of the BBGs at the protocluster’s redshift are too faint for inclusion in Fig. 3.12. It is possible most of the protocluster BBGs are faint, and would only be revealed as an overdensity at faint magnitudes, however the control fields are not deep enough to warrant a proper comparison.

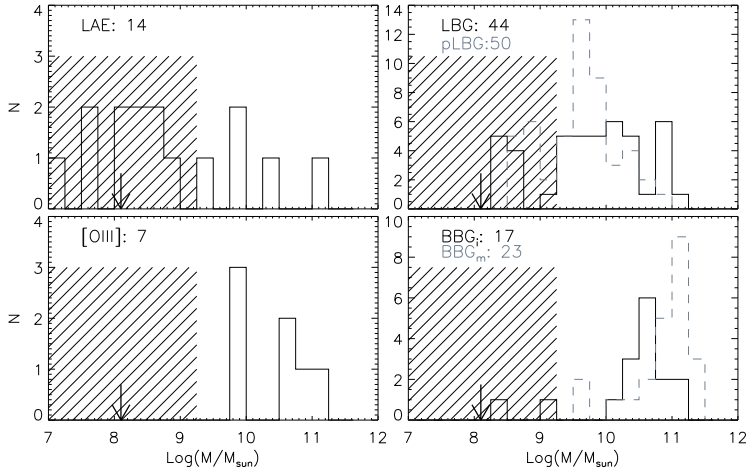


**Figure 3.13** – Stellar mass distributions for each protocluster population. Objects that are strongly affected by confusion in the IRAC images, or galaxies with  $M \leq 10^7 M_{\odot}$  are not included. The total number of objects in each population is shown in the upper left corner of each panel with the same colour coding as the respective histograms. The arrow indicates the best-fitting mass that is found for the LAE stack (Sect. 3.6.2.5). The hatched region indicates where mass estimates become highly uncertain due to faintness in the restframe optical.

### 3.6.2 Properties of protocluster galaxy candidates

Below we present the results of the SED fitting for all protocluster populations. The LAEs are treated separately in Sect. 3.6.2.5, because they are generally very faint across the entire wavelength range. This results in poorly constrained SED fits and therefore a different approach was taken for this population.

#### 3.6.2.1 Mass

The mass distributions of all protocluster candidate populations are shown in Fig. 3.13. The estimate of the stellar mass is dominated by the flux in the IRAC bands, so all objects that are strongly contaminated by neighbouring sources have been excluded from the samples. Table 3.2 lists the median mass values for each population.

The upper right panel of Fig. 3.13 shows that most LBGs have masses between  $10^9$  and  $10^{11} M_{\odot}$  and the median stellar mass is a few times  $10^9 M_{\odot}$ . This mass increases to  $\sim 2 \times 10^{10} M_{\odot}$  when limiting the sample to LBGs with  $R \leq 25.5$ . The median mass of the pLBG population is approximately a factor 2 lower than the LBGs, and a KS test shows that the mass distributions differ at the  $2\sigma$  level. Thus the  $z \sim 3$  galaxies that are not included in the LBG sample due to insufficient depth of the  $U$  band are generally less massive than the LBG galaxies.

A large fraction of the [OIII] emitters is detected in the [3.6] and [4.5] bands, whilst a few are also detected in the [5.8] and [8.0] bands. Six objects (the RG

and source IDs 2, 6, 10, 11 and 12 in M08) are strongly contaminated by nearby bright objects. The remaining 7 objects are all detected in the [3.6] and [4.5] bands. This implies that the [OIII] emitters have significant stellar masses. The median stellar mass of the [OIII] emitters is larger than the median LBG mass, however, this median mass is based on a sample of only 7 objects.

[OIII] emitters are selected as high equivalent width objects in the observed  $K_s$  band, thus they are selected to have low  $K_s$  band magnitudes relative to the [OIII] narrowband<sup>15</sup>. Hence it is surprising that such a selection criterion identifies massive galaxies.

Not all [OIII] emitters have been spectroscopically confirmed, so it is possible the sample contains low redshift interlopers. The prime suspects for interlopers would be H $\alpha$  emitters at  $z \sim 2.15$ . Three out of the 7 [OIII] emitters with reliable mass estimates are not spectroscopically confirmed and two of these have  $z_{\text{phot}} \sim 2.17$ . Moreover, all spectroscopically confirmed [OIII] emitters have  $z_{\text{phot}} > 3$ . Thus it is possible that these two objects are interlopers. Removing these objects from the sample leaves three galaxies with  $M = 6 - 8 \times 10^9 M_{\odot}$  and two galaxies with  $\sim 10^{11} M_{\odot}$ .

The BBGs have masses of a few times  $10^{10} M_{\odot}$  with some exceeding  $10^{11} M_{\odot}$ . The BBGs comprise the population with the highest masses of the protocluster candidate populations. Since the BBGs are  $K_s$  band selected it is expected that they will have high stellar masses. The ISAAC-selected BBGs are on average less massive than the MOIRCS-selected BBGs, but this is only due to the larger depth of the ISAAC data. When the same magnitude cut is applied to both datasets the mass of the ISAAC-selected BBGs agrees with that of the MOIRCS-selected BBGs.

### 3.6.2.2 Age and extinction

The SED fitting procedure results in degeneracies between the best-fit age, extinction and SFH. Because of the large uncertainties on the best-fit ages of the LBGs, we do not discuss them further in this work. The ages of the BBGs are easier to constrain, because they were selected to have strong Balmer breaks. The median age at which the BBGs started forming stars is  $\sim 1$  Gyr ago (see Table 3.2).

### 3.6.2.3 UV slope

Assuming the restframe UV continuum has the form  $f_{\lambda} = C\lambda^{\beta}$ , we calculated the UV slope  $\beta$  of the candidate protocluster members. Either the  $R$  and  $I$  or  $r_{625}$  and  $I_{814}$  bands were used, depending on whether ACS coverage is available. At  $z \sim 3$  these bands correspond to restframe 1500 Å and 2000 Å, respectively. The

---

<sup>15</sup>At low redshifts the [OIII] line is often found to be an indicator of AGN activity. Therefore part of the IRAC flux may be caused by heated dust close to an AGN.



UV slope was calculated as

$$\beta = \frac{\log f_{\lambda,R} - \log f_{\lambda,I}}{\log \lambda_{\text{eff},R} - \log \lambda_{\text{eff},I}} \quad (3.4)$$

with  $\lambda_{\text{eff},R/I}$  the effective wavelength of the  $R$  or  $I$  filters, respectively. The uncertainty on  $\beta$  was obtained by varying the flux by an amount drawn randomly from the normal photometric error distribution.

The median  $\beta$  for the LBG population  $\beta$  is  $-1.52$ , but the bright subset ( $R \leq 25.5$ ) has a redder UV slope of  $-1.38$ . This reddening of  $\beta$  with increasing brightness was also found by Bouwens et al. (2009). An unobscured, young population has a UV slope ranging from  $-2$  to  $-2.5$ . Thus the LBGs are slightly attenuated by dust. The pLBGs are on average bluer than the LBGs, indicating there is less dust in these objects.

The [OIII] emitters have similar UV colours to the LBGs. Whereas the BBGs have significantly redder colours than the LBGs so they are either more heavily obscured or older than the LBGs.

#### 3.6.2.4 Star formation rate

The star formation rates (SFRs) of the candidate protocluster galaxies were estimated from the rest-frame  $1500 \text{ \AA}$  luminosity using the relation from Kennicutt (1998)

$$SFR_{\text{UV}} [M_{\odot} \text{ yr}^{-1}] = \frac{L_{1500}}{8 \times 10^{27}}. \quad (3.5)$$

This relation is valid for a Salpeter IMF and does not take the presence of dust into account. For simplicity we assume that all objects are located at the redshift of the protocluster. Furthermore, this relation is only valid for starbursts that have reached an equilibrium between the number of stars forming and evolving off of the main sequence. The SFRs of extremely young starburst galaxies that have not yet reached this equilibrium will be underestimated.

The SFRs of the candidate protocluster galaxies are shown in Fig. 3.14. Most galaxies have SFRs less than  $10 M_{\odot} \text{ yr}^{-1}$ , irrespective of galaxy population, with a small fraction of outliers having SFRs up to  $40 M_{\odot} \text{ yr}^{-1}$ . Both the median dust-uncorrected and dust-corrected SFRs for each population are listed in Table 3.2. The extinction was derived from the UV slopes using  $E(B - V) = (\beta - \beta_0)/8.067$  (Meurer et al. 1995) and  $A(1500) = 4.39E(B - V)$  (Calzetti et al. 2000). Here  $\beta_0$  is the UV slope for an unattenuated ionizing population of stars, assumed to be  $-2.5$ . This method of estimating SFRs gives good agreement with SFRs derived from radio observations for galaxies at  $z \sim 2$  (Pannella et al. 2009).

The LBGs have a relatively small amount of dust extinction with a median  $A(1500) = 0.53$  ( $A_V = 0.21$ ). Shapley et al. (2001) found generally larger dust extinction with a median value of  $A_V \sim 0.6$ . We revisit this difference in a more thorough comparison in Sect. 3.7.2.2. No significant difference was found between the uncorrected SFRs of the LBGs and pLBGs, but the dust-corrected SFRs of

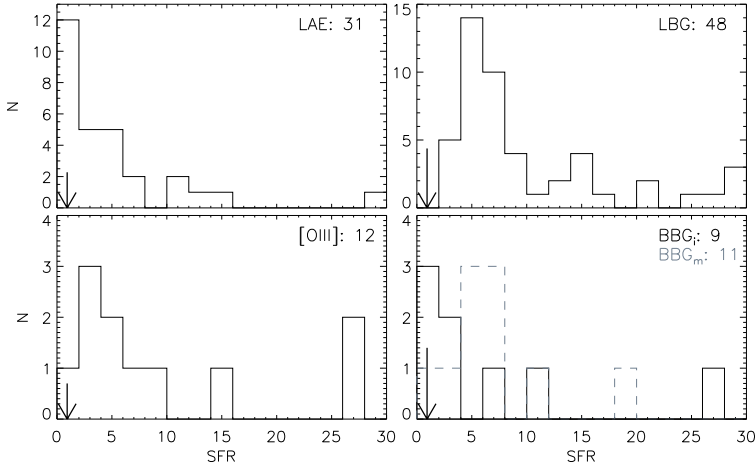


**Figure 3.14** – Extinction uncorrected star formation rates for the various populations obtained from the restframe  $1500 \text{ \AA}$  luminosity. The arrow indicates the SFR obtained for the LAE stack. For simplicity, we have assumed that all LBGs and BBGs with  $2.7 < z < 3.5$  are located at the protocluster’s redshift.

the pLBGs are systematically lower, consistent with the UV slopes of the pLBGs being systematically bluer.

The slope of the UV continuum can become redder due to both aging of the stellar populations, and attenuation by dust. Thus it is ambiguous to use the UV slope as an indicator of extinction for BBGs. Therefore the amount of extinction was measured from both the UV slopes and the value for  $A(1500)$  derived from the SED fitting. Both values of the dust-corrected SFR are listed in Table 3.2.

The estimated SFRs of the MOIRCS BBGs are systematically larger than those of the ISAAC BBGs. However, the MOIRCS data are shallower than the ISAAC data and therefore include objects with systematically larger mass. The observed difference in SFRs between MOIRCS and ISAAC objects is consistent with the increase of SFR with increasing mass at  $z < 1$  (Noeske et al. 2007) and at  $z \sim 2$  (Daddi et al. 2007).

### 3.6.2.5 $Ly\alpha$ emitters

In the sample of LAEs, 27 are not detected in any IRAC band, indicating that the LAEs have small stellar masses. Figure 3.13 shows that most LAEs have  $M < 10^9 M_{\odot}$ . The properties of these IRAC-undetected LAEs were investigated by mean stacking 16 LAEs that lie within the field-of-view of the  $U_{\nu}BVRI$  and MOIRCS datasets and are not contaminated by bright neighbours in the IRAC data.

**Table 3.2** – Upper part: median values of various properties for the samples discussed in this work. Uncertainties here are mean absolute deviations on the median divided by the square root of the number of objects. Lower part: Properties for the stacked and bright, individual LAEs.

Object	$\log(M)_{\text{CB07}}$	$\log(M)_{\text{BC03}}$	SFR ( $M_{\odot} \text{ yr}^{-1}$ )	SFR <sub>corr</sub> ( $M_{\odot} \text{ yr}^{-1}$ )	$\log(\text{Age})_{\text{CB07}}$	$\beta$
LBG	9.92	10.1	7.0	11.3	- <sup>a</sup>	-1.52±0.07
LBG <sub>R&lt;25.5</sub>	10.16	10.29	11.4	23.1	- <sup>a</sup>	-1.38±0.09
pLBG	9.65	9.79	5.7	9.1	- <sup>a</sup>	-1.72±0.08
pLBG <sub>R&lt;25.5</sub>	9.79	9.95	8.7	13.9	- <sup>a</sup>	-1.54±0.15
OIII <sup>b</sup>	10.51	10.62	6.3	9.5	- <sup>a</sup>	-1.50±0.13
BBG <sub>I</sub>	10.55	10.77	2.2 <sup>c</sup>	5.1/6.9 <sup>c,d</sup>	9	-1.12±0.21 <sup>c</sup>
BBG <sub>M</sub>	11.0	11.15	6.6 <sup>c</sup>	15.0/6.8 <sup>c,d</sup>	8.9	-0.91±0.19 <sup>c</sup>
LAE <sub>stack</sub>	8.1 <sup>+0.42</sup> <sub>-0.3</sub>	8.1 <sup>+0.53</sup> <sub>-0.32</sub>	0.9	1.0	7.0 <sup>+1.0</sup>	-2.40±0.43
LAE <sub>1518</sub>	9.97 <sup>+0.11</sup> <sub>-0.19</sub>	10.07 <sup>+0.14</sup> <sub>-0.19</sub>	15.7	20.4	8.8 <sup>+0.1</sup> <sub>-0.2</sub>	-1.97±0.32
LAE <sub>1867</sub>	11.08 <sup>+0.05</sup> <sub>-0.12</sub>	11.22 <sup>+0.08</sup> <sub>-0.11</sub>	40.2	64.2	8.8 <sup>+0.1</sup> <sub>-0.3</sub>	-1.56±0.73
LAE <sub>3101</sub>	10.48 <sup>+0.22</sup> <sub>-0.68</sub>	10.74 <sup>+0.09</sup> <sub>-0.94</sub>	11.3	27.6	8.8 <sup>+0.5</sup> <sub>-1.7</sub>	-0.7±1.8

<sup>a</sup> Individual ages are unconstrained

<sup>b</sup> Values for the SFRs and  $\beta$  taken from M08

<sup>c</sup> Only objects with  $2.7 < z < 3.5$  are taken into consideration

<sup>d</sup> First value calculated using the UV slope and second value calculated using the SED fit results

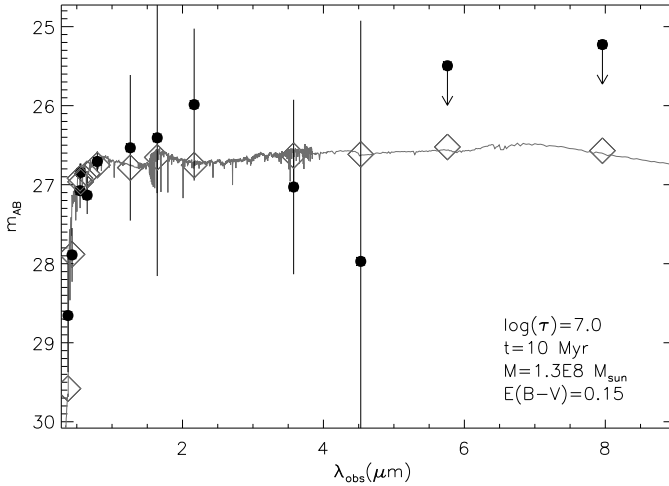


**Figure 3.15** – Photometry of a stack of 16 LAEs and the corresponding best-fitting SED. The diamonds indicate the photometry as computed from the best fit SED. Best-fitting parameters are listed in the bottom right corner.  $1\sigma$  upper limits are used for [5.8] and [8.0] as the stack yields negative flux in these bands. The best-fitting model is very young and has a low mass, but a significant amount of dust extinction. Due to the large uncertainties on the JHK and IRAC photometry a model SED without dust would lead to an equally acceptable fit.

The photometry and the best-fitting SED for the stacked data are shown in Fig. 3.15. The stack reveals robust detections in the *BVRI* bands, but not in bands redward of *I*. The derived stellar mass is approximately  $10^8 M_{\odot}$  and this is marked in Fig. 3.13 with an arrow. It is much smaller than the average LBG stellar mass. The best-fit age is 10 Myr, which is the lowest age allowed by the SED fitting process. The amount of dust extinction is unconstrained from the fit to the SED, but the UV slope determined from the  $r_{625}$  and  $I_{814}$  bands is  $\beta = -2.4$ . Thus the average protocluster LAE contains little dust. These results are in agreement with previous studies that show that LAEs are in general young objects experiencing their first burst of star formation (e.g. Hu & McMahon 1996; Malhotra & Rhoads 2002; Tapken et al. 2004).

Only 4 of 32 LAEs have robust detections in [3.6] and [4.5], whilst 1 LAE has a marginal detection. The four objects with significant IRAC detections include the RG. However, since the RG is located close on the sky to a foreground galaxy, the photometry in all bands is compromised. It is therefore not included in further analysis (but see also Seymour et al. 2007, who estimate its mass to be  $1.6 \times 10^{11} M_{\odot}$  based on a Kroupa IMF). The remaining 4 LAEs are discussed below using the IDs designated in V05.

**1518:** The detection of this object in the [3.6] and [4.5] bands is marginal. However, it has significant detections in both *J* and  $K_1$  ( $6\sigma$  and  $7.5\sigma$ , respectively). The photometry and the best-fit SED are shown in the upper left panel of Fig. 3.16. The galaxy is best fit by a model with continuous SFR and an age of 600 Myr.

No dust attenuation is required. The best-fit stellar mass is  $\sim 10^{10} M_{\odot}$ , making it almost two orders of magnitude more massive than the average LAE.

**1867:** Excluding the RG, this object is the second brightest LAE in the sample. It has a clear IRAC detection in all four bands and is also bright in the restframe UV/optical continuum. The photometric redshift of this object is 3.15, which is consistent with the spectroscopic redshift of 3.134. The galaxy is of similar age to object #1518 with a best fit age of 600 Myr and  $\tau \sim 200$  Myr. It contains no dust and it is very massive, having a stellar mass of approximately  $10^{11} M_{\odot}$ . This galaxy is also selected as an LBG and a BBG. It has a clumpy morphology as seen in ACS data (V05, Venemans et al. in prep.) and is located  $50''$  (or 350 kpc in projection) from the RG.

**2487:** This object hosts an AGN, as evidenced by the broadness of the Ly $\alpha$  line and the presence of a broad CIV emission line (V05, Le Fèvre et al. 1996). Since the SED fitting does not account for an AGN contribution, the best fit parameters are not valid and are not discussed further.

**3101:** This LAE has similar properties to #1867, but it is less massive by a factor 3. Because of the absence of ISAAC data, the best-fit properties are poorly constrained.

An overview of the properties including  $1\sigma$  uncertainty intervals can be found in Table 3.2. Note that the two objects for which only MOIRCS NIR data is available (#2487 and #3101) have significantly larger uncertainties on the best-fitting age. This reflects the aforementioned need for deep NIR observations in order to constrain the age.

### 3.6.3 Dependence of galaxy properties on location within the proto-cluster

An important question in studying the history of cluster evolution is whether there are systematic variations in the properties of the protocluster members that depend on their location within the protocluster, e.g. distance from the radio galaxy.

In Fig. 3.17 the stellar mass of the LBGs is plotted as a function of distance from the RG. The main panel of Fig. 3.17 shows the area-normalized integrated mass  $M_{\text{int}}$  within annuli of  $50''$ , whilst the inset shows the individual masses and the mean mass per annulus.

Two massive LBGs near the RG result in a high  $M_{\text{int}}$  in the innermost annulus.  $M_{\text{int}}$  then sharply decreases out to  $150''$ , but slightly increases at greater distances.

The inset in Fig. 3.17 shows a large scatter in the masses of the LBGs at all radii, which is expected with such a large number of interlopers. This large scatter in combination with the small sample size could also cause the upturn at distances greater than  $150''$ .

The two most massive LBGs are located near the RG: one is a confirmed LAE protocluster member, whereas the other is an [OIII] emitter with  $z_{\text{phot}} = 3.23$ . Both galaxies have stellar masses of approximately  $10^{11} M_{\odot}$  making them almost

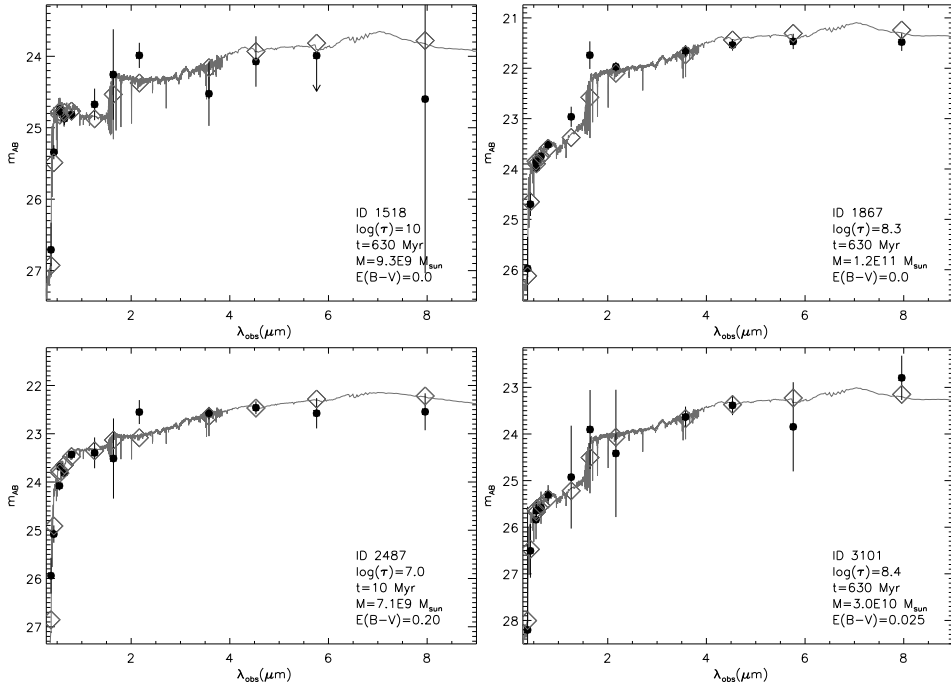


**Figure 3.16** – Photometry and SED fits for the four LAEs that were detected in the [3.6] and [4.5] bands. Best-fitting parameters are shown in the bottom right corner of each panel. Diamonds denote magnitudes as calculated from the best-fitting SED. ID numbers correspond to the ones used in V05. The first two objects fall inside the limited ISAAC field-of-view and are shown with the ISAAC  $J$  and  $K_s$  data for the restframe optical. For the remaining two objects no ISAAC data was available and the shallower MOIRCS  $JHK_s$  data is used. Three out of four SED fits return ages of 500 Myr and higher and all masses are approximately larger than  $5 \times 10^9 M_{\odot}$ . Non-detections are replaced with  $1\sigma$  upper limits.

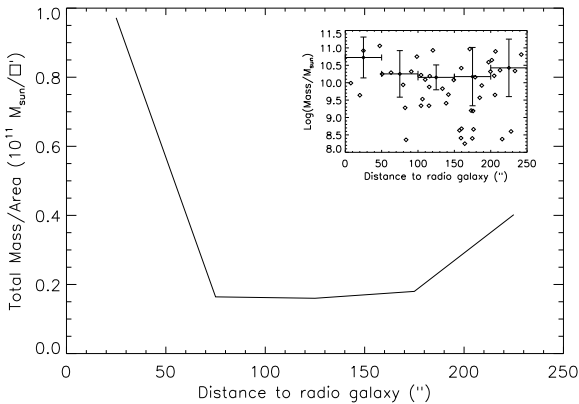
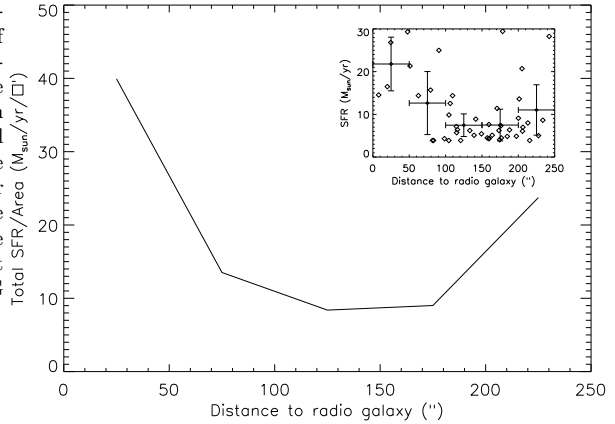


**Figure 3.17** – Stellar mass of all LBGs as function of distance to the RG. Masses of individual objects within annuli of 50'' width are summed and normalized to the area of the annuli. The inset shows the individual values as function of distance to the RG and mean values for each of the annuli. The individual values show a weak trend, but the integrated mass shows a sharp decrease as the distance to the RG increases.

**Figure 3.18** – Total area-normalized SFRs for annuli of  $50''$  width. SFRs are dust-uncorrected. The inset shows the individual values and the mean values for bins of  $50''$ . Vertical error bars are mean absolute deviations. The seemingly lower limit to the SFR present in the inset is due to the magnitude cut at  $R = 26$  used to select LBGs. Objects close to the RG are forming stars more rapidly.



as massive as the RG itself ( $2.5\text{--}3 \times 10^{11} M_{\odot}$  for a Salpeter IMF). This is different from what is found for radio-selected protoclusters at  $4 < z < 5$ , where the RG is approximately an order of magnitude more massive than the brightest of the surrounding LBGs (Overzier et al. 2009).

Figure 3.18 shows the area-normalized integrated SFR in annuli of  $50''$ . A similar trend is observed for the SFR as for  $M_{\text{int}}$ : galaxies close to the RG have larger SFRs, although again the scatter is large. At small distances ( $< 100''$ ) all objects are forming stars at rates of  $> 15 M_{\odot} \text{ yr}^{-1}$ , whereas at larger distances the majority of the objects are forming stars at  $\sim 5 M_{\odot} \text{ yr}^{-1}$ . That galaxies with the highest SFR are located in the centre of the protocluster is in stark contrast with the situation in galaxy clusters at  $z < 1$  where the SFR drops towards the cluster core (e.g. Balogh et al. 1998, 1999; Hashimoto et al. 1998; Postman et al. 2001; Lewis et al. 2002).

The above figures show that the RG is surrounded by some of the most massive and active galaxies in the protocluster. How unique is the position of the RG in the protocluster? The above procedure was repeated for 200 random locations in the 0316 field, and the resulting mass and SFR distributions for the innermost annulus are shown in Fig. 3.19. There are few locations that yield similar or larger  $M_{\text{int}}$  or total area-normalized SFR, and these are all located close to the RG. Thus the immediate surroundings of the RG are unique within the 0316 field. The radio galaxy likely lies in the core of the forming protocluster and the protocluster core galaxies are affected by their environment.

Note that there are several effects that will weaken such observed spatial trends. First, since the photometric redshifts alone cannot establish protocluster membership, there will be contamination by interlopers in such an analysis. The observed LBG surface overdensity of 0.6 implies that slightly less than 2 out of every 3 LBGs is an interloper. Secondly, many protocluster systems show filamentary structures (e.g. Ouchi et al. 2005; Matsuda et al. 2005; Overzier et al. 2008), hence the assumption of a circular symmetry used above will also weaken the signal. Thirdly, the

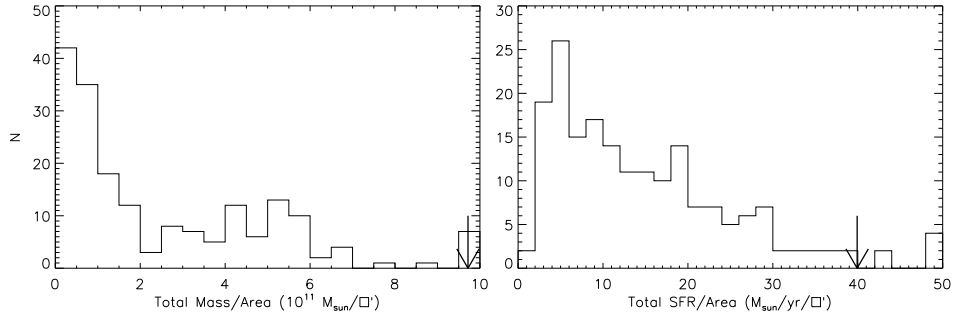


**Figure 3.19** – Left panel: Distribution of total area-normalized mass within a  $50''$  radius for 200 random locations across the 0316 field. Right panel: Same as left panel but for SFR. Arrows indicate the total area-normalized mass and SFR in a  $50''$  annulus when the RG is taken as the centre of the protocluster.

RG itself is not included in this analysis, and its large mass ( $> 10^{11} M_{\odot}$ ) and SFR ( $110 M_{\odot} \text{ yr}^{-1}$  without dust correction) will lead to an even stronger correlation if included. Thus the radial dependence is likely to be stronger than observed.

We conclude from the observed radial trends in stellar mass and SFR that galaxy evolution is strongly influenced by the protocluster environment, with larger SFRs and stellar masses occurring in the protocluster core.

## 3.7 Discussion

### 3.7.1 Surface and volume overdensities

#### 3.7.1.1 Lyman Break galaxies

The measured LBG surface overdensity of the 0316 field is  $0.6 \pm 0.3$ . Because the uncertainties of the photometric redshifts ( $\sigma_z/(1+z)$ ) range between 0.02 and 0.35, the derived surface density will be diluted by the fore- and background objects that are in the sample as well. The surface overdensity of  $0.6 \pm 0.3$  that is found is thus a lower limit to the volume overdensity of the LBGs. How strong must the volume overdensity of LBGs be to produce a surface overdensity of 0.6?

V05 showed that the FWHM of LAE redshifts in the 0316 protocluster is  $\Delta z \sim 0.025$ . LAEs are in general significantly less massive than LBGs so they may relax within the protocluster potential more easily. We assumed that the protocluster spans a line-of-sight distance of  $\Delta z = 0.04$  (as found in the study of Steidel et al. (1998) for LBGs in the SSA22 protocluster at  $z = 3.09$ ). In the field-of-view covered by the  $U_k$  band, the protocluster spans a volume of  $\sim 5.6 \times 10^3 \text{ Mpc}^3$ .

The LBG selection criterion selects galaxies in the redshift interval  $2.9 < z < 3.4$ , as shown in the inset in Fig. 3.3. Although the spread in the  $z_{\text{phot}}$  distribution exceeds this interval, this can be attributed to the uncertainties in the  $z_{\text{phot}}$  estimates. There are 448 LBGs with  $R < 25.5$  in the ECDF-S and these span a



volume of  $1.8 \times 10^6 \text{ Mpc}^3$ . This implies that there should be approximately 16–17 ‘field’ LBGs in the 0316 field.

To obtain a surface overdensity of  $\delta_g = 0.6$  an additional 10–11 LBGs are needed in the protocluster volume. The protocluster volume can host approximately 1.3 ‘field’ LBGs. Hence the protocluster is a factor  $\sim 8 \pm 4$  denser than the field and the volume overdensity  $\delta_{g,V}$  is  $7 \pm 4$ , with the  $1\sigma$  uncertainties calculated by propagation of the uncertainty on the surface overdensity. This is larger than the overdensities observed in the LAEs and [OIII] emitters, but this volume overdensity is little more than an order of magnitude estimate due to the many uncertainties in the assumptions that were made.

Furthermore, based on the presence of three [OIII] emitters at  $z = 3.1$ , M08 speculated the 0316 protocluster is part of a larger 60 comoving Mpc superstructure. This superstructure would extend beyond the redshift range probed by the Ly $\alpha$  NB filter. If the protocluster is part of a larger superstructure, the protocluster volume assumed above would result in an overestimate of the LBG overdensity.

The mass of the protocluster was computed using the comoving volume  $V$  occupied by the protocluster, the mean density of the Universe  $\bar{\rho}$  and the matter overdensity  $\delta_m$  which relates to the galaxy volume overdensity  $\delta_{g,V}$  as  $\delta_m = \delta_{g,V}/b$  with  $b$  being the bias parameter. Using  $V = 5.6 \times 10^3 \text{ Mpc}^3$ ,  $\bar{\rho} = 1.9 \times 10^{10} \text{ M}_\odot \text{ Mpc}^{-3}$  and  $b = 1\text{--}5$  (e.g., Adelberger et al. 1998; Giavalisco et al. 1998; Ouchi et al. 2004; Lee et al. 2006) the protocluster mass is  $M = 2\text{--}12 \times 10^{14} \text{ M}_\odot$ . The range was determined by the combination of the  $1\sigma$  uncertainty and the range in the bias value. This protocluster mass is consistent with V05 and is similar to the mass of the Virgo cluster. Since it was shown in Sect. 3.6.1.1 that the overdensity is spread over multiple VIMOS quadrants, the protocluster volume is likely underestimated. Therefore, the cluster mass should be considered a lower limit.

### 3.7.1.2 Balmer Break galaxies

We found no surface overdensity of BBGs in the 0316 field based on the number densities. But would we expect to detect a surface overdensity in the BBGs assuming the protocluster has the same volume overdensity of BBGs as it has of LBGs? Or will the overdensity be smoothed out due to the large redshift range that is probed by the BBG selection criterion?

The 554 BBGs detected in the four MUSYC fields are assumed to lie between  $2 < z < 3.5$  and are homogeneously spread across this redshift interval. Thus the volume spanned by this population is  $2.2 \times 10^6 \text{ Mpc}^3$ . This implies that there should be 7–8 ‘field’ BBGs with  $K_s < 23$  in the ISAAC field-of-view. The protocluster occupies  $755 \text{ Mpc}^3$  (within the ISAAC field-of-view), and this volume contains on average 0.2 ‘field’ BBG. So if the BBGs are overdense by the same factor as the LBGs (volume overdensity of 7), the protocluster will host  $\sim 1.4$  BBG. This results in a surface number density in the ISAAC field that is 1.2 times as high as the field density and thus a surface overdensity  $\delta_g = 0.2$ . This is consistent with the  $1\sigma$  uncertainties on the cumulative number densities at  $K_s = 23$  as shown in Fig. 3.12.

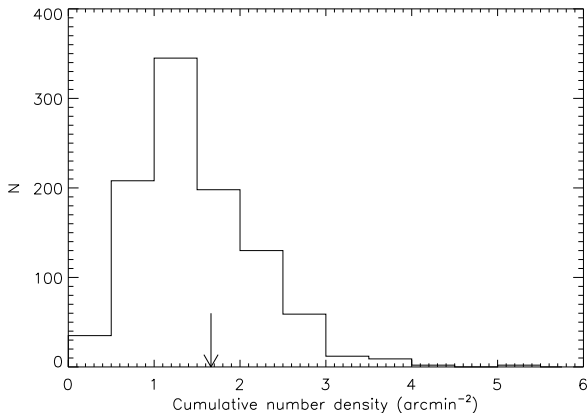


**Figure 3.20** – Distribution of BBG number densities with  $K_s \leq 23$  in the UDS field (Williams et al. 2009) for 1000 randomly chosen ISAAC-sized (5.4 arcmin<sup>2</sup>) fields. The arrow indicates the respective number density found for the 0316 field. To obtain a  $3\sigma$  overdensity signal with respect to the field-to-field variations a number density of at least 3.5 arcmin<sup>-2</sup> is needed.

We conclude that a volume overdensity of 7 cannot be ruled out due to the small sample size.

It is doubtful whether systematic searches for BBG overdensities at  $z \sim 3$  have any chance of succeeding considering the range in redshift that is probed. To evaluate this the amplitude of field-to-field variations for an ISAAC-sized field is assessed. A similar method as described in Sect. 3.6.1.1 is employed. As reference the UDS catalogue from Williams et al. (2009) is used. This field is complete down to  $K_s = 23$  and covers a total of  $\sim 0.8$  degrees<sup>2</sup>. The BBG number density was evaluated in 1000 ISAAC-sized fields placed randomly across the UDS field. The resulting distribution is shown in Fig. 3.20. The arrow indicates the BBG density found in the 0316 field. It is clear that this result is not significant with respect to the field-to-field variations. In fact, a number density of  $\sim 3.5$  arcmin<sup>-2</sup> is needed to obtain a surface overdensity that is significant at the  $3\sigma$  level. This would imply a surface overdensity  $\delta_g \sim 1.2$ , equivalent to a volume overdensity of  $\sim 45$ . Such a strong overdensity is highly unlikely to exist over a large field-of-view. We conclude that selection criteria that span a considerable redshift range are poorly suited for the detection of overdensity signals around HzRGs.

### 3.7.2 Field and cluster ensemble properties

Does the evolution of galaxies in crowded environments in the early Universe, such as protoclusters, differ significantly from galaxy evolution in the field? At  $z = 2.3$ , Steidel et al. (2005) found that both ages and masses of galaxies in a protocluster are  $\sim 2$  times larger than similarly selected galaxies in the field. A similar study at  $4 < z < 5$  has shown no significant difference between protocluster and field galaxies (Overzier et al. 2009). This study can give a better insight in the situation at  $z \sim 3$ .

We compare galaxy masses, SFRs and UV slopes for the various protocluster populations with those of equivalent populations in the field. There is no sample of field [OIII] emitters in the literature, hence this population will not be discussed.

We also refrain from comparing the 0316 BBGs to field BBGs as there is no strong evidence for an overdensity in the 0316 field. The SED fit results given here have been obtained using BC03 models with a Salpeter IMF to facilitate comparison with previous studies.

### 3.7.2.1 *Ly $\alpha$ emitters*

Studies of LAEs at  $z \sim 3$  find stellar masses ranging between  $10^8$  and  $10^9 M_{\odot}$  (Gawiser et al. 2006a; Nilsson et al. 2007; Lai et al. 2008) which is fully consistent with the results presented in this study.

We also presented SEDs for a small population of massive LAEs that do not fit the picture of galaxies that experience their first burst of star formation. This subpopulation of massive LAEs is found frequently in recent studies. Finkelstein et al. (2009) found that two objects in their sample of 14 LAEs at  $z = 4.4$  were best fit by a model SED with an age of 800 Myr and a mass of  $6.5 \times 10^9 M_{\odot}$ . This fraction of 2 out of 14 is similar to the fraction of massive objects found in this study. Lai et al. (2008) find a fraction of massive LAEs of approximately 30 per cent, but they quote a  $2\sigma$  detection limit of 25.2 for [3.6]. This is approximately half a magnitude deeper than the 0316 data. Pentericci et al. (2009) investigated Ly $\alpha$ -emitting LBGs, finding a small fraction of objects that are significantly older than the average LAE. In summary, there is no evidence that the LAEs in the protocluster are significantly different from the field population.

### 3.7.2.2 *Lyman break galaxies*

Taking all LBGs with  $R \leq 25.5$ , the median mass of the 0316 LBGs is  $\sim 1.6$  times more massive than that of 'field' LBGs, which have a median mass of  $1.2 \times 10^{10} M_{\odot}$  (Shapley et al. 2001). In addition, LBGs close to the RG are more massive than LBGs at larger radii, indicating that the protocluster environment promotes the increased stellar mass of its members. However, the BC03 population synthesis models were not available at the time of the study of Shapley et al. (2001), so a fully consistent comparison can not be made.

Lehmer et al. (2009) find that LBGs suspected to be in the protocluster SSA22 at  $z = 3.09$  have on average  $H$  band luminosities that are 1.2–1.8 times larger than LBGs that are unrelated to the protocluster. Since the  $H$  band can be interpreted as a proxy for stellar mass at  $z \sim 3$  this also indicates that the masses of the protocluster LBGs are larger by the same factor. This factor of 1.2–1.8 is similar to the difference in median masses found in this study.

The 0316 LBGs have dust-uncorrected SFRs of  $\sim 7$ – $11 M_{\odot} \text{ yr}^{-1}$  (depending on whether the whole sample is considered or only the objects that have  $R \leq 25.5$ ). The  $\mathcal{R}$  data presented in Steidel et al. (2003) yields a median dust-uncorrected SFR for field LBGs of  $\sim 10 M_{\odot} \text{ yr}^{-1}$ . This is consistent with the median dust-uncorrected SFR found for the 0316 LBGs. If the SFRs are corrected for dust extinction, the SFRs increase on average by a factor of 2. This small increase

in SFR indicates the presence of small amounts of dust in the LBGs. Shapley et al. (2001) used SED fitting to find that field LBGs have a median extinction of  $E(B-V) = 0.155$  ( $A_V = 0.62$ ). This is larger than found in the 0316 protocluster as half of the 0316 LBGs are best fit by  $A_V \leq 0.1$ . However,  $A_V$  is poorly constrained, with 31 out of 48 LBGs having  $1\sigma$  uncertainties that are consistent with  $A_V = 0.6$ . We can therefore not conclude whether the 0316 LBGs are less dusty than field LBGs.

Meurer et al. (1999) composed a sample of  $z \sim 3$  LBGs from the HDF V2.0 catalog (Williams et al. 1996) using a *UVI* filter combination. This filter set is similar to the set used in this study. They find a median UV slope ( $\beta$ ) for field LBGs of approximately -1.6, similar to 0316 LBGs. We thus find no evidence for a difference in the UV slopes between field and cluster LBGs at  $z \sim 3$ . Shapley et al. (2003) find significantly redder slopes for field LBGs, but the filter set used in their work differs significantly from this study, so it does not offer a fair comparison.

We find that the 0316 LBGs have stellar masses, SFRs and UV slopes that are consistent with those of field LBGs. We thus conclude that at  $z \sim 3$  the ensemble properties of all possible protocluster galaxies is not significantly different from what is found in a low-density environment.

### 3.7.3 The future of MRC 0316–257

We have found that the 0316 field contains an overdensity of star forming galaxies. How will the protocluster LBGs evolve and at what epoch will a quiescent population emerge?

Using a simple ‘back of the envelope’ calculation we estimate how the protocluster will appear at later times. The peak of the cosmic SFH lies below  $z \sim 3$  (e.g. Steidel et al. 1999) and therefore new LBGs will emerge at later times. These ‘new’ objects are not taken into account and we only evolve the LBGs that are currently identified. The sample is therefore static and no new objects are introduced.

The SED fitting yields both a best-fitting age and SFH, so it is possible to evolve the LBGs according to this information. We find, however, that both these quantities are poorly constrained. Hence, we make the following assumptions. Since the distribution of SFHs peaks at approximately  $\tau = 10^8$  yr, we assume that the typical LBG has an SFH of 100–500 Myr. An age of 50–500 Myr is assumed, in accordance with earlier studies that state 100 Myr to be the typical age for LBGs at  $z \sim 3$  (Shapley et al. 2001). Finally, the initial SFR is assumed to be 40–60  $M_\odot \text{ yr}^{-1}$ . These SFRs are to be interpreted as being intrinsic SFRs. They are based on the results from Shapley et al. (2001) and as shown in Sect. 3.7.2 are consistent with the results for the 0316 LBGs. For simplicity the influence of dust extinction will not be taken into account in this scenario.

If a quiescent galaxy is defined as having an  $\text{SFR} \leq 2 M_\odot \text{ yr}^{-1}$  we find that the majority of a population of LBGs will have reached quiescence after a period of approximately 1 Gyr. This corresponds to  $z \sim 2$ . Only the youngest LBGs having  $\tau = 500$  Myr will last until  $z \sim 1.5$  before they reach quiescence. Therefore, the

0316 protocluster should harbour a substantial ‘dead’ population after 1 Gyr of evolution.

These predictions can be compared to observations of protocluster structures at lower redshifts. One of the best studied protoclusters is the overdense region surrounding the  $z = 2.16$  radio galaxy PKS 1138–262 (1138) (Miley et al. 2006). This radio galaxy has a intricate, clumpy morphology and seems to be in an advanced stage of merging with several smaller galaxies. It is surrounded by a diffuse UV halo which is evidence for in-situ star formation outside the main radio galaxy (Hatch et al. 2008). Furthermore, the field has been shown to harbour overdensities in both Ly $\alpha$  and H $\alpha$  emitting galaxies, extremely red objects (EROs), X-ray emitters and sub-mm bright galaxies (Pentericci et al. 2000; Kurk et al. 2004b,a; Stevens et al. 2003; Croft et al. 2005; Zirm et al. 2008; Kodama et al. 2007). Kurk et al. (2004b) has also shown that the EROs and H $\alpha$  emitting galaxies are located closer to the radio galaxy than the bluer star forming galaxies. The 1138 protocluster is therefore a prime example of a  $z \sim 0$  galaxy cluster progenitor.

Zirm et al. (2008) have shown that the 1138 system contains red galaxies, some of which might be quiescent. However, the red sequence is still in the stages of formation and has not been properly established yet. This is in agreement with studies by Blakeslee et al. (2006) and van Dokkum & van der Marel (2007) that state that the formation redshift of the red sequence lies in the range  $z = 2-2.5$ . This roughly agrees with our toy model for the 0316 protocluster. A significant number of red galaxies should be in place as early as  $z = 2.5$ . This is earlier than what most studies predict but we are limited by the simplicity of this calculation. If the SFH is episodic and burst-like the time it takes for an LBG to become quiescent increases, so we expect the red sequence will form at a later time than estimated by this toy model.

We predict that the population of galaxies currently residing in the 0316 protocluster will resemble the 1138 protocluster after 1 Gyr of evolution and 0316, like the 1138 protocluster, will evolve into a rich galaxy cluster at  $z < 1$ .

### 3.8 Summary and conclusions

We have presented a comprehensive study of several galaxy populations in the protocluster associated with MRC 0316-257 at  $z = 3.13$ , using restframe FUV to optical images. In addition to studying the LAEs and [OIII] emitters found in previous studies, we identify samples of LBG and BBG candidates whose properties provide additional evidence for the presence of a protocluster.

1. The cumulative number density of the LBG candidates in the 0316 field is a factor of  $1.6 \pm 0.3$  larger than for comparable non-protocluster fields at similar redshifts, indicating a surface overdensity of  $0.6 \pm 0.3$  for LBGs in the protocluster. The surface overdensity is significant at the  $3\sigma$  level with respect to the field-to-field variations. This measured LBG surface overdensity strengthens the conclusion of V05 that a protocluster surrounds MRC 0316-257. Us-

ing estimates of the protocluster size, the measured surface overdensity gives an LBG volume density that is  $8 \pm 4$  larger than that of the field. Such an overdensity implies a minimum mass for the protocluster of  $2\text{--}12 \times 10^{14} M_{\odot}$ .

2. The redshift distribution of the BBG candidates shows a peak at the redshift of the radio galaxy. This is further evidence that there is an overdensity of galaxies and a protocluster around MRC 0316-257. There is no significant surface overdensity of BBGs, but this is not surprising due to the small sample size. A volume overdensity of BBGs comparable with the measured volume density of LBGs could not have been detected. Selection criteria that probe large redshift ranges are poorly suited for such overdensity studies.

We are unable to reproduce the results obtained by K07 who found that the 0316 field is a factor 1.5–2 denser in BBGs than blank fields. We attribute this to the choice of control field. According to van Dokkum et al. (2006) the GOODS-S field, used by K07, is underdense in  $2 < z < 3$  red galaxies by a factor of  $\sim 2$ . In this study four control fields are used with a total area exceeding  $400 \text{ arcmin}^2$ , reducing the effect of cosmic variance on the control fields.

3. The masses and ages of candidate protocluster galaxies were determined using SED fitting. LAEs generally have faint continuum emission at  $3.6 \mu\text{m}$  and  $4.5 \mu\text{m}$  and relatively blue UV slopes, indicating that they contain little dust. Typical stellar masses of the LAEs are  $\sim 10^8 M_{\odot}$ . Four of the LAEs have larger IRAC fluxes and stellar masses in excess of  $10^{10} M_{\odot}$ . This supports results in previous studies that there is also a non-negligible number of older evolved LAEs
4. The median mass determined for the protocluster LBGs is a factor of two larger than that for the field LBGs. Although this is not significant, considering the uncertainties of SED fitting, it agrees with the results of Lehmer et al. (2009), who found that protocluster LBGs are more luminous at  $H$  band and therefore more massive than field galaxies. No significant difference between cluster and field LBGs is found for SFRs and UV-slopes.
5. The most massive and intensely star forming galaxies are located primarily near to the radio galaxy indicating that proximity to the radio galaxy influences galaxy evolution. No other high mass and high SFR regions are found in the 0316 field, indicating that the radio galaxy is near the centre of the protocluster. The trend in SFR is radically different from what is observed in local galaxy clusters where the SFR decreases systematically towards the cluster centre.

We conclude that the protocluster surrounding MRC 0316-257 is in a relatively early stage of formation. The blue LBG population will likely evolve into a population of passive, red galaxies over a timescale of 1 Gyr, forming a structure similar to the well-studied protocluster surrounding MRC 1138-262 at  $z = 2.2$

Spectroscopic follow-up of the LBG and BBG candidates is needed to refine their redshifts and establish which individual objects are indeed located within the protocluster. Furthermore, population studies of a large sample of radio-selected

protoclusters over a range of redshift are needed to obtain a more comprehensive view of how these structures form and evolve. Such studies would clarify whether the protocluster around MRC 0316–257 is representative of large-scale overdensities in the early Universe.

## Acknowledgements

We wish to thank the anonymous referee for all the useful suggestions that have improved this paper significantly. This research has been based on observations made with the VLT at ESO Paranal, programs 072.A-0284(A), 077.A-0310(A,B), 078.A-0002(A,B) and 167.A-0409(A,B). Also based on observations made with the NASA/ESA *HST*, obtained at the Space Telescope Science Institute (STScI). STScI is operated by Association of Universities for Research in Astronomy, Inc., under NASA contract NAS 5-26555. This study is also based on data collected at Subaru Telescope, which is operated by the National Astronomical Observatory of Japan. The W.M. Keck Observatory is a scientific partnership between the University of California and the California Institute of Technology, made possible by a generous gift of the W.M. Keck Foundation. The authors wish to recognize and acknowledge the significant cultural role and reverence that the summit of Mauna Kea has always within the indigenous Hawaiian community; we are fortunate to have the opportunity to conduct observations from this mountain. EK acknowledges funding from Netherlands Organization for Scientific Research (NWO). NAH and GK acknowledge funding from the Royal Netherlands Academy of Arts and Sciences (KNAW). The work by SAS at LLNL was performed under the auspices of the U.S. Department of Energy under Contract No. W-7405-ENG-48 and in part under Contract DE-AC52-07NA27344. This work is based [in part] on observations made with the Spitzer Space Telescope, which is operated by the Jet Propulsion Laboratory, California Institute of Technology under a contract with NASA. Support for this work was provided by NASA through an award issued by JPL/Caltech. SC acknowledges support for radio galaxy studies at UC Merced, including the work reported here, with the Hubble Space Telescope and Spitzer Space Telescope via NASA grants HST #10127, SST #1264353, SST #1265551 and SST #1279182.

## References

- Adelberger K. L., Steidel C. C., Giavalisco M., Dickinson M., Pettini M., Kellogg M., 1998, *ApJ*, 505, 18
- Balogh M. L., Schade D., Morris S. L., Yee H. K. C., Carlberg R. G., Ellingson E., 1998, *ApJ*, 504, L75+
- Balogh M. L., Morris S. L., Yee H. K. C., Carlberg R. G., Ellingson E., 1999, *ApJ*, 527, 54
- Bertin E., Arnouts S., 1996, *A&AS*, 117, 393
- Blakeslee J. P. et al., 2006, *ApJ*, 644, 30
- Bouwens R. J., et al., 2009, *ApJ*, 705, 936
- Brammer G. B., van Dokkum P. G., Coppi P., 2008, *ApJ*, 686, 1503
- Bruzual G., Charlot S., 2003, *MNRAS*, 344, 1000
- Calzetti D., Armus L., Bohlin R. C., Kinney A. L., Koornneef J., Storchi-Bergmann T., 2000, *ApJ*, 533, 682
- Cimatti A. et al., 2002, *A&A*, 392, 395
- Clemens M. S., Bressan A., Nikolic B., Alexander P., Annibali F., Rampazzo R., 2006, *MNRAS*, 370, 702
- Cowie L. L., Songaila A., Hu E. M., Cohen J. G., 1996, *AJ*, 112, 839
- Croft S., Kurk J., van Breugel W., Stanford S. A., de Vries W., Pentericci L., Röttgering H., 2005, *AJ*, 130, 867
- Daddi E. et al., 2007, *ApJ*, 670, 156
- Damen M., Labbé I., Franx M., van Dokkum P. G., Taylor E. N., Gawiser E. J., 2009, *ApJ*, 690, 937
- Fazio G. G. et al., 2004, *ApJS*, 154, 10
- Finkelstein S. L., Malhotra S., Rhoads J. E., Hathi N. P., Pirzkal N., 2009, *MNRAS*, 393, 1174
- Ford H. C. et al., 1998, in *Society of Photo-Optical Instrumentation Engineers (SPIE) Conference Series*, Vol. 3356, *Society of Photo-Optical Instrumentation Engineers (SPIE) Conference Series*, Bely P. Y., Breckinridge J. B., eds., pp. 234–248
- Franx M. et al., 2003, *ApJ*, 587, L79
- Gawiser E. et al., 2006a, *ApJ*, 642, L13
- Gawiser E. et al., 2006b, *ApJS*, 162, 1
- Giavalisco M., Steidel C. C., Adelberger K. L., Dickinson M. E., Pettini M., Kellogg M., 1998, *ApJ*, 503, 543
- Gobat R., Rosati P., Strazzullo V., Rettura A., Demarco R., Nonino M., 2008, *A&A*, 488, 853
- Grazian A. et al., 2007, *A&A*, 465, 393
- Hashimoto Y., Oemler A. J., Lin H., Tucker D. L., 1998, *ApJ*, 499, 589
- Hatch N. A., Overzier R. A., Röttgering H. J. A., Kurk J. D., Miley G. K., 2008, *MNRAS*, 383, 931
- Hu E. M., McMahan R. G., 1996, *Nature*, 382, 231
- Ichikawa T. et al., 2006, in *Society of Photo-Optical Instrumentation Engineers (SPIE) Conference Series*, Vol. 6269, *Society of Photo-Optical Instrumentation Engineers (SPIE) Conference Series*
- Intema H. T. et al., 2006, *A&A*, 456, 433
- Kennicutt Jr. R. C., 1998, *ARA&A*, 36, 189
- Kodama T., Tanaka I., Kajisawa M., Kurk J., Venemans B., De Breuck C., Vernet J., Lidman C., 2007, *MNRAS*, 377, 1717



- Kriek M., van Dokkum P. G., Labbe I., Franx M., Illingworth G. D., Marchesini D., Quadri R. F., 2009, *ApJ*, 700, 221
- Kurk J. D., Pentericci L., Overzier R. A., Röttgering H. J. A., Miley G. K., 2004a, *A&A*, 428, 817
- Kurk J. D., Pentericci L., Röttgering H. J. A., Miley G. K., 2004b, *A&A*, 428, 793
- Labbé I. et al., 2003, *AJ*, 125, 1107
- Labbé I. et al., 2005, *ApJ*, 624, L81
- Lai K. et al., 2008, *ApJ*, 674, 70
- Le Fèvre O., Deltorn J. M., Crampton D., Dickinson M., 1996, *ApJ*, 471, L11+
- Le Fèvre O. et al., 2003, in *Society of Photo-Optical Instrumentation Engineers (SPIE) Conference Series*, Vol. 4841, *Society of Photo-Optical Instrumentation Engineers (SPIE) Conference Series*, Iye M., Moorwood A. F. M., eds., pp. 1670–1681
- Le Fèvre O. et al., 2004, *A&A*, 428, 1043
- Lee K.-S., Giavalisco M., Gnedin O. Y., Somerville R. S., Ferguson H. C., Dickinson M., Ouchi M., 2006, *ApJ*, 642, 63
- Lehmer B. D. et al., 2009, *ApJ*, 691, 687
- Lewis I. et al., 2002, *MNRAS*, 334, 673
- Madau P., 1995, *ApJ*, 441, 18
- Makovoz D., Khan I., 2005, in *Astronomical Society of the Pacific Conference Series*, Vol. 347, *Astronomical Data Analysis Software and Systems XIV*, Shopbell P., Britton M., Ebert R., eds., pp. 81–+
- Malhotra S., Rhoads J. E., 2002, *ApJ*, 565, L71
- Maschietto F. et al., 2008, *MNRAS*, 389, 1223
- Matsuda Y. et al., 2005, *ApJ*, 634, L125
- Meurer G. R., Heckman T. M., Calzetti D., 1999, *ApJ*, 521, 64
- Meurer G. R., Heckman T. M., Leitherer C., Kinney A., Robert C., Garnett D. R., 1995, *AJ*, 110, 2665
- Miley G., De Breuck C., 2008, *A&A Rev*, 15, 67
- Miley G. K. et al., 2006, *ApJ*, 650, L29
- Moorwood A. et al., 1998, *The Messenger*, 94, 7
- Mullis C. R., Rosati P., Lamer G., Böhringer H., Schwobe A., Schuecker P., Fassbender R., 2005, *ApJ*, 623, L85
- Nilsson K. K. et al., 2007, *A&A*, 471, 71
- Noeske K. G. et al., 2007, *ApJ*, 660, L43
- Oke J. B. et al., 1995, *PASP*, 107, 375
- Oke J. B., Gunn J. E., 1983, *ApJ*, 266, 713
- Ouchi M. et al., 2004, *ApJ*, 611, 685
- Ouchi M. et al., 2005, *ApJ*, 620, L1
- Overzier R. A. et al., 2008, *ApJ*, 673, 143
- Overzier R. A. et al., 2006, *ApJ*, 637, 58
- Overzier R. A. et al., 2009, *ApJ*, 704, 548
- Pannella M. et al., 2009, *ApJ*, 698, L116
- Pentericci L., Grazian A., Fontana A., Castellano M., Giallongo E., Salimbeni S., Santini P., 2009, *A&A*, 494, 553
- Pentericci L. et al., 2000, *A&A*, 361, L25
- Postman M., Lubin L. M., Oke J. B., 2001, *AJ*, 122, 1125
- Quadri R. et al., 2007, *AJ*, 134, 1103
- Ravikumar C. D. et al., 2007, *A&A*, 465, 1099

- Rocca-Volmerange B., Le Borgne D., De Breuck C., Fioc M., Moy E., 2004, *A&A*, 415, 931
- Sánchez-Blázquez P., Gorgas J., Cardiel N., González J. J., 2006, *A&A*, 457, 809
- Schlegel D. J., Finkbeiner D. P., Davis M., 1998, *ApJ*, 500, 525
- Seymour N. et al., 2007, *ApJS*, 171, 353
- Shapley A. E., Steidel C. C., Adelberger K. L., Dickinson M., Giavalisco M., Pettini M., 2001, *ApJ*, 562, 95
- Shapley A. E., Steidel C. C., Pettini M., Adelberger K. L., 2003, *ApJ*, 588, 65
- Stanford S. A. et al., 2005, *ApJ*, 634, L129
- Stanford S. A. et al., 2006, *ApJ*, 646, L13
- Steidel C. C., Adelberger K. L., Dickinson M., Giavalisco M., Pettini M., Kellogg M., 1998, *ApJ*, 492, 428
- Steidel C. C., Adelberger K. L., Giavalisco M., Dickinson M., Pettini M., 1999, *ApJ*, 519, 1
- Steidel C. C., Adelberger K. L., Shapley A. E., Erb D. K., Reddy N. A., Pettini M., 2005, *ApJ*, 626, 44
- Steidel C. C., Adelberger K. L., Shapley A. E., Pettini M., Dickinson M., Giavalisco M., 2003, *ApJ*, 592, 728
- Stevens J. A. et al., 2003, *Nature*, 425, 264
- Suzuki R. et al., 2008, *PASJ*, 60, 1347
- Tanaka M. et al., 2008, *A&A*, 489, 571
- Tanaka M., Kodama T., Arimoto N., Okamura S., Umetsu K., Shimasaku K., Tanaka I., Yamada T., 2005, *MNRAS*, 362, 268
- Tanaka M., Kodama T., Kajisawa M., Bower R., Demarco R., Finoguenov A., Lidman C., Rosati P., 2007, *MNRAS*, 377, 1206
- Tapken C., Appenzeller I., Mehlert D., Noll S., Richling S., 2004, *A&A*, 416, L1
- Taylor E. N. et al., 2009, *ApJ*, 694, 1171
- Toomre A., 1977, in *Evolution of Galaxies and Stellar Populations*, Tinsley B. M., Larson R. B., eds., pp. 401–+
- van Dokkum P. G. et al., 2006, *ApJ*, 638, L59
- van Dokkum P. G., van der Marel R. P., 2007, *ApJ*, 655, 30
- Venemans B. P. et al., 2005, *A&A*, 431, 793
- Venemans B. P. et al., 2007, *A&A*, 461, 823
- Williams R. E. et al., 1996, *AJ*, 112, 1335
- Williams R. J., Quadri R. F., Franx M., van Dokkum P., Labbé I., 2009, *ApJ*, 691, 1879
- Zirm A. W. et al., 2008, *ApJ*, 680, 224

---

# A $z \sim 3$ RADIO GALAXY AND ITS PROTOCLUSTER: EVIDENCE FOR A SUPERSTRUCTURE?

We present spectroscopic follow-up observations of Lyman Break Galaxies (LBGs) selected in the field surrounding the radio galaxy MRC 0316-257 at  $z \sim 3.13$  (0316). Robust spectroscopic redshifts are determined for 20 out of 24 objects. Three of the spectroscopically confirmed galaxies have  $3.12 < z < 3.13$  indicating that these objects reside in a protocluster structure previously found around the radio galaxy. An additional 5 objects are found  $1600 \text{ km s}^{-1}$  blue-shifted with respect to the main protocluster structure. This is in addition to three [OIII] emitters found at this redshift in a previous study. This is further evidence that a structure exists directly in front of the 0316 protocluster. We estimate that the foreground structure is responsible for half of the surface overdensity of LBGs found in the field as a whole. The foreground structure is associated with a strong surface density peak  $1.4 \text{ Mpc}$  to the North-West of the radio galaxy and a 2D Kolmogorov-Smirnov test indicates that the spatial distributions of the 0316 and foreground galaxies differ at the  $3\sigma$  level. In addition, we compare the properties of protocluster, foreground structure and field galaxies, but we find no significant differences. In terms of the nature of the two structures, a merger scenario is considered. This option cannot be rejected on the basis of merger dynamics: the observed relative velocity of  $1600 \text{ km s}^{-1}$  can be reproduced if the two structures have masses of  $\sim 5 \times 10^{14} M_{\odot}$  and have starting separations of  $2.5$  to  $3 \text{ Mpc}$ . It is also possible that the foreground structure is unrelated to the 0316 protocluster in which case the two structures will not interact before  $z = 0$ .

E. Kuiper, B. P. Venemans, N. A. Hatch, G. K. Miley, H. J. A. Röttgering  
Submitted to the *Monthly Notices of the Royal Astronomical Society*

## 4.1 Introduction

The exact role the environment plays in the evolution of galaxies has been a long standing question in astronomy. It has been widely observed that the properties of galaxies depend on environment. High density environments in the local Universe, such as galaxy groups and clusters, are dominated by red early-type galaxies. This is in contrast with the lower density environments where blue star-forming late-type galaxies are more frequent. In addition, cD galaxies, the most massive galaxies known, are located exclusively in galaxy clusters.

In order to adequately explain the differences between low- and high-density environments it is essential to study galaxy clusters at all epochs. By doing so it may be possible to identify what exact physical processes constitute the more general term of 'environmental influence'. Unfortunately, the search for galaxy clusters at  $> 1.5$  is difficult and only a handful of spectroscopically confirmed galaxy clusters at  $z > 1.5$  with X-ray emission are currently known (Wilson et al. 2008; Papovich et al. 2010; Tanaka et al. 2010; Henry et al. 2010; Gobat et al. 2011).

One of the most successful methods to push the search for galaxy clusters beyond  $z = 2$  is targeting high- $z$  radio galaxies (hereafter HzRGs, Miley & De Breuck 2008). With large observed  $K$  band luminosities, these galaxies are thought to have large stellar masses of the order of  $10^{11} - 10^{12} M_{\odot}$  (Rocca-Volmerange et al. 2004; Seymour et al. 2007). Following hierarchical galaxy formation, these galaxies should therefore be located in dense environments and are thus possible galaxy cluster progenitors. These structures are often referred to as 'protoclusters', because at these redshifts galaxy clusters are likely still in the process of formation and therefore have not yet virialised (e.g. Kuiper et al. 2011, Chapter 2).

By targeting a HzRG field with a narrowband filter chosen such that it contains a strong emission line at the redshift of a radio galaxy, it is possible to select galaxies in a narrow redshift interval around the radio galaxy. This has resulted in evidence that HzRGs indeed probe overdense regions in the early Universe (e.g. Pascarella et al. 1996; Knopp & Chambers 1997; Pentericci et al. 2000; Kurk et al. 2004b,a; Venemans et al. 2007; Matsuda et al. 2011; Kuiper et al. 2011b).

Although this method is efficient in locating overdensities, it is also limited in the number of galaxies that can be selected. The emission line most commonly used for these searches is  $\text{Ly}\alpha$ , thus only galaxies with strong  $\text{Ly}\alpha$  emission are selected. As a consequence, a large number of galaxies that reside in the overdensity are missed altogether. This method is therefore not suited for more in-depth studies that attempt to obtain a more complete picture of the protocluster.

There is a variety of other methods that are aimed at selecting other classes of high- $z$  galaxies. The most well-known uses the Lyman break to select UV-bright star-forming galaxies (Lyman Break Galaxies or LBGs) in a relatively broad redshift range compared to the narrowband technique. This method was pioneered by Steidel et al. (1995) and has been successfully used in many studies since then. The Lyman break selection technique selects a much larger sample of star forming

galaxies than methods relying on Ly $\alpha$  narrowband data, as only 20 per cent of LBGs at a given luminosity can also be qualified as Ly $\alpha$  emitters taking into account current selection criteria (Steidel et al. 2000, 2011).

The Lyman break method has been used only sparingly on HzRG fields (Intema et al. 2006; Overzier et al. 2008). This is mainly because the redshift range probed by the LBG criterion is  $\sim 0.3 - 0.7$ , significantly larger than the redshift range spanned by a typical protocluster ( $\Delta z \sim 0.03$  or  $\Delta v \sim 2000 \text{ km s}^{-1}$  at  $z \sim 3$ ). One of the HzRG fields for which the LBG selection criterion has been used is MRC 0316-257 at  $z = 3.13$ . This is one of the best studied HzRGs at  $z > 2.5$  and it has been shown to host an overdensity of Ly $\alpha$  emitters (Venemans et al. 2005, hereafter V05). A study by Maschietto et al. (2008, hereafter M08) has found tentative evidence for a similar overdensity of [OIII] emitters. In an attempt to obtain a complete galaxy census, Kuiper et al. (2010, Chapter 3) assembled photometry of the field in 18 bands ranging from  $U$  band to *Spitzer* 8  $\mu\text{m}$ . This also involved selecting galaxies using the Lyman break technique. It was found that the 0316 field is overdense in LBGs. Also, the most massive and actively star-forming galaxies are located near to the radio galaxy, indicating the presence of environmental influence. However, the inability to distinguish protocluster galaxies from field galaxies is likely to diminish any real trend in the data.

In this work we present spectroscopic follow-up of the sample of LBGs composed in Chapter 3. By spectroscopically confirming the redshifts of the individual LBG candidates we can determine which galaxies are truly in the protocluster and which are in the field. This will therefore give us a better estimate of the true volume overdensity. Also, it allows us to compare the properties of field and protocluster LBGs in a fully self-consistent manner. This is particularly important in determining whether the protocluster environment influences the evolution of its constituent galaxies.

The paper is structured as follows: a brief summary of the sample selection of Chapter 3, a description of the data and its reduction are given in Sect. 4.2. Spectroscopic redshifts and the resulting velocity distribution are discussed in Sect. 4.3 and further discussion concerning the presence of a possible superstructure is presented in Sect. 4.4. Finally, conclusions and a future outlook are presented in Sect. 4.5. Throughout this paper a standard  $\Lambda$  cold dark matter ( $\Lambda$ CDM) cosmology is used, with  $H_0 = 71 \text{ km s}^{-1}$ ,  $\Omega_M = 0.27$  and  $\Omega_\Lambda = 0.73$ . All magnitudes are given in the AB magnitude system.

## 4.2 Sample selection & data

In Chapter 3 a *UVR* colour criterion was introduced that was designed to select star-forming galaxies in the redshift range  $3.0 < z < 3.3$ .

$$\begin{aligned} U - V &\geq 1.9, \\ V - R &\leq 0.51, \\ U - V &\geq 5.07 \times (V - R) + 2.43, \\ R &\leq 26. \end{aligned} \tag{4.1}$$

A total of 52 galaxies were found to satisfy the criterion. Photometric redshifts were derived for this sample using the *EAZY* code (Brammer et al. 2008) and broadband photometry in 18 bands ranging from *U* band to *Spitzer* 8  $\mu\text{m}$ . The initial sample was then reduced to 48 by applying a photometric redshift cut of  $2.8 < z_{\text{phot}} < 3.5$ .

Chapter 3 also presented an additional sample of 55 potential LBGs (pLBGs). These objects satisfy all selection criteria, except that they are too blue to make the  $U - V \geq 1.9$  cut. However, all these objects are undetected in the *U* band used and deeper *U* band data may yield redder  $U - V$  colours. These objects are thus not strictly LBGs when considering the selection criterion of Chapter 3, but deeper data may show that they do in fact satisfy all criteria.

Only objects with  $R < 25.5$  were considered for the spectroscopy, because the continuum and absorption lines of fainter objects are unlikely to be detected. This reduced the samples to 29 LBGs and 27 pLBGs, respectively. The samples were subsequently divided in three brightness categories: objects with  $R < 24.5$  are classified as ‘bright’, objects with  $24.5 < R < 25.0$  as ‘intermediate’ and objects with  $R > 25.0$  as ‘faint’. To ensure the most detections, the objects in the mask were prioritised according to their brightness. Further restrictions were imposed by the locations of the individual objects, as slits in the mask are not allowed to overlap. The final mask contained 13 LBGs and 11 pLBGs of which 10 are classified as ‘bright’, 9 as ‘intermediate’ and 5 as ‘faint’. Therefore, a total of 24 protocluster candidates have been observed spectroscopically. One of these objects is the  $\text{Ly}\alpha$  emitter #1867 from V05. This galaxy has been spectroscopically confirmed to be at the redshift of the protocluster.

The spectroscopy was performed with the FOcal Reducer and low dispersion Spectrograph (FORs2) in the mask multi-object spectroscopy mode (MXU) at the Very Large Telescope during the nights of 10 and 11 December 2010. The seeing varied during the two nights between  $0.7''$  and  $1.2''$ . The width of the slits in the mask was  $1.0''$ . The objects were observed through the “300V” grism and GG435 blocking filter, with a resolution of 440. The spectral range covered is approximately  $4500 < \lambda < 8500 \text{ \AA}$ . The pixels were binned  $2 \times 2$ , which resulted in a spatial scale of  $0.25'' \text{ pixel}^{-1}$  and a dispersion of  $3.36 \text{ \AA pixel}^{-1}$ . A total of 25 exposures of 1560 seconds each were obtained. Between the individual exposures, the pointing of the telescope was shifted in steps of  $0.25''$  along the slit to enable more accurate sky subtraction and cosmic ray removal. The total integration time per object was 39.000 seconds (10.83 hr).

Data reduction was performed with various IRAF<sup>1</sup> routines. The reduction included the following steps: individual frames were bias subtracted and flat fielded using lamp flats. Cosmic rays were identified and removed before the background was subtracted. The background subtracted two-dimensional frames were combined and one-dimensional spectra were extracted. Wavelength calibration was performed using arc lamp spectra and night sky lines in the science frames. The uncertainty in the wavelength calibration is  $\sim 0.3 \text{ \AA}$ , which corresponds to a systematic redshift uncertainty of  $\sigma_z \sim 0.0002$ .

## 4.3 Results

### 4.3.1 Redshift determination

Spectroscopic redshifts are obtained for 20 objects out of the 24 observed. For the other 4 objects no continuum or emission lines are detected. Examining the data we find artefacts in two of the 2D spectra indicating slit defects as the possible cause of these two non-detections. The remaining two undetected objects either have a low surface brightness or are very faint ( $R \sim 25.5$ ) making it impossible to obtain a spectroscopic redshift.

The spectra of the objects that do allow for a redshift determination are shown in Figs. 4.1(a) and 4.1(b). The spectra have been plotted in the restframe to facilitate comparison between the different objects. Also, the locations of the most important spectral features have been marked. The 2D spectra have also been included because the Ly $\alpha$  break is more obviously apparent in the 2D spectra.

The results obtained from the spectra are summarised in Table 4.1. Spectroscopic redshifts based on both emission and absorption lines are listed as the possible presence of outflows can affect the Ly $\alpha$  spectroscopic redshift (e.g. Shapley et al. 2003). For the spectroscopic redshift we take the mean value of the redshifts obtained for the individual discernible absorption features. Uncertainties listed in Table 4.1 are calculated by varying the spectra according to a normal distribution characterised by the rms noise level. The individual lines are subsequently fitted again. This process is repeated 1000 times for each of the spectral features.

Approximately half of the objects show an emission line, which is assumed to be Ly $\alpha$ . This is consistent with what is found in other spectroscopic studies of LBGs (Shapley et al. 2003; Steidel et al. 2011). The emission line is used for determining a preliminary redshift. Based on this redshift the spectrum is searched for consistent absorption lines. For objects that do not show an emission line the redshift is determined by identifying multiple interstellar absorption lines such as SiII $\lambda$ 1260, CII $\lambda$ 1335 or CIV $\lambda$ 1549 in combination with a possible spectral break. Almost all objects show either a combination of an emission and an absorption line or multiple absorption lines. This indicates that these redshifts are robust.

---

<sup>1</sup>IRAF is distributed by the National Optical Astronomy Observatory, which is operated by the Association of Universities for Research in Astronomy, Inc., under cooperative agreement with the National Science Foundation.

There is one object where the redshift is possibly ambiguous. Object #12 has only one identifiable absorption feature and evidence for a break. Since the Lyman break is a poor redshift indicator, this makes it difficult to set an accurate redshift. The single absorption feature is very strong and based on the approximate location of the break, the line can be identified as either the OI/SiII doublet at  $\sim 1303 \text{ \AA}$  or CII at  $1335 \text{ \AA}$ . This indicates its redshift is either  $z \sim 3.11$  or  $z \sim 3.01$ . To ascertain which is the more likely, the 2D spectrum of #12 is compared to the 2D spectra of other objects with strong breaks and clear OI/SiII and CII features. The former option better resembles the other 2D spectra and therefore we conclude that the redshift of #12 is  $z = 3.1127$ .

### 4.3.2 Redshift distribution

The full distribution of spectroscopic redshifts is shown in the left panel of Fig. 4.2. Here the redshifts based on the absorption lines are used. The redshift of the radio galaxy is marked by an arrow. All spectroscopically confirmed LBGs are included in the figure. This indicates that all objects have redshifts consistent with  $2.7 < z < 3.5$ . The low- $z$  interloper rate is therefore small. Assuming that the four non-detected LBG candidates are low- $z$  galaxies a worst-case success rate of  $\sim 83$  per cent is obtained.

The left panel of Fig. 4.2 also shows a clear concentration of galaxies near the redshift of the radio galaxy. This could be consistent with the presence of a structure. To verify this we compare the observed  $z_{\text{spec}}$  distribution to the selection efficiency curve also shown in Fig. 4.2. The curve indicates that the LBG selection criterion of Chapter 3 is most efficient in selecting objects between  $2.8 < z < 3.5$ . A Kolmogorov-Smirnov (KS) test shows that there is a probability of 0.012 that the observed spectroscopic distribution is drawn from the distribution defined by the selection efficiency curve. The two distributions are thus different at the  $2.5\sigma$  level, indicating that there is evidence for a concentration near  $z \sim 3.1$ .

As M08 found evidence for a possible foreground structure at  $z \sim 3.1$ , it is worthwhile to look in more detail at the redshift interval  $3.05 < z < 3.20$ . This is shown in the right panel of Fig. 4.2. The distribution includes the [OIII] emitters of M08 and the relevant LBGs presented in this work. We correct the redshifts of the M08 [OIII] emitters that have  $\text{Ly}\alpha$  based redshifts, because the  $\text{Ly}\alpha$  line is commonly redshifted with respect to the absorption lines. This redshift is due to outflows and the resonant nature of the  $\text{Ly}\alpha$  line. The applied correction is taken to be the mean difference in redshift of all galaxies in our sample that show both  $\text{Ly}\alpha$  emission and absorption lines. This correction is  $\Delta z \sim 0.005$  or  $\Delta v \sim 350 \text{ km s}^{-1}$ , which is roughly consistent with Shapley et al. (2003).



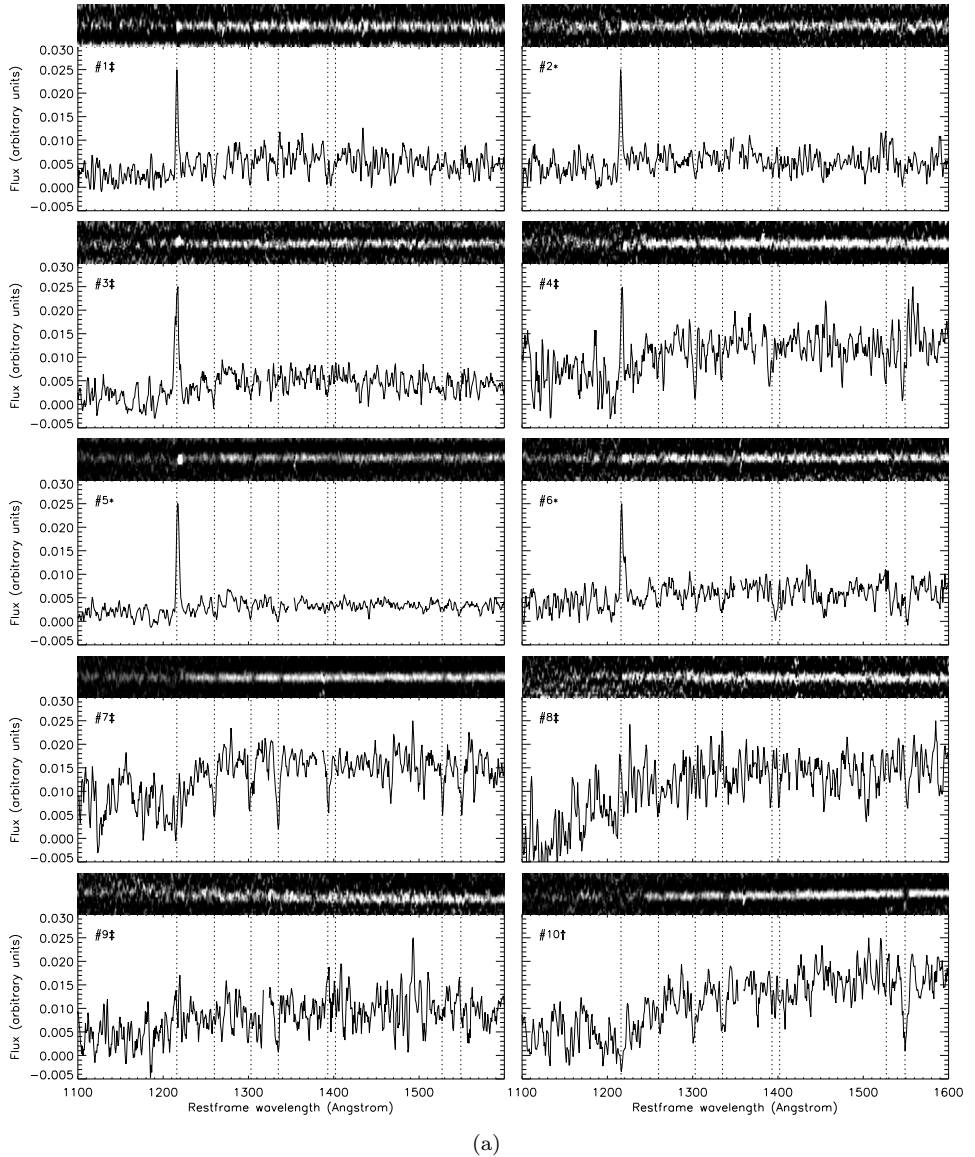
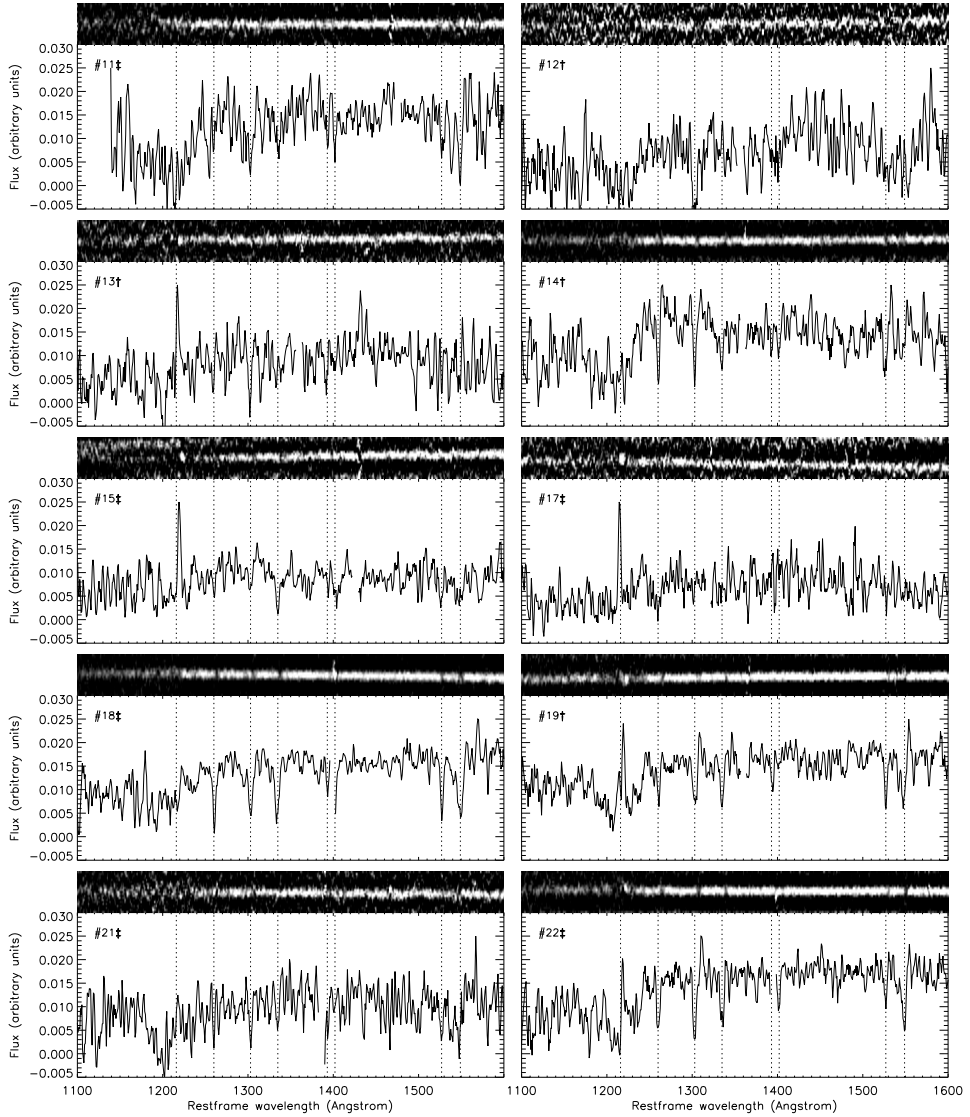


**Figure 4.1** – 1D and 2D restframe spectra of individual objects for which a redshift can be determined. The 1D spectra have been scaled to a common arbitrary flux scale. Vertical dotted lines denote the most important spectral features in this wavelength range. From left to right these features are:  $\text{Ly}\alpha$ ,  $\text{Nv}\lambda 1240$ ,  $\text{SiII}\lambda 1260$ ,  $\text{OI/SiII}\lambda 1303$ ,  $\text{CII}\lambda 1335$ ,  $\text{SiIV}\lambda 1392, 1402$ ,  $\text{SiII}\lambda 1527$  and  $\text{CIV}\lambda 1549$ . The symbols next to the ID number indicate whether the object is located in the 0316 structure (\*), the foreground structure (†) or the field (‡).



(b)

Figure 4.1 – Remainder of the spectra.

Table 4.1 – Properties of all LBGs and pLBGs for which spectra can be extracted.

Object ID	RA	Dec.	Type	$R$	$z_{\text{spec,Ly}\alpha}$	$z_{\text{spec,abs}}$	Spectral features
#1	03:18:01.10	-25:35:56.1	pLBG	25.09	$3.4004^{+0.0003}_{-0.0003}$	$3.3965^{+0.0011}_{-0.0009}$	Break, Ly $\alpha$ , OI/SiII, SiIV
#2	03:18:12.30	-25:35:42.2	pLBG	24.80	$3.1258^{+0.0004}_{-0.0004}$	$3.1282^{+0.0023}_{-0.0026}$	Break, Ly $\alpha$ , OI/SiII
#3	03:18:08.72	-25:35:22.4	LBG	24.11	$3.2306^{+0.0004}_{-0.0005}$	$3.2303^{+0.0016}_{-0.0015}$	Break, Ly $\alpha$ , SiII, OI/SiII, SiIV
#4	03:18:11.53	-25:35:08.2	LBG	24.52	$3.0521^{+0.0005}_{-0.0005}$	$3.0442^{+0.0011}_{-0.0010}$	Break, Ly $\alpha$ , OI/SiII
#5	03:18:08.94	-25:34:59.6	LAE/LBG	23.77	$3.1343^{+0.0001}_{-0.0001}$	$3.1266^{+0.0011}_{-0.0007}$	Break, Ly $\alpha$ , OI/SiII, CII, CIV
#6	03:18:05.35	-25:34:40.8	LBG	24.95	$3.1251^{+0.0010}_{-0.0010}$	$3.1219^{+0.0016}_{-0.0015}$	Break, Ly $\alpha$ , SiII, CII
#7	03:18:07.75	-25:34:26.1	pLBG	24.37	-	$3.0324^{+0.0007}_{-0.0007}$	Break, SiII, OI/SiII, CII, CIV, SiII, CIV, FeII, AlII
#8	03:18:18.40	-25:34:17.1	LBG	24.54	-	$2.9352^{+0.0017}_{-0.0006}$	Break, SiII, CIV
#9	03:18:20.28	-25:34:02.0	LBG	25.06	$3.2257^{+0.0042}_{-0.0040}$	$3.2181^{+0.0034}_{-0.0019}$	Break, Ly $\alpha$ , CII
#10	03:17:58.79	-25:33:49.9	pLBG	24.12	-	$3.1121^{+0.0010}_{-0.0011}$	Break, OI/SiII, CII, CIV
#11	03:18:08.39	-25:33:39.6	LBG	24.69	-	$2.7795^{+0.0017}_{-0.0019}$	Break, OI/SiII, CII
#12	03:17:58.93	-25:33:27.7	pLBG	25.19	-	$3.1127^{+0.0017}_{-0.0019}$	Break, OI/SiII
#13	03:18:04.10	-25:33:09.1	pLBG	25.42	$3.1032^{+0.0017}_{-0.0012}$	$3.0988^{+0.0015}_{-0.0016}$	Break, Ly $\alpha$ , OI/SiII
#14	03:18:07.43	-25:32:51.2	pLBG	24.47	-	$3.1041^{+0.0009}_{-0.0012}$	Break, SiII, OI/SiII, CII
#15	03:18:19.41	-25:38:16.9	pLBG	24.42	$2.9215^{+0.0006}_{-0.0005}$	$2.9109^{+0.0015}_{-0.0015}$	Break, Ly $\alpha$ , CII
#16	03:18:13.19	-25:38:06.1	pLBG	24.83	-	-	-
#17	03:17:58.33	-25:37:59.0	pLBG	24.94	$3.2252^{+0.0006}_{-0.0006}$	$3.2295^{+0.0046}_{-0.0057}$	Break, Ly $\alpha$ , SiII
#18	03:17:59.20	-25:37:37.9	LBG	23.80	-	$2.9865^{+0.0005}_{-0.0007}$	Break, SiII, OI/SiII, CII, CIV, FeII, AlII
#19	03:18:19.73	-25:37:26.8	LBG	23.76	$3.1115^{+0.0007}_{-0.0007}$	$3.1003^{+0.0016}_{-0.0009}$	Break, Ly $\alpha$ , SiII, OI/SiII, CII, CIV, FeII, AlII
#20	03:18:03.91	-25:37:14.1	LBG	25.44	-	-	-
#21	03:18:02.78	-25:37:05.5	pLBG	24.99	-	$3.0233^{+0.0023}_{-0.0013}$	Break, OI/SiII, SiII
#22	03:18:13.25	-25:36:39.7	LBG	23.94	-	$2.9996^{+0.0006}_{-0.0007}$	Break, SiII, OI/SiII, CII, CIV, FeII, AlII

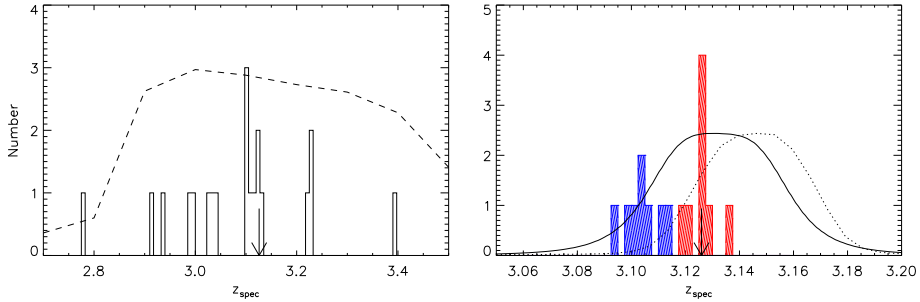


**Figure 4.2** – Left panel: Distribution of all spectroscopic redshifts obtained in this work. The dashed curve shows the selection efficiency of the LBG selection criterion. Right panel: Redshift distribution of the [OIII] emitters of M08 and the LBGs from this work that are located between  $3.08 < z < 3.18$ . Also included is LAE #1518 of V05 which has been identified as an LBG. The objects in the red dashed histogram are those LBGs that are associated with the 0316 radio galaxy, whereas the blue dashed histogram includes [OIII] emitters and LBGs that are likely in a foreground structure. The solid and dotted curves indicate the transmission curves of the narrowband filters used to select the [OIII] emitters and LAEs, respectively. The arrow marks the redshift of the radio galaxy in both of the panels. All Ly $\alpha$  based redshifts are corrected for the commonly observed shift between Ly $\alpha$  emission and absorption lines.

The LAEs of V05 are not included in Fig. 4.2 because the narrowband filter used to select this sample does not allow detection of objects at  $z \sim 3.1$ . This is illustrated by the dotted line in Fig. 4.2. The distribution of LAEs is thus strongly concentrated near  $z \sim 3.13$  by design and including it would unfairly skew the overall distribution. The exception to this is LAE #1518. The study in Chapter 3 identified this object as an LBG and as such it is included in the right panel of Fig. 4.2. It is also included in the subsequent analysis where possible.

The work of M08 aimed to identify [OIII] emitters in the 0316 protocluster. Spectroscopic follow-up of three of the candidate [OIII] emitters showed that these objects are not located at  $z \sim 3.13$  as expected but at  $z \sim 3.1$ . Taking into account the correction for the Ly $\alpha$  redshifts, this amounts to a  $\sim 1700 \text{ km s}^{-1}$  blueshift with respect to the radio galaxy. The confirmation of an additional 5 objects at  $z \sim 3.1$  presented in this work further strengthen the notion that a structure exists in front of the 0316 protocluster.

The question is whether the structures are separate or whether they belong to one larger protocluster. When we look in detail at the LAE distribution of V05 we find that the latter is a possibility. The velocity dispersion of this sample is  $535 \text{ km s}^{-1}$  and the median redshift is similar to the median redshift of the red distribution shown in Fig. 4.2. If we use a KS test to compare this to the expected distribution based on the transmission of the Ly $\alpha$  narrowband filter (dotted line), then we find a probability of  $1.2 \times 10^{-6}$  that the LAE distribution is drawn from the expected distribution. This indicates that the blueshift of the LAE distribution with respect to the central redshift targeted by the narrowband filter is real. This in turn implies that the distribution of LAEs may extend to lower redshifts, but

that these objects have been missed due to the location of the narrowband filter.

On the other hand, a normalized tail index (Bird & Beers 1993) of 0.66 implies that the composite distribution more closely resembles a uniform distribution rather than a single Gaussian. For this work we will follow the approach of M08 and assume that the foreground structure is a separate structure. More evidence for this will be provided in Sect. 4.4.2.

Assuming that there are two subgroups we find mean redshifts of  $z = 3.1039$  and  $z = 3.1262$  which implies a velocity difference of  $\sim 1620 \text{ km s}^{-1}$ . Using a Gapper scale estimator (Beers et al. 1990) we find a velocity dispersion of  $965 \pm 112 \text{ km s}^{-1}$  for the composite distribution and individual velocity dispersions of  $492 \pm 120 \text{ km s}^{-1}$  and  $364 \pm 120 \text{ km s}^{-1}$  for the blue- and redshifted subgroups, respectively.

For the remainder of this work we will refer to the objects associated with the possible foreground structure as foreground objects, whereas those objects at  $z \sim 3.13$  will be classified as 0316 galaxies. Objects not associated with either of the  $z \sim 3.1 - 3.13$  structures will be referred to as field galaxies.

## 4.4 Discussion

### 4.4.1 A possible superstructure and implications for the overdensity

In Chapter 3, the LBG surface density of the 0316 field was found to be a factor  $1.6 \pm 0.3$  larger than the control field used. Using a volume argument and assuming that the surface overdensity is caused by a single structure connected to the  $z = 3.13$  radio galaxy, this surface density translated to a volume density which is  $8 \pm 4$  larger than the field density.

Based on the surface overdensity, one expects spectroscopic follow-up to reveal approximately 1 out of 3 objects to be in the 0316 protocluster. Instead, 3 out of 20 objects are found to be associated with the radio galaxy and an additional 5 objects are found to be located at  $\sim 3.1$ . Although the surface overdensity is formally correct, it is not solely caused by the 0316 protocluster. The volume overdensity around the 0316 radio galaxy reported in Chapter 3 is thus not as large as previously assumed and must be adjusted.

To correct the volume overdensity we must assess what fraction of the overdensity is due to the foreground structure. Due to the small samples that are considered, this cannot be more than a rough estimate. In the sample of 13 [OIII] emitters found by M08 a total of eight have spectroscopic redshifts; five due to overlap with the Ly $\alpha$  emitter sample of V05 and three through spectroscopic confirmation of the [OIII] line. The latter three were all found to be at  $z \sim 3.1$ . Taking into account that the five unconfirmed [OIII] emitters may be in either of the two structures, the fraction of foreground objects is thus 25–60 per cent.

In this work, five out of eight objects (or  $\sim 60$  per cent) are found to be in the foreground structure. Based on these numbers we therefore assume that half of

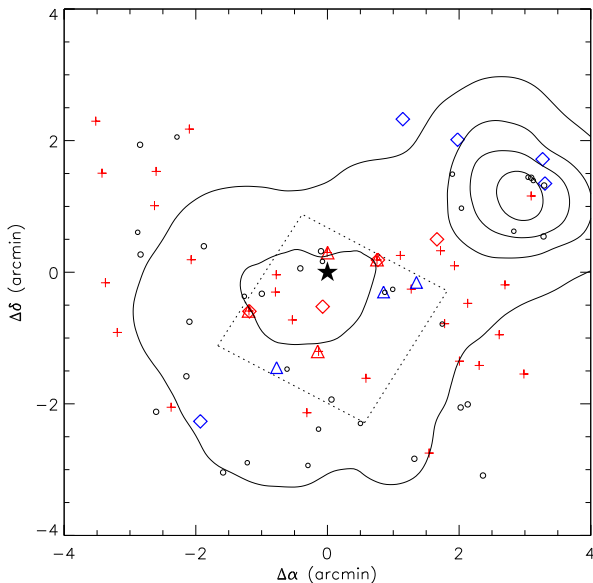


**Figure 4.3** – Spatial distribution of all spectroscopically confirmed objects that reside in the 0316 protocluster (red symbols) or the foreground structure (blue symbols).  $\text{Ly}\alpha$  emitters are denoted by plus signs, [OIII] emitters by triangles and spectroscopically confirmed LBGs/pLBGs by diamonds. Also shown are the locations of the unconfirmed LBGs and pLBGs as small open circles. The location of the radio galaxy is marked by the star. The dotted lines denote the size and location of the narrowband image used for the detection of the [OIII] emitters. The contours indicate the surface density of unconfirmed LBGs and the LBGs that are shown to be either at  $z \sim 3.10$  or  $z \sim 3.13$ .

the surface overdensity can be attributed to the foreground structure. The volume overdensity of the 0316 protocluster is thus not 8, but rather  $\sim 4$ . This is very similar to the overdensity of  $\text{Ly}\alpha$  emitters of  $3.3^{+0.5}_{-0.4}$  found in V05. Based on these numbers we also expect that the foreground structure is similar in richness and mass as the 0316 protocluster.

#### 4.4.2 Spatial distribution

Figure 4.3 shows the spatial distribution of all objects that are spectroscopically confirmed to be either in the 0316 protocluster or in the  $z = 3.1$  foreground structure. This includes the 32  $\text{Ly}\alpha$  emitters of V05 and the three [OIII] emitters of M08. The blue objects are those identified to be in the foreground structure. Interestingly, four out of five of the foreground LBGs are located in a small area in the North-West region of the field. This specific region is also mostly devoid of  $z = 3.13$   $\text{Ly}\alpha$  emitters. The North-West region is thus dominated by foreground objects. Interesting to note also is that eight of the non-confirmed LBGs reside in that general region, four of which are strongly clustered.

The distribution of the foreground [OIII] emitters does not reflect this apparent concentration of objects. This is, however, due to the small size of the narrowband image used for the detection of these objects, as illustrated by the outline shown in Fig. 4.3. This limits the location of the foreground [OIII] emitters to the central region of the field.

To further illustrate the subclustering, Fig. 4.3 also shows LBG surface density contours. The LBGs that have been shown to be field galaxies are not considered,

but LBGs that have not been spectroscopically confirmed or have been confirmed to be in either of the two  $z \sim 3.1$  structures are included. The contours have been obtained by making a grid with a gridsize of  $3''$ . For each cell of the grid the surface density is calculated by determining the distance to the  $N$ th nearest neighbour and subsequently using  $\sigma = N/\pi r_N^2$ . The contours shown have been obtained with  $N = 8$ . The resulting surface density map is smoothed with a smoothing length of  $0.5'$ . A clear peak in the surface density map is located in the North-West region, near the concentration of foreground objects and  $\sim 3'$  or  $\sim 1.4$  Mpc from the radio galaxy. A second, less pronounced peak in the surface density is located in the centre of the field, near the radio galaxy. This is thus further evidence that the foreground structure is offset from the 0316 protocluster.

The significance of the spatial subclustering can be quantified by using a 2D KS test. First we determine whether the distribution of foreground structure LBGs is consistent with being drawn from a random distribution. We find a probability of 0.033, which implies that the distribution is different from random at the  $\sim 2\sigma$  level only.

When the spatial distribution of foreground objects is compared to that of the 0316 objects, we find a probability of 0.0034 that both originate from the same parent distribution. The two distribution therefore differ at the  $\sim 3\sigma$  significance level. The foreground [OIII] emitters have not been taken into account in this comparison. The foreground structure thus seems to be centred on a different location on the sky than the 0316 structure. We consider this evidence that the two structures are two separate groups of galaxies and not one single protocluster.

#### 4.4.3 Influence of protocluster environment on galaxy properties

The influence of environment on galaxy evolution is an important topic in present day astronomy. Locally galaxies in dense environments are generally older, redder and have lower star formation rates (SFRs) than those in less dense environments. There has, however, been mounting evidence that the decrease in star formation observed locally in dense regions turns around at earlier cosmic times (Elbaz et al. 2007; Cooper et al. 2008; Tran et al. 2010; Hilton et al. 2010; Popesso et al. 2011).

Protocluster fields make excellent targets for studying these environmental effects at  $z > 2$  and several studies have presented ample evidence that the environment influences galaxy properties at  $z > 2$ . In Tanaka et al. (2010a) it has been shown that galaxies in the well-studied  $z \sim 2.15$  protocluster around PKS 1138-262 have assembled their mass earlier than field galaxies. Hatch et al. (2011) found that H $\alpha$  emitters in the protocluster around radio galaxy 4C+10.48 at  $z = 2.35$  are twice as massive as their field counterparts. Similarly, Steidel et al. (2005) showed that galaxies in a serendipitously discovered protocluster at  $z = 2.3$  are approximately twice as old and twice as massive as their field counterparts.

For the 0316 protocluster, no significant differences have been found between the field and the protocluster galaxies in terms of mass or SFR (Chapter 3). There are, however, trends of decreasing mass and SFR with increasing distance from the

radio galaxy. One of the main problems is that the field interlopers in the LBG sample of Chapter 3 possibly dilute any differences that may be apparent in a pure protocluster sample. With the spectroscopy presented in this work a first division between protocluster LBGs and field LBGs can be made.

#### 4.4.3.1 SED fitting

With such a division it is possible to revisit the spectral energy distribution (SED) fitting done in Chapter 3. For this we use the FAST SED fitting code (Kriek et al. 2009) in combination with the Bruzual & Charlot (2003) evolutionary population synthesis models. Originally, all objects were assumed to be located at  $z = 3.13$ . The addition of spectroscopic redshifts allows for a fully self-consistent comparison between field and protocluster galaxies. The free parameters in the fitting routine are the age, mass, SFH and the extinction by dust, but as in Chapter 3 we only focus on the stellar mass, because this is the only property that can be determined with reasonable accuracy.

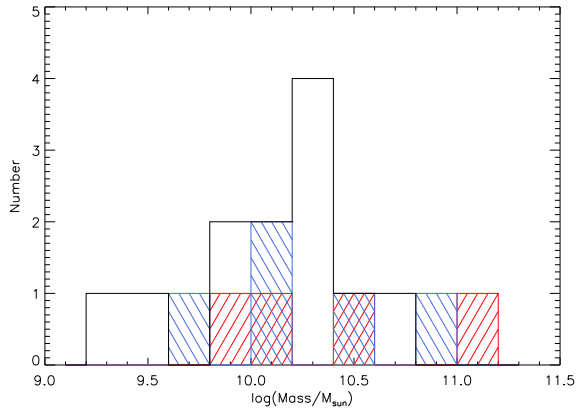
Briefly summarising the details of the SED fitting process employed in Chapter 3: we consider exponentially declining SFHs with decay times,  $\tau$ , ranging from 10 Myr to 10 Gyr with steps of 0.1 dex. The ages we consider range from  $\log(\text{age/yr})=7$  to the age of the Universe at  $z \sim 3.13$  which is  $\log(\text{age/yr})=9.3$ . The Calzetti et al. (2000) extinction law is used for the internal dust extinction, with  $A_V$  ranging from 0 to 3 with steps of 0.1. For all cases a Salpeter mass function and solar metallicity are assumed.

The updated SED fitting results show a marginally larger mean stellar mass of  $4.8 \times 10^{10} M_\odot$  for the 0316 galaxies compared to  $2.9 \times 10^{10} M_\odot$  for the foreground structure and  $1.7 \times 10^{10} M_\odot$  for the field galaxies. When we combine the 0316 and foreground samples we obtain a mean mass of  $3.7 \times 10^{10} M_\odot$ . However, the small samples considered in this work imply that this difference is not significant. This is also apparent from the stellar mass distributions shown in Fig. 4.4. The small samples make it impossible to distinguish the distributions. KS tests also reflect this, yielding probabilities of 0.75–0.9 that the various distributions are drawn from the same parent distribution. There is therefore no discernible difference between the various populations.

The radial trend observed in K10 is also revisited here. The same analysis is done as in K10 and the results are shown in Fig. 4.5. The main panels in the left column show the integrated mass and SFR in a series of annuli centred on the radio galaxy. Here only the LBGs are considered and only those that are (potentially) in the 0316 structure, meaning those without a spectroscopic redshift and those with  $z_{\text{spec}} \sim 3.13$ . The resulting sample shows qualitatively the same trends of decreasing mass and SFR with increasing distance from the radio galaxy. This trend is apparent in both the integrated values in the main panels and the individual panels shown in the insets. The upturn at large distances observed in both trends also persists. However, potential foreground cluster members in the North-West corner of the field that have not been confirmed yet may be partially



**Figure 4.4** – Stellar mass distributions of galaxies residing in the field (black), the 0316 protocluster (red dashed) and the foreground structure (blue dashed).



responsible for this. Since we observe no discernible difference between the LBGs and pLBGs we add the latter to the analysis in the right column of panels. Again, we only consider those objects that are (potentially) at  $z \sim 3.13$ ; the confirmed foreground and field galaxies are not taken into account. The integrated properties remain qualitatively the same, but the individual values for the mass as function of distance to the radio galaxy now show no discernible trend. On the other hand, the SFRs still show an indication that galaxies close to the radio galaxy have larger SFRs than galaxies that are at larger distances. The trends of decreasing mass and SFR with increasing distance to the radio galaxy observed in K10 are therefore robust.

#### 4.4.3.2 Stacked spectra

The presence or absence of environmental dependence is studied further using the stacked spectra of the different categories we have defined. In Fig. 4.6 we show a series of stacked spectra of each of the categories. These stacked spectra have been obtained by shifting the individual spectra to a common restframe wavelength scale using the absorption line redshifts. The individual spectra are then scaled to the same mean flux level in the restframe wavelength range  $1300 < \lambda_{\text{rest}} < 1500 \text{ \AA}$  and subsequently added together. Here the observed wavelength range  $5565 < \lambda < 5590 \text{ \AA}$  is excluded due to the presence of strong night-skyline residuals. Since we are dealing with small samples no other outliers are excluded in the stacking process.

The properties of all detectable spectral lines in the stacked spectra are listed in Table 4.2. Uncertainties on the properties have been obtained by repeating the stacking process, but with a number of the spectra replaced by randomly drawn spectra from the same sample. This is to obtain a measure of the intrinsic scatter between the different spectra. For the field galaxies we replace three of the spectra, for the combined 0316+foreground sample we replace two spectra, whereas for the

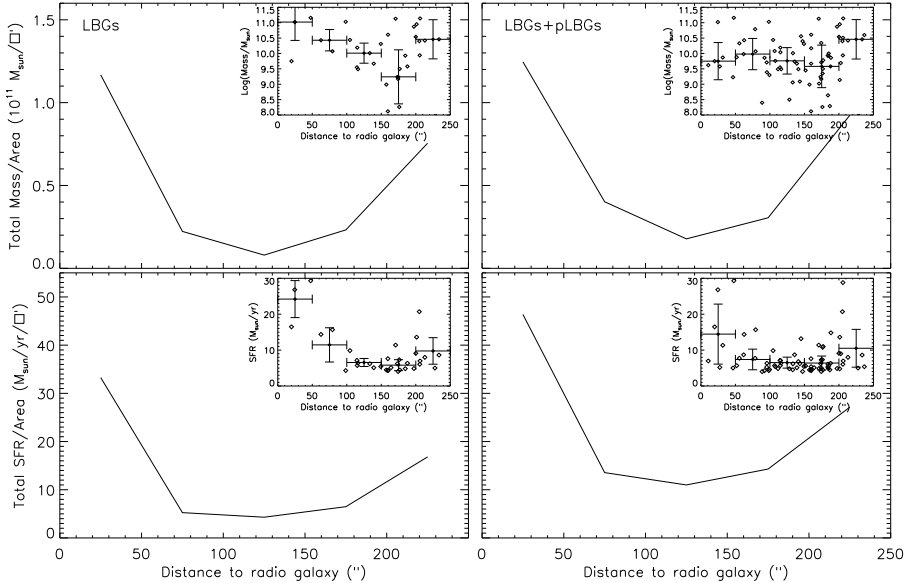


**Figure 4.5** – Top and bottom panels: Total stellar mass and total dust uncorrected star formation rate per unit area as a function of distance to the radio galaxy. Quantities have been calculated by summing the stellar mass and SFR in a series of annuli centred on the radio galaxy. The insets in each of the panels show the stellar masses and SFRs of individual galaxies as function of radius. For the panels in the left column only the LBGs are considered, whereas both the LBG and pLBG sample are considered in the panels in the right column.

0316 and foreground structures only one spectrum is replaced. In total 10, 15, 20 and 50 fake spectra are constructed for the 0316, foreground, 0316+foreground and field galaxies, respectively. The fake stacked spectra are subsequently varied according to their rms noise after which all properties are recalculated. For each fake spectrum this process is repeated 100 times. The standard deviations of the subsequent distributions are taken as  $1\sigma$  uncertainties. Also, the  $\text{Ly}\alpha$  FWHM are measured from stacked spectra that have been obtained using the  $\text{Ly}\alpha$  redshifts rather than the absorption line redshifts. Using the latter will result in an increase of a factor of 1.5-2 for the FWHM.

The top-left panel of Fig. 4.6 shows the stacked spectrum of the three objects identified to be in the 0316 protocluster. The main feature of the spectrum is the strong  $\text{Ly}\alpha$  emission with  $EW_0 = 26.4 \pm 3.8 \text{ \AA}$ , but this is mostly driven by the LAE included in the sample. Removing this galaxy lowers the  $EW_0$  to  $17.9 \text{ \AA}$ . The field galaxies, in the middle-right panel, also show  $\text{Ly}\alpha$  emission, but with an  $EW_0 = 7.4 \pm 2.1 \text{ \AA}$  it is on average not as strong as in the 0316 protocluster.

The average spectrum of the foreground galaxies shows no  $\text{Ly}\alpha$  emission, but considering the small sample size this is likely not a significant difference. In fact, Shapley et al. (2003) show that approximately half of all LBGs show  $\text{Ly}\alpha$

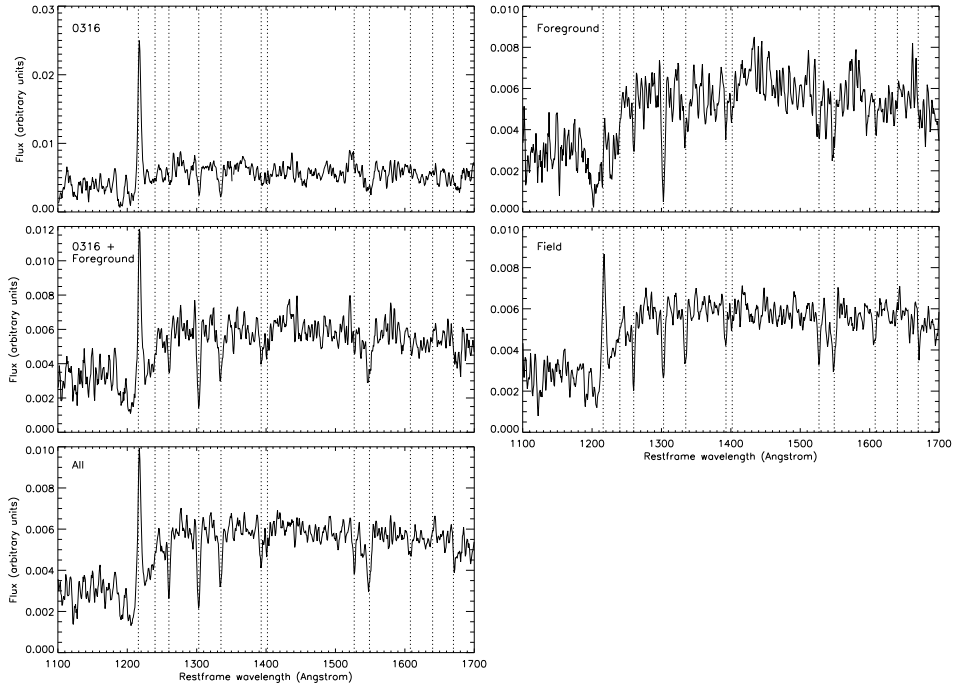


**Figure 4.6** – A series of stacked spectra. Stacks include, from left to right and top to bottom: 0316 objects with  $3.12 < z < 3.13$ , foreground structure objects with  $3.1 < z < 3.12$ , combined sample of 0316 and foreground objects, field objects and all spectroscopically confirmed objects. Dotted vertical lines indicate the location of the most important spectral features as in Fig. 4.1(a). Spectral features above 1600 Å are FeII $\lambda$ 1608, HeII $\lambda$ 1640 and AlII $\lambda$ 1670.

in emission and the other half shows Ly $\alpha$  in absorption. With sample sizes of 3 for the 0316 protocluster and 5 for the foreground structure, the chance that the observed difference between the 0316 and foreground structure is a mere statistical fluctuation should be considered significant. We can therefore draw no conclusions based on this. It would, however, be interesting to see whether this difference persists with more spectroscopic observations.

We can slightly alleviate the problem with the sample size by combining the 0316 and foreground structure samples and comparing this to the field population. The presence of such a difference would be a strong indication of environmental influence at  $z \sim 3$ . The stacked spectrum is shown in the middle-left panel of Fig. 4.6 and the relevant properties are listed in Table 4.2. The spectrum shows Ly $\alpha$  emission with  $EW_0 = 11.3 \pm 3.7$  Å. This is consistent with the field population within the  $1\sigma$  uncertainties. The strength of the absorption lines of the combined sample are also consistent with that found for the field population. The composite of the overdense structures shows therefore no evidence for environmental differences with respect to the field.

**Table 4.2** – Properties of the emission and absorption lines found in the stacked spectra of the 0316 protocluster, the foreground structure and the field. Restframe equivalent widths are taken to be positive for emission lines and negative for absorption lines. Velocity offsets are given with respect to the OI/SiII doublet. FWHM values are corrected for the instrumental resolution. <sup>a</sup> Based on a stack of the three objects that do show Ly $\alpha$  emission. <sup>b</sup> These values are obtained from stacked spectra created using the Ly $\alpha$  redshift where available. <sup>c</sup> This value cannot be constrained and is therefore not listed. <sup>d</sup> The UV slope  $\beta$  is calculated using the  $R$  and  $I$  band data used in Chapter 3.

	0316	Foreground	0316+Foreground	Field
$\Delta v_{\text{Ly}\alpha}$ (km s <sup>-1</sup> )	+442 ± 142	+734 ± 225 <sup>a</sup>	+451 ± 156	+396 ± 162
$EW_{0,\text{Ly}\alpha}$ (Å)	26.4 ± 3.8	-13.3 ± 5.3	11.3 ± 3.7	7.4 ± 2.1
$\text{FWHM}_{\text{Ly}\alpha}$ (km s <sup>-1</sup> ) <sup>b</sup>	561 ± 118	- <sup>c</sup>	493 ± 122	803 ± 241
$\Delta v_{\text{SiII}}$ (km s <sup>-1</sup> )	-	+308 ± 178	+340 ± 167	+281 ± 152
$EW_{0,\text{SiII}}$ (Å)	-	-1.9 ± 0.8	-1.5 ± 0.8	-2.2 ± 0.8
$\text{FWHM}_{\text{SiII}}$ (km s <sup>-1</sup> )	-	400 ± 352	- <sup>c</sup>	558 ± 212
$\Delta v_{\text{OI/SiII}}$ (km s <sup>-1</sup> )	0	0	0	0
$EW_{0,\text{OI/SiII}}$ (Å)	-2.1 ± 0.7	-4.5 ± 1.1	-3.5 ± 0.9	-2.4 ± 0.5
$\text{FWHM}_{\text{OI/SiII}}$ (km s <sup>-1</sup> )	365 ± 233	799 ± 233	708 ± 223	623 ± 201
$\Delta v_{\text{CII}}$ (km s <sup>-1</sup> )	-263 ± 169	+103 ± 360	-117 ± 202	-61 ± 188
$EW_{0,\text{CII}}$ (Å)	-3.0 ± 1.1	-3.1 ± 1.1	-2.7 ± 0.8	-1.8 ± 0.6
$\text{FWHM}_{\text{CII}}$ (km s <sup>-1</sup> )	726 ± 309	1802 ± 545	1127 ± 559	509 ± 205
$\Delta v_{\text{SiIV}}$ (km s <sup>-1</sup> )	-	-	+151 ± 196	-61 ± 204
$EW_{0,\text{SiIV}}$ (Å)	-	-	-1.4 ± 0.8	-0.9 ± 0.5
$\text{FWHM}_{\text{SiIV}}$ (km s <sup>-1</sup> )	-	-	- <sup>c</sup>	102 ± 226
$\Delta v_{\text{SiII}}$ (km s <sup>-1</sup> )	-	-75 ± 263	-	+88 ± 216
$EW_{0,\text{SiII}}$ (Å)	-	-2.1 ± 0.9	-	-1.7 ± 0.5
$\text{FWHM}_{\text{SiII}}$ (km s <sup>-1</sup> )	-	711 ± 266	-	315 ± 231
$\Delta v_{\text{CIV}}$ (km s <sup>-1</sup> )	-369 ± 267	-194 ± 220	-213 ± 226	-120 ± 324
$EW_{0,\text{CIV}}$ (Å)	-5.3 ± 1.5	-3.1 ± 0.9	-3.4 ± 1.1	-2.7 ± 0.8
$\text{FWHM}_{\text{CIV}}$ (km s <sup>-1</sup> )	1881 ± 414	800 ± 334	1408 ± 607	887 ± 286
$\Delta v_{\text{FeII}}$ (km s <sup>-1</sup> )	-	-	-	+24 ± 252
$EW_{0,\text{FeII}}$ (Å)	-	-	-	-1.2 ± 0.5
$\text{FWHM}_{\text{FeII}}$ (km s <sup>-1</sup> )	-	-	-	414 ± 278
$\beta^d$	-1.7 ± 0.2	-0.8 ± 0.4	-1.2 ± 0.3	-1.3 ± 0.1

The properties listed in Table 4.2 can be compared to the results of Shapley et al. (2003, hereafter S03). In S03 the spectra of  $\sim 1000$  LBGs were stacked to perform a detailed study of the average properties of these galaxies. In general, the LBG properties in Table 4.2 show similarities to what was found in S03. There is a velocity difference of  $\sim 400 - 900$  km s<sup>-1</sup> between the Ly $\alpha$  line and the absorption lines, where the Ly $\alpha$  line is redshifted with respect to the absorption. This is also seen in the individual LBG spectra of S03 and is indicative of outflows. The LBGs in the 0316 field therefore also show evidence of outflows.

Shapley et al. (2003) also divided their sample of LBGs into four bins based on Ly $\alpha$  equivalent width, ranging from Ly $\alpha$  in absorption to strong Ly $\alpha$  emission. LBGs with strong Ly $\alpha$  emission were found to have weaker low-ionisation lines, bluer UV slopes and smaller kinematic offsets between Ly $\alpha$  and interstellar absorption lines. Based on the stacked spectra presented here we can make a similar division between the various samples. For this purpose we will only consider the field population and the combined 0316+foreground population as the individual 0316 and foreground samples are too small to make a meaningful comparison. Both

populations fall into the moderate emission category or group 3 of S03.

Beginning with the field sample, we see little difference between the values in Table 4.2 and the results of S03. All  $EW_0$  values are consistent within  $1\sigma$  with the properties of group 3 in S03. Since we make no distinction in  $EW_{Ly\alpha}$  when stacking the spectra we also expect this spectrum to match closely to the full LBG stack of S03. Indeed, all absorption line equivalent widths are fully consistent with the average LBG of S03.

When comparing the 0316+foreground objects with group 3 of S03 we see that the OI/SiII doublet and the CII line of the combined sample is stronger. This is partially due to the inclusion of #12 in the stack, which has an exceptionally strong OI/SiII doublet. Removing this object from the summed spectrum reduces the equivalent width to  $-2.7 \pm 0.6 \text{ \AA}$  which is formally consistent with the results of S03. This, however, does not explain the strong CII feature. The other properties are consistent with what is found in S03.

Following the physical picture presented by S03, stronger absorption lines may be explained by a larger covering fraction of the outflowing gas. This would, however, also diminish the Ly $\alpha$  flux. Since the 0316+foreground sample does show significant Ly $\alpha$  emission there must be something compensating for the larger covering fraction. This could be related to a lower than expected dust content. The UV slopes of galaxies are sensitive to dust content, but the values listed in 4.2 show no significant difference between this work and S03. Furthermore, we must consider that the samples used in this study are much smaller than the samples presented in S03. This could indicate that the strong CII absorption line is due to statistical fluctuation. It is therefore necessary to increase the number of spectroscopically confirmed galaxies in order to put proper constraints on any possible differences between the various populations and the results of S03.

The stacked spectra can also be used to determine whether IGM absorption blueward of the Ly $\alpha$  line is more prevalent in either of the structures or in the field. To do this we assess the mean flux level for  $\lambda_{\text{rest}} < 1185 \text{ \AA}$  and compare it to the mean flux level for  $\lambda_{\text{rest}} > 1280 \text{ \AA}$ . The ratio of these flux levels is highest for 0316 at  $0.67 \pm 0.02$ , whereas the foreground and field galaxies show ratios of  $0.53 \pm 0.02$  and  $0.50 \pm 0.01$ , respectively. The combined sample of the two structures yields  $0.59 \pm 0.01$ . The Ly $\alpha$  break is thus less pronounced in the protocluster galaxies indicating that there is less IGM absorption in the overdense structures.

Finally, a brief comparison between the field spectrum and the stacked spectrum that includes all spectroscopically confirmed LBGs shows that there is little discernible difference in both the strength of the Ly $\alpha$  emission and the absorption lines. This is illustrative of how differences can be diluted if there is no clear way to discern between the field and the protocluster objects.

#### 4.4.4 Interacting or unrelated structures?

The presence of a foreground structure is not the first indication that HzRG-selected protoclusters are part of superstructures. Kuiper et al. (2011, Chapter 2) has shown

that the well-studied protocluster around PKS 1138-262 (1138) at  $z = 2.15$  exhibits a broad bimodal velocity structure which has been independently found for both the megaparsec scale structure and the central kiloparsec scale structure. This is best explained by a line-of-sight merger scenario of two massive haloes. Could this also be the case for the 0316 protocluster and its foreground companion?

In Sect. 4.4.2 we show that the spatial distributions of the two structures in the 0316 field are not drawn from the same distribution and Fig. 4.3 indicates a projected separation of  $\sim 1.4$  Mpc. If there is a merger it is not along the line of sight.

The velocity difference between the 0316 protocluster and the foreground structure is  $\sim 1600$  km s $^{-1}$ , but this is only the line-of-sight velocity component. If this is indeed a merging or interacting system, then additional transverse velocity components may be present. This implies that the true relative velocity may be larger than 1600 km s $^{-1}$ . The relative velocity is thus similar to the 1600 km s $^{-1}$  found in the 1138 system. The work presented in Chapter 2 showed that the Millennium simulation (Springel et al. 2005; De Lucia & Blaizot 2007) could reproduce such a velocity difference, but only for the largest halo masses. Doing the same analysis at  $z \sim 3$  as in Chapter 2 reveals no such mergers in the Millennium simulation.

In order to determine whether such a merger is possible at  $z \sim 3$ , we calculate how the relative velocity evolves with decreasing distance  $d$  in the case of two merging massive haloes. For this we use the equations described in Sarazin (2002). Conservation of energy dictates

$$\frac{1}{2}mv^2 - \frac{GM_1M_2}{d} = -\frac{GM_1M_2}{d_0} \quad (4.2)$$

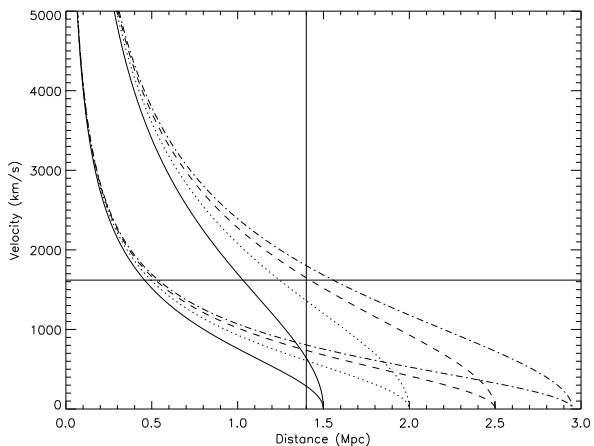
with  $m = M_1M_2/(M_1 + M_2)$  and  $d_0$  the separation between the structures when they drop out of the Hubble flow. Here we have assumed for simplicity that the transverse velocity is zero. This yields

$$v = \sqrt{2G(M_1 + M_2) \left( \frac{1}{d} - \frac{1}{d_0} \right)}. \quad (4.3)$$

In Fig. 4.7 we show how the velocity increases with decreasing distance in a merger scenario. The curves shown are for a variety of values for  $d_0$ . The largest value for  $d_0$  was chosen such that the time it takes to reach a relative velocity of 1600 km s $^{-1}$  is equal to the age of the Universe at  $z = 3.13$ . We also consider two specific halo masses, but in all cases it is assumed that the 0316 and foreground structure are of equal mass. We see that for masses of  $10^{14} M_\odot$  a velocity of  $\sim 1600$  km s $^{-1}$  is only reached at small separations of the order of  $< 0.6$  Mpc. For masses closer to the estimated mass of the 0316 protocluster, the distance at which 1600 km s $^{-1}$  is reached ranges between  $1.0 < d < 1.6$  Mpc.

As we have shown in Sect. 4.4.2, the projected distance between the structures is of the order of  $\sim 1.4$  Mpc. If the two structures are interacting then the true

**Figure 4.7** – Evolution of the relative velocity of two massive structures with distance for a variety of starting distances  $d_0$  and halo masses. The starting separations are 1.5, 2.0, 2.5 and 2.95 Mpc. These are denoted by the solid, dotted, dashed and dash-dotted curves respectively. For each starting distance two halo masses are considered. The halo mass ratio is fixed at 1:1 and the masses considered are  $1$  and  $5 \times 10^{14} M_\odot$  with the steeper curves corresponding to the larger halo masses. The horizontal and vertical lines indicate the relative velocity of  $1600 \text{ km s}^{-1}$  and the projected separation between the two structures as observed in the 0316 field.



distance is likely larger. The relative velocity of  $1600 \text{ km s}^{-1}$  is also likely a lower limit due to projection effects. If the merger scenario is possible we therefore expect the curves to cross through the upper right quadrant of Fig. 4.7. There are two curves that meet this requirement, with starting separations of 2.5 and 2.95 Mpc and masses of  $5 \times 10^{14} M_\odot$ . It is therefore possible that the system is undergoing a merger, but only if the two structures are massive and the starting separation is roughly 2.5 to 3 Mpc.

The other option is that the 0316 protocluster and the foreground structure are ‘unrelated’ structures in the Hubble flow at the time of observing. Assuming that the Hubble flow dominates the relative motions of the two structures we use the Hubble law to find that a velocity difference along the line of sight of  $1620 \text{ km s}^{-1}$  implies a distance of at least 23 comoving Mpc. Following Bahcall et al. (2004) we assume that the mean distance between two clusters in the Hubble flow at  $z \sim 3$  is  $\sim 50$  Mpc. What is the chance of encountering such a line-of-sight alignment as possibly witnessed here? In a field of  $100 \times 100 \text{ Mpc}^2$  we expect a total of  $\sim 15$  structures. The 0316 field covers approximately  $9 \text{ Mpc}^2$ . So the probability of having one additional structure directly in front of the main structure is  $\sim 1$  per cent. If we lower the mean distance to  $\sim 30$  Mpc, then the chance increases to  $\sim 4$  per cent. These probabilities are small, but they are not negligible. It is thus not unreasonable to find an unrelated foreground structure and the possibility that this is a chance alignment of two unrelated structures in the Hubble flow cannot be rejected.

If the two structures are a chance alignment then they are separated by  $\sim 23$  Mpc. This does not preclude that at some later epoch the two structures will interact. We try to determine whether two massive haloes separated by  $\sim 23$  Mpc at  $z \sim 3$  will merge before  $z = 0$  by using the Millennium simulation. Only the

most massive haloes at  $z \sim 3$  are considered, because the estimated mass of the 0316 protocluster is large ( $\sim 5 \times 10^{14} M_{\odot}$ , V05) and the foreground structure seems to have a similar mass. Using a lower limit of  $2 \times 10^{13} M_{\odot}$  we find a total of 20 halo pairs with relative distances between 20 and 25 Mpc. For the majority of the pairs the separation decreases, but none reach separations smaller than 8 Mpc. None of the pairs therefore interact or merge before  $z = 0$ . Thus, if the two structures in the 0316 field are not interacting at  $z \sim 3$ , then it is likely that there will be no interaction between the structures on the timescale of  $\sim 10$  Gyr.

## 4.5 Conclusions

We have presented spectroscopic follow-up to the work of Chapter 3. We have observed a total of 24 LBG candidates that are located in the field of the protocluster around MRC 0316-257 at  $z = 3.13$ . By obtaining spectroscopy for the LBG candidates we have been able to distinguish between field and protocluster galaxies. This in turn allows us to make a self-consistent comparison between the field and protocluster galaxy samples.

1. We determine redshifts for 20 out of 24 objects, finding that all objects are located between  $2.7 < z < 3.5$ . This implies an interloper fraction of at most  $\sim 17$  per cent. Out of the 20 confirmed objects, 5 are located at  $z \sim 3.10$  and 3 at  $z \sim 3.13$ . The number of 0316 protocluster objects is too small to account for the surface overdensity presented in Chapter 3, but is consistent with the presence of two structures; the 0316 protocluster at  $z \sim 3.13$  and a foreground structure at  $z \sim 3.1$ . The presence of such a foreground structure was already hypothesised in Maschietto et al. (2008).
2. The presence of the foreground structure implies that the volume overdensity of LBGs presented in Chapter 3 is overestimated. Instead of the previously determined overdensity of 8, the true volume density is a factor  $\sim 4$  larger than the field. We also estimate that the foreground structure is of equal mass and richness as the 0316 protocluster.
3. The spatial distribution of the foreground and 0316 LBGs shows two distinct density peaks: one centred on the radio galaxy and a stronger peak located in the North-West corner of the field. This latter stronger peak coincides with a concentration of foreground objects indicating that the foreground structure is not directly in front of the 0316 protocluster. A 2D Kolmogorov-Smirnov test confirms this, indicating that the spatial distributions of the 0316 and foreground LBGs differ at the  $3\sigma$  level.
4. There are no systematic differences between the protocluster galaxies and field galaxies in terms of mass. Stacking the spectra shows that the galaxies associated with the 0316 protocluster have stronger Ly $\alpha$  emission than the field galaxies, whereas the galaxies in the foreground structure show very little Ly $\alpha$  emission. However, considering the limited sample size this is likely due to statistical fluctuation. Combining the galaxies in the two structures in one composite sample shows no difference with respect to the field. This



implies that, based on these data, there is no discernible evidence for environmental effects on galaxy evolution at  $z \sim 3$ . The equivalent width of the CII absorption line, on the other hand, is larger than what would be expected based on the Ly $\alpha$  equivalent width. It is not clear whether this is real or a statistical fluctuation due to the small sample size. More data is necessary to see whether this difference persists. Also, the Lyman break is less pronounced in the combined 0316+foreground sample indicating that there is less absorption by the IGM in these structures.

5. Based on merger dynamics we find that the observed relative velocity at the observed separation can be reproduced for large masses of  $\sim 5 \times 10^{14} M_{\odot}$  and starting separations of  $> 2.5$  Mpc. A merger scenario can therefore not be ruled out. The possibility of a chance alignment can also not be ruled out. If the structures are unrelated then this implies that the distance between the structures is  $\sim 23$  Mpc. With such a separation at  $z \sim 3$  it is unlikely that the two structures will interact before  $z \sim 0$ .

The results presented here for the different samples of galaxies should be considered preliminary. Further spectroscopic observations are necessary to get a better census of which galaxies are in which of the structures. This will also give better constraints on the potential differences between the protocluster and field galaxies at  $z \sim 3$ . Furthermore, extra data will provide stronger constraints on the merger scenario considered in this work. If additional spectroscopic redshifts result in smaller separations on the sky and in redshift space, then this may increase the likelihood of the merger scenario.

## Acknowledgements

We would like to thank the anonymous referee for the very useful comments that have helped improve this paper. This research is based on observations carried out at the European Southern Observatory, Paranal, Chile, with program number 086.A-0930(A). The authors wish to thank the staff at the VLT for their excellent support during the observations. EK acknowledges funding from Netherlands Organization for Scientific Research (NWO). NAH acknowledges support from STFC and the University of Nottingham Anne McLaren Fellowship.

## References

- Bahcall N. A., Hao L., Bode P., Dong F., 2004, *ApJ*, 603, 1
- Beers T. C., Flynn K., Gebhardt K., 1990, *AJ*, 100, 32
- Bird C. M., Beers T. C., 1993, *AJ*, 105, 1596
- Brammer G. B., van Dokkum P. G., Coppi P., 2008, *ApJ*, 686, 1503
- Bruzual G., Charlot S., 2003, *MNRAS*, 344, 1000
- Calzetti D., Armus L., Bohlin R. C., Kinney A. L., Koornneef J., Storchi-Bergmann T., 2000, *ApJ*, 533, 682
- Cooper M. C. et al., 2008, *MNRAS*, 383, 1058
- De Lucia G., Blaizot J., 2007, *MNRAS*, 375, 2
- Elbaz D. et al., 2007, *A&A*, 468, 33
- Gobat R. et al., 2011, *A&A*, 526, A133+
- Hatch N. A., Kurk J. D., Pentericci L., Venemans B. P., Kuiper E., Miley G. K., Röttgering H. J. A., 2011, *MNRAS*, 415, 2993
- Henry J. P. et al., 2010, *ApJ*, 725, 615
- Hilton M. et al., 2010, *ApJ*, 718, 133
- Intema H. T., Venemans B. P., Kurk J. D., Ouchi M., Kodama T., Röttgering H. J. A., Miley G. K., Overzier R. A., 2006, *A&A*, 456, 433
- Knopp G. P., Chambers K. C., 1997, *ApJS*, 109, 367
- Kriek M., van Dokkum P. G., Labbé I., Franx M., Illingworth G. D., Marchesini D., Quadri R. F., 2009, *ApJ*, 700, 221
- Kuiper E. et al., 2011a, *MNRAS*, 415, 2245
- Kuiper E. et al., 2010, *MNRAS*, 405, 969
- Kuiper E. et al., 2011b, *MNRAS*, 1376
- Kurk J. D. et al., 2004a, *A&A*, 428, 817
- Kurk J. D., Pentericci L., Röttgering H. J. A., Miley G. K., 2004b, *A&A*, 428, 793
- Maschietto F. et al., 2008, *MNRAS*, 389, 1223
- Matsuda Y. et al., 2011, *MNRAS*, 1087
- Miley G., De Breuck C., 2008, *A&A Rev*, 15, 67
- Overzier R. A. et al., 2008, *ApJ*, 673, 143
- Papovich C. et al., 2010, *ApJ*, 716, 1503
- Pascarelle S. M., Windhorst R. A., Driver S. P., Ostrander E. J., Keel W. C., 1996, *ApJ*, 456, L21+
- Pentericci L. et al., 2000, *A&A*, 361, L25
- Popesso P. et al., 2011, *A&A*, 532, A145+
- Rocca-Volmerange B., Le Borgne D., De Breuck C., Fioc M., Moy E., 2004, *A&A*, 415, 931
- Sarazin C. L., 2002, in *Astrophysics and Space Science Library*, Vol. 272, *Merging Processes in Galaxy Clusters*, L. Feretti, I. M. Gioia, & G. Giovannini, ed., pp. 1–38
- Seymour N. et al., 2007, *ApJS*, 171, 353
- Shapley A. E., Steidel C. C., Pettini M., Adelberger K. L., 2003, *ApJ*, 588, 65
- Springel V. et al., 2005, *Nature*, 435, 629
- Steidel C. C., Adelberger K. L., Shapley A. E., Erb D. K., Reddy N. A., Pettini M., 2005, *ApJ*, 626, 44
- Steidel C. C., Adelberger K. L., Shapley A. E., Pettini M., Dickinson M., Giavalisco M., 2000, *ApJ*, 532, 170
- Steidel C. C., Bogosavljević M., Shapley A. E., Kollmeier J. A., Reddy N. A., Erb D. K., Pettini M., 2011, *ApJ*, 736, 160

- 
- Steidel C. C., Pettini M., Hamilton D., 1995, *AJ*, 110, 2519  
Tanaka M., De Breuck C., Venemans B., Kurk J., 2010a, *A&A*, 518, A18+  
Tanaka M., Finoguenov A., Ueda Y., 2010b, *ApJ*, 716, L152  
Tran K.-V. H. et al., 2010, *ApJ*, 719, L126  
Venemans B. P. et al., 2005, *A&A*, 431, 793  
Venemans B. P. et al., 2007, *A&A*, 461, 823  
Wilson G. et al., 2008, in *Astronomical Society of the Pacific Conference Series*, Vol. 381, *Infrared Diagnostics of Galaxy Evolution*, R.-R. Chary, H. I. Teplitz, & K. Sheth, ed., pp. 210–+



---

# DISCOVERY OF A HIGH- $z$ PROTOCLUSTER WITH TUNABLE FILTERS: THE CASE OF 6C0140+326 AT $z = 4.4$

We present the first results obtained using a tunable narrowband filter in the search for high- $z$  protoclusters. Using the recently commissioned red tunable filter on the Gran Telescopio Canarias we have searched for Ly $\alpha$  emitters in a 75 arcmin<sup>2</sup> field centered on the  $z = 4.413$  radio galaxy 6C0140+326. With three different wavelength tunings we find a total of 27 unique candidate Ly $\alpha$  emitters. The availability of three different wavelength tunings allows us to make estimates of the redshifts for each of the objects. It also allows us to separate a possible protocluster from structure in the immediate foreground. This division shows that the foreground region contains significantly fewer Ly $\alpha$  emitters. Also, the spatial distribution of the objects in the protocluster field deviates from a random distribution at the  $2.5\sigma$  level. The observed redshift distribution of the emitters is different from the expected distribution of a blank field at the  $\sim 3\sigma$  level, with the Ly $\alpha$  emitters concentrated near the radio galaxy at  $z > 4.38$ . The 6C0140+326 field is denser by a factor of  $9 \pm 5$  than a blank field, and the number density of Ly $\alpha$  emitters close to the radio galaxy is similar to that of the  $z \sim 4.1$  protocluster around TN J1338-1942. We thus conclude that there is an overdensity of Ly $\alpha$  emitters around the radio galaxy 6C0140+326. This is one of few known overdensities at such a high redshift.

E. Kuiper, N. A. Hatch, B. P. Venemans, G. K. Miley, H. J. A. Röttgering,  
J. D. Kurk, R. A. Overzier, L. Pentericci, J. Bland-Hawthorn, J. Cepa  
*Monthly Notices of the Royal Astronomical Society*, **417**, 1088 (2011)

## 5.1 Introduction

The identification of the progenitors of local galaxy clusters at  $z > 2$  is a difficult task. For the interval  $1 < z < 1.5$ , galaxy clusters are most often identified by infrared red sequence searches or observations of the X-ray emitting intracluster gas and the number of galaxy clusters at these redshifts is growing steadily (e.g. Stanford et al. 1997; Rosati et al. 1999, 2004; Mullis et al. 2005; Stanford et al. 2006; Muzzin et al. 2009; Brodwin et al. 2010; Bielby et al. 2010). Unfortunately, these methods become increasingly less effective when moving beyond  $z = 1.5$  as the number of red galaxies decreases and X-ray emission becomes too faint to be easily observed. However, if we wish to understand the role of environment on galaxy evolution and the emergence of large scale structure it is essential to locate and study galaxy clusters at all possible epochs. Recent results have presented the spectroscopic confirmation of galaxy clusters with X-ray emission at  $z > 1.5$  (Wilson et al. 2008; Papovich et al. 2010; Tanaka et al. 2010; Henry et al. 2010), with the current distance record being the galaxy cluster CLJ1449+0856 at  $z \sim 2.07$  presented by Gobat et al. (2011) (but see also Andreon & Huertas-Company 2011). However, this sample of high- $z$  clusters remains small.

Another successful method of identifying galaxy cluster progenitors at  $z > 2$  is to search for overdensities of line emitting galaxies using narrowband imaging. These searches are often aimed at fields containing high- $z$  radio galaxies (hereafter HzRGs, Miley & De Breuck 2008), since these are thought to have large stellar masses of the order of  $10^{11}$  to  $10^{12} M_{\odot}$  (Rocca-Volmerange et al. 2004; Seymour et al. 2007). According to hierarchical galaxy formation, the most massive galaxies form in the densest environments. The massive nature of HzRGs thus indicates that these objects may trace overdensities in the early Universe. In recent years many studies have focused on finding galaxy overdensities around HzRGs (e.g. Pascarelle et al. 1996; Knopp & Chambers 1997; Pentericci et al. 2000; Kurk et al. 2004a,b; Overzier et al. 2006; Venemans et al. 2007; Overzier et al. 2008; Kuiper et al. 2010; Galametz et al. 2010; Hatch et al. 2011). Since these overdensities show no evidence of X-ray emission (at luminosities  $> 10^{44}$  erg s $^{-1}$ ) it is thought that these are forming clusters, not yet dynamically relaxed (Carilli et al. 2002; Overzier et al. 2005). They are therefore often called ‘protoclusters’.

However, even though the number of spectroscopically confirmed  $z > 2$  HzRGs approaches 200, the fraction of these that have been studied for the presence of galaxy overdensities remains small. This is partly due to the small number of existing narrowband filters and the fact that the central wavelengths of these existing filters are often based on strong lines at  $z = 0$ , such as [OIII] $\lambda$ 5007. This severely limits the redshifts at which protoclusters can be studied and therefore the absolute number of confirmed protoclusters has remained small.

In this Chapter we present the results of a pilot study that utilizes tunable narrowband filters in the search for line emitting galaxies around the HzRG 6C0140+326 at  $z = 4.413$  (Rawlings et al. 1996; De Breuck et al. 2001). Tunable filters (TFs) allow the user to set the central wavelength and width of the narrowband filter.

TFs use two plane parallel transparent plates coated with films of high reflectivity and low absorption. By separating the two plates by a small distance of the order of a  $\mu\text{m}$ – $\text{mm}$  a cavity is formed which is resonant at a specific wavelength. Constructive interference at the resonant wavelength then causes all the incident light at that wavelength to be transmitted. Changing the separation between the plates then allows the central wavelength or the width of the filter to be adjusted. TFs therefore alleviate the limitations imposed by a small number of available narrowband filters at fixed wavelengths and are thus ideally suited for searching for protoclusters at a range of redshifts. More information and details concerning tunable filters can be found in Bland-Hawthorn (1995) and Jones et al. (2002).

Similar studies involving the search for line emitting galaxies around  $z \sim 1$  quasars have been successfully performed by Baker et al. (2001) and Barr et al. (2004). An attempt to use this technique at higher redshifts has led to mixed results. In work by Swinbank et al. (in prep.), a TF study is presented for two radio-loud quasars located at  $z \sim 2$  and one radio-quiet quasar at  $z \sim 4.5$ . The  $z \sim 4.5$  field shows evidence for an overdensity, whereas the two  $z \sim 2$  fields lack depth and do not allow for strong conclusions. With the advent of a TF instrument at a 8-10 meter class telescope, it has now become possible to obtain sufficiently deep data to efficiently search for  $\text{Ly}\alpha$  emitters in the environments of HzRGs at arbitrary redshifts  $z > 2$ .

This chapter is organised as follows: in Sect. 5.2 we describe the data, its reduction and the object detection. The sample selection and redshift estimation is treated in Sect. 5.3 and we discuss the evidence for the presence of an overdensity in Sect. 5.4. Finally, conclusions and future outlook are presented in Sect. 5.5. Throughout this work we use a standard  $\Lambda\text{CDM}$  cosmology with  $H_0 = 71 \text{ km s}^{-1} \text{ Mpc}^{-1}$ ,  $\Omega_{\text{M}} = 0.27$  and  $\Omega_{\Lambda} = 0.73$ . All magnitudes given in this Chapter are in the AB magnitude system.

## 5.2 Data

The radio galaxy 6C0140+326 (hereafter 6C0140) was observed for a total of 18 hours using the Optical System for Imaging and low Resolution Integrated Spectroscopy instrument (OSIRIS, Cepa et al. 2000, 2003) at the Gran Telescopio Canarias (GTC), La Palma. OSIRIS consist of two  $2048 \times 4096$  pixel Marconi CCDs with a 72 pixel gap between the two CCDs. The observations were done on several dates from September 2010 to January 2011. The  $2 \times 2$  binning mode was used resulting in a pixel scale of  $\sim 0.25'' \text{ pixel}^{-1}$  and a total field-of-view of  $\sim 8.7'' \times 8.6''$ . The radio galaxy was positioned near the optical centre, approximately  $15''$  from the left edge of CCD 2. The individual exposures have been dithered with offsets of approximately  $10$ – $12.5''$  in right ascension and  $2$ – $4''$  in declination. The larger offsets in right ascension have been chosen such as to cover the gap of  $\sim 8''$  between the two CCDs without losing the radio galaxy in the gap. A full list of details concerning the observations can be found in Table 5.1.

Broadband images were obtained in the  $r$  and  $i$  bands. The narrowband images

**Table 5.1** – Details of the observations. The  $5\sigma$  limiting magnitudes have been calculated for an aperture diameter of twice the seeing disk. Also note that the values given for  $\lambda_{\text{eff}}$  for the TF observations are the values at the optical centre.

Band	Exp. time (sec.)	$\lambda_{\text{eff}}$ (Å)	$\Delta\lambda$ (Å)	Seeing (arcsec)	$5\sigma$ limiting magnitude
$r$	2400	6417	1685	0.8	25.8
$i$	2100	7719	1483	0.8	24.8
TF1	15680	6565	31.4	0.8	25.1
TF2	15680	6575	31.4	0.8	25.2
TF3	13440	6585	31.4	0.8	25.1

were obtained at three different central wavelengths  $\lambda_c$ . This was done because the central wavelength of the TFs varies across the field of view approximately as

$$\lambda(r) = \lambda_c (1 - 0.0007930r^2) \quad (5.1)$$

as given in the OSIRIS TF user manual. Here  $r$  is the distance to the optical centre of the instrument in arcminutes and  $\lambda_c$  the wavelength at the optical centre. The maximum FWHM of the TF is 20 Å, therefore it was necessary to perform several passes with different  $\lambda_c$  in order to cover the entire redshift range of a possible protocluster. At  $z \sim 4.4$  the Ly $\alpha$  line is shifted to 6580 Å, so the central wavelengths were chosen to be 6565 Å, 6575 Å and 6585 Å (hereafter TF1, TF2 and TF3 for brevity). Note that the redshift of the radio galaxy ( $z = 4.413$ ) indicates that it falls between TF2 and TF3.

As noted above, the maximum formal width of the TF is 20 Å. However, the shape of the response curve is Lorentzian rather than Gaussian and is approximately given by

$$T = \left\{ 1 + \left[ \frac{2(\lambda - \lambda_c)}{\delta\lambda} \right]^2 \right\}^{-1} \quad (5.2)$$

with  $\lambda_c$  the central wavelength and  $\delta\lambda$  the formal FWHM. Due to the shape being Lorentzian, the transmission has relatively extended wings which results in an effective band width that is larger than the formal value for the FWHM by a factor of  $\pi/2$ . Thus the TF tunings have an effective FWHM of  $\sim 31$  Å. Taking this into account, our observations probe the redshift range  $4.386 < z < 4.428$  near the optical centre. The true redshift range that is covered is larger due to the variation of the central wavelength across the field. The relevant filter response curves are shown in Fig. 5.1 together with a night-sky emission line spectrum. As can be seen, the sky line contamination is relatively mild.

### 5.2.1 Data reduction

The reduction of all the data is done using IRAF<sup>1</sup>. The reduction of the broadband images includes the standard steps of bias subtraction and flat-fielding, where the

<sup>1</sup>IRAF is distributed by the National Optical Astronomy Observatory, which is operated by the Association of Universities for Research in Astronomy, Inc., under cooperative agreement with the National Science Foundation.



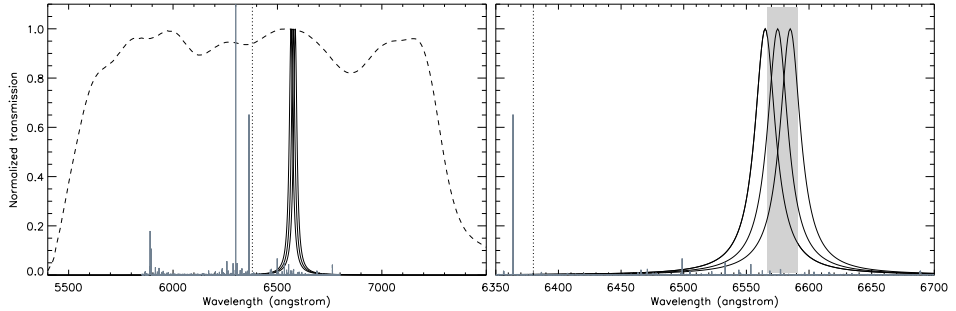


**Figure 5.1** – Left panel: Filter response curves for the three TF tunings (solid curves) and the  $r$  band (dashed curve). Right panel: A zoom in of the three TF response curves in order to show more detail. This panel shows also the approximate area wavelength range where protocluster galaxies are expected to lie. Also shown in grey in both panels is the night-sky emission line spectrum (Hanuschik 2003). The minimum wavelength reached at the edge of the field in TF1 is denoted by the vertical dotted line.

latter is done using sky flats. To remove further large scale gradients a superflat is made from the unregistered science images. This superflat is smoothed and the science frames are subsequently divided by the superflat. The flat science images are then registered with simple offsets in the  $x$  and  $y$  direction using the IRAF task XREGISTER and co-added together.

The reduction of the TF images follows the same general outline as that for the broadband images with two exceptions. The flat-fielding is done with dome flats and an additional step is included which involves the removal of sky rings. As the central wavelength of the TF filter varies across the field, skylines shift in and out of the filter bandpass causing a pattern of alternating bright and faint concentric rings superimposed on the image. These large scale gradients are of the order 3 to 9 times the rms noise in the individual images. The rings are removed by subtracting a smoothed superflat made using the unregistered science exposures. This superflat is created for each exposure individually as the sky level (and therefore the sky rings) varies between different nights and airmasses. The individual frames are subsequently registered and combined. Finally, all fully reduced science images are registered to the same pixel coordinates using the IRAF tasks GEOMAP and GEOREGISTER.

Due to the wavelength variation across the field and the dithering there is a variation in wavelength in each of the individual pixels. This variation is larger near the edge of the field of view. The wavelength assigned to each pixel in the final images is the mean of the wavelengths of the pixel in question in the individual images. This also implies that the effective FWHM of the TF increases when moving away from the optical centre. This effect is strongest in the right ascension direction because the dithering steps are larger in this direction, with a maximum increase of  $\sim 50$  per cent at the very edges of the images.

Flux calibration for both broad and narrowband imaging is achieved using stan-

standard star observations obtained at the end of each observing block of 1 hour. The standard stars used for the TF flux calibration have full SEDs available allowing flux calibration at the exact wavelength of each of the TF observations. A further independent check of the flux calibration of the TF observations is obtained using the broadband data. The  $r$  and  $i$  magnitudes of all objects in the science frames with  $19 < r < 23$  are measured. Then, assuming a power law spectral energy distribution, the magnitudes of these objects at the wavelength of interest are determined. The median zeropoints derived with this method deviate by -0.1, -0.04 and +0.005 magnitude with respect to the standard star zeropoints of TF1, TF2 and TF3. The larger deviation for TF1 and TF2 are likely due to the stronger presence of the  $H\alpha$  absorption line at 6563 Å.

The final reduced and coadded TF images show some artifacts of the reduction. The sky ring subtraction is not optimal due to the applied smoothing and therefore a residual ring pattern remains in the final images. Also the unique properties of the TF lead to pupil ghosts near bright stars. Point source ghosts, however, are not present in the final TF images. The dithering results in an offset in point source ghosts opposite to the actual offset. When combining the individual images the point source ghosts will therefore be removed.

## 5.2.2 Source detection and photometry

Object detection and photometry are done using SExtractor (Bertin & Arnouts 1996) in double image mode. We create three different catalogues based on each of the three TF tunings. A detection is defined as a minimum of 9 adjacent pixels that each exceed the  $2\sigma$  rms noise. Colours are measured using the  $2\sigma$  isophotal apertures as determined from the respective detection image whereas total magnitudes are measured using SExtractor's MAG\_AUTO apertures. Image depth and uncertainties on the photometry are determined using the method of Labbé et al. (2003).

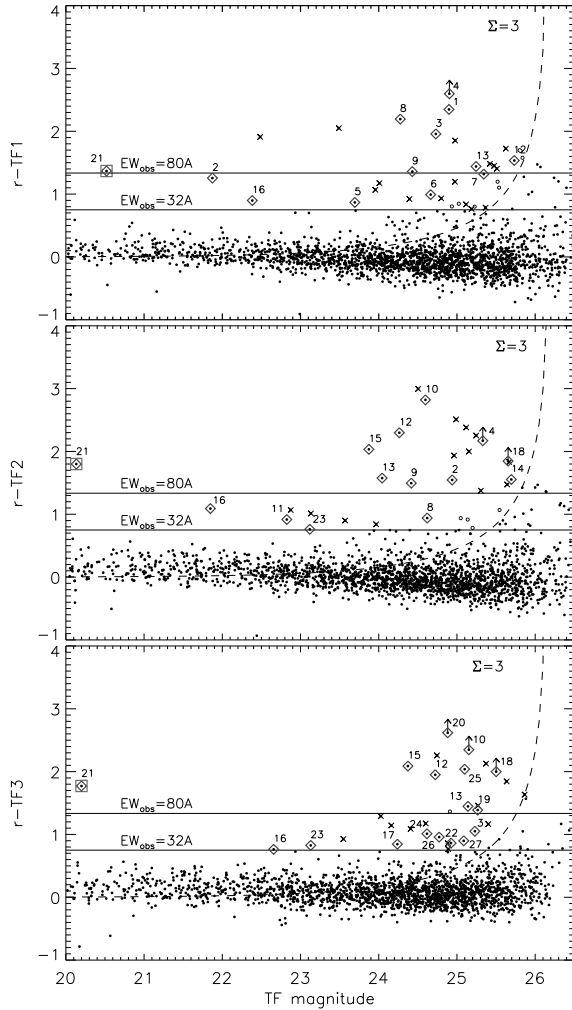
Completeness of the image is measured by adding point sources of a range of magnitudes to the respective images after which source extraction is repeated and the number of recovered objects is assessed. To avoid overcrowding the image we limit the number of added objects to 150 per magnitude. This process is repeated 10 times in order to obtain better statistics. We find that the data is 50 per cent complete for point sources down to  $r=26.0$ , TF1=25.1, TF2=25.1 and TF3=25.0 magnitudes.

## 5.3 Results

### 5.3.1 Selection of LAEs

For each of the three TF tunings a separate sample of Ly $\alpha$  emitters (hereafter LAEs) is selected. The criterium for identifying LAEs is based on the colour-magnitude diagrams of the 6C0140 field as shown in Fig. 5.2. The galaxies with line emission at the relevant redshift will show an excess of flux in the TF band

**Figure 5.2** – Colour-magnitude diagrams for each of the three TF tunings. The horizontal solid lines indicate  $EW_{\text{obs}}$  values of 32 and 80 Å respectively, whereas the dashed curve indicates the  $\Sigma = 3$  line. Objects identified as LAEs are denoted by diamonds and labeled with the respective ID numbers as listed in Table 5.2 and Table 5.3. The radio galaxy is denoted by the square symbol. The  $\Sigma = 3$  curve is calculated using a median aperture size. Individual objects may therefore be located inside the selection area as depicted here, but are still not identified as being a LAE. These objects are denoted by open circles. Spurious detections are indicated by crosses.



relative to the  $r$  band flux. Most objects do not have emission lines in the TF and thus have  $r - \text{TF} \sim 0$ . The rms scatter around  $r - \text{TF} \sim 0$  at  $\text{TF} \sim 24 - 25$  mag is  $\sim 0.15$ . For an object to be identified as LAE we require at least a  $5\sigma$  deviation from  $r - \text{TF} \sim 0$  and thus that  $r - \text{TF} > 0.75$ .

This excess flux relates to an observed line equivalent width using the relationship

$$EW_{\text{obs}} = \frac{\Delta\lambda_r \Delta\lambda_{\text{TF}} [1 - 10^{-0.4(r-\text{TF})}]}{[\Delta\lambda_r 10^{-0.4(r-\text{TF})} - \Delta\lambda_{\text{TF}}]} \quad (5.3)$$

from Bunker et al. (1995). Here  $\Delta\lambda$  is the FWHM of the filter in question and  $r$  and TF are the measured magnitudes in the broad- and narrowband respectively.

The restframe equivalent width  $EW_0$  is obtained by dividing by  $(1+z)$ . Note that this relation does not account for IGM absorption. For LAEs at  $z \sim 4.4$  this implies that  $EW_{\text{obs}}$  and  $EW_0$  are overestimated by a factor of  $\sim 1.5 - 2$ . We will return to this correction factor in Sect. 5.3.2.

Using Eq. 5.3, the colour cut corresponds to approximately  $EW_{\text{obs}} > 32 \text{ \AA}$  at the optical centre of the field. However, as described in Sect. 5.2.1, the dithering results in an effective broadening of the TF when moving away from the optical centre. At the West and East edges of the image the increase in effective FWHM is  $\sim 50$  per cent, thus the equivalent width cut varies approximately between  $EW_{\text{obs}} > 32 \text{ \AA}$  and  $EW_{\text{obs}} > 48 \text{ \AA}$  across the field.

The equivalent width cut used in this work is less stringent than the more commonly used  $EW_{\text{obs}} > 80 \text{ \AA}$ . This is because the TF is narrower than conventional narrowband filters, thus allowing for lower equivalent width objects to be included. We further require that the error parameter  $\Sigma > 3$ , i.e. the excess flux is at least three times larger than the combined noise of the measured broad- and narrowband fluxes. Finally, due to the artifacts present in the images we visually inspect all of the objects that satisfy the above criteria and discard any spurious detections.

As can be seen from Fig. 5.2, there is a significant number of objects located in the selection area that are not identified as being LAEs. Visual inspection shows that these objects are likely spurious detections because they are often found in the sky ring residuals, have unphysical shapes, coincide with the pupil ghosts or are located near bright stars and saturation spikes. These objects are therefore not included in the candidate LAE sample. Figure 5.3 shows the regions of the image where most of these spurious are located, i.e. the sky rings and the pupil ghosts. Also shown are the locations of bright stars and portions of the image that are affected by vignetting. The bright stars cover  $\sim 4$  per cent of the field and therefore do not influence any of the conclusions presented in this work.

Other objects in the selection area may actually have  $\Sigma < 3$ . Individual values of  $\Sigma$  depend on the aperture size for each object. The  $\Sigma = 3$  curves shown in Fig. 5.2, however, are calculated for a fixed aperture size that is taken to be the median aperture size of the LAEs. Thus individual objects inside the selection area may have  $\Sigma < 3$  or vice versa.

For the TF1 filter, which probes exclusively  $z < 4.407$ , we find a total of 13 candidate LAEs, including the radio galaxy which has  $EW_{\text{obs}} = 88.3 \text{ \AA}$ . This is smaller than expected as visual inspection of the TF1 image indicates that the radio galaxy does have a strong narrowband excess. However, the Ly $\alpha$  emission is extended and coincides with a  $z \sim 0.9$  foreground galaxy (Rawlings et al. 1996). This results in strong contamination of the  $r$  band flux and therefore the expected narrowband excess is significantly diminished. To alleviate this problem we use the  $r$  band to define the colour apertures for the radio galaxy. This results in  $EW_{\text{obs}} = 217 \text{ \AA}$  indicating that the presence of the foreground galaxy is indeed important.

**Table 5.2** – Coordinates and magnitudes of the detected LAEs. The table is divided in three sections. The objects in the first section are brightest in TF1 and so forth. <sup>a</sup>The radio galaxy. The  $r$  band was used as the detection image for this object.

ID	RA	Dec.	Detected in	$r$	TF1	TF2	TF3
#1	01:43:58.2	+32:49:49.8	TF1	$27.2 \pm 0.8$	$24.9 \pm 0.2$	$25.34 \pm 0.3$	$26.3 \pm 0.6$
#2	01:43:44.6	+32:49:42.6	TF1	$23.1 \pm 0.1$	$21.87 \pm 0.04$	$22.55 \pm 0.06$	$22.9 \pm 0.1$
#3	01:43:44.8	+32:57:06.0	TF1,TF2,TF3	$26.7 \pm 0.4$	$24.7 \pm 0.1$	$25.0 \pm 0.2$	$25.4 \pm 0.2$
#4	01:43:38.9	+32:53:37.2	TF1,TF2	$> 27.5$	$24.9 \pm 0.2$	$25.2 \pm 0.2$	$25.7 \pm 0.3$
#5	01:43:38.3	+32:49:58.3	TF1	$24.6 \pm 0.1$	$23.7 \pm 0.1$	$23.9 \pm 0.1$	$24.2 \pm 0.2$
#6	01:43:35.7	+32:54:36.0	TF1	$25.7 \pm 0.2$	$24.7 \pm 0.1$	$25.1 \pm 0.2$	$25.4 \pm 0.3$
#7	01:43:35.4	+32:52:11.5	TF1	$26.7 \pm 0.3$	$25.3 \pm 0.2$	$25.8 \pm 0.2$	$25.8 \pm 0.2$
#8	01:43:24.8	+32:54:09.5	TF1,TF2	$26.5 \pm 0.4$	$24.3 \pm 0.1$	$25.4 \pm 0.3$	$25.1 \pm 0.2$
#9	01:43:45.9	+32:53:58.0	TF1,TF2	$25.9 \pm 0.2$	$24.4 \pm 0.1$	$24.4 \pm 0.1$	$24.8 \pm 0.2$
#10	01:43:43.3	+32:52:08.1	TF2,TF3	$27.4 \pm 1.0$	$25.5 \pm 0.3$	$24.6 \pm 0.1$	$24.8 \pm 0.2$
#11	01:43:42.1	+32:55:27.6	TF2	$23.7 \pm 0.1$	$23.1 \pm 0.1$	$22.8 \pm 0.1$	$23.1 \pm 0.1$
#12	01:43:41.5	+32:54:17.2	TF1,TF2,TF3	$26.6 \pm 0.5$	$25.3 \pm 0.3$	$24.3 \pm 0.1$	$24.5 \pm 0.2$
#13	01:43:41.4	+32:53:49.3	TF1,TF2,TF3	$25.6 \pm 0.3$	$24.6 \pm 0.2$	$24.0 \pm 0.1$	$24.4 \pm 0.1$
#14	01:43:41.0	+32:53:48.5	TF2	$27.2 \pm 0.5$	$26.0 \pm 0.3$	$25.7 \pm 0.2$	$26.3 \pm 0.4$
#15	01:43:40.2	+32:55:02.5	TF2,TF3	$25.9 \pm 0.4$	$24.7 \pm 0.2$	$23.9 \pm 0.1$	$24.1 \pm 0.2$
#16	01:43:38.0	+32:49:51.9	TF1,TF2,TF3	$22.9 \pm 0.1$	$22.19 \pm 0.07$	$21.85 \pm 0.05$	$22.35 \pm 0.08$
#17	01:43:59.8	+32:52:16.2	TF3	$25.1 \pm 0.1$	$25.0 \pm 0.2$	$24.8 \pm 0.1$	$24.2 \pm 0.1$
#18	01:43:56.4	+32:54:41.1	TF2,TF3	$> 27.5$	$26.2 \pm 0.3$	$25.7 \pm 0.2$	$25.5 \pm 0.2$
#19	01:43:44.8	+32:56:01.9	TF3	$26.7 \pm 0.2$	$26.7 \pm 0.4$	$27.0 \pm 0.5$	$25.3 \pm 0.1$
#20	01:43:43.9	+32:52:28.6	TF3	$> 27.5$	$27.5 \pm 1.6$	$25.7 \pm 0.3$	$24.9 \pm 0.1$
#21 <sup>a</sup>	01:43:43.8	+32:53:49.9	TF1,TF2,TF3	$23.65 \pm 0.05$	$21.54 \pm 0.01$	$20.91 \pm 0.01$	$20.75 \pm 0.01$
#22	01:43:38.0	+32:52:00.9	TF3	$25.8 \pm 0.1$	$25.8 \pm 0.2$	$25.6 \pm 0.2$	$24.9 \pm 0.1$
#23	01:43:36.1	+32:55:00.9	TF2,TF3	$24.0 \pm 0.1$	$23.8 \pm 0.1$	$23.17 \pm 0.05$	$23.13 \pm 0.05$
#24	01:43:33.3	+32:54:09.0	TF3	$25.6 \pm 0.2$	$26.1 \pm 0.5$	$25.2 \pm 0.2$	$24.6 \pm 0.1$
#25	01:43:27.3	+32:51:32.4	TF3	$27.1 \pm 0.5$	$27.5 \pm 1.4$	$25.7 \pm 0.3$	$25.1 \pm 0.2$
#26	01:43:26.6	+32:52:17.3	TF3	$25.7 \pm 0.2$	$27.1 \pm 0.9$	$25.5 \pm 0.2$	$24.8 \pm 0.1$
#27	01:43:25.9	+32:52:01.8	TF3	$26.0 \pm 0.2$	$26.4 \pm 0.6$	$25.9 \pm 0.3$	$25.1 \pm 0.2$



**Figure 5.3** – A mask of the 6C0140 field showing the location of regions with large numbers of spurious detections and regions where source detection is impeded. The large grey and black rings are the approximate locations of the sky rings in TF1 and TF3, respectively. For TF2 the sky rings fall in between the two sets shown here. The small black arcs denote the locations of the pupil ghosts, whereas the filled circles denote the location of bright stars. The two light grey regions at the left side of the image are affected by vignetting and therefore not considered.

The TF2 band at  $6575 \text{ \AA}$  reveals a total of 14 candidate LAEs, including the radio galaxy with  $EW_{\text{obs}} = 470 \text{ \AA}$ . Eight of the LAEs have been identified in TF1 as well.

Finally, a total of 17 objects are identified as being candidate LAEs in the TF3 band at  $6585 \text{ \AA}$ . Again, the radio galaxy has been included and its equivalent width is highest in TF3 with  $EW_{\text{obs}} = 578 \text{ \AA}$ . Out of the remaining galaxies eight have not been detected in TF1 or TF2, thus yielding a total number of 27 unique LAEs (including the radio galaxy) in the field of 6C0140. The properties of the emitters are listed in Table 5.2 and Table 5.3.

### 5.3.2 Redshift distribution

Having the multiple tunings of the TF means the redshift of the LAEs can be constrained to a greater accuracy than with a single narrowband image. This allows us to investigate the approximate redshift distribution of the candidate LAEs in the field.

In order to obtain the best possible estimated redshifts we model what the effect is of a variety of weighting schemes. We model a simple flat spectrum ( $\beta = -2$ ) with an emission line with restframe FWHM of  $250 \text{ km s}^{-1}$  or  $500 \text{ km s}^{-1}$  at certain wavelengths in the range  $6555 < \lambda < 6595 \text{ \AA}$ . These values for the FWHM are consistent with the values found for 80 to 90 per cent of LAEs around HzRGs (Venemans et al. 2005, 2007). Absorption by the IGM is taken into account using the Madau (1995) recipe. The modeled spectra are then convolved with the TF response curve as given in Eq. 5.2 with  $\lambda_c = 6565, 6575$  and  $6585 \text{ \AA}$ . Using the

fluxes in each of the TF tunings we then derive estimates for the wavelength of the emission line.

The results of this process are shown in Fig. 5.4. We show two different weighting schemes which can be given in general form as

$$\lambda_{\text{eff}} = \frac{\sum_{i=1,3} w_i F_i \lambda_i}{\sum_{i=1,3} w_i F_i}. \quad (5.4)$$

Here  $i$  is TF1, TF2 or TF3 respectively,  $F_i$  is the flux in the respective bands,  $\lambda_i$  is the central wavelength of the tuning in question at the relevant location in the field and  $w_i$  is a weighting factor. The black data points represent the case of  $w_i = 1$  for all bands and the red data points denote the results obtained for

$$w_i = 2^{F_i / \min(F_{\text{TF1}}, F_{\text{TF2}}, F_{\text{TF3}})}. \quad (5.5)$$

As noted above, the results shown in Fig. 5.4 are obtained when using the central wavelength values of the optical centre, i.e.  $\lambda_{\text{TF1}} = 6565 \text{ \AA}$ ,  $\lambda_{\text{TF2}} = 6575 \text{ \AA}$  and  $\lambda_{\text{TF3}} = 6585 \text{ \AA}$ . However, the wavelength shift acts on each tuning identically and thus the qualitative behaviour shown in Fig. 5.4 is valid for the entire field, irrespective of wavelength shift.

We see that the more involved weighting scheme yields better results for almost all redshifts. However, for both weighting schemes the largest discrepancy between the input and output redshifts is at either end of the investigated redshift range. This is to be expected, because no data is available to bracket the existing tunings, hence skewing the output redshift towards a central value. The more elaborate weighting scheme alleviates this slightly, but does not yield full agreement. Figure 5.4 also shows that the results of the two weightings schemes are fairly robust with respect to the choice of restframe FWHM.

The redshifts obtained when using the weights as described in Eq. 5.5 are listed in Table 5.3. Uncertainties have been calculated by varying the measured fluxes according to their respective uncertainties and recalculating  $\lambda_{\text{eff}}$ . An additional systematic uncertainty was added in quadrature to take into account the limitations of the weighting scheme. This systematic uncertainty is based on the bands in which the object is detected and the offset from the input redshift implied by this as measured from Fig. 5.4. Finally, to account for the variation in wavelength in each pixel we add an additional location-dependent uncertainty in quadrature.

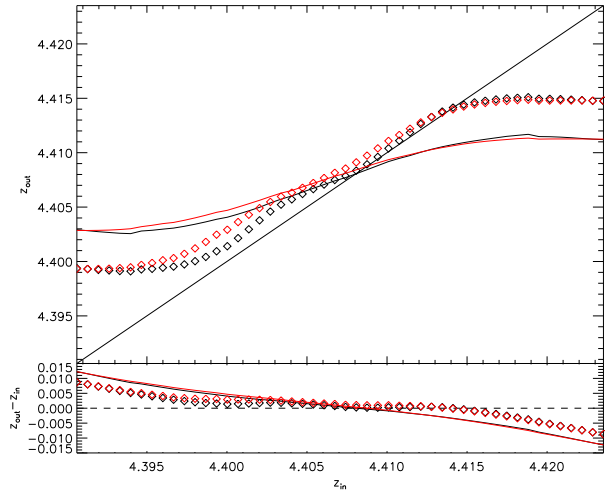
None of the LAEs are located at larger redshifts than that of the radio galaxy. This is a selection effect as the highest value of  $\lambda_c$  is  $6585 \text{ \AA}$  whereas the Ly $\alpha$  line for  $z_{\text{RG}} = 4.413$  falls at  $\sim 6580 \text{ \AA}$ . Combined with the wavelength shift towards shorter wavelengths across the field this means that the observations are biased towards redshifts lower than the redshift of the radio galaxy. Also, note that the estimated redshift of the radio galaxy is only marginally inconsistent with the spectroscopic redshift of  $z = 4.413$ . The slight underestimate with respect to the spectroscopic redshift is possibly due to the fact that we modeled the Ly $\alpha$  line with a maximum FWHM of  $500 \text{ km s}^{-1}$ , whereas the line is observed to have a FWHM

**Table 5.3** – Properties of the detected LAEs. <sup>a</sup> $EW_{\text{obs}}$  calculated using Eq. 5.3, whereas  $EW_0$  is calculated using the method of Venemans et al. (2005). <sup>b</sup> $EW_{\text{obs}}$ ,  $EW_0$ ,  $\Sigma$  and  $F_{\text{Ly}\alpha}$  for the radio galaxy are calculated on the basis of TF3. The horizontal dividers are as in Table 5.2.

ID	$EW_{\text{obs}}/EW_0$ (Å) <sup>a</sup>	$\Sigma$	$F_{\text{Ly}\alpha}$ (erg s <sup>-1</sup> cm <sup>-2</sup> )	$z_{\text{eff}}$
#1	411/36.2	5.2	$1.4 \times 10^{-17}$	$4.310^{+0.005}_{-0.009}$
#2	84.5/9.1	17.9	$9.0 \times 10^{-17}$	$4.337^{+0.002}_{-0.008}$
#3	209/24.7	6.8	$1.7 \times 10^{-17}$	$4.352^{+0.003}_{-0.007}$
#4	> 463/ > 49.8	6.2	$1.7 \times 10^{-17}$	$4.394^{+0.007}_{-0.006}$
#5	47.6/8.0	5.0	$2.3 \times 10^{-17}$	$4.340^{+0.004}_{-0.009}$
#6	60.3/6.5	4.8	$1.5 \times 10^{-17}$	$4.380^{+0.005}_{-0.008}$
#7	96.9/13.0	4.7	$1.8 \times 10^{-17}$	$4.377^{+0.005}_{-0.009}$
#8	266/29.6	8.9	$2.2 \times 10^{-17}$	$4.327^{+0.002}_{-0.008}$
#9	106/11.7	6.7	$1.9 \times 10^{-17}$	$4.404^{+0.002}_{-0.004}$
#10	552/61.5	6.9	$1.5 \times 10^{-17}$	$4.399^{+0.004}_{-0.002}$
#11	47.5/5.0	10.3	$3.7 \times 10^{-17}$	$4.391^{+0.001}_{-0.002}$
#12	299/31.0	7.4	$2.5 \times 10^{-17}$	$4.404^{+0.004}_{-0.002}$
#13	122/12.9	7.2	$3.7 \times 10^{-17}$	$4.404^{+0.002}_{-0.002}$
#14	120/12.4	3.5	$7.0 \times 10^{-18}$	$4.403^{+0.003}_{-0.006}$
#15	225/23.5	7.8	$4.3 \times 10^{-17}$	$4.395^{+0.003}_{-0.002}$
#16	68.8/7.1	12.3	$1.1 \times 10^{-16}$	$4.340^{+0.003}_{-0.003}$
#17	52.0/4.5	5.8	$1.1 \times 10^{-17}$	$4.368^{+0.009}_{-0.005}$
#18	> 247/ > 25.9	5.0	$1.1 \times 10^{-17}$	$4.385^{+0.006}_{-0.006}$
#19	96.8/10.0	6.0	$5.5 \times 10^{-18}$	$4.387^{+0.009}_{-0.004}$
#20	> 434/ > 45.0	6.4	$1.9 \times 10^{-17}$	$4.409^{+0.008}_{-0.001}$
#21 <sup>b</sup>	578/75.0	95.5	$3.6 \times 10^{-15}$	$4.412^{+0.001}_{-0.001}$
#22	47.3/4.5	5.0	$6.9 \times 10^{-18}$	$4.394^{+0.008}_{-0.003}$
#23	45.6/4.6	8.7	$2.8 \times 10^{-17}$	$4.388^{+0.003}_{-0.003}$
#24	65.5/5.9	4.8	$1.6 \times 10^{-17}$	$4.388^{+0.008}_{-0.004}$
#25	300/24.3	5.2	$1.8 \times 10^{-17}$	$4.339^{+0.009}_{-0.005}$
#26	68.2/5.8	5.3	$9.6 \times 10^{-18}$	$4.344^{+0.009}_{-0.006}$
#27	57.8/5.3	3.2	$1.0 \times 10^{-17}$	$4.339^{+0.009}_{-0.005}$



**Figure 5.4** – Upper panel: Output versus input redshift when using the two different weighting schemes tested on modeled Ly $\alpha$  spectral lines. The solid curves indicate the results obtained when using  $w_i = 1$ , whereas the diamonds denote the results obtained with the weights described as in Eq. 5.5. Black and red indicate restframe FWHM of 250 km s $^{-1}$  and 500 km s $^{-1}$ , respectively. Lower panel: Difference between the output and input redshifts.



of  $\sim 1500$  km s $^{-1}$  (Rawlings et al. 1996; De Breuck et al. 2001). A larger line width will introduce stronger systematic uncertainties that have not been taken into account in the case of the estimated redshift of the radio galaxy. This may therefore account for the discrepancy.

The redshift estimates can be used to correct the equivalent width values for IGM absorption. As discussed in Sect. 5.3.1, Eq. 5.3 does not take this into account and underestimates the  $r$  continuum flux density. Therefore  $EW_{\text{obs}}$  and  $EW_0$  are overestimated. The corrections are calculated following the method of Venemans et al. (2005). The resulting corrected restframe equivalent widths and corresponding Ly $\alpha$  fluxes are listed in Table 5.3. The difference between  $EW_{\text{obs}}$  and  $EW_0$  is typically a factor  $\sim 10$ . This is consistent with a factor  $(1+z)$  in combination with a factor  $\sim 1.7$ . Here the latter factor originates from the fact that a larger portion of the  $r$  band flux is absorbed by the IGM compared to the TF flux. The exact factor varies between  $\sim 1 - 2$  and depends on the location of the line within the filters and therefore both the redshift of the object and its position in the field.

### 5.3.3 Contamination

One of the larger caveats of using narrowband imaging to select high- $z$  emission line galaxies is that the final sample may be contaminated by low- $z$  interlopers that have a strong emission line falling in the narrowband. For our study the most likely interlopers are [OII] emitters at  $z \sim 0.76$  or [OIII] emitters at  $z \sim 0.3$ . Spectroscopic follow-up is needed to accurately determine the success rate of the sample presented in this work. However, based on previous spectroscopic studies of  $z \sim 4$  narrowband surveys the expected number of interlopers in our sample can be estimated and it can be determined whether the results presented here are robust when this is taken into account.

We base our estimate of the success rate on the studies of HzRG TN J1338-1942 (hereafter 1338) by Venemans et al. (2002, 2007), the field study at  $z \sim 4.5$  by Dawson et al. (2007) and the study of the LAEs around  $z \sim 5.2$  HzRG TN J0924-2201 by Venemans et al. (2004). The success rates in each of these works are fairly similar to each other, ranging from  $\sim 75$  per cent to  $\sim 95$  per cent depending on whether non-detections are counted as non-confirmations. To investigate the ‘worst case scenario’ we use for our sample the minimum success rate of 75 per cent.

## 5.4 Does 6C0140+326 reside in a protocluster?

Based on our sample of LAEs we determine whether there is an overdensity around 6C0140. Due to the wavelength shift across the field, part of the observed field can act as a control field.

In Fig. 5.5 the spatial distribution of the LAEs is shown. Also shown are two concentric circles indicating the boundaries of two fields: the inner circle of  $\sim 12.5$  arcmin<sup>2</sup> and the annulus of  $\sim 16.3$  arcmin<sup>2</sup>, respectively. The central field covers the redshifts closest to the radio galaxy and can therefore be considered a possible protocluster field. The annulus outside this field delimited by the dashed circle probes lower redshifts and is considered to be field environment. To make the distinction between protocluster and foreground stronger we will only consider TF2 and TF3 detected objects (diamonds and asterisks) in the central field, whereas in the annulus only TF1 detected objects are considered (squares). This selection effectively means we are limited to  $z > 4.38$  in the central field and  $z < 4.38$  in the annulus. Furthermore, the width of the TF does not change significantly across the central field and the annulus. Since we only consider TF1 in the annulus, the physical depth of the annulus is thus  $\sim 1.3$  times smaller. We thus require the area of the annulus to be larger by the same factor to have the same volume in each of the fields. We find 9 objects (excluding the radio galaxy) in the possible protocluster field versus 2 in the foreground field. This thus indicates that there is a concentration of LAEs near to the radio galaxy.

It is striking that almost all of the objects within the protocluster field are located west of the radio galaxy in a North-South filamentary structure. We test whether the spatial distribution is consistent with a random distribution by applying a two dimensional Kolmogorov-Smirnov test. There is a probability of 0.01 that the distribution as shown in Fig. 5.5 is drawn from a random distribution. The distribution is thus different from random at the  $\sim 2.5\sigma$  level. This further indicates that the LAEs are clustered.

Since our control field is not very large, it is susceptible to cosmic variance. To better quantify the overdensity of LAEs around the radio galaxy, we also compare it to the blank field LAEs observed by Dawson et al. (2007). Dawson et al. (2007) presented a differential Ly $\alpha$  luminosity function for field LAEs with  $EW_{\text{obs}} > 80$  Å at  $z \sim 4.5$ . Fitting a Schechter function to the luminosity function using a fixed value of  $\alpha = -1.6$  they find  $\Phi^* = (1.7 \pm 0.2) \times 10^{-4}$  Mpc<sup>-3</sup> and  $L^* = (10.9 \pm 3.3) \times 10^{42}$  erg s<sup>-1</sup>.

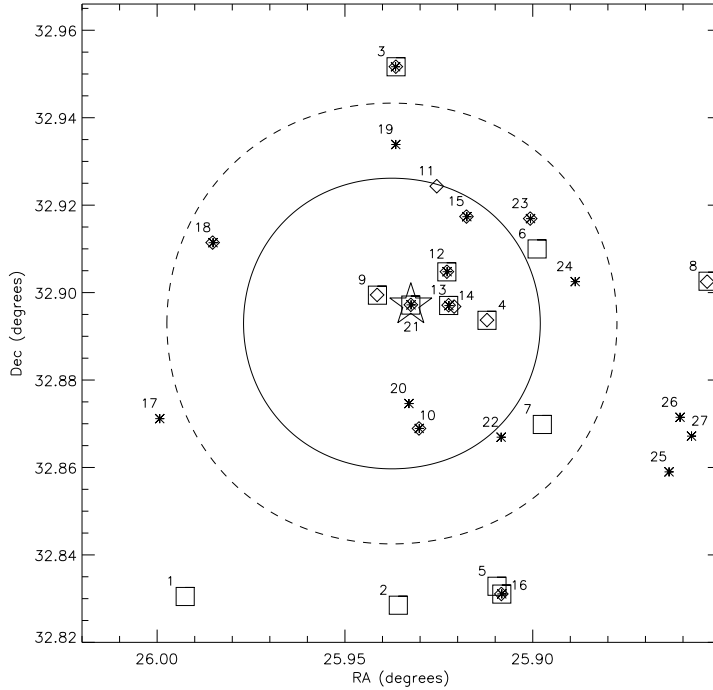


**Figure 5.5** – The spatial distribution of the LAEs. Objects detected in TF1, TF2 and TF3 are marked by squares, diamonds and asterisks respectively. Each object is also marked by its ID number. The location of the radio galaxy is marked by a star. Also shown are two circles denoting the border of a protocluster field (within the full circle) and a foreground field (between dashed and full circle).

For the 6C0140 field, if we take into account the overlap between the different tunings, the total ‘unique’ volume probed by the protocluster field is  $1570 \text{ Mpc}^3$ . Using the same selection procedure as in Dawson et al. (2007), we find eight emitters (excluding the radio galaxy) in the central field. We calculate the expected number of LAEs in the same field (assuming it is a blank field) using the field luminosity function. The expected number of LAEs is found to be  $0.9^{+0.4}_{-0.3}$ , with the uncertainty derived from the uncertainties on  $\Phi^*$  and  $L^*$ . Here we use the Ly $\alpha$  flux of the faintest emitter with  $EW_{\text{obs}} > 80 \text{ \AA}$  (#14) in the protocluster field as lower limit ( $7.0 \times 10^{-18} \text{ erg s}^{-1} \text{ cm}^{-2}$ , this equals  $L = 1.4 \times 10^{42} \text{ erg s}^{-1}$  for the cosmology used by Dawson et al. 2007). We therefore find that the 6C0140 field is denser than a blank field by a factor  $9 \pm 5$ , where the uncertainty is based on Poisson statistics and the uncertainty on the expected number. Defining galaxy overdensity as  $\delta_g = n_{\text{cluster}}/n_{\text{field}} - 1$ , we thus find a galaxy overdensity of  $8 \pm 5$ .

Using the overdensity in 6C0140 protocluster field we can make a rough estimate of the mass contained in this central field. As in Venemans et al. (2005) we use the

relation

$$M = \bar{\rho}V \left( 1 + \frac{\delta_g}{b} \right) \quad (5.6)$$

with  $\bar{\rho}$  the mean density of the Universe,  $V$  the comoving volume considered and  $b$  the bias parameter which relates the galaxy overdensity to the matter overdensity. Following Steidel et al. (1998) and Shimasaku et al. (2003) we use  $b = 3 - 6$ . Using  $\bar{\rho} = 3.5 \times 10^{10} \text{ M}_\odot \text{ Mpc}^{-3}$  and  $V = 1570 \text{ Mpc}^3$  a mass of  $0.8 - 2.9 \times 10^{14} \text{ M}_\odot$  is found. This is a strict lower limit to the mass of the entire overdensity because the true extent of the protocluster is likely larger than what is indicated by the central protocluster field.

We also determine whether the number density and redshift distribution of LAEs in the 6C0140 field are consistent with that of a  $z \sim 4$  protocluster. However, the number of known protoclusters above  $z = 4$  is limited. One of the few spectroscopically confirmed cases is the protocluster around 1338 at  $z \sim 4.1$ . Venemans et al. (2002) and Venemans et al. (2007) have shown that the field around the radio galaxy is denser in LAEs than a blank field by a factor of  $4.8_{-0.8}^{+1.1}$ . Also, Overzier et al. (2006) provided evidence for a relatively large number of Lyman Break Galaxies (LBGs) in this field.

Venemans et al. (2007) found a total of 54 LAEs with  $EW_0 > 15 \text{ \AA}$  in a field of  $79.7 \text{ arcmin}^2$  around 1338. The narrowband filter used was a custom filter with  $\lambda_c = 6199 \text{ \AA}$  and a FWHM of  $59 \text{ \AA}$  (hereafter NB620 for brevity), i.e. approximately twice as wide as the TF tunings used in this study. This difference in width implies that the same emission line, at the respective proper redshifts, will yield a brighter magnitude in the TF. Applying the 50 per cent magnitude limits to the 1338 catalogue will therefore not yield a proper comparison. The recovered Ly $\alpha$  flux is, however, relatively independent of filter width. We therefore use a cut of  $F_{\text{Ly}\alpha} > 7.0 \times 10^{-18} \text{ erg s}^{-1} \text{ cm}^{-2}$ . At  $z \sim 4.1$  the width of NB620 implies a comoving volume of  $12292 \text{ Mpc}^3$ . Applying the  $F_{\text{Ly}\alpha}$  cut the density of LAEs in the 1338 field is found to be  $3.6 \times 10^{-3} \text{ Mpc}^{-3}$ .

Applying the Venemans et al. (2007) selection criteria and excluding the radio galaxy, we find a total of 5 unique LAEs with  $EW_0 > 15 \text{ \AA}$  in the central protocluster field. With a volume of  $1570 \text{ Mpc}^3$  the density of candidate LAEs is thus  $(3.2 \pm 1.4) \times 10^{-3} \text{ Mpc}^{-3}$  where we used Poisson statistics for the  $1\sigma$  uncertainty. Thus the number density of LAEs around 6C0140 is comparable to that in the 1338 protocluster.

The velocity distribution of the spectroscopically confirmed 1338 LAEs have a FWHM of  $625 \pm 150 \text{ km s}^{-1}$ . This is very narrow with respect to local galaxy clusters, but it is in agreement with the trend of decreasing velocity dispersion with increasing redshift (Venemans et al. 2007).

The estimated redshifts of the candidate LAEs are compared to the expected redshift range of the protocluster in the lower panel of Fig. 5.6. Note that the location of the protocluster region does not coincide with the redshift of the radio galaxy. Instead we have chosen the redshift of the protocluster such that the

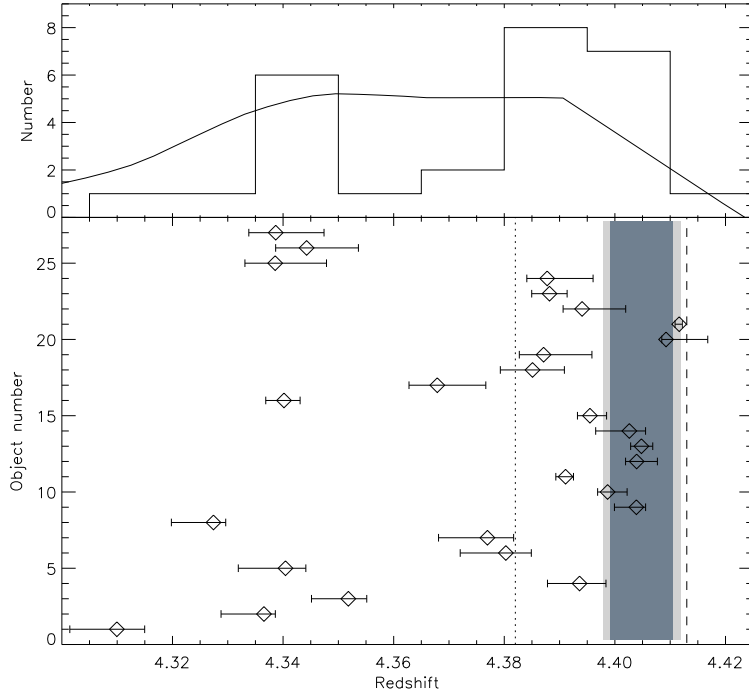


**Figure 5.6** – Lower panel: the estimated redshifts of the individual objects with their respective uncertainties. The dark shaded region represents the redshift interval the protocluster would have based on the 1338 velocity distribution, whereas the light shaded region takes into account the  $1\sigma$  uncertainty. The protocluster region is chosen such as to maximise the number of protocluster candidates. The spectroscopic redshift of the radio galaxy ( $z = 4.413$ ) is marked by the vertical dashed line. The dotted line at  $z \sim 4.38$  indicates the approximate redshift limit set by the edge of the circular protocluster field as shown in Fig. 5.5. Upper panel: distribution of the estimated redshifts. Also shown is a curve that indicates how the effective selection area varies as function of redshift.

number of LAEs consistent with being in the protocluster is maximised. This results in an offset with respect to the radio galaxy of  $\Delta z = 0.0084$  or  $\Delta v \sim 465 \text{ km s}^{-1}$ . This is consistent with what is observed in the 1338 protocluster where the 1338 radio galaxy is redshifted by  $440 \text{ km s}^{-1}$  ( $\Delta z = 0.0075$ ) with respect to the majority of the confirmed line emitters. Thus the radio galaxy does not have to be at the centre of the structure in redshift space. In the situation as shown in Fig. 5.6 a total of 10 LAEs are consistent with being in the protocluster. This number decreases to 4 when we assume that the protocluster is centred on the radio galaxy. Note that a similar displacement of the radio galaxy with respect to the bulk of the galaxies is seen for the spatial distribution of both the 6C0140 and 1338 fields. Both radio galaxies are located not at the centre of the spatial distribution of emitters, but more at the edge.

Also shown in the upper panel of Fig. 5.6 is the distribution of the estimated redshifts and a curve that indicates how the effective selection area varies as function of redshift. The area was estimated by determining the portion of the image for which  $\lambda_{\text{low}} < \lambda < \lambda_{\text{high}}$  with  $\lambda_{\text{low}}$  and  $\lambda_{\text{high}}$  being respectively the lower edge of the TF1 tuning and the upper edge of the TF3 tuning. The curve indicates that, based on the effective selection area, we would expect the majority of the objects to have  $4.35 < z < 4.39$ . However, we find a disproportionately large number of objects at  $z > 4.38$  indicating that there is some concentration of LAEs close to the redshift of the radio galaxy. Applying a Kolmogorov-Smirnov test we determine that there is a probability of  $4 \times 10^{-3}$  that the observed distribution is drawn from the expected distribution. The two distributions therefore differ at the  $\sim 3\sigma$  level.

The top panel of Fig. 5.6 also shows that we are unable to observe objects that are located at  $z > 4.42$ . This makes the reported overdensity of  $8 \pm 5$  difficult to interpret. It may be that the protocluster structure extends beyond  $z > 4.42$ . If this is the case, then the true overdensity may differ from the value presented here. Likewise, if the distribution of  $\lambda_c$  of the TFs had been chosen to probe larger redshift values, then such a blueshifted overdensity as found for 6C0140 may be underestimated or even missed altogether.

How do our results hold up when we account for the estimated contamination fraction discussed in Sect. 5.3.3? In both the comparison with a blank field and the comparison with a  $z \sim 4.1$  protocluster we found 8 emitters in the 6C0140 field. Based on the minimum success rate of 75 per cent we therefore expect two interlopers in our ‘protocluster’ sample. Redoing the comparison with a sample of six emitters the following results are obtained. In the comparison with the blank field of Dawson et al. (2007) it is found that the 6C0140 field is denser by a factor of  $7 \pm 4$ . Thus the 6C0140 field harbours an overdensity of  $\delta_g = 6 \pm 4$ . The corrected number density in the 6C0140 field is  $(2.5 \pm 1.3) \times 10^{-3} \text{ Mpc}^{-3}$ , which is also still in agreement with the 1338 field. The results presented here are therefore valid when contamination is taken into account and we conclude that the 6C0140 field is similarly overdense as the 1338 protocluster. This indicates that it may evolve into a massive galaxy cluster at  $z = 0$ . Furthermore, this result supports the hypothesis that HzRGs are good tracers for galaxy overdensities in the early Universe.

## 5.5 Conclusions & outlook

We have presented the first search for high- $z$  protoclusters employing tunable narrowband filters. This pilot study focuses on the radio galaxy 6C0140+326 at  $z \sim 4.4$ . Using a combination of three TF tunings we find a total of 27 unique LAEs in the field around 6C0140+326. Division of the field in a protocluster and a foreground field shows that the protocluster field contains significantly more objects than the foreground field. This indicates that there is a concentration of LAEs near the redshift of the radio galaxy.

A comparison to a blank field shows that the 6C0140 protocluster field contains an overdensity of  $8 \pm 5$ . The number density in the protocluster field is also com-

parable to that found in the 1338 protocluster at  $z \sim 4.1$ . Both these results are robust when taking into account the possible presence of interlopers.

With the availability of three separate TF tunings we also estimate the redshift distribution of the LAEs. Using results obtained for the 1338 protocluster we find that 4-10 of the LAEs have redshifts consistent with being in a redshift interval spanned by a typical  $z \sim 4$  protocluster. Also, the redshift distribution is different at the  $3\sigma$  level from the expected distribution with a relatively large number of objects at  $z > 4.38$ . This further strengthens the notion that there is a concentration of LAEs near the radio galaxy.

These results are further evidence that HzRGs pinpoint high density regions in the early Universe. The overdensity around 6C0140 may collapse at a later time to form a structure similar to a local galaxy group or cluster. Spectroscopic follow-up is needed to confirm this result.

We have shown that tunable filters are an excellent method of confirming the presence of protoclusters around HzRGs at any redshift. At the moment the wavelength range accessible to the red TF used in this study is limited to  $\lambda > 6500 \text{ \AA}$  and therefore  $z > 4.3$ . However, a blue TF covering the wavelength range  $\lambda < 6500 \text{ \AA}$  will be commissioned in the near future. This will open up the redshift range  $2 < z < 4$  which is where most of the known HzRGs are located. Our allocated GTC ESO large programme can then significantly expand the sample of protoclusters across cosmic time and this would allow an in-depth study of the evolution of these structures.

## Acknowledgements

The authors would like to thank the anonymous referee for the useful comments that have helped in improving this paper. This work is based on observations made with the Gran Telescopio Canarias, installed in the Spanish Observatorio del Roque de los Muchachos of the Instituto de Astrofísica de Canarias, in the island of La Palma. This work was partially supported by the Spanish Plan Nacional de Astronomía y Astrofísica under grant AYA2008-06311-C02-01. EK acknowledges funding from Netherlands Organization for Scientific Research (NWO). NAH acknowledges support from STFC and the University of Nottingham Anne McLaren Fellowship. JK thanks the DFG for support via German-Israeli Project Cooperation grant STE1869/1-1.GE625/15-1.

## References

- Andreon S., Huertas-Company M., 2011, *A&A*, 526, A11+
- Baker J. C., Hunstead R. W., Bremer M. N., Bland-Hawthorn J., Athreya R. M., Barr J., 2001, *AJ*, 121, 1821
- Barr J. M., Baker J. C., Bremer M. N., Hunstead R. W., Bland-Hawthorn J., 2004, *AJ*, 128, 2660
- Bertin E., Arnouts S., 1996, *A&AS*, 117, 393
- Bielby R. M. et al., 2010, *A&A*, 523, A66+
- Bland-Hawthorn J., 1995, in *Astronomical Society of the Pacific Conference Series*, Vol. 71, IAU Colloq. 149: Tridimensional Optical Spectroscopic Methods in Astrophysics, G. Comte & M. Marcelin, ed., pp. 72–+
- Brodwin M. et al., 2010, *ApJ*, 721, 90
- Bunker A. J., Warren S. J., Hewett P. C., Clements D. L., 1995, *MNRAS*, 273, 513
- Carilli C. L., Harris D. E., Pentericci L., Röttgering H. J. A., Miley G. K., Kurk J. D., van Breugel W., 2002, *ApJ*, 567, 781
- Cepa J. et al., 2000, in Presented at the Society of Photo-Optical Instrumentation Engineers (SPIE) Conference, Vol. 4008, Society of Photo-Optical Instrumentation Engineers (SPIE) Conference Series, M. Iye & A. F. Moorwood, ed., pp. 623–631
- Cepa J. et al., 2003, in Presented at the Society of Photo-Optical Instrumentation Engineers (SPIE) Conference, Vol. 4841, Society of Photo-Optical Instrumentation Engineers (SPIE) Conference Series, M. Iye & A. F. M. Moorwood, ed., pp. 1739–1749
- Dawson S., Rhoads J. E., Malhotra S., Stern D., Wang J., Dey A., Spinrad H., Jannuzi B. T., 2007, *ApJ*, 671, 1227
- De Breuck C. et al., 2001, *AJ*, 121, 1241
- Galametz A. et al., 2010, *A&A*, 522, A58+
- Gobat R. et al., 2011, *A&A*, 526, A133+
- Hanuschik R. W., 2003, *A&A*, 407, 1157
- Hatch N. A. et al., 2011, *MNRAS*, 410, 1537
- Henry J. P. et al., 2010, *ApJ*, 725, 615
- Jones D. H., Shopbell P. L., Bland-Hawthorn J., 2002, *MNRAS*, 329, 759
- Knopp G. P., Chambers K. C., 1997, *ApJS*, 109, 367
- Kuiper E. et al., 2010, *MNRAS*, 405, 969
- Kurk J. D., Pentericci L., Overzier R. A., Röttgering H. J. A., Miley G. K., 2004a, *A&A*, 428, 817
- Kurk J. D., Pentericci L., Röttgering H. J. A., Miley G. K., 2004b, *A&A*, 428, 793
- Labbé I. et al., 2003, *AJ*, 125, 1107
- Madau P., 1995, *ApJ*, 441, 18
- Miley G., De Breuck C., 2008, *A&A Rev*, 15, 67
- Mullis C. R., Rosati P., Lamer G., Böhringer H., Schwobe A., Schuecker P., Fassbender R., 2005, *ApJ*, 623, L85
- Muzzin A. et al., 2009, *ApJ*, 698, 1934
- Overzier R. A. et al., 2008, *ApJ*, 673, 143
- Overzier R. A., Harris D. E., Carilli C. L., Pentericci L., Röttgering H. J. A., Miley G. K., 2005, *A&A*, 433, 87
- Overzier R. A. et al., 2006, *ApJ*, 637, 58
- Papovich C. et al., 2010, *ApJ*, 716, 1503



- Pascarelle S. M., Windhorst R. A., Driver S. P., Ostrander E. J., Keel W. C., 1996, *ApJ*, 456, L21+
- Pentericci L. et al., 2000, *A&A*, 361, L25
- Rawlings S., Lacy M., Blundell K. M., Eales S. A., Bunker A. J., Garrington S. T., 1996, *Nature*, 383, 502
- Rocca-Volmerange B., Le Borgne D., De Breuck C., Fioc M., Moy E., 2004, *A&A*, 415, 931
- Rosati P., Stanford S. A., Eisenhardt P. R., Elston R., Spinrad H., Stern D., Dey A., 1999, *AJ*, 118, 76
- Rosati P. et al., 2004, *AJ*, 127, 230
- Seymour N. et al., 2007, *ApJS*, 171, 353
- Shimasaku K., et al., 2003, *ApJ*, 586, L111
- Stanford S. A., Elston R., Eisenhardt P. R., Spinrad H., Stern D., Dey A., 1997, *AJ*, 114, 2232
- Stanford S. A. et al., 2006, *ApJ*, 646, L13
- Steidel C. C., Adelberger K. L., Dickinson M., Giavalisco M., Pettini M., Kellogg M., 1998, *ApJ*, 492, 428
- Tanaka M., Finoguenov A., Ueda Y., 2010, *ApJ*, 716, L152
- Venemans B. P. et al., 2002, *ApJ*, 569, L11
- Venemans B. P. et al., 2005, *A&A*, 431, 793
- Venemans B. P. et al., 2007, *A&A*, 461, 823
- Venemans B. P. et al., 2004, *A&A*, 424, L17
- Wilson G. et al., 2008, in *Astronomical Society of the Pacific Conference Series*, Vol. 381, *Infrared Diagnostics of Galaxy Evolution*, R.-R. Chary, H. I. Teplitz, & K. Sheth, ed., pp. 210–+



---

# DISSECTING THE LIGHT FROM HIGH REDSHIFT RADIO GALAXIES

We present deep multicolour Hubble Space Telescope images of two powerful  $z \sim 2.5$  radio galaxies, MRC 0406-244 and TX 0828+193, that appear to be undergoing active galactic nucleus (AGN) feedback. These galaxies consist of several clumps and filaments that extend for tens of kpc along the radio jets. We decompose the emission into several components and find that the extended emission seems to result from scattered AGN light, nebular emission and possibly from ultraviolet light from young stars and is likely to last only as long as the lifetime of the radio source (10 Myr). In each case the red, and likely older, stellar population is concentrated in a single central region that is not elongated along the radio jet axis. The lack of a disturbed morphology in the red stellar population suggests that no major merger has taken place on the timescale of the young radio emission ( $\sim 10$  Myr). The galaxies have optical half-light radii of  $r_e \sim 2 - 3$  kpc and thus are similar in size to other massive high redshift galaxies. If the scattered AGN and nebular light are not removed from the rest-frame optical images, then the effective radii increase by 65%, and the radio galaxies appear larger than typical high redshift galaxies of similar mass. Therefore, beneath the illuminated extended material, these radio galaxies appear to have similar sizes and reside in similar environments as other massive high redshift galaxies.

N. A. Hatch, E. Kuiper, G. K. Miley, H. J. A. Röttgering, C. De Breuck, H. Ford,  
J. D. Kurk, R. A. Overzier, J. Schaye, B. P. Venemans, A. W. Zirm.  
To be submitted to the *Monthly Notices of the Royal Astronomical Society*.

## 6.1 Introduction

High redshift radio galaxies (HzRGs) are among the brightest known galaxies in the early Universe and are unique laboratories for studying massive galaxy formation. However, many of their properties appear to differ from other distant massive galaxies. HzRGs appear larger than passive or sub-millimetre galaxies at the same redshift (Targett et al. 2011). They comprise several clumps extending over tens of kpc in both the rest-frame ultraviolet (UV) and optical (e.g. Pentericci et al. 1999, 2001), and their extended emission is often aligned with the radio jets (McCarthy et al. 1987; Chambers et al. 1987). HzRGs are usually surrounded by giant Ly $\alpha$  halos of hot gas that can extend for hundreds of kiloparsecs.

The properties of HzRGs, and the fact that several are located within proto-clusters (Venemans et al. 2007), led to the suggestion that these galaxies are the progenitors of brightest cluster galaxies (Miley & De Breuck 2008) and are thus a separate population to other massive galaxies. However, since these galaxies are caught in a short-lived but very luminous phase of AGN activity, their morphology and other properties may be distorted by this activity.

The Spiderweb galaxy (MRC 1138-262) at  $z = 2.2$  is a powerful HzRG that differs from other massive galaxies at the same epoch. It resides in one of the densest  $z > 2$  protoclusters (Kurk et al. 2000), it is surrounded by tens of galaxies that could merge with it or form an extended cD halo (Miley et al. 2006; Hatch et al. 2009), and it is bathed in diffuse UV light emitted from young intergalactic stars (Hatch et al. 2008). The galaxy is caught undergoing a dramatic feedback episode in which a significant fraction of the ambient gas in its halo could become unbound (Nesvadba et al. 2006). Cosmological simulations suggest these feedback episodes in the early Universe may play an important role in galaxy evolution (Croton et al. 2006). But are these extreme feedback episodes limited to a special population of brightest cluster galaxy progenitors, such as the Spiderweb galaxy, or do they affect other populations with properties more typical of massive distant galaxies?

We selected two massive HzRGs (MRC 0406-244 and TX 0828+193) at  $z \sim 2.5$  that consist of multiple components aligned with the radio jets, which are also undergoing similarly powerful feedback episodes (Nesvadba et al. 2008). Using deep high-resolution optical and near-infrared Hubble Space Telescope (*HST*) images, we have decomposed the light from these galaxies into their constituent parts: scattered AGN light, nebular emission, and light from the blue and red stellar populations, in order to determine whether HzRGs are a special population, or normal massive galaxies undergoing a special event.

## 6.2 Observations

Deep images of MRC 0406-244 and TX 0828+193 were obtained with the Advance Camera for Surveys (ACS) and the Wide Field Camera 3 (WFC3) on board the Hubble Space Telescope (*HST*). A single  $3.5' \times 3.4'$  ACS and  $2.3' \times 2.1'$  WFC3 field

was observed for each HzRG through the optical filters F606W ( $R_{606}$ ) and F814W ( $I_{814}$ ) with ACS, and near-infrared filters F110W ( $J_{110}$ ) and F160W ( $H_{160}$ ) with WFC3. The total exposure time was 1 orbit in the  $J_{110}$  and  $H_{160}$  filters (2612 seconds), and 4 orbits in the  $R_{606}$  and  $I_{814}$  filters (10173 seconds). The exception was the  $H_{160}$  image of TX 0828+193, which suffered from strong persistence, due to an earlier observation of Omega Cen, and so was re-observed. The total exposure time of the TX 0828+193  $H_{160}$  image was 2 orbits. The observations were reduced using the PYRAF task MULTIDRIZZLE to produce cosmic-ray removed, registered images. Images were corrected for Galactic extinction using a Calzetti extinction law and  $E(B - V) = 0.053$  mag for MRC 0406-244 and  $E(B - V) = 0.035$  mag for TX 0828+193.

To examine the environment of the HzRGs, a comparison control field was compiled from 4 separate  $J_{110}$  and  $H_{160}$  images of the Subaru Deep Field obtained with program 11149 (PI Egami).  $H$ -band selected catalogues of the HzRG and control fields were created using SExtractor (Bertin & Arnouts 1996) in double image mode. A detection was defined as a minimum of 5 adjacent pixels exceeding the  $3\sigma$  noise. With these detection parameters we found that the catalogues were 85% complete to  $H = 26$  mag. Colours were measured in circular apertures with a  $1.6''$  diameter and total magnitudes were measured using SExtractor's MAG\_AUTO apertures. The edges, bright stars and diffraction spikes were masked to avoid spurious sources and incorrect photometry. After masking, the area covered was approximately  $\sim 4.3$  arcmin<sup>2</sup> for each HzRG fields, and  $\sim 17.2$  arcmin<sup>2</sup> for the control field.

In Sect. 6.3.2 the  $I_{814}$  images are subtracted from the  $H_{160}$  images. Therefore the  $I_{814}$  images were convolved to match the point spread function (PSF) of the  $H_{160}$  images using convolution kernels determined with the IRAF task PSFMATCH. High frequency noise was removed from the PSF matching function by applying a cosine bell taper. The resulting growth curves of stars in the images matched to within 2 per cent at all radii.

## 6.3 Results

### 6.3.1 Colour images

Three-colour [ $R_{606}$ ,  $J_{110}$ ,  $H_{160}$ ] images of the radio galaxies are shown in Figure 6.1. MRC 0406-244 comprises several large clumps and filaments extending approximately 36 kpc ( $4.4''$ ) along the same orientation as the radio jets. There is a strong asymmetry in the colour of the northern and southern extensions. TX 0828+193 consists of 5 bright knots lying approximately north-south, in the same orientation as the radio jets. Two diffuse twisted filaments extend north from the top of the northern-most knot. The emission has a total extent of 28 kpc ( $3.4''$ ). The filaments are most pronounced in  $R_{606}$  and  $J_{110}$ , suggesting that they consist primarily of nebular emission (see Sect. 6.3.2). One of the central knots has a red colour (prominent in  $H_{160}$ ). The other knots are dominated by bluer emission, of

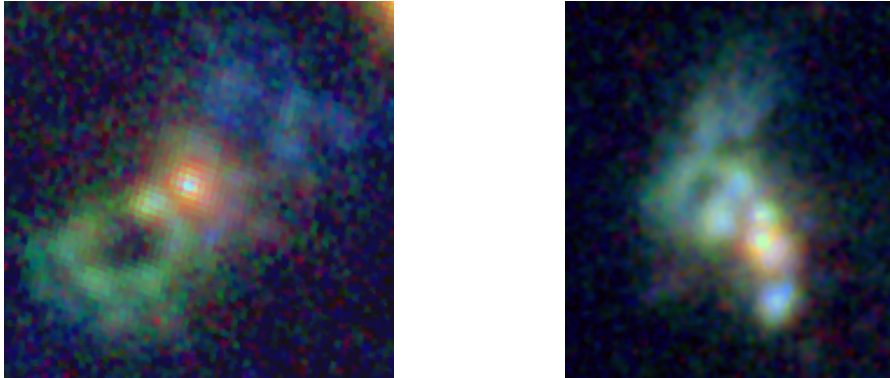


**Figure 6.1** – False colour images of MRC 0406-244 (left) and TX 0828+193 (right). The colours are blue –  $R_{606}$ , green –  $J_{110}$  and red –  $H_{160}$ , and the images are  $5.0'' \times 4.8''$  ( $41 \times 40$  kpc) and  $4.3'' \times 4.8''$  ( $35 \times 39$  kpc), respectively. The yellow object at the top right of the MRC 0406-244 image is a foreground galaxy that is not part of MRC 0406-244.

similar colour to the filaments, suggesting the same processes are involved in their illumination.

### 6.3.2 Decomposing the light from HzRGs

In the following section we use the available data to estimate the respective contributions of different emission mechanisms. The emission line contribution within each filter was calculated using the long-slit spectroscopy of Taniguchi et al. (2001); Vernet et al. (2001); Iwamuro et al. (2003) and Humphrey et al. (2007). Nebular continuum contribution was calculated with the DIPSO STARLINK code NEBCONT using the  $H\beta$  flux, and assuming an electron density of  $500 \text{ cm}^{-3}$  and a temperature of 1100 K (Nesvadba et al. 2008). Table 6.1 lists the amount of light contributed by nebular emission (both line and continuum) within each observed filter. The uncertainties were minimised where possible by taking continuum and line fluxes from the same slit. However, this was not possible for the  $R_{606}$  and  $I_{814}$  bands of MRC 0406-244 where instead the continuum was measured directly from the *HST* images from an area matched to the slit size. Furthermore, the nebular contributions quoted are integrated across the slits and there are likely to be significant variations across the HzRGs.

We note that the nebular emission contributions for MRC 0406-244 listed in Table 6.1 are significantly larger than those reported by Rush et al. (1997) who performed a similar study. Based on a composite radio galaxy spectrum they reported contributions of 12, 2.5 and 7 per cent to their  $r$ ,  $i$  and  $J$  bands with an uncertainty as high as a factor 2. The difference is likely caused by the much improved data that is used in this work to calculate the nebular emission contributions.

**Table 6.1** – Contribution from nebular emission (continuum and line). <sup>1</sup>Only nebular continuum. Nebular line contribution in this filter will be of the order a few per cent.

Band	TX 0828+193	MRC 0406-244	Contributing emission lines
$R_{606}$	34%	62%	HeII1640, Civ 1550, CIII] 1909, OIII] 1663
$I_{814}$	24%	33% <sup>1</sup>	CII] 2326, [NeIV] 2429, [OII] 2471
$J_{110}$	39%	45%	MgII 2798, [NeV] 3426, [OII]3727, [NeIII] 3869
$H_{160}$	31%	23%	H $\gamma$ 4363, HeII 4686, H $\beta$ 4861 (MRC 0406-244 only)

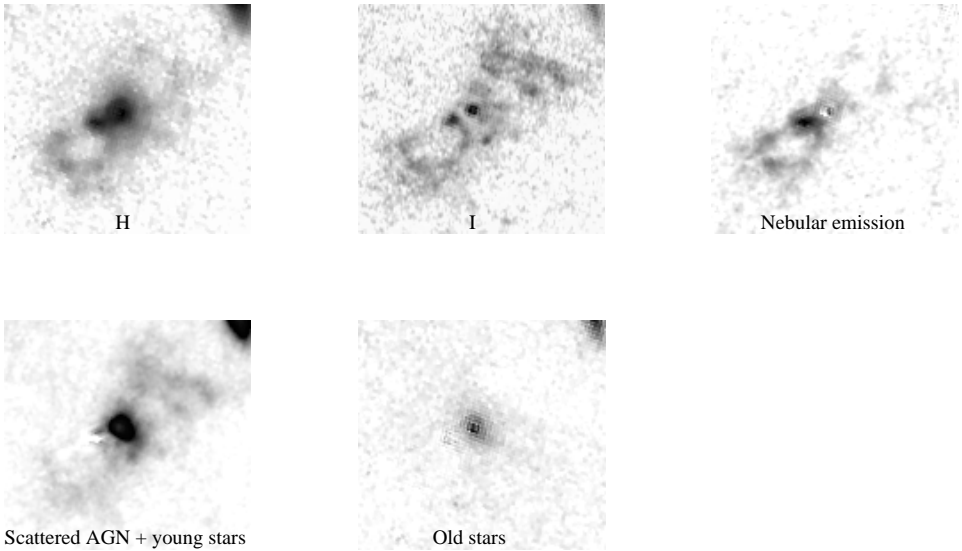


**Figure 6.2** – Decomposing MRC 0406-244 into its separate components: *HST*  $H_{160}$  (WFC3) and  $I_{814}$  images, nebular emission (as traced by [OIII]), scattered AGN light and young stars, and old stars. The old stars are concentrated in a central galaxy, whilst the nebular emission, scattered AGN light and light from the young stars are more extended and aligned along the radio jet axis.

### 6.3.2.1 MRC 0406-244

**Nebular emission:** MRC 0406-244 was observed through the  $H_{160}$  filter with WFC3 (first panel of Fig. 6.2) and has previously been observed with NICMOS (Pentericci et al. 2001). The NICMOS-F160W filter is marginally wider than the WFC3  $H_{160}$  filter so it also encompassed the bright [OIII] doublet at 4959/5007 Å. Subtracting the WFC3 emission from the NICMOS image therefore shows the exact distribution of [OIII] emission.

Details on the reduction of the NICMOS image can be found in Pentericci et al. (2001). The NICMOS image was registered and flux calibrated to match the WFC3 image using 6 nearby objects visible in both images. We could not apply a PSF

correction as there were no stars in the NICMOS images to measure the PSF. The resulting image showing the distribution of the [OIII] emission is displayed in the third panel of Fig. 6.2. The [OIII]/H $\beta$  ratio is fairly constant across the entire galaxy (Humphrey et al. 2009) so this image also shows the distribution of H $\beta$  and nebular continuum within MRC 0406-244.

**Scattered AGN light and young stars:** The  $I_{814}$  image, shown in the 2nd panel of Fig. 6.2, shows rest-frame  $\sim 2300$  Å emission and hence it potentially contains nebular emission, scattered AGN light, and UV light from young stars. Most of the nebular emission in the  $I_{814}$  band is due to nebular continuum since the CII], [NIV] and [OII]2471 Å lines are relatively weak, contributing only a few percent of the emission in the  $I_{814}$ -band. Thus, the distribution of nebular emission in this image is likely to be similar to the [OIII] emission. To remove the nebular component, the nebular emission image was scaled to 33% of the  $I_{814}$  flux and subtracted from the  $I_{814}$ -band image.

The resulting image, displayed in the 4th panel of Fig. 6.2, indicates the distribution of scattered AGN light and young stars. Unfortunately, we are unable to directly distinguish between these two sources of emission. However, the morphology of the residual  $I_{814}$  emission resembles a biconical shape, suggesting the extended UV emission is due to scattered AGN light rather than young stars. Furthermore, the residual  $I_{814}$  emission does not resemble that of the nebular emission, as would be expected if both resulted from ionization by young stars. Dust extinction may reduce the UV light with respect to the nebular emission, but the northwest extension is brighter in UV relative to the nebular emission, so this cannot be caused by reddening.

**Red stellar population:** The  $H_{160}$  band covers emission from just beyond rest-frame 4000 Å, so it also traces light from both the old and young stellar populations, as well as nebular emission and scattered AGN light. The nebular emission was removed by scaling the [OIII] image to 23% of the  $H_{160}$  band flux and then subtracting it from the  $H_{160}$  image.

Scattered AGN light was removed by subtracting a scaled version of the residual  $I_{814}$  image. Grey-scattered AGN light will have a spectral energy distribution (SED) that is similar to the quasar spectrum. Dust-scattered quasar light and light from unobscured young stellar populations have bluer SEDs between 2300 Å and 4000 Å than the average quasar. We can thus estimate the maximum amount of scattered light and young population by assuming that all the light from the residual- $I_{814}$  images comes from grey-scattered quasar light. The average quasar SED has a relative  $I_{814}$ -to- $H_{160}$  flux of 2.83 determined from the spectrum of Vanden Berk et al. (2001). If the residual- $I_{814}$  light is primarily due to a young stellar population or dust scattered quasar light, then we may oversubtract the contribution to the  $H_{160}$  images. We check this possibility in Sect. 6.3.2.3.

The location of the red stellar population is shown in the fifth panel of Fig. 6.2.



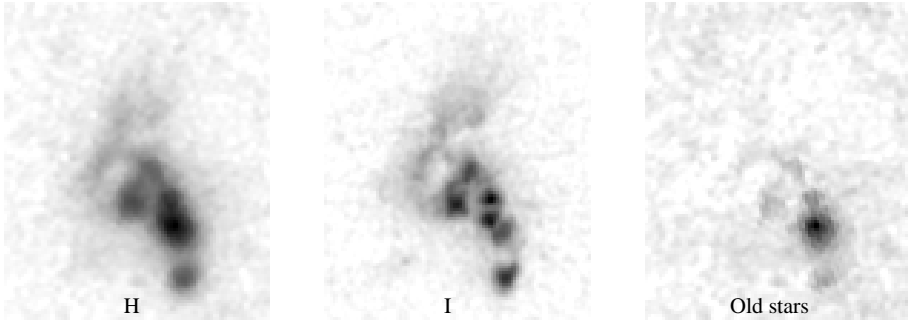


**Figure 6.3** – Decomposing TX 0828+193: original *HST*  $H_{160}$  and  $I_{814}$  images and red stellar population. The residual H-band light (right panel) is concentrated in a central clump corresponding to the brightest knot in the H-band image.

Red stellar populations are often interpreted as being old with little to no ongoing star formation, but may also be young stars that are heavily obscured. The red light originates from a single nuclear region with a regular ellipsoidal morphology. There is no extension along the radio jet axis and the red population shows no signs of tidal features that would have suggested a recent disturbance that may be caused by a major merger.

### 6.3.2.2 TX 0828+193

Fig. 6.3 displays the  $H_{160}$  and  $I_{814}$  *HST* images and the rest-frame optical emission from the underlying red stellar population.

**Red stellar population:** Unfortunately, we cannot determine the distribution of nebular emission as we do not have the appropriate data. However, this galaxy does not display a strong variation in colour, except for the central red knot. The outer parts of the galaxy have similar colours, and Humphrey et al. (2007) report that the spatial distribution of the continuum and emission lines are similar across their long-slit spectra. We thus assume that the distribution of the nebular emission is similar to the continuum in each band, and that the emission in the  $I_{814}$  image displays the distribution of the scattered AGN light and young stars.

To obtain the distribution of the red, and possibly old, stellar population, the nebular emission was removed from the  $H_{160}$  and  $I_{814}$  images by scaling the respective images by the amounts given in Table 6.1. Scattered AGN and young star light was removed by subtracting a scaled version of the  $I_{814}$  image from the  $H_{160}$  image, assuming the same relative  $I_{814}$ -to- $H_{160}$  flux of 2.83 as for MRC 0406-244.

The red stellar population is concentrated into a single clump containing 65% of the residual  $H_{160}$  light. The other 4 bright knots have SEDs that are almost entirely consistent with nebular emission and scattered AGN light, although some of the UV light may also be due to a young stellar population.

### 6.3.2.3 Mass of red stellar population

The residual- $H_{160}$  light shown in the right panels of Figs. 6.2 and 6.3 is greatly reduced compared to the original  $H_{160}$  images. To check that we have not over-subtracted light from the  $H_{160}$  images, we compare the luminosity derived from the residual  $H_{160}$  band images to the expected luminosity from the HzRGs given their large stellar masses determined from Spitzer IRAC measurements (i.e. rest-frame  $1.6\mu\text{m}$  light). Seymour et al. (2007) derive a mass of  $2.4 \times 10^{11} M_{\odot}$  for MRC 0406-244 and obtain an upper limit of  $4 \times 10^{11} M_{\odot}$  for TX 0828+193, but De Breuck et al. (2010) show that the typical mass of a HzRG is approximately  $2 \times 10^{11} M_{\odot}$ , so for simplicity we assume that TX 0828+193 has the same mass as that of MRC 0406-244. TX 0828+193 has 23.1 mag of residual  $H_{160}$  light and MRC 0406-244 has 22.4 mag of residual  $H_{160}$  light.

Based on Bruzual & Charlot (2003) stellar synthesis models, a  $z = 2.5$  galaxy of  $2.4 \times 10^{11} M_{\odot}$  may have an observed  $H_{160}$  magnitude in the range of 20 – 25  $\text{mag}_{\text{AB}}$  depending on dust content and the age of the stellar population. We model the HzRGs as galaxies with exponentially declining star formation histories with  $\tau = 1$  Gyr, that started to form stars prior to  $z = 2.5$ . Assuming this model, a  $2.4 \times 10^{11} M_{\odot}$  galaxy will have an observed  $H_{160}$  magnitude of 23 mag if it contains enough dust to extinguish the light by  $A_V = 1 - 1.5$  mag. Nesvadba et al. (2008) measure  $A_{H\beta} = 1 - 4$  mag in these HzRGs, so the residual  $H_{160}$  luminosities in Figs. 6.2 and 6.3 are more than sufficient to account for an old stellar population of a few  $\times 10^{11} M_{\odot}$ .

### 6.3.3 Sizes of HzRGs

It has been suggested that radio galaxies at  $z > 2$  have larger sizes than normal massive galaxies or sub-mm galaxies (Targett et al. 2011). However, Figs. 6.2 and 6.3 show that much of the extended light above  $4000 \text{ \AA}$  is due to nebular emission, scattered quasar light and young stars. Hence the sizes of the galaxies, as measured from the red stellar population, are likely to be smaller than those measured from the original  $H_{160}$  images.

An ellipsoid model was fit to the  $H_{160}$  and residual- $H_{160}$  images of each HzRG. Since the galaxies do not have regular Sersic profiles, we did not fit a galaxy model to the profiles, but instead determined the circularised effective radius as the half-light radius measured from growth curves. We do not take into account the PSF of the images, but this does not greatly affect our measurements because the measured radii are at least twice as large as the PSF. Uncertainties include contributions from both sky subtraction and measurement errors.

The circularised effective radius ( $r_e$ ) of TX 0828+193 from the  $H_{160}$  image is  $3.3 \pm 0.3$  kpc, but the galaxy appears significantly smaller in the residual- $H_{160}$  image with  $r_e = 2.0 \pm 0.3$  kpc. A similar decrease in size is observed for MRC 0406-244, with  $r_e = 4.4 \pm 0.3$  kpc measured from the  $H_{160}$  image, and  $r_e = 2.9 \pm 0.3$  kpc measured from the residual- $H_{160}$  image. Not taking into account the contribution

of the scattered quasar light and the nebular emission results in sizes that are approximately 65% larger than the true sizes of the red stellar population.

If the effective radii of the HzRGs are measured from the raw  $H_{160}$  images, then the HzRGs lie close to the mass-size relation of local galaxies. However, when we remove the nebular emission and scattered light, then the HzRGs lay below the relation for local galaxies, and have a similar mass-size relationship as other  $z \sim 2$  galaxies (e.g. van de Sande et al. 2011).

#### 6.3.4 Large-scale environment

HzRGs are frequently found within large overdensities of Ly $\alpha$  emitting galaxies (e.g. Venemans et al. 2007), indicating that many lie in forming protoclusters. Establishing protocluster association is more difficult for non-emission line galaxies. However, in a few cases, including the Spiderweb Galaxy, the excess of Ly $\alpha$  galaxies is found to be accompanied by an overdensity of red galaxies (Zirm et al. 2008), indicating a protocluster with an old galaxy population. No Ly $\alpha$  imaging is available for the MRC 0406-244 and TX 0828+193 fields, but the multicolour *HST* images allow us to search for an overdensity of red evolved galaxies.

The area-normalised  $J_{110} - H_{160}$  colour distributions of the surrounding galaxies are shown in Fig. 6.4. For comparison we also plot the distribution of objects in the Spiderweb protocluster (labelled as 1138). To ensure that both the HzRG and control fields are at least 85% complete, we impose a magnitude cut of  $H = 26$ .

There is a marked difference between the density of red galaxies around, on the one hand MRC 0406-244 and TX 0828+193 and, on the other hand the Spiderweb galaxy. Although the uncertainties are large, the density of objects around MRC 0406-244 is not significantly different to that in the control field. The field around TX 0828+193 shows only a mild excess of objects with  $J_{110} - H_{160} > 1.25$ : the TX 0828+193 field is denser by a factor  $1.7 \pm 0.5$ , where the uncertainty is based on Poisson statistics. The strong difference with the Spiderweb protocluster observed at  $J - H > 1.25$  cannot be due to selection effects since such a colour cut is slightly more efficient at selecting  $z \sim 2.5$  galaxies than at selecting  $z = 2.15$  galaxies. We therefore conclude that MRC 0406-244 and TX 0828+193 do not reside in protoclusters that are as dense in evolved galaxies as that around the Spiderweb galaxy.

The lack of evidence for a significant surface overdensity around 0406 and 0828, however, does not mean that these two fields do not host protoclusters. Following a similar argument as used in Kuiper et al. (2010), selecting high- $z$  galaxies through a single near-infrared colour cut probes a large redshift range and therefore only a large volume overdensity can be detected as a significant surface overdensity. We therefore conclude that although we find no evidence that the large-scale environments of these HzRGs differ from that of other distant massive galaxies, the 0406 and 0828 fields may still host protoclusters. Narrowband imaging is needed to determine this.

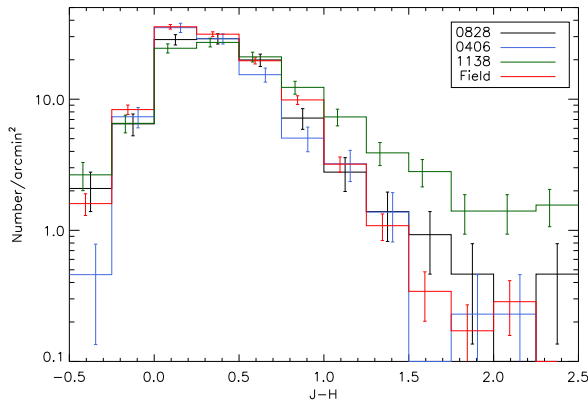


**Figure 6.4** – Number of objects per unit area as a function of  $J - H$  colour for all objects with  $H < 26$  mag for the fields around TX 0828+193 (black), MRC 0406-244 (blue), the Spiderweb galaxy (1138; green), and the combined control fields (red). There is no sign of a significant overdensity of red galaxies in either of the radio galaxy fields.

## 6.4 Discussion

H<sub>z</sub>RGs are spectacularly beautiful galaxies, consisting of multiple clumps and filaments that extend tens of kpc from the galaxy core. Decomposing the light from MRC 0406-244 and TX 0828+193 shows that the nebular emission, scattered AGN light and young stars are aligned with the radio jets and contribute to the alignment effect, but that the red stellar population is not extended nor aligned with the young radio jets. Underneath all the AGN activity, these galaxies appear similar in size and environment to other distant massive galaxies. The red stellar population is located in a single central region, of similar size as sub-millimetre and other high redshift galaxies. It is just their short-lived AGN activity that places them in a league of their own. Once the AGN stops feeding, the jets, induced star formation and any associated winds will die down, and these galaxies may be difficult to distinguish from the rest of the massive galaxy population.

The extended light, however, does imply the presence of a large reservoir of cool and warm gas that extends tens of kpc from the radio galaxy. Nesvadba et al. (2008) estimate the ionised gas component is approximately  $10^{10} M_{\odot}$ , however there is likely to be much more because AGN light is scattered off material in MRC 0406-244 that does not emit emission lines and the cool gas component is likely to be much larger. Does the large reservoir of material exist around all massive galaxies, and are these examples merely illuminated by the AGN activity, or are they a product of AGN outflows?

If these reservoirs are common to all distant massive galaxies, then maybe these will provide an answer concerning the existence of the undersized red galaxies observed at high redshift (e.g. Trujillo et al. 2007; Cimatti et al. 2008; van Dokkum et al. 2008, 2009). If a large, but unseen, gas reservoir is present around these galaxies then that might partially provide the increase in radius needed to put these extreme galaxies on the local size-mass relation. More work is needed to investigate whether this is a plausible scenario.

When comparing to the Spiderweb galaxy, we see that the Spiderweb galaxy shows several characteristics that suggest it is destined to evolve into a brightest cluster galaxy: it resides in one of the densest  $z > 2$  protoclusters, is surrounded by tens of smaller galaxies that can be stripped to form an extended cD halo, and its mass of  $10^{12} M_{\odot}$  makes it one of the most massive galaxies at that redshift. MRC 0406-244 and TX 0828+193 are similar in appearance to the Spiderweb as they consist of several extended clumps which are aligned with the radio jets and are likely to be undergoing AGN feedback. However, neither MRC 0406-244 nor TX 0828+193 show as extreme behaviour as the Spiderweb galaxy: they contain only a fifth of the mass of the Spiderweb galaxy, there is no evidence that they lie in denser than average environments, and their immediate neighbourhood is not populated by many smaller galaxies which can form an extended cD halo. So whilst some HzRGs appear destined to become brightest cluster galaxies, the evolution and fate of TX 0828+193 and MRC 0406-244 is less clear and they may evolve to become more typical massive elliptical galaxies. All of these galaxies are undergoing powerful AGN feedback, that is sufficient to expel a significant fraction of the gas within their halos (Nesvadba et al. 2008). Thus, these AGN feedback phenomena neither require multiple galaxy mergers nor dense protocluster environments.

## References

- Bertin E., Arnouts S., 1996, *A&AS*, 117, 393
- Bruzual G., Charlot S., 2003, *MNRAS*, 344, 1000
- Chambers K. C., Miley G. K., van Breugel W., 1987, *Nature*, 329, 604
- Cimatti A. et al., 2008, *A&A*, 482, 21
- Croton D. J. et al., *MNRAS*, 365, 11
- De Breuck C. et al., 2010, *ApJ*, 725, 36
- Hatch N. A., Overzier R. A., Kurk J. D., Miley G. K., Röttgering H. J. A., Zirm A. W., 2009, *MNRAS*, 395, 114
- Hatch N. A., Overzier R. A., Röttgering H. J. A., Kurk J. D., Miley G. K., 2008, *MNRAS*, 383, 931
- Humphrey A., Iwamuro F., Villar-Martín M., Binette L., Fosbury R., di Serego Alighieri S., 2007, *MNRAS*, 382, 1729
- Humphrey A., Iwamuro F., Villar-Martín M., Binette L., Sung E. C., 2009, *MNRAS*, 399, L34
- Iwamuro F. et al., 2003, *ApJ*, 598, 178
- Kuiper E. et al., 2010, *MNRAS*, 405, 969
- Kurk J. D., Röttgering H. J. A. et al., 2000, *A&A*, 358, L1
- McCarthy P. J., van Breugel W., Spinrad H., Djorgovski S., 1987, *ApJ*, 321, L29
- Miley G., De Breuck C., 2008, *A&A Rev*, 15, 67
- Miley G. K. et al., 2006, *ApJ*, 650, L29
- Nesvadba N. P. H., Lehnert M. D., De Breuck C., Gilbert A. M., van Breugel W., 2008, *A&A*, 491, 407
- Nesvadba N. P. H., Lehnert M. D., Eisenhauer F., Gilbert A., Tecza M., Abuter R., 2006, *ApJ*, 650, 693
- Pentericci L., McCarthy P. J., Röttgering H. J. A., Miley G. K., van Breugel W. J. M., Fosbury R., 2001, *ApJS*, 135, 63
- Pentericci L., Röttgering H. J. A., Miley G. K., McCarthy P., Spinrad H., van Breugel W. J. M., Macchetto F., 1999, *A&A*, 341, 329
- Rush B., McCarthy P. J., Athreya R. M., Persson S. E., 1997, *ApJ*, 484, 163
- Seymour N. et al., 2007, *ApJS*, 171, 353
- Taniguchi Y. et al., 2001, *ApJ*, 559, L9
- Targett T. A., Dunlop J. S., McLure R. J., Best P. N., Cirasuolo M., Almaini O., 2011, *MNRAS*, 412, 295
- Trujillo I., Conselice C. J., Bundy K., Cooper M. C., Eisenhardt P., Ellis R. S., 2007, *MNRAS*, 382, 109
- van de Sande J. et al., 2011, *ApJ*, 736, L9+
- van Dokkum P. G. et al., 2008, *ApJ*, 677, L5
- van Dokkum P. G., Kriek M., Franx M., 2009, *Nature*, 460, 717
- Vanden Berk D. E., et al., 2001, *AJ*, 122, 549
- Venemans B. P. et al., 2007, *A&A*, 461, 823
- Vernet J., Fosbury R. A. E., Villar-Martín M., Cohen M. H., Cimatti A., di Serego Alighieri S., Goodrich R. W., 2001, *A&A*, 366, 7
- Zirm A. W. et al., 2008, *ApJ*, 680, 224



---

## APPENDIX: SINFONI RESULTS ON INDIVIDUAL GALAXIES IN THE SPIDERWEB

In this appendix we present additional results obtained with the SINFONI instrument of the Spiderweb galaxy at  $z \sim 2.15$ . Four protocluster galaxies are bright enough to study the emission line properties of individual pixels. We present velocity and linewidth maps for each of these galaxies. For those galaxies that show [OII], H $\beta$ , [OIII] and H $\alpha$  we also present line diagnostics that can be used to quantify dust extinction, ionising flux and metallicity. For the radio galaxy we find strongly disturbed internal dynamics, consistent with previous studies. We find tentative evidence that the central region of the radio galaxy is relatively unobscured and that dust attenuation becomes stronger further out from the centre. This is in sharp contrast with previous studies. The  $R_{23}$  value for the radio galaxy are uniformly larger than expected from photoionisation models, which may indicate that shocks are the principal means of ionisation in the radio galaxy. The other object which can be studied in great detail is located at a break in the radio jet (#10). The FWHM map shows possible evidence of an interaction between the jet and #10. We further find that this galaxy has little to no dust and  $Z \sim \frac{1}{3}Z_{\odot}$ . Further study is needed to draw conclusions from the figures presented here.

E. Kuiper  
In preparation

## 7.1 Data

### 7.1.1 Integral field spectroscopy

We observed the Spiderweb galaxy and the surrounding field with the Spectrograph for INtegral Field Observations in the Near Infrared (SINFONI, Eisenhauer et al. 2003) on UT4 at the Very Large Telescope (VLT) on several nights in 2007 December and 2008 February. The field was observed in the  $J$ ,  $H$  and  $K$  bands with extra focus on the  $H$  band.

SINFONI is a medium-resolution, image-slicing integral-field spectrograph that has a  $8'' \times 8''$  field of view. A special dithering pattern was adopted to cover most of the central galaxies, leading to an effective field-of-view of approximately  $15'' \times 15''$  centred on the radio galaxy. The spectral resolution of SINFONI varies among the three observed bands from  $R = 2000$  in  $J$  to  $R = 4000$  in  $K$ , corresponding to approximately  $\Delta\lambda = 6 \text{ \AA}$ .

Reduction of the data is summarized in Kuiper et al. (2011, Chapter 2) and is done in a method similar to the method described in Nesvadba et al. (2006) and Nesvadba et al. (2008). We refer to these works for further details.

### 7.1.2 Additional data

The SINFONI data is supplemented by deep Hubble Space Telescope (HST) data. These data were obtained with the Advanced Camera for Surveys (ACS, Ford et al. 1998) in the  $g_{475}$  and  $I_{814}$  bands (Miley et al. 2006) and with the Near Infrared Camera and Multi-Object Spectrometer (NICMOS) in the  $J_{110}$  and  $H_{160}$  bands (Zirm et al. 2008). Details on the data reduction can be found in these papers.

## 7.2 Results

### 7.2.1 Kinematics of individual objects

In Chapter 2 the redshifts of all protocluster candidates near the central radio galaxy have been determined. Here we go into more detail concerning the internal kinematics and emission line properties and diagnostics of the brightest of the protocluster galaxies. For all galaxies discussed here we set the systemic redshift to the redshift presented in Chapter 2. We also use the numbering adopted in that work. For clarity this numbering is shown in Fig. 7.1. Also, in all maps shown, North is up and East is to the left.

**#1/the radio galaxy:** The most prominent source of emission in each of the bands is the central radio galaxy itself. In Fig. 7.2 we show the full summed spectrum of the radio galaxy. The spectrum shows strong [OII], [OIII] and  $H\alpha$  lines that are due to its large star formation rate and the presence of an active supermassive black hole. In addition, several weaker emission lines can be seen as well. The  $J$  band spectrum shows the presence of the [NeIII] $\lambda$ 3869, 3967 doublet indicating hard ionisation possibly caused by shocks. Furthermore, a strong, but



**Figure 7.1** – Overview of the Spiderweb system. Image composed by coadding the  $g_{475}$ ,  $J_{814}$ ,  $J_{110}$  and  $H_{160}$  images. Numbers indicate the labeling used in this work.

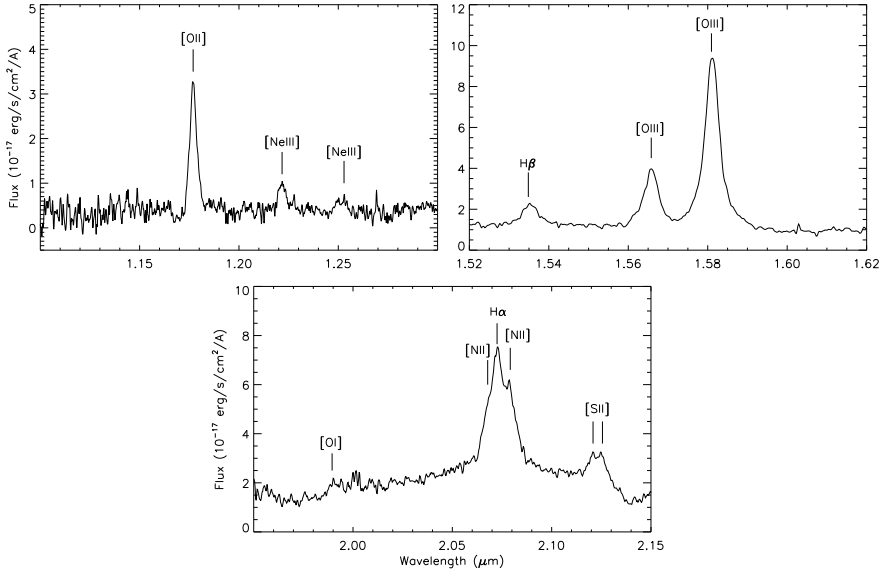
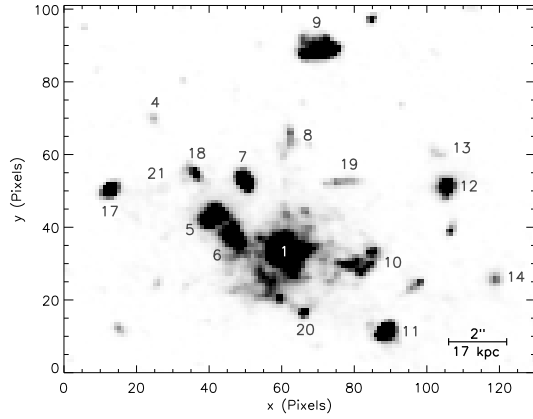


**Figure 7.2** – Summed spectrum of the central radio galaxy in the  $J$ ,  $H$  and  $K$  band.

unresolved  $[\text{SII}]$  doublet is present in  $K$  band. Finally, a weak feature can be seen at  $\sim 19900 \text{ \AA}$  that is consistent with being the  $[\text{OI}]\lambda 6300$  line. However, its location in the wings of the broad  $\text{H}\alpha$  feature makes it difficult to assess whether this feature is real. All three SINFONI bands also show stellar continuum emission from the radio galaxy. The data are not deep enough to identify stellar absorption lines.

The internal kinematics of the radio galaxy have been studied before in Nesvadba et al. (2006, hereafter N06). As is indicated by its disturbed continuum morphology, the kinematic structure of the radio galaxy is complex with evidence

for multiple outflowing ‘bubbles’. The properties of these bubbles and the energy necessary to power them are consistent with being driven by the central AGN.

In the left column of Fig. 7.3 we show a series of three velocity maps based on the [OII], [OIII] and H $\alpha$  emission lines. The [OII] and H $\alpha$  velocity maps have been obtained by fitting the relevant emission line in each pixel with a single Gaussian. For the [OIII] emission line two Gaussians are used, because the complex kinematic structure leads to an additional [OIII] emission line in certain regions. Using a single Gaussian can result in ambiguity when determining the velocities if this additional emission feature is present. The velocities shown in the central panel of Fig. 7.3 denote the weighted mean of the individual velocities, with the fluxes of the individual lines acting as weights.

For all three bands the individual spectra are inspected visually in order to determine whether there is an emission line present and if so, whether it is fit properly. In addition, the panels in Fig. 7.3 show only those pixels with a fitted line flux at the  $> 10\sigma$  level with respect to the rms noise. This is to ensure that the most uncertain pixels are removed from the maps.

The central panel, which is based on the [OIII] emission line, closely resembles the results obtained by N06. A strong redshifted outflow, corresponding to region 1 in N06, is seen to the East of the radio galaxy core, whereas a blueshifted region is seen to the West, corresponding to region 3 in N06. This general picture is also reflected in the H $\alpha$  velocity map. The [OII] velocity map shows a lack of [OII] emission in the North-East region of the radio galaxy. This is the region that shows clear evidence for a high velocity outflow. Summing the  $J$  band spectra in this particular region we do find evidence for [OII] emission with a redshift of  $z = 2.170$  or  $\Delta v \sim +1000$  km s $^{-1}$  with respect to the systemic redshift. This is consistent with the mean velocity of this particular region in the [OIII] velocity map.

The line width maps for the [OII], the [OIII] and the H $\alpha$  line are shown in Fig. 7.3. The [OIII] FWHM map in the central panel shows a line width of 500-1000 km s $^{-1}$  for large parts of the galaxy, but there are distinct regions with larger line widths up to 2000 km s $^{-1}$ . These regions of larger line width are partially seen as well in the [OII] line width map. The H $\alpha$  map in the bottom panel, however, shows larger FWHMs for almost the entire galaxy. This is due to the fact that the H $\alpha$  line is blended with the [NII] $\lambda$ 6548, 6584 doublet, thereby appearing broader. Regardless of this overall increase in the values for the FWHM, the H $\alpha$  map still shows regions of relatively larger line width. These regions coincide roughly with the regions of increased FWHM seen in the [OIII] FWHM map.

Comparing the FWHM maps to the velocity maps of Fig. 7.3 it can be seen that the regions of large FWHM coincide with those regions that show large velocity gradients. This could indicate that the large FWHM regions are associated with the outflows.

The complexity of the kinematic structure is further illustrated in the spectra shown in Fig. 7.4. Five spectra are shown, each corresponding to a certain region

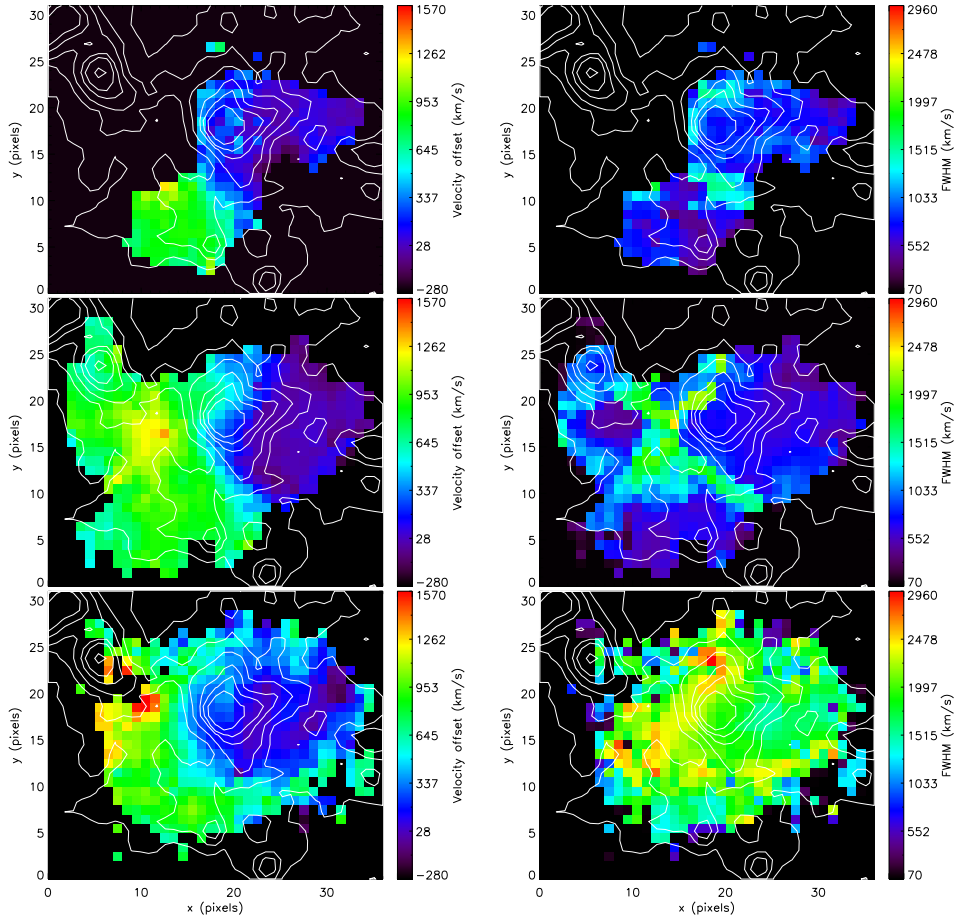


**Figure 7.3** – Velocity and line width maps of the central radio galaxy in the left and right columns respectively. The maps have been made using, from top to bottom, [OII], [OIII] and H $\alpha$ . White contours are obtained from the ACS  $I_{814}$  image.

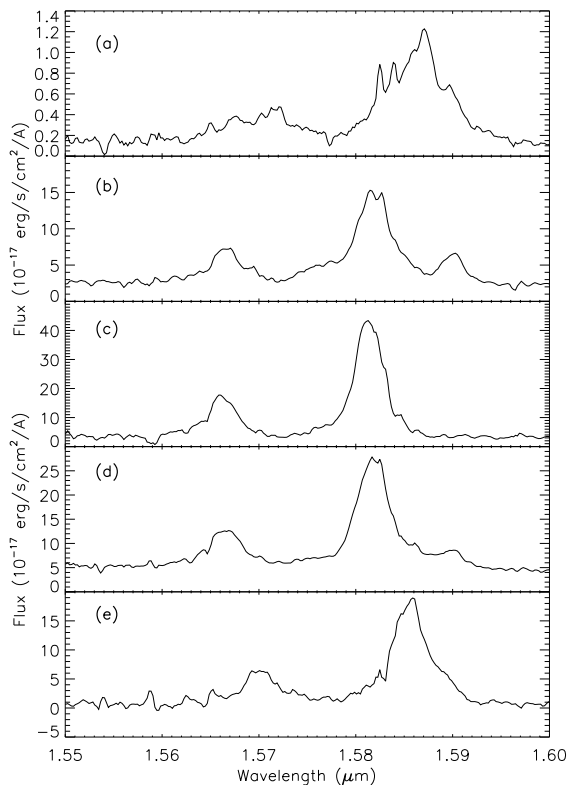


**Figure 7.4** – Summed  $H$  band spectra of five distinct regions of the radio galaxy illustrating the complex kinematics of the galaxy. The regions are from top to bottom: East, North, West, central and South.

of the radio galaxy. Panel (c) shows the summed spectrum of the Western region which is largely blueshifted. This spectrum shows a regular [OIII] doublet without additional features. This is also the case for panel (e), which shows the southern region. Panels (a) and (b) show summed spectra of the Eastern and the Northern region, respectively. In panel (b) we see an additional emission feature redward of the main [OIII] emission line, the two of which have merged in panel (a). Panel (d) (the central region) also shows evidence of this additional, strongly redshifted [OIII] line.

The brightness of the radio galaxy allows us to study in some detail a number of line diagnostics that give information on a few galaxy properties. The ratio of  $H\alpha$  flux to  $H\beta$  flux, for instance, is a measure of extinction. This is given as

$$E(B - V) = \frac{2.5}{k(H\beta) - k(H\alpha)} \log \left( \frac{F_{H\alpha}}{2.85 F_{H\beta}} \right) \quad (7.1)$$

where 2.85 is the intrinsic ratio for Case B recombination (Osterbrock 1989) and  $k(H\alpha)$  and  $k(H\beta)$  are calculated using the Calzetti et al. (2000) extinction law. The resulting extinction map is shown in the left panel of Fig 7.5. Only those areas

are shown for which we are able to determine a robust  $H\beta$  flux. The map shows that the extinction in the radio galaxy is large, with  $0.5 < E(B - V) < 1.5$ . These values are likely overestimated due to the blending of  $H\alpha$  with the  $NII$  doublet.

It is interesting to note that the location with the largest line emission flux is also the location with the least extinction in the  $E(B - V)$  map. The extinction at this location is  $E(B - V) \sim 0.5$  mag. Going outward from this brightest pixel the extinction increases up to  $E(B - V) \sim 1.3$  mag. This implies that the central regions of the radio galaxy are relatively unobscured in comparison with the outer regions.

For the regions that do not show significant  $H\beta$  emission it is difficult to assess how large the dust obscuration is. We try to estimate how large the dust extinction is by assuming a  $3\sigma$  upper limit to the  $H\beta$  flux for those pixels that do not show  $H\beta$  emission. The FWHM values we assume are taken from the  $[OIII]$  linewidth map shown in Fig. 7.3. The resulting map is shown in the right panel of Fig. 7.5. There is a clear discontinuity between the region with ‘accurate’  $E(B - V)$  measurements and the region with  $H\beta$  upper limits, jumping from  $E(B - V) \sim 1.0$  mag to  $E(B - V) \sim 2.0$  mag. Since we consider  $H\beta$  upper limits, the  $E(B - V)$  values are formally to be considered as lower limits. This implies that the discontinuity is even larger. However, the blending of  $H\alpha$  implies that the  $H\alpha$  flux is an upper limit further complicating the interpretation of the outer regions in terms of  $E(B - V)$ . If we consider an extreme contamination by  $[NII]$  and assume the flux ratio between  $H\alpha$  and  $[NII]$  is 1:1, then the  $E(B - V)$  values in the maps would decrease by 0.6 mag. If we only apply this to the outer regions without  $H\beta$  emission, then  $E(B - V)$  would decrease to  $\sim 1.5$  mag. Therefore, the outer regions would still have larger extinction than the central regions. There is thus evidence that the outer regions of the radio galaxy are dustier than the inner regions. However, we must note that this can also be caused by a gradient in the contribution of the  $[NII]$  doublet to the  $H\alpha$  flux. If the contribution of the  $[NII]$  doublet is larger in the outer regions than in the central region, then there might not be any  $E(B - V)$  gradient.

If there is such a gradient, then this is surprising. In Kurk (2003) a  $Ly\alpha/H\alpha$  map was presented which showed a small line ratio of 0.09 at the core of the radio galaxy. This would indicate that the  $Ly\alpha$  flux is strongly suppressed by possibly dust. However, based on the  $H\alpha/H\beta$  ratio we find evidence that the core should be relatively unobscured. Further study is necessary to explain this apparent discrepancy.

Another useful line diagnostic is  $R_{23}$  (Pagel et al. 1979) which is, in the absence of  $[OIII]\lambda 4363$ , the best measure of metallicity. It is defined as

$$R_{23} = \frac{F_{[OII]} + F_{[OIII]\lambda 4959} + F_{[OIII]\lambda 5007}}{F_{H\beta}}. \quad (7.2)$$

The resulting  $R_{23}$  maps of the central region of the radio galaxy are shown in Fig. 7.6. The left and right panel show the  $R_{23}$  values obtained without and with correcting for dust extinction, respectively. These maps should therefore be

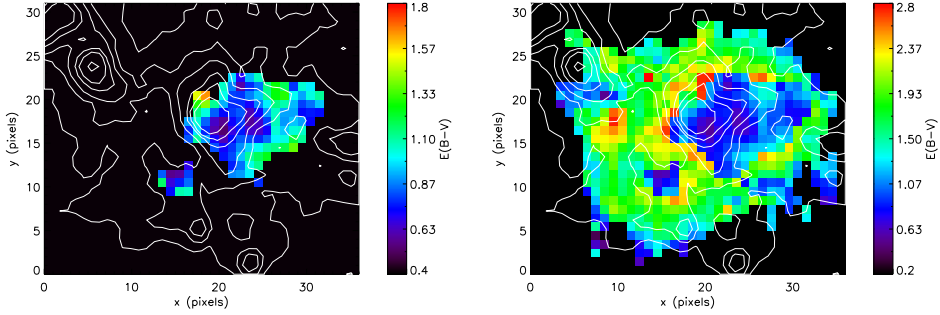


**Figure 7.5** – Maps of colour excess  $E(B - V)$  across the radio galaxy. The left panel shows the map for only those pixels with  $H\beta$  line emission. The right panel shows  $E(B - V)$  values for all pixels with  $H\alpha$  emission and assumes upper limits for the  $H\beta$  emission. White contours are obtained from the ACS  $I_{814}$  image.

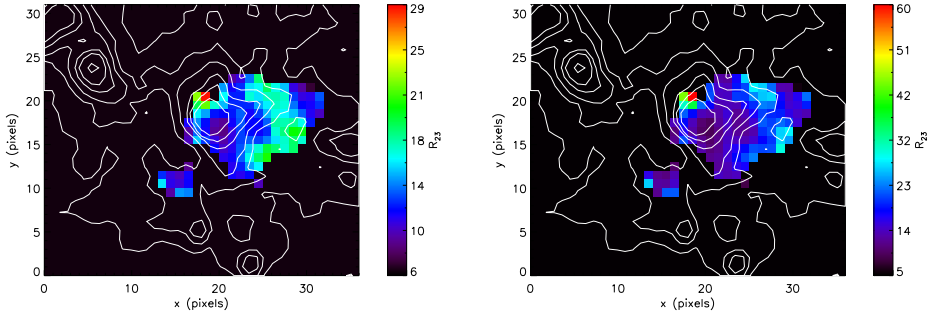


**Figure 7.6** – Maps of the  $R_{23}$  ratio across the radio galaxy. In the left panel no correction for dust extinction is applied. For the right panel the relevant emission line fluxes are corrected for dust attenuation. White contours are obtained from the ACS  $I_{814}$  image.

considered the upper and lower limits to the true  $R_{23}$  values.

A similar trend is seen as in the  $E(B - V)$  map: the central region has low  $R_{23}$  values of  $\sim 10 - 15$  and this increases going out. There is also a small number of pixels with very large values for  $R_{23}$  in the North-East. These values are due to large dust extinction, strongly boosting the dust-corrected [OII] flux. In general, however, the  $R_{23}$  values in both maps are large. In low- $z$  studies  $R_{23}$  is generally found to be  $< 12$  (e.g. Nagao et al. 2006). High- $z$  studies tend to find similar values (Maiolino et al. 2008). The majority of the pixels in both  $R_{23}$  maps show values  $> 12$  and even exceeding  $R_{23} = 15$ . It therefore seems that even without reddening correction, the properties of the emission line gas in the radio galaxy are fundamentally different from that observed in local HII regions. It may be that, rather than photoionisation, the emission lines are caused by shock ionisation. Further study is needed to clarify this. Since the  $R_{23}$  maps show anomalously large values we cannot determine an actual metallicity.

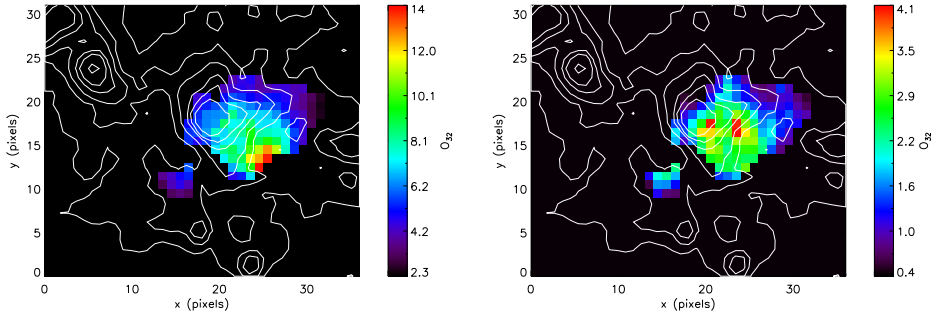


**Figure 7.7** – Maps of the  $O_{32}$  ratio across the radio galaxy. The left and right panel show results with observed fluxes and dust-corrected fluxes, respectively. White contours are obtained from the ACS  $I_{814}$  image.

The final line diagnostic that we will consider is  $O_{32}$ . The  $O_{32}$  ratio is defined as the ratio between the total [OIII] and total [OII] flux.  $O_{32}$  is representative of the ionisation parameter  $U$ , because the lines are of the same element, but different ionisation states. Figure 7.7 shows the dust-uncorrected and dust-corrected  $O_{32}$  panels for the radio galaxy. Larger values of  $O_{32}$  correspond to a larger ionisation parameter: a larger number ionising photons. The ionisation parameter is found to be largest near the central regions. This is probably due to the powerful AGN at the centre of the galaxy. This region also hosts the [NeIII] lines seen in the left panel of Fig. 7.2. Being higher ionisation state lines, these features already indicate the presence of a large ionising flux.

**#10:** This is an interesting object due to its close proximity with respect to the main radio galaxy. It is located approximately  $2''$  to the West of the radio galaxy. More importantly though, the radio jet originating from the central AGN shows a break at this exact location. The galaxy shows a large Ly $\alpha$  flux (Pentericci et al. 1997; Kurk 2003) and is also one of the brightest objects in the SINFONI data. In Chapter 2, its redshift was determined to be  $2.1446 \pm 0.0001$  which is  $\sim 1300 \text{ km s}^{-1}$  blueshifted with respect to the systemic redshift of the radio galaxy. Is it possible that the radio jet and the galaxy have a physical connection?

The velocity map of this galaxy is shown in the upper panel of Fig. 7.8 and is based on the [OIII] emission line. This is because the  $H$  band data is deepest and of the best quality. The [OIII] velocity map shows a smooth, but irregular velocity structure. The velocity structure can be divided into three general regions: redshifted motion in the east, blueshifted motion in the southwest and redshifted motion in the northwest. This division in three distinguishable regions is reminiscent of the UV continuum morphology which also shows three separate clumps. This is illustrated by contours in Fig. 7.8. These contours have been obtained from the  $g_{475}$  image. The pixel scale has been matched to the pixel scale of SINFONI, but the  $g_{475}$  image has not been smoothed to match the PSF of SINFONI. Doing this would result in the loss of the clumpy substructure. Nevertheless, even

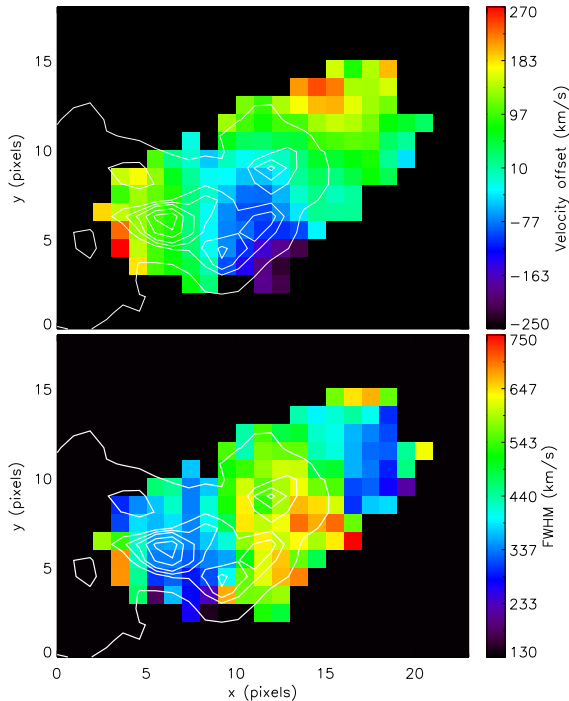


**Figure 7.8** – Top panel and bottom panels show the velocity and linewidth map of satellite #10, respectively. Both maps have been made using the [OIII] emission line. White contours are obtained from the ACS  $g_{475}$  image.

though the PSFs do not match, the locations of the different regions in SINFONI match with distinct clumps in the continuum image. This indicates that the individual clumps are moving relative to each other with velocities of the order of  $\sim 200 \text{ km s}^{-1}$ .

The division in different regions is also apparent in the linewidth map shown in the bottom panel of Fig. 7.8. Both of the redshifted regions show relatively small linewidths of  $300\text{--}400 \text{ km s}^{-1}$  whereas the southwest region shows larger linewidths of  $500\text{--}700 \text{ km s}^{-1}$ . The more turbulent gas is located at the approximate position of where the radio jet bends. This could be tentative evidence that there really is an interaction between the jet and the galaxy. However, this needs to be studied in more detail to draw any strong conclusions.

Since #10 shows a few additional emission lines, such as  $\text{H}\beta$ , we can check several line diagnostics as we have done for the central radio galaxy. However, galaxy #10 is substantially fainter than the central radio galaxy, severely limiting the number of pixels that show significant emission. Therefore we will limit our analysis to the average properties of the galaxy. In Fig. 7.9 we show the full summed spectrum of the galaxy. All pixels that show [OIII] emission have been included and individual spectra have been corrected to match the systemic redshift.

From the summed spectrum we find a small amount of dust extinction with  $E(B - V) = 0.12 \text{ mag}$ .  $\text{H}\alpha$  cannot be distinguished from [NII], therefore the



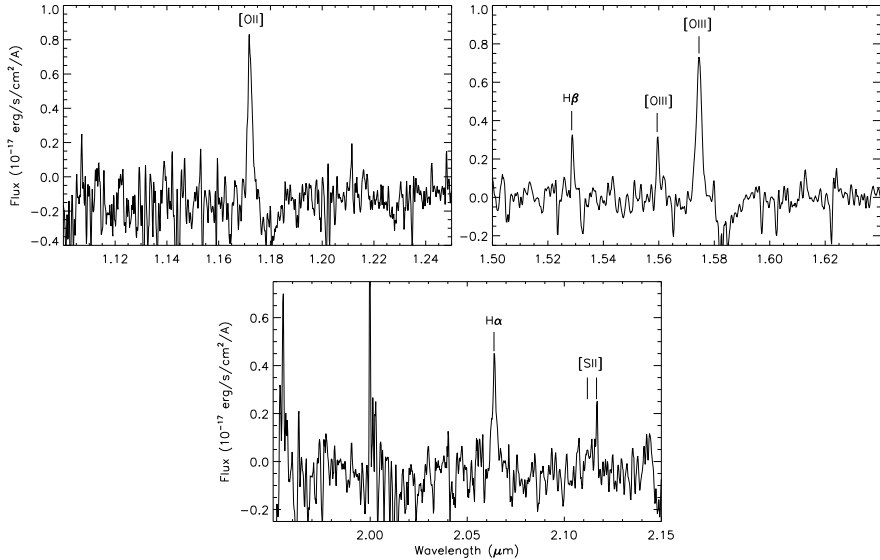


**Figure 7.9** – Summed spectrum of galaxy #10. Main emission lines are marked.

$H\alpha$  flux is likely overestimated. This in turn means that  $E(B - V)$  should be considered an upper limit. There is thus very little dust attenuation in galaxy #10. This is consistent with the  $Ly\alpha/H\alpha$  map of Kurk (2003), where a value of 11.3 was found. This is close to the value of 10 which is expected from case B recombination (Osterbrock 1989) and therefore consistent with little to no dust extinction. Ignoring any correction for dust, we find  $R_{23} = 11.2$  and  $O_{32} = 0.9$ . In comparison to the radio galaxy, the  $R_{23}$  ratio of #10 is more in line with what is found for other galaxies.

Obtaining a metallicity from  $R_{23}$  is difficult due to the fact that  $R_{23}$  has a ‘two-branch’ degeneracy in metallicity and depends on the ionisation parameter  $U$ . We attempt to get an estimate of the metallicity by applying the upper branch parametrisation of Tremonti et al. (2004) and the lower branch parametrisation of Hu et al. (2009). The upper branch is given by

$$12 + \log(O/H) = 9.185 - 0.313x - 0.264x^2 - 0.321x^3 \quad (7.3)$$

with  $x \equiv \log R_{23}$  and the lower branch is given by

$$12 + \log(O/H) = 6.45 + 0.15R_{23}. \quad (7.4)$$

This yields values of  $12 + \log(O/H) = 8.2$  and  $12 + \log(O/H) = 8.1$ , respectively.  $R_{23}$  is thus such that the two metallicity branches almost meet and the degeneracy is not that strong. These values in turn convert to  $\log(Z/Z_{\odot}) = -0.5$  and  $\log(Z/Z_{\odot}) = -0.6$  using  $\log(Z_{\odot}) = 8.69$  (Allende Prieto et al. 2001). These values are also consistent with the parametrisation of Maiolino et al. (2008) which is

based on  $z > 3$  objects. The metallicity of galaxy #10 is therefore  $\sim \frac{1}{3} Z_{\odot}$ . Note that this is a very rough estimate and further study is needed to verify this value.

The  $O_{32}$  ratio found for #10 seems to fall at the lower end of what is found for the radio galaxy. The ionisation parameter and the ionising flux therefore seem to be considerably smaller in #10 in comparison with the radio galaxy. Nevertheless, the galaxy still shows a remarkably large Ly $\alpha$  flux. The narrowband imaging of Pentericci et al. (1997) shows evidence that the extended Ly $\alpha$  halo of the system as a whole seems to have its peak flux at the location of #10 rather than the radio galaxy itself. Further research is needed to examine what this means in the context of the results presented here.

**#12:** This galaxy has an H $\alpha$  narrowband excess indicating H $\alpha$  line emission at the protocluster redshift. It was also selected as a protocluster candidate through its red colour (Hatch et al. 2009) and spectroscopically confirmed to be at the redshift of the radio galaxy in Chapter 2. In Fig. 7.10 the velocity and FWHM map are shown. Only maps obtained with the [OIII] line are shown as there is no indication of [OII] emission and the H $\alpha$  emission is affected by poor night-sky transmission. This also means we will only present velocity and linewidth maps for this galaxy.

The velocity map shows a structure that may resemble a rotating disk, with redshifted motion on the top right and blueshifted motion on the bottom left of the galaxy. The FWHM maps, however, show a marked increase in the linewidth at the exact location of the blueshifted velocities. To determine whether this is truly a rotating disk an in depth kinemetry study is necessary (Krajinović et al. 2006; Shapiro et al. 2008). This is beyond the scope of this work.

**#21:** In Hatch et al. (2009) a bridge of red light was found between galaxies #17 and #18. The origin of the bridge of red light is unknown, but relatively strong line emission is found in the  $H$  band at the approximate location of this bridge. In Chapter 2 this was identified as being [OIII] at  $z = 2.1505 \pm 0.0010$ . No [OII] or H $\alpha$  emission is found to verify this. The velocity and FWHM maps of the bridge are shown in Fig. 7.11.

The velocity map shows a clear bimodal velocity distribution with blueshifted emission in the West and redshifted emission in the East. The blueshifted clump coincides with the peak of the  $H$  band emission, whereas the redshifted line emission is in an arc and does not show any clear spatial correlation with the continuum flux. The two clumps are shifted  $\sim 800 \text{ km s}^{-1}$  with respect to each other. Furthermore, there is no velocity gradient in either of the clumps which would indicate a continuous velocity variation between the clumps.

Hatch et al. (2009) hypothesised that the red light comes from gas that is gas being stripped from a merging system. This would imply that both #17 and #18 are protocluster galaxies as well even though no evidence for this can be found. An alternative possibility is that this is a heavily obscured galaxy, with all UV radiation being extinguished by large amounts of dust. If this is the case, one may expect some emission at longer wavelengths. Therefore we have visually

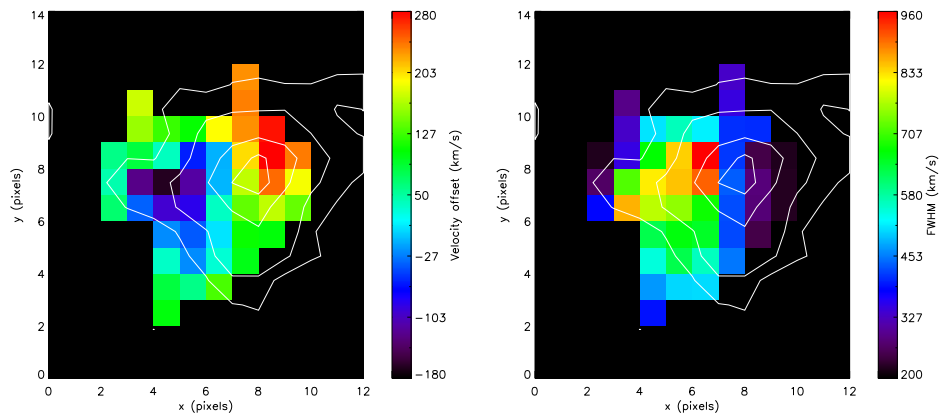


**Figure 7.10** – Velocity and FWHM maps of satellite #12 in the top and bottom panel, respectively. Both maps are obtained using the  $[\text{OIII}]$  emission line. White contours are obtained from the NICMOS  $H_{160}$  image.

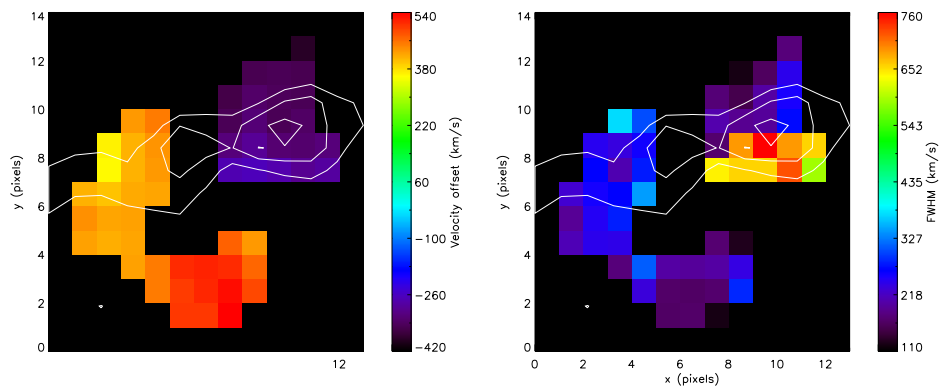


**Figure 7.11** – Velocity and FWHM maps of satellite #21. White contours are obtained from the NICMOS  $H_{160}$  image.

investigated Spitzer images at 3.6-24  $\mu\text{m}$  for traces of restframe optical emission (Audrey Galametz, private communication). However, the crowded nature of the field, the brightness of the radio galaxy and the relatively poor spatial resolution of the Spitzer images make it difficult to find strong evidence for this. Considering the large velocity difference between the two clumps, it may be that this is the result of a strong outflow. More data is needed to verify this. The nature of the line emission of #21 thus remains unknown for now.

## References

- Allende Prieto C., Lambert D. L., Asplund M., 2001, *ApJ*, 556, L63
- Calzetti D., Armus L., Bohlin R. C., Kinney A. L., Koornneef J., Storchi-Bergmann T., 2000, *ApJ*, 533, 682
- Eisenhauer F. et al., 2003, in Presented at the Society of Photo-Optical Instrumentation Engineers (SPIE) Conference, Vol. 4841, Society of Photo-Optical Instrumentation Engineers (SPIE) Conference Series, M. Iye & A. F. M. Moorwood, ed., pp. 1548–1561
- Ford H. C. et al., 1998, in Society of Photo-Optical Instrumentation Engineers (SPIE) Conference Series, Vol. 3356, Society of Photo-Optical Instrumentation Engineers (SPIE) Conference Series, Bely P. Y., Breckinridge J. B., eds., pp. 234–248
- Hatch N. A., Overzier R. A., Kurk J. D., Miley G. K., Röttgering H. J. A., Zirm A. W., 2009, *MNRAS*, 395, 114
- Hu E. M., Cowie L. L., Kakazu Y., Barger A. J., 2009, *ApJ*, 698, 2014
- Krajnović D., Cappellari M., de Zeeuw P. T., Copin Y., 2006, *MNRAS*, 366, 787
- Kuiper E. et al., 2011, *MNRAS*, 415, 2245
- Kurk J. D., 2003, PhD thesis, Leiden University, P.O. Box 9504, 2300 RA Leiden, The Netherlands
- Nagao T., Maiolino R., Marconi A., 2006, *A&A*, 459, 85
- Maiolino R. et al., 2008, *A&A*, 488, 463
- Miley G. K. et al., 2006, *ApJ*, 650, L29
- Nesvadba N. P. H., Lehnert M. D., De Breuck C., Gilbert A. M., van Breugel W., 2008, *A&A*, 491, 407
- Nesvadba N. P. H., Lehnert M. D., Eisenhauer F., Gilbert A., Tecza M., Abuter R., 2006, *ApJ*, 650, 693
- Osterbrock D. E., 1989, *Astrophysics of gaseous nebulae and active galactic nuclei*, Osterbrock, D. E., ed.
- Pagel B. E. J., Edmunds M. G., Blackwell D. E., Chun M. S., Smith G., 1979, *MNRAS*, 189, 95
- Pentericci L., Roettgering H. J. A., Miley G. K., Carilli C. L., McCarthy P., 1997, *A&A*, 326, 580
- Shapiro K. L. et al., 2008, *ApJ*, 682, 231
- Tremonti C. A. et al., 2004, *ApJ*, 613, 898
- Zirm A. W. et al., 2008, *ApJ*, 680, 224



# NEDERLANDSE SAMENVATTING

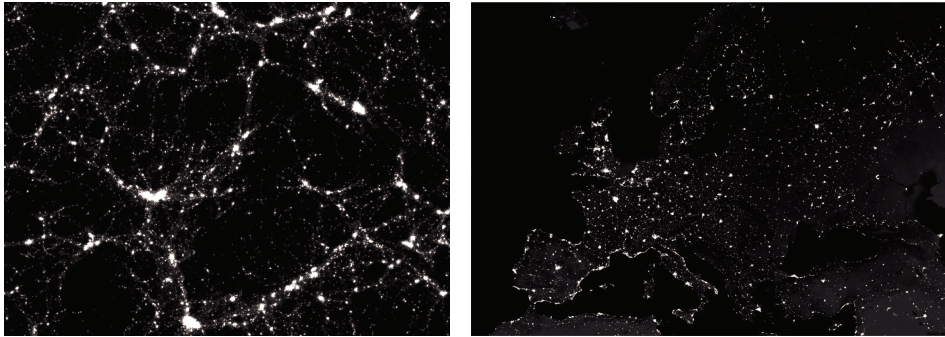
De titel van dit proefschrift is ‘Growing up in the city: a study of galaxy cluster progenitors at  $z > 2$ ’. Dit kan in het Nederlands ongeveer vertaald worden als ‘Opgroeien in de stad: een studie van de voorouders van clusters van sterrenstelsels op  $z > 2$ ’. Nu zullen sommigen die dit proefschrift onder ogen krijgen zich misschien afvragen wat ‘steden’ en ‘opgroeien’ te maken hebben met sterrenkunde in het algemeen en clusters van sterrenstelsels in het bijzonder. Het doel van dit hoofdstuk is om het onderzoek beschreven in dit proefschrift, en dus ook de titel ervan, uit te leggen op een laagdrempelige manier. We zullen dit doen door een introductie te geven van de belangrijkste concepten die in dit proefschrift voorkomen. Door deze concepten toe te lichten zal ook direct de relevantie van dit onderzoek voor de sterrenkunde als geheel duidelijk worden. Aan het einde van dit hoofdstuk zullen de belangrijkste resultaten in dit proefschrift worden samengevat.

## Het begin

Volgens onze huidige kennis is het heelal zoals wij het kennen 13.7 miljard (of 13.700.000.000) jaar geleden ontstaan in wat we de oerknal noemen. We weten niet precies wat deze oerknal is, maar we weten wel dat het heelal ooit in één punt begonnen moet zijn. Dit weten we doordat het heelal uitdijt; alles beweegt van elkaar af. Na de oerknal is er waarschijnlijk een hele korte periode geweest waarin het heelal heel snel uitzette. Dit noemen we de inflatieperiode. Het heelal was hierna te vergelijken met een soort hete oersoep: een bijna homogeen mengsel van elementaire deeltjes en fotonen. Na ongeveer 400.000 jaar was het heelal zover afgekoeld dat waterstof gevormd kon worden: het materiaal waaruit sterren worden geboren.

## Sterren, sterrenstelsels en clusters

Doordat de verdeling van materie tijdens het ontstaan van het heelal niet geheel gelijkmatig was kon zwaartekracht op een gegeven moment een rol gaan spelen. De gebieden waar de dichtheid van de materie groter was begonnen materie uit de omgeving naar zich toe te trekken, waardoor de dichtheid in deze gebieden alleen



**Figuur 8.1** – Links zien we de materieverdeling in het heelal zoals voorspeld door een simulatie. De helderste punten in deze afbeelding zijn clusters van sterrenstelsels. De afbeelding rechts is een satellietfoto van Europa bij nacht. Het contrast van de linker afbeelding is aangepast om beter overeen te komen met de rechter afbeelding.

maar toenam. Uiteindelijk werd de dichtheid van het gas zo groot dat het onder zijn eigen zwaartekracht begon in te storten en sterren begon te vormen. Sterren, zoals bijvoorbeeld onze zon, zijn dus eigenlijk niets meer dan grote bollen waterstofgas.

Sterren vormen niet alleen, maar vaak met duizenden tegelijk. Op plekken waar de gasdichtheid groot is beginnen dan ook sterrenstelsels te ontstaan; grote verzamelingen van vele miljarden sterren. Zulke sterrenstelsels zullen door hun zwaartekracht andere sterrenstelsels naar zich toe trekken. Hierdoor ontstaan er groepen van sterrenstelsels: clusters. Deze clusters worden steeds groter doordat naarmate de tijd verstrijkt steeds meer sterrenstelsels door de zwaartekracht naar het cluster worden getrokken en uiteindelijk worden opgenomen.

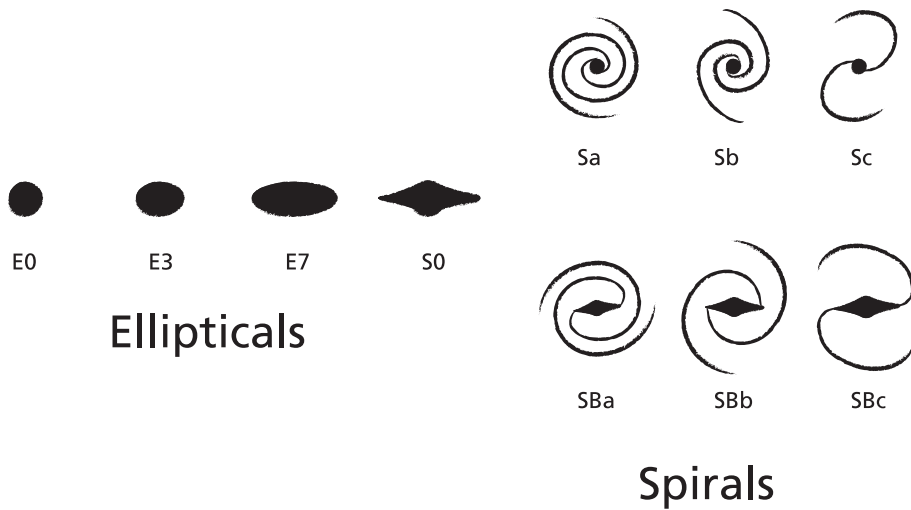
Als we sterrenstelsels zien als mensen, dan kunnen we clusters van sterrenstelsels dus, in zekere zin, zien als steden. De overeenkomst is ook te illustreren door de materieverdeling in het heelal te vergelijken met een satellietfoto van Europa bij nacht, zoals te zien is in Fig. 8.1. Hoewel de afbeeldingen iets geheel anders laten zien, lijkt de algemene structuur in beide afbeeldingen sterk op elkaar. We kunnen dus clusters van sterrenstelsels zien als de metropolen van het heelal.

## De invloed van omgeving

Sterrenstelsels zijn een vrij bonte familie die in veel verschillende vormen en maten voorkomen. Hier zullen we één specifieke methode hanteren en toelichten die gebruikt wordt om onderscheid te maken tussen verschillende types sterrenstelsels.

De twee types sterrenstelsels die we onderscheiden zijn gekwalificeerd als ‘early-type’ of ‘late-type’, wat we kunnen vertalen als ‘vroeg’ of ‘laat’. Deze kwalificatie is een simpelere versie van de Hubble reeks (afgebeeld in Fig. 8.2) en is vooral gebaseerd op de vorm van het sterrenstelsel. Let op dat deze benamingen niet betekenen dat een vroeg-type sterrenstelsel met de tijd zal veranderen in een laat-type sterrenstelsel.





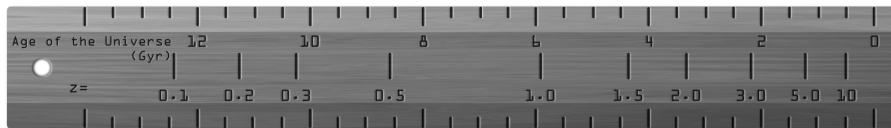
**Figuur 8.2** – De Hubble reeks. De stelsels aan de linkerkant zijn ‘ellipticals’; voorbeelden van vroeg-type stelsels. De stelsels aan de rechterkant zijn typische spiraalstelsels en vallen daarom in de categorie van de laat-type stelsels. Image credit: Bakabaka design.

De laat-type stelsels zijn typisch spiraalstelsels: sterrenstelsels waarin de sterren zich in een dunne platte schijf bevinden. Deze schijven vertonen vaak een spiraalpatroon, zoals de naam al aangeeft. Een belangrijk kenmerk van deze sterrenstelsels is dat ze over het algemeen een grote hoeveelheid blauwe sterren bevatten. Blauwe sterren zijn over het algemeen massief en leven kort. De aanwezigheid van blauwe sterren is dus een duidelijke indicatie dat het sterrenstelsel nog actief sterren vormt.

De vroeg-type stelsels zien er echter heel anders uit. Deze sterrenstelsels zijn meer bolvormig en hun vorm wordt vaak vergeleken met die van een rugbybal. Deze stelsels worden dan ook vaak elliptische stelsels genoemd. Een interessant contrast met de laat-type stelsels is dat vroeg-type stelsels voornamelijk bestaan uit rode sterren. Het ontbreken van blauwe sterren duidt er dus op dat er geen sterren meer worden gevormd in deze sterrenstelsels.

Als we nu kijken naar welke types sterrenstelsels er gevonden worden in clusters, dan zien we iets opvallends: het is geen mengsel waarin zowel vroeg als laat-type stelsels even vaak voorkomen. Echter, de vroeg-type stelsels komen veel vaker voor. Daartegenover staat dat in gebieden met een lage dichtheid, het veld, de laat-type sterrenstelsels wel vaak voorkomen. Het is zelfs zo dat hoe hoger de dichtheid is hoe minder blauwe laat-type stelsels er zijn.

Dit verschil tussen stelsels in het veld en stelsels in clusters is een duidelijke aanwijzing dat de omgeving van sterrenstelsels een invloed heeft op hoe sterrenstelsels veranderen en evolueren met de tijd. Dit wordt des te meer duidelijk doordat clusters van sterrenstelsels de enige locaties zijn waar een uniek type sterrenstelsel voorkomt: het cD stelsel. Deze stelsels zien eruit als vroeg-type stelsels, maar zijn



**Figuur 8.3** – Een liniaal die beschrijft hoe roodverschuiving zich verhoudt tot de leeftijd van het heelal. Een Gigayear (Gyr) is 1 miljard jaar. Image credit: Bakabaka design.

veel massiever. Daarbij komt ook dat ze een grote halo hebben van sterren die niet voorkomt bij andere sterrenstelsels. Het feit dat deze sterrenstelsels alleen maar voorkomen in clusters is een teken dat de omgeving een essentiële rol heeft gespeeld in de vorming van deze stelsels.

We weten dus dat de omgeving een rol speelt in de evolutie van sterrenstelsels. Het is echter nog niet duidelijk welk fysische processen deze verschillen precies veroorzaken. Dit is één van de belangrijke vragen in de hedendaagse sterrenkunde en één van de vragen die de basis is voor dit proefschrift.

## Clusters in het vroege heelal

Om erachter te komen wat precies de verschillen veroorzaakt tussen veld- en clustersterrenstelsels en wanneer dit gebeurt is het van essentieel belang dat we clusters bestuderen op elk mogelijk punt tijdens de geschiedenis van het heelal. De geschiedenis van het heelal kunnen we heel simpel bestuderen omdat we dit nog steeds kunnen zien. Het licht dat wij zien heeft namelijk tijd nodig om ons te bereiken. Licht heeft bijvoorbeeld ongeveer 8 minuten nodig om van de zon naar ons te reizen, dus de zon die wij zien is die van 8 minuten geleden. Uiteraard zal een grotere afstand betekenen dat de reistijd voor het licht langer is en dus kijk je verder terug in de tijd. Als we nu kijken naar objecten die heel ver weg staan, dan zien we deze toen het heelal nog relatief jong was. We kunnen dus terug in de tijd te kijken doordat de snelheid van het licht eindig is.

Omdat de objecten in het vroege heelal erg ver weg staan is afstand geen handige maat meer om mee te meten. In plaats daarvan gebruiken we roodverschuiving die we aanduiden met  $z$ . Sterrenstelsels die heel dichtbij staan hebben  $z \sim 0$  en hoe verder weg iets staat des te groter de roodverschuiving zal zijn. De liniaal in Fig. 8.3 illustreert hoe de roodverschuiving samenhangt met de leeftijd van het heelal. Op  $z = 1$  bijvoorbeeld, was het heelal iets minder dan de helft van zijn huidige leeftijd.

Als we zeggen dat we clusters van sterrenstelsels willen bestuderen voor de gehele geschiedenis van het heelal, dan betekent dat dus dat we dat op elke roodverschuiving willen doen. Om dit te doen moeten we eerst clusters van sterrenstelsels vinden. Dit kan op verschillende manieren. Clusters van sterrenstelsels bevatten een grote hoeveelheid heet gas dat röntgenstraling uitzendt. Het vinden van röntgenstraling is dus een goede indicator voor de aanwezigheid van een cluster. Ook wordt er vaak gezocht naar concentraties van rode sterrenstelsels aan

de hemel, want zoals we al gezien hebben, clusters van sterrenstelsels hebben veel rode sterrenstelsels. Deze methodes zijn echter alleen effectief tot  $z \sim 1.5$ . Er is dus een groot gebrek aan clusters tijdens de eerste 4 miljard jaar van het heelal. Dit is jammer omdat clusters gedurende deze periode nog aan het vormen zijn en er zich dus mogelijk een hoop belangrijke processen afspelen. Om (de voorlopers van) clusters van sterrenstelsels te vinden zal er dus een andere methode gebruikt moeten worden.

## Radiosterrenstelsels en protoclusters

Een veel gebruikte methode om de voorlopers van hedendaagse clusters te vinden is door te focussen op zogenaamde ‘high- $z$  radio galaxies’ of hoge roodverschuiving radiosterrenstelsels (HzRGs). Zoals de naam al impliceert zijn dit speciale sterrenstelsels die op hoge roodverschuiving staan ( $z > 2$ ). Daar komt bij dat ze zeer veel radiostraling uitzenden en dus zelfs op hele grote afstanden makkelijk zijn te identificeren. De radiostraling wordt geproduceerd door een superzwaar zwart gat dat zich in het centrum van een dergelijke radiosterrenstelsel bevindt. Als er materie op het zwarte gat valt, dan komt er een grote hoeveelheid energie en straling vrij. Dit wordt vaak ook ‘AGN feedback’ genoemd.

Een belangrijke eigenschap van deze HzRGs is dat ze een grote massa hebben van  $\sim 10^{11} - 10^{12}$  maal de massa van de zon. Dit is vergelijkbaar met de massa van ons eigen Melkwegstelsel, maar de HzRGs hebben veel minder tijd gehad om zo massief te worden. Dus ondanks dat de HzRGs relatief jong zijn, bevatten ze een zeer groot aantal sterren. Dit is belangrijk omdat we denken dat sterrenstelsels zich hiërarchisch vormen. Dit betekent dat kleine sterrenstelsels als eerste vormen en deze smelten vervolgens samen om de grotere, massievere sterrenstelsels te vormen. Om zeer massieve sterrenstelsels, zoals de HzRGs, te vormen is het dus logisch dat er een groot aantal kleinere stelsels aanwezig moet zijn. Oftewel, rondom HzRGs verwachten we een hoge dichtheid aan sterrenstelsels. Dit betekent dus dat HzRGs zich misschien middenin vormende clusters bevinden. Omdat deze clusters nog aan het vormen zijn worden ze ook wel ‘protoclusters’ genoemd.

Dit idee is al eerder getest en het blijkt dat veel HzRGs zich inderdaad in protoclusters bevinden. Dus door de omgeving van HzRGs te bestuderen kunnen we een hoop leren over vormende clusters van sterrenstelsels. Verder kunnen we de eigenschappen van de sterrenstelsels in de protoclusters vergelijken met de eigenschappen van de sterrenstelsels in het veld. Dit geeft mogelijk een hoop informatie over wanneer de invloed van de omgeving duidelijk wordt en welk fysische processen hier verantwoordelijk voor zijn. En omdat HzRGs zo massief zijn, zijn ze uitstekende kandidaten om later cD sterrenstelsels te worden. Door HzRGs te bestuderen kunnen we dus mogelijk ook veel leren over hoe deze extreme stelsels zich vormen.

## Dit proefschrift

De afgelopen vier jaar hebben we, met behulp van meerdere grote telescopen, een aantal HzRGs en hun omgevingen in detail bestudeerd. We hebben nieuwe protoclusters geprobeerd te identificeren en geprobeerd meer te weten te komen over reeds bekende protoclusters. De resultaten van dit onderzoek worden in dit proefschrift gepresenteerd.

In **hoofdstuk 2** presenteren we resultaten van één van de meest bestudeerde HzRGs: de Spiderweb galaxy. Deze HzRG bevindt zich in een protocluster en is omgeven door kleine sterrenstelsels. Of deze kleine stelsels daadwerkelijk in de protoclusters liggen, is onbekend. Met behulp van waarnemingen genomen met het SINFONI instrument laten wij zien dat veel van de kleine stelsels in de kern van de protocluster zich inderdaad in de protocluster bevinden. Dit betekent dat de kern van de protocluster een erg hoge dichtheid heeft. We meten ook de snelheden van de stelsels ten opzichte van elkaar en vinden een brede snelheidsverdeling met twee pieken. Deze verdeling kan moeilijk verklaard worden door de aanwezigheid van één structuur, maar een interactie tussen twee kleine protoclusters kan de waarnemingen wel verklaren. Gezien de bijzondere aard van de Spiderweb galaxy speculeren wij dat de interactie de centrale HzRG mogelijk beïnvloedt. Dit zou betekenen dat zulke interacties een belangrijke rol spelen in de vorming van cD sterrenstelsels.

In **hoofdstuk 3** bestuderen we de protocluster rond HzRG MRC 0316-257 (0316) door sterrenstelsels te selecteren die zich mogelijk in de protocluster bevinden. We selecteren zowel een groep van blauwe, stervormende stelsels, als een groep rode stelsels waar stervorming mogelijk gestopt is. De dichtheid van blauwe stelsels is hoger dan in het veld wat meer bewijs is voor het bestaan van een protocluster. De dichtheid van rode stelsels is echter hetzelfde als in het veld. Dit komt waarschijnlijk doordat de selectiemethode niet nauwkeurig genoeg is. We vergelijken de eigenschappen van de blauwe stelsels in ons veld met resultaten uit de literatuur. Er lijken geen verschillen te zijn in termen van massa en stervormingssnelheid. Er is echter wel een indicatie dat binnen de protocluster de meest massieve en meest actief stervormende stelsels zich in het centrum, dichtbij de HzRG, bevinden. Dat is een indicatie dat de omgeving de sterrenstelsels beïnvloedt.

**Hoofdstuk 4** is een vervolgstudie gebaseerd op de resultaten van **hoofdstuk 3**. In dit hoofdstuk proberen we van een aantal sterrenstelsels te bepalen welke zich daadwerkelijk in de protocluster bevinden. We vinden dat drie sterrenstelsels zich in de protocluster bevinden, terwijl vijf andere stelsels in een mogelijke tweede protocluster liggen die zich direct vóór de eerste bevindt. We laten zien dat, in tegenstelling tot de resultaten van **hoofdstuk 2**, deze twee protoclusters ongerelateerd zijn. Ook onderzoeken we of er verschillen zijn tussen de stelsels in het veld en in de twee protoclusters. We vinden aanwijzingen dat de stelsels in de 0316 protocluster mogelijk minder stof hebben dan de veldstelsels. Ook lijkt het dat de stelsels in de voorgrondcluster verschillen van de stelsels in de 0316 protocluster. Wat het verschil veroorzaakt tussen de twee protoclusters is nog onbekend,

maar het wijst erop dat de omgeving invloed heeft gehad op de sterrenstelsels in de protoclusters.

In **hoofdstuk 5** gebruiken we het nieuwe OSIRIS instrument op de recent in gebruik genomen Gran Telescopio Canarias om te onderzoeken of de HzRG 6C014+326 op  $z \sim 4.4$  zich in een protocluster bevindt. Hiervoor gebruiken we een relatief nieuwe techniek die gebruik maakt van verstelbare smalle filters. We vinden dat er zich relatief veel sterrenstelsels dichtbij de HzRG bevinden. De verdeling in roodverschuiving duidt ook op een concentratie van stelsels dichtbij de HzRG. Deze verdeling wijkt significant af van wat we zouden verwachten als er geen protocluster zou zijn. We concluderen dus dat er een protocluster is rondom de HzRG. Dit laat ook zien dat deze nieuwe techniek een goede manier is om protoclusters rond andere HzRGs te identificeren.

In **hoofdstuk 6** worden twee HzRGs onderzocht met behulp van data genomen met het nieuwe WFC3 instrument op de Hubble Space Telescope. De twee HzRGs zien er complex uit met meerdere componenten. Door het licht van de HzRGs te ontleden in verschillende componenten vinden we dat de ongebruikelijke vorm grotendeels verklaard kan worden door oplichtende nevels en gereflecteerd licht van het centrale zwarte gat. Het licht komt dus waarschijnlijk niet van sterren. De sterren bevinden zich namelijk in een compacte centrale component die vergelijkbaar is in grootte met andere massieve sterrenstelsels. Ook is er geen bewijs dat de omgevingen van deze twee HzRGs protoclusters bevatten. We concluderen dat sommige HzRGs dus in principe niet veel afwijken van andere massieve sterrenstelsels op hoge roodverschuiving en dat het verschil in verschijning tijdelijk is en veroorzaakt wordt door de straling van het centrale zwarte gat.

**Hoofdstuk 7** is een appendix waarin we kort een aantal resultaten laten zien die met behulp van de SINFONI data van de Spiderweb galaxy zijn behaald. Deze appendix dient als inspiratie voor toekomstig onderzoek.



# CURRICULUM VITAE

Ik ben geboren op 21 mei 1984 in Amersfoort waar ik later op 12-jarige leeftijd begon aan het VWO op Het Atrium (voorheen Het Vallei College). Zo rond mijn 14e was ik al dusdanig geïntrigeerd door sterrenkunde dat ik toen al had voorgenomen dit na de middelbare school te gaan studeren.

In 2002, na het VWO cum laude te hebben afgerond, ben ik vervolgens inderdaad begonnen met de studie Natuur- en Sterrenkunde aan de Universiteit Utrecht. De interesse voor sterrenkunde bleef bestaan en ik heb dan ook een groot gedeelte van de vrij in te richten vakken gevuld met sterrenkunde. Voor mijn bacheloronderzoek heb ik gewerkt aan röntgenbronnen in een bolvormige cluster onder de begeleiding van prof. Frank Verbunt.

Na het afronden van de bachelor Natuur- en Sterrenkunde in 2005 ben ik begonnen aan de Master Astrophysics aan de Universiteit Utrecht. Tijdens mijn Masteropleiding heb ik ook meegeholpen aan het opzetten van het eerstejaars vak ‘Het Fascinerend Heelal’, een cursus gericht op studenten die graag iets willen leren over sterrenkunde, maar geen of weinig achtergrond hebben in exacte vakken. Voor deze cursus ben ik ook twee jaar studentassistent geweest. Ook heb ik de kans gehad om een week lang stage te lopen bij de Dutch Optical Telescope op La Palma onder leiding van prof. dr. Rob Rutten. Als afsluitend onderzoek heb ik een jaar samen met dr. Søren Larsen gewerkt aan de nauwkeurigheid van leeftijdsbepaling van extragalactische sterclusters, waarna ik in 2007 de Masteropleiding cum laude heb mogen afronden.

Vervolgens heb ik mijn academische activiteiten verhuisd van Utrecht naar Leiden, waar ik in oktober 2007 mijn promotieonderzoek ben begonnen onder de supervisie van prof. dr. George Miley en prof. dr. Huub Röttgering. De resultaten van dit onderzoek zijn in dit boekwerk te vinden. Deze resultaten zijn gedeeltelijk ook gepresenteerd op conferenties in Heidelberg, Pucón (Chili) en Kashiwa (Japan). Tevens heb ik tijdens mijn promotieonderzoek de kans gehad om te gaan waarneemen op de William Herschel Telescope op La Palma en de Very Large Telescope in Chili. Naast het onderzoek ben ik gedurende drie jaar met veel plezier studentassistent geweest voor het vak Speciale Relativiteitstheorie en ben ik lid geweest van de LOCNOG, een commissie die zich bezig houdt met het sterrenkunde onderwijs op master en promovendusniveau.





# PUBLICATIONS

## Refereed papers

1. **E. Kuiper**, N. A. Hatch, H. J. A. Röttgering, G. K. Miley, R. A. Overzier, B. P. Venemans, C. de Breuck., S. Croft, M. Kajisawa, T. Kodama, K. D. Kurk, L. Pentericci, S. A. Stanford, I. Tanaka, A. W. Zirm, *A galaxy populations study of a radio-selected protocluster at  $z$  3.1*, Monthly Notices of the Royal Astronomical Society, Volume 405, Issue 2, 969-986 (Chapter 3)
2. **E. Kuiper**, N. A. Hatch, G. K. Miley, N. P. H. Nesvadba, H. J. A. Röttgering, K. D. Kurk, M. D. Lehnert, R. A. Overzier, L. Pentericci, J. Schaye, B. P. Venemans, *A SINFONI view of flares in the Spiderweb: a galaxy cluster in the making*, Monthly Notices of the Royal Astronomical Society, Volume 415, Issue 3, 2245-2256 (Chapter 2)
3. N. A. Hatch, J. D. Kurk, L. Pentericci, B. P. Venemans, **E. Kuiper**, G. K. Miley, H. J. A. Röttgering, *The disparity between proto-cluster and field galaxies*, Monthly Notices of the Royal Astronomical Society, Volume 415, Issue 4, 2993-3005
4. D. J. Mortlock, S. J. Warren, B. P. Venemans, M. Patel, P. C. Hewett, R. G. McMahon, C. Simpson, T. Theuns, E. A. González-Solares, A. Adamson, S. Dye, N. C. Hambly, P. Hirst, M. J. Irwin, **E. Kuiper**, A. Lawrence, H. J. A. Röttgering, *A luminous quasar at a redshift of  $z = 7.085$* , Nature, Volume 474, Issue 7353, 616-619
5. **E. Kuiper**, N. A. Hatch, B. P. Venemans, G. K. Miley, H. J. A. Röttgering, J. D. Kurk, R. A. Overzier, L. Pentericci, J. Bland-Hawthorn, J. Cepa, *Hunting for a high- $z$  protocluster with tunable filters: the case of 6C0140+326 at  $z=4.4$* , Monthly Notices of the Royal Astronomical Society, Volume 417, Issue 2, 1088-1097 (Chapter 5)

## In preparation

1. **E. Kuiper**, B. P. Venemans, N. A. Hatch, G. K. Miley, H. J. A. Röttgering, *A  $z \approx 3$  radio galaxy and its protocluster: evidence for a superstructure?*, submitted to Monthly Notices of the Royal Astronomical Society (Chapter 4)
2. N. A. Hatch, **E. Kuiper**, G. M. Miley, H. J. A. Röttgering, C. de Breuck, H. Ford, J. D. Kurk, R. A. Overzier, J. Schaye, B. P. Venemans, A. W. Zirm, *Decomposing the light from high redshift radio galaxies* (Chapter 6)

# DANKWOORD

Bringing a PhD to a successful end is something that you can only achieve with the help of others. I would like to take this opportunity to thank a few people for their support during the past four years.

Firstly, I would like to thank Nina Hatch. Nina, it has been a pleasure and an honour working with you for the past four years. You have been so patient and committed in helping me with everything, down to the stupidest questions (there must have been quite a few). This thesis would not have turned out this well if it wasn't for you. Also, I'd like to express my sincerest gratitude to frequent collaborators Bram Venemans, Roderik Overzier, Jaron Kurk and Laura Pentericci for all the help and wisdom that you have given me over the course of the past four years.

Binnen de Sterrewacht ben ik uiteraard veel dank verschuldigd aan de support staff die het werken bij de Sterrewacht zo soepel maakte. Aan zowel de computer-groep als het secretariaat: bedankt voor het draaiende houden van de Sterrewacht. Evelijn, erg bedankt voor alle assistentie met de financiële zaken, je vriendelijkheid en je interesse in wat mijn volgende stap zou zijn.

Although I have seen a lot of offices during my stay in Leiden, office 527 is the one where I ultimately belong. To my former 527 office mates Sergio and Karoliina, thank you for adopting this weird non-astrochemist. And Karoliina, thanks for organising the Friday afternoon borrel with me. It was a pleasure. To my other former office mate Silvia: what can I say? Let's just put it like this: the Sterrewacht became a lot more fun when you got here. Even after I switched offices you dragged me from behind my computer every day, something I am very grateful for. It has been an absolute joy and don't ever forget that you're awesome. Niruj, first of all thanks for spicing up the Sterrewacht with your fabulousness, but also for sharing your wisdom with me and giving me all these advices. I may not have been the most receptive person, but it really does mean a lot to me.

To the numerous other former and current Sterrewachters that I cannot mention here, but who I have spent countless tea breaks and Friday afternoon beers with, thank you for the last four years and for making the Sterrewacht such a great place to work.

I would like to express my utmost gratitude to cocoip, from [www.flickr.com](http://www.flickr.com), for being so generous as to let a total stranger use this photo for on the cover. It really is the perfect picture.

Mijn familie: mama, bedankt voor alles in de afgelopen 27 jaar. Zonder jouw onvoorwaardelijke steun en liefde was ik niet zo ver gekomen en zou ik nu niet zijn wie ik ben. Joep, mijn grote broer en paranimf. Ik weet dat jullie er altijd voor me zullen zijn en dat betekent meer dan wat ik in woorden uit kan drukken.

Tonny en Gerard, ten eerste ontzettend bedankt voor de hulp bij het verhuizen naar Leiden. Ik was zo verbaasd dat jullie zo voor me klaar stonden ondanks dat jullie mij pas een maand of drie kenden. Het is kenmerkend voor jullie vriendelijkheid, gastvrijheid en hartelijkheid. Ik kan niet anders zeggen dan dat jullie twee van de liefste mensen zijn die ik ooit heb ontmoet. Ik vind het dan ook een eer dat jullie mij tot jullie familie rekenen.

Martijn (en je ouders uiteraard), erg bedankt voor de 5 jaar die ik bij je in huis heb mogen wonen. De verbouwing was soms een uitdaging, zeker de overvloed aan lagen plastic die het soms bijna onmogelijk maakten om het huis uit te komen, maar uiteindelijk kan ik niet anders zeggen dan het een erg fijne tijd was. Bedankt voor alle goede gesprekken en natuurlijk voor alle keren dat ik je keuken heb mogen misbruiken voor al mijn kook- en bakexperimenten.

Maaïke, Johannes, Ilaan, Nicole, Gideon, Mark en Nora. De meeste van jullie ken ik al ruim negen jaar. Een periode gevuld met verregende vakanties, kamikaze roleplay-acties en filmmarathons waarvan ik me de volgende ochtend de films niet meer kon herinneren. Een periode vol met gezelligheid en vooral geweldige herinneringen. Jullie allemaal ontzettend bedankt daarvoor. Maaïke, jou wil ik in het bijzonder bedanken. Ook al zaten we ongeveer 70 kilometer van elkaar af, volgens mij hebben we elkaars onderzoek op de voet gevolgd. Onze dagelijkse chatsessies waren een essentieel deel van mijn dag en soms echt een lichtpuntje in een wereld vol frustratie. Bedankt voor alle steun, voor het zijn van mijn paranimf en bedankt voor alle uurtjes rock 'n roll waar we die frustratie er eens goed uit konden kicken.

Vincent, mijn superbaka, jou wil ik uiteraard ook bedanken. Ten eerste voor de mooie cover natuurlijk, maar ook voor zoveel meer. De afgelopen twee jaar waren geweldig en jij bent daar de oorzaak van. Van samen onder een afdakje in regenachtig Kyoto tot samen op de bank met een aflevering van Buffy. Jij bent het beste wat mij ooit is overkomen. Kimi ga daisuki.